Title

Thermalization and Transport in Hyperpolarized Nuclear Spins

Author

Beatrez, William Smith

Publication Date

2024

Peer reviewed|Thesis/dissertation

Thermalization and Transport in Hyperpolarized Nuclear Spins

by

William Smith Beatrez

A dissertation submitted in partial satisfaction of the

requirements for the degree of

Doctor of Philosophy

in

Chemistry

in the

Graduate Division

of the

University of California, Berkeley

Committee in charge:

Professor Ashok Ajoy, Chair
Professor K. Birgitta Whaley
Professor Jeffrey A. Reimer

Spring 2024

Thermalization and Transport in Hyperpolarized Nuclear Spins

Abstract

Thermalization and Transport in Hyperpolarized Nuclear Spins

by

William Smith Beatrez

Doctor of Philosophy in Chemistry

University of California, Berkeley

Professor Ashok Ajoy, Chair

Conventional phases of matter are described in the limit of thermal equilibrium. Recent advances have suggested that periodically driven, non-equilibrium systems can exhibit novel phases of matter with properties that are highly unusual or not possible in their static counterparts. A broad effort is underway to quantify these systems and explore their applications in quantum information science and materials physics. Hyperpolarized nuclear spin systems have properties that are favorable toward enabling these studies. Conventionally probed by Nuclear Magnetic Resonance (NMR), nuclear spins are highly coherent quantum objects that can be controlled via resonant radiofrequency (RF) pulses. This thesis focuses on ^{13}C nuclear spins in diamond, which can be hyperpolarized to highly non-thermal spin state populations via interaction with optically pumped Nitrogen Vacancy (NV) defect centers in the lattice. This hyperpolarization provides a vast acceleration in experiment throughput by $\sim 10^{10}$ over conventional thermal NMR, enabling highly precise studies of Floquet prethermalization and discrete time crystalline behavior. Further, two novel techniques for nanoscale magnetic resonance imaging are developed with proofs-of-concept shown using hyperpolarized ^{13}C.

To Paula and Hilary Beatrez

Underlying all of the work in this thesis is the 27 years of tender loving care I have received from my parents.

Contents

List of Figures

List of Tables

Acknowledgments

These years of graduate school in Berkeley have been extremely formative for me, both professionally and personally. To make an attempt at a proper acknowledgment for all of the above, I will start with professional and then go through personal.

My advisor, mentor, colleague, collaborator, and sparring partner all in one, Ashok Ajoy. Four years ago, you took a chance on me as your first graduate student, and in doing so you invested the time to introduce the world of NMR to someone who had absolutely no prior knowledge of the field. You gave me the chance to help grow our lab from the ground up into one that is now a blossoming environment of intellectual and social enrichment. Thank you for all of it.

I also want to thank my other dissertation committee members, Birgitta Whaley and Jeff Reimer, for serving in this role for me. You have both provided critical and timely advice over the years in the classroom and also served as extremely helpful and inquisitive members of my qualifying exam committee.

To my collaborators over the years: Dieter Suter, Marin Bukov, Christoph Fleckenstein, and Paul Schindler. Thank you for offering your precious time and shrewd scientific observations. Each of you has deeply impacted the direction of my research projects as well as my own understanding of the field.

All of my labmates over the years. Manny you have saved my life on countless occasions. I know who to call if I ever need someone to bail me out. Ozgur, you are the best late-night Yu Gi Oh duel partner and close friend I never knew I needed in my labspace– thank you for keeping me sane. Anika, Noella, and Adrisha, you have all been in my life for so long that I'm having a hard time imagining my work day without all of you. Zack and David, you both always somehow know exactly what I need to hear. I hope to see you both at the chessboard for years to come! Blake, Joseph, Leo, Cooper, Chongwei, Brooke, Brian– it's been so fun getting to know all of you. I will greatly miss all of your shenanigans. All of the undergraduates and visiting scholars I've worked with over the years deserve a shout-out as well: Otto, Arjun, Amala, Erica, Jesus, Aakriti, Sophie, Victor, Nicolas, Matthias, Matthew, and of course Quentin!! And to the 'new' postdocs Harpreet, Brandon, Madhur, Ryan, Christian– BLAH. Lastly a special shout-out to the future of the 300 setup, Leo and Ryan! I'm very glad to know I'm leaving the project in hands more capable than my own. Everyone I've had the pleasure to work with: thank you for making my time at work very special over the years.

Mom and Dad: thank you for all the love, encouragement, hard lessons, birthday presents, cards in the mail, phone calls, and so much more you've given me. I really mean it when I say that all of the work in this thesis is because of you. You've taught me how to appreciate life and cherish all the blessings that come with it. You've taught me to try to be a good person, but be humble when I know I've messed up. You've taught me the perseverance that fueled me to finish my graduate degree. And above all, you have loved me since day one. Thank you for everything.

Mimi, Farfar, Sarah, Leland, Tristan, Bryan, Patrick, and Nina: I love you all and hope we can all get together for a party soon! I wish that Papa and Farmor could join us – we will dedicate this work to their honor as well.

Emily: you are the partner-in-crime that I did not know I needed. Ever since the day I met you, I've felt that your presence would enrich my life beyond words. Boy was I right– we've gone on countless adventures, spent countless hours making dinner together, and argued about pretty much everything I can think of. Thank you for being such a big part of my life.

All of my friends at Berkeley: Ozgur, Liz, Bailey, Finn, Khalid, Nick, Sean, Orion, Diego, Aaron, Madi, Christie, Gabriel, and all the frisbee teams, softball teams, and pinochle squads. You've lifted me up and shown me unconditional love in many different ways during a stretch of years that hasn't been the easiest. Thank you for walking alongside with me.

Chris: I really appreciate your love and support from afar. Here's to staying close friends through the passage of time and barrier of space! I'll find a time to visit in New York soon, I promise.

I need to give a special thank-you to Eva for helping me with my personal statements in 2019. You helped me get into grad school and eventually win NSF– thank you for being a great friend!!

There are so many teachers and mentors over the years I need to thank as well. Starting in elementary school, Mrs. Kalnasy was the my first ever chemistry teacher, and her lessons left a lasting desire to understand more about solids, liquids and gases! In middle school, Mr. Wolf pushed me to succeed and opened my mind to a wider world of literature. In high school, I had the pleasure of learning from so many great teachers, especially Mrs. Lavelle, Mr. Corrigan, and Ms. McTernan. These three teachers gave me such a strong foundation in chemistry and physics that I won't ever forget the lessons they gave, from dimensional analysis to approaching new questions with inherent curiosity. Other teachers such as Mr. Bosley, Mrs. Fairfield, Mr. Urban, Mr. Stemm, and Mr. Merriman all played an important part in shaping how I see the world today.

I wanted to write a special acknowledgment and heartbreaking farewell to DJ Cavoli, my Latin teacher and coach for four years who always somehow made me feel like I was the most important person in the world every time we interacted. Mr. Cavoli, you accompanied me through so many critical experiences in high school, from jubilant victories at the national Latin conventions, to painful funerals of loved ones, to awe-inspiring moments of personal revelation. You are gone too soon, but I know your soul rests easy now, after a life lived to its absolute fullest. *Atque in perpetuum, frāter, avē atque valē.*

And finally, I need to thank my undergraduate research mentor, Chris Koenigsmann (a.k.a. Dr. K) for showing me how the magic happens. You introduced me to the world of scientific research and encouraged me at every opportunity to dig deeper, consider the implications, and come up with the answer. You put me through the gauntlet my senior year when I told you I wanted to do an independent study and write an honors thesis. It is hard to express how much I learned in these experiences. Thank you for supporting me along this whole journey!

Citations to Previously Published Work

Much of the work in this thesis is adapted from previously published work. In order of appearance:

Chapter 4 is adapted from the following paper:
William Beatrez, Otto Janes, Amala Akkiraju, Arjun Pillai, Alexander Oddo, Paul Reshetikhin, Emanuel Druga, Maxwell McAllister, Mark Elo, Benjamin Gilbert, Dieter Suter, and Ashok Ajoy. "Floquet Prethermalization with Lifetime Exceeding 90 s in a Bulk Hyperpolarized Solid". In: *Physical Review Letters* **127** (17 Oct. 2021), p. 170603. DOI: 10.1103/PhysRevLett.127.170603. URL: `https://journals.aps.org/prl/abstract/10.1103/PhysRevLett.127.170603`.

Chapters 6 and 7 are adapted from the following paper and its Supplementary Material:
William Beatrez,* Christoph Fleckenstein,* Arjun Pillai, Erica de Leon Sanchez, Amala Akkiraju, Jesus Diaz Alcala, Sophie Conti, Paul Reshetikhin, Emanuel Druga, Marin Bukov, and Ashok Ajoy. "Critical Prethermal Discrete Time Crystal Created by Two Frequency Driving". In: *Nature Physics* **19** (12 Jan. 2023), pp. 407-413. DOI: 10.1038/s41567-022-01891-7 URL: `https://www.nature.com/articles/s41567-022-01891-7`.

Chapter 11 is adapted from the following paper:
William Beatrez, Arjun Pillai, Otto Janes, Dieter Suter, and Ashok Ajoy. "Electron Induced Nanoscale Nuclear Spin Relaxation Probed by Hyperpolarization Injection". In: *Physical Review Letters* **131** (1 July 2023), p. 010802. DOI: 10.1103/PhysRevLett.131.010802. URL: `https://journals.aps.org/prl/abstract/10.1103/PhysRevLett.131.010802`.

Chapter 12 is partly adapted from the following paper:
Kieren Harkins,* Christoph Fleckenstein,* Noella D'Souza,* Paul M. Schindler,* David Marchiori,* Claudia Artiaco, Quentin Reynard-Feytis, Ushoshi Basumallick, **William Beatrez,** Arjun Pillai, Matthias Hagn, Aniruddha Nayak, Samantha Breuer, Xudong Lv, Maxwell McAllister, Paul Reshetikhin, Emanuel Druga, Marin Bukov, Ashok Ajoy. "Nanoscale Engineering and Dynamical Stabilization of Mesoscopic Spin Textures". In: arXiv:2310.05635 [quant-ph] (9 Oct. 2023).
DOI: 10.48550/arXiv.2310.05635. URL: `https://arxiv.org/abs/2310.05635`.

Part I

Introduction

Chapter 1

Introduction

1.1 Background and importance of nuclear magnetic resonance

Nuclear magnetic resonance (NMR) is a pivotal technique widely used in chemistry, physics, and biology for the structure determination of molecules and the study of molecular dynamics. Traditionally, NMR studies are limited by the requirement of thermal equilibrium where the nuclear spins are in a Boltzmann distribution. This dependence on thermal equilibrium has placed severe restrictions on the types of possible NMR studies due to the inherently low signal-to-noise ratio, particularly when examining nuclei with low natural abundance or in dilute conditions.

The principle behind NMR involves the absorption and re-emission of radiofrequency (RF) energy by nuclear spins when placed in a strong magnetic field. This process is sensitive to the subtle electronic environments that surround nuclear spins, making NMR an invaluable tool for gaining insights into molecular structure and interactions at the atomic level. However, the sensitivity of conventional NMR is often hampered by the small difference in energy levels between the spin states at room temperature, which limits the detection of signals from nuclei present at low concentrations or those that relax rapidly.

To overcome these challenges, advancements such as hyperpolarization have been developed to enhance the population differences between nuclear spin states far beyond what is achievable under normal thermal conditions. Hyperpolarization significantly increases the NMR signal by increasing nuclear spin polarization, thus amplifying the detectable signal and enabling the study of otherwise inaccessible molecular systems. This technique has opened up new possibilities for NMR, opening applications for real-time reaction monitoring, investigating materials with low natural abundance isotopes, and conducting detailed imaging and analysis with unprecedented sensitivity and speed [48, 90, 114]. Such enhancements not only broaden the scope of NMR applications but also push the boundaries of what can be explored and discovered through this essential analytical method.

1.2 Non-equilibrium systems and novel phases of matter

Recent advancements in the study of non-equilibrium systems have significantly shifted our understanding of how matter behaves under periodic driving forces [49]. Unlike systems at thermal equilibrium, which are well understood and characterized by a static distribution of energy states, non-equilibrium systems are constantly evolving and driven by external forces [36, 37]. This dynamic nature allows for the exploration of physical phenomena and properties that do not manifest in equilibrium conditions, offering new insights into fundamental concepts such as thermalization and transport in many-body systems, and opening the door to novel technological applications.

A phenomenon that can occur in periodically driven systems is Floquet prethermalization, characterized by a system quench to a state that is not thermal equilibrium. This quench occurs on a timescale commensurate with the Floquet Hamiltonian which governs the effective system dynamics in a stroboscopic frame of reference. Systems will always undergo thermalization, but in some cases can be held in this prethermal state for exceedingly long periods of time.

One of the most intriguing aspects of non-equilibrium physics is the emergence of novel phases of matter, such as discrete time crystals (DTCs), which in theory exhibit perpetual motion without energy input, defying traditional intuition regarding thermodynamics in an isolated system [50, 170]. The dominant approach toward creating and observing DTC phases has been to subject systems to periodic driving, known as Floquet systems, where the external perturbation modifies the energy landscape, leading to new and exotic quasi-steady states which sometimes cannot occur in static equilibrium systems. The study of these phases has practical implications in the field of quantum computing and information processing, where control over quantum states in non-equilibrium conditions can lead to new ideas based on the stability provided by many-body dynamical systems [73].

The exploration of these novel non-equilibrium phases requires precise control and measurement techniques. Traditional NMR techniques are inherently limited by low signal-to-noise ratio, and sometimes also low measurement throughput when T_1 relaxation times are long. However, the advent of hyperpolarization methods, as discussed in this thesis, dramatically enhances the sensitivity and throughput of NMR spectroscopy, making it possible to detect subtle changes and dynamics in the spin systems of nuclei without disturbing their state. By studying hyperpolarized ^{13}C nuclear spins in diamond, this thesis aims to uncover deeper insights into the mechanisms of Floquet prethermalization and other non-equilibrium phenomena, thereby contributing to the broader field of non-equilibrium physics and its application in modern science and technology.

With respect to "transport" studies, we are referring to the transport of spin polarization. Since the spins in a solid-state lattice are stuck in place, this requires spin states to be exchanged freely by their mutual interactions. Indeed, the long-range dipolar interactions in this system allow Fickian-type spin diffusion to take place.

1.3 The role of hyperpolarization

Hyperpolarization techniques, which enhance the magnetic resonance signals by orders of magnitude, have revolutionized the field of NMR. By utilizing optically pumped Nitrogen Vacancy (NV) centers in diamond, ^{13}C nuclear spins can be hyperpolarized, leading to a non-thermal distribution of spin states [169]. This significant enhancement not only improves the sensitivity of NMR experiments but also allows for sensing targets to be specially highlighted due to proximity from the hyperpolarization source.

An additional aspect of the hyperpolarization scheme employed in this thesis is the controllability and reproducibility. A single diamond crystal chip was used in all of the experiments displayed here. Additionally, hyperpolarization can be quickly turned on or off, or switched between positive and negative. This allows for the unique observation in Chapter 11 of hyperpolarization extent increasing the rotating-frame lifetime of the spins, as well as the creation of shell-like spin textures in Chapter 12.

Perhaps the most consequential result of hyerpolarization in this thesis is the vast acceleration of experimental throughput. As mentioned in Chapter 4, a signal enhancement of ϵ would require signal averaging for ϵ^2 longer period of time to achieve the same signal-to-noise ratio. Additionally, the solid-state crystal diamond lattice environment results in extremely long T_1 lifetimes for the ^{13}C spins, about 25 minutes at room temperature. Waiting for nuclear spins to polarize close to thermal levels would require at least $3T_1 = 75$minutes of wait time in between measurements.

1.4 Focus on hyperpolarized carbon-13 in diamond

This thesis focuses on hyperpolarized ^{13}C nuclear spins in diamond, a system that benefits from long T_1 lifetimes and controlled interactions via resonant radiofrequency pulses. The unique properties of diamond and NV centers provide an ideal platform for studying complex non-equilibrium phenomena such as Floquet prethermalization and discrete time crystalline states.

The figure of merit for whether a system will prethermalize under a periodic drive in this case is $J\tau$, where J is the median interaction strength and τ is the drive period. When $J\tau \ll 1$, the drive period is significantly smaller than the inverse of the interaction strength. This is a sufficient condition for prethermalization because the interaction is what gives rise to thermalization, and the periodic drive dresses the interaction Hamiltonian in such a way that it now commutes with the initial density matrix. In the hyperpolarized diamond ^{13}C, we show in Chapter 4 NMR experiments that achieve a $J\tau$ value range of 0.066-3.0. The result is a highly tunable prethermal state whose lifetime depends strongly on the set drive parameters. This is what allows us to apply $>$ 1.4 million Floquet cycles worth of control pulses, several orders of magnitude greater than contemporary experiments where prethermalization was studied.

1.5 Objectives

The primary objectives of this thesis are to investigate the thermalization and transport processes in hyperpolarized diamond ^{13}C nuclear spins and develop novel methodologies for bringing this system closer to practical use in sensing and imaging. Through precise control and measurement of hyperpolarized ^{13}C spins, this work aims to contribute significantly to our understanding of non-equilibrium physics and its applications. The experimental system required several innovations to get off the ground, both in physical infrastructure as well as many-body spin control. These details, in furtherance of the thermalization and transport studies which they support, represent significant contributions to their respective fields.

Secondary objectives include the stimulation of interest in old research topics in light of new technological advancements. Certain types of measurements which were not possible in previous decades can be revisited given the recent advancements in radiofrequency and microwave electronics, cryogenics, hyperpolarization, and more. For example, the spin diffusion barrier is an engineering challenge that appears in papers as early as the 1950s, but given the ability to continuously track spin polarization over minutes-long periods, it makes sense to revisit as we do in Chapter 11.

Additionally, some of the observations detailed in this thesis are included purely to provoke curiosity. For example, the investigation into a "rotating-frame solid echo" in Chapter 8 is motivated largley by curiosity, and in fact began with an accidental observation while analyzing DTC data for Chatper 6. This result may or may not find practical use in the field of quantum control, for example, but such is the pleasure of academic freedom.

1.6 Structure of the thesis

This thesis is organized into several chapters which build upon each other logically. Part II begins by describing the development of the experimental hardware and optimizing the performance of the ^{13}C system with respect to Floquet prethermalization. Chapter 3 describes the physical implementation of an NMR spectrometer with the ability to hyerpolarize diamond ^{13}C using the advancements of robust radiofrequency and microwave electronic equipment. Chapter 4 displays preliminary results of the hyperpolarized nuclear spin system as a testbed for periodically driven physics.

Part III builds upon these results by exploring more phenomena that are accessible due to the long-lived prethermal state observed in Part II. For example, Chapters 6 and 7 focus on the prethermal discrete time crystalline behavior observed in the system, exploring the implications for non-equilibrium matter and demonstrating the power of Floquet engineering. Chapters 8 and 9 further display the high level of quantum control afforded by the interacting spin network by investigating echo phenomena, namely the solid echo and the Loschmidt echo.

Part IV of this thesis seeks to bring all of these experimental results closer to the realm of practical use. In order to reap the benefits of Floquet systems, we envision the ability

to controllably transport bulk levels of hyperpolarization across nanometer length distances and interfaces. By bulk levels, we mean significantly large amounts of spin polarization that can appreciably increase the NMR signal of a target spin ensemble. Chapter 11 demonstrates a proof-of-concept by matching spatially dependent nuclear spin relaxation data to a simple model driven by spin diffusion and local damping effects from the NV center. Chapter 12 takes this concept one step further by initializing and controlling mesoscale spin textures through hyperpolarization and quantum control schemes.

Part II

System Hardware and Thermodynamics

Chapter 2

NMR Spectroscopy and Floquet Prethermalization

In this part of the thesis, we develop hyperpolarized nuclear spins as a platform for quantum technologies. Despite not being individually addressable, ensembles of solid state spins offer advantages for sensing and simulation. Hardware development and studies of the system thermodynamics are necessary first steps toward realizing such applications.

In Chapter 3 we introduce the hardware which forms the basis for all of the experiments reported in this thesis, focusing on details of construction of the NMR spectrometer. The central piece is an arbitrary waveform transceiver which can generate and digitize signals from radio-frequency to x-band microwave.

A wealth of recent interest in periodically driven systems has opened new opportunities to study non-equilibrium phenomena. The study of so-called "Floquet" (periodically driven) systems has revealed novel dynamic phases of matter, many of which have no static counterparts.

In Chapter 4 we consider one such phenomenon, "Floquet prethermalization" in ^{13}C nuclear spins in diamond. Under rapid periodic driving which imposes quasi-conserved quantities, this system enters a state with lifetimes predicted to scale exponentially with the driving frequency.

While Floquet prethermalization has been observed in recent studies using ultra-cold atom and NMR systems, our research offers a fresh look at the thermalizing dynamics in large systems, attributable to two unique aspects of our system: (i) hyperpolarized ^{13}C nuclear spins, which can be precisely controlled, allowing for significantly more Floquet drive periods than previous experiments, and (ii) technological enhancements that enable continuous monitoring of the thermalizing dynamics over multi-minute durations with an exceptionally high signal-to-noise ratio.

Leveraging these capabilities, we have developed a periodic driving protocol that maintains the ^{13}C nuclei in a Floquet prethermal state with lifetimes exceeding 90 seconds at room temperature—a more than 60,000-fold increase over the typical T_2^* free induction decay time. Our protocol involves 5.8 million pulses, during which we continuously monitor

the thermalizing spins for up to 573 seconds with high fidelity. These values, in terms of both Floquet control and prethermalization lifetimes, are among the highest reported in the scientific literature to our knowledge.

The high signal-to-noise ratio of our measurements also provides unprecedented clarity into the thermalization process. Following theoretical frameworks, we have experimentally delineated four distinct regimes within the Floquet prethermalization process, including the onset and decline of the prethermal plateau, accurately determining heating rates and transient oscillations within these regimes.

Beyond foundational insights, our findings reveal promising possibilities for exploiting Floquet control in dipolar-interacting spin networks. The ability to protect and continuously monitor spins for extended periods opens up prospects for developing high-resolution magnetometers and spin sensors using hyperpolarized ^{13}C nuclei.

Chapter 3

High-Speed, High-Memory NMR Spectrometer and Hyperpolarizer

3.1 Introduction

Recent advancements in nuclear magnetic resonance (NMR) spectroscopy have underscored the need for novel instrumentation, particularly in areas involving integrated electron-nuclear spin control, dynamic nuclear polarization (DNP), and non-traditional NMR pulse sequences [48, 25]. Historically, significant advancements in NMR have been driven by novel instrument design [78, 81, 79]. However, as the field has matured and commercial instrumentation has focused predominantly on mainstream applications, available NMR instruments have experienced a reduction in both hardware and software flexibility. Furthermore, the number of vendors offering spectrometer technology has diminished, raising the perception that this limitation may impede innovative NMR methodologies in future years.

Addressing this gap, this Chapter introduces a new NMR spectrometer that capitalizes on the evolving capabilities of commercially available arbitrary waveform transceivers (AWTs) for the integrated control of electron and nuclear spins. While the use of AWT technology is established, having seen considerable recent developments in areas such as radar and communication systems, the enhancement in AWT capability over the past decade is remarkable, and has become the basis for spin control infrastructure in the adjacent field of quantum computing (QC). The increasing number of vendors in this field, partly driven by growth of the QC technologies, has rendered the technology more accessible, cost-effective, and functionally robust.

In this study, we present an NMR spectrometer built using a commercial arbitrary waveform transceiver (AWT), specifically the Tabor Proteus P9484M, that integrates multiple critical features into a single unit. This spectrometer exploits the AWT's rapid sampling rate, substantial memory capacity, and rapid data transfer capabilities. The combination of these attributes results in a system with robust NMR transmit-receive functions, and the use of multiple channels enables effective electron-nuclear spin control.

The capabilities of this instrument enable numerous innovative features. For instance, it allows the ability to directly synthesize and receive signals at the Larmor frequency, even at high frequencies up to 2.7GHz. On the reception side, this eliminates the need for signal heterodyning, thus reducing passive components and minimizing insertion loss, ultimately yielding signal-to-noise (SNR) gains. Additionally, the high sampling rate enables effective digital filtering with reduced aliasing. A key advantage is the rapid, on-board, phase-sensitive detection capability, facilitated by on-board numerically controlled oscillators (NCO), even when carried out over several minutes of acquisition. This feature allows new possibilities, such as the long-time Bloch-sphere tracking of nuclear spins in three dimensions in the rotating frame.

For transmission, the high-sampling rates allow for high-fidelity pulse shaping, minimizing errors and enhancing the versatility of the excitation spectrum. The use of customizable software, alongside on-board digital oscillators and filters, adds flexibility and simplifies the hardware configuration. The instrument's substantial memory capacity and rapid data transmission rates support the design of complex sequences, enabling data acquisition over millions of pulses. Finally, the spectrometer's capacity to synthesize arbitrarily shaped microwave pulses at frequencies up to 12 GHz significantly improves its functionality in DNP applications.

Bringing together these features, this Chapter presents a compact, rack-mountable NMR spectrometer integrating advanced features for NMR, electron-nuclear control, and DNP. We begin in Sec. 3.2 by detailing the internal architecture and key technical aspects of the Proteus device. Sec. 3.3 highlights the key features of the Proteus which help in electron spin control. Then, Sec. 3.4 focuses on transmit-receive functions, phase sensitive detection, and quantifies SNR improvements in the spectrometer construction. Sec. 3.5 shows applications in DNP, using the case of ^{13}C nuclear spins optically hyperpolarized in diamond as a model system. Finally, Sec. 3.6 concludes by discussing prospects for future advancements, including in closed-loop feedback.

3.2 Device architecture

The Tabor Proteus P9484M AWT (referred to hereafter as the "Proteus") is an FPGA-based module that slots easily into any standard PXI chassis. Commands can be issued to the device through standard VISA protocols incorporated into existing coding languages such as Python, Matlab, or Labview. Shown in Figure 3.1 is the block diagram of the Proteus and its use in the context of a hyperpolarized NMR experiment.

On the output side, the Proteus features two digital-to-analog converters with a maximum sampling rate of 9GS/s. Two channels are connected to each DAC for a total of four output channels. Each channel also has two associated marker channels. The high sampling rate allows for the direct generation of frequencies up to 4.5 GHz (9 GHz) in the first (second) Nyquist zone. Each channel also features two numerically controlled oscillators (NCOs), which can be used for frequency up-conversion through the built-in IQ modulation mode.

Baseband IQ waveforms can be written to the device and stored in the large FPGA memory (16 GS). Since this process is completely digital, the device can directly output pulses in the RF and microwave ranges with no external mixing or calibration required. The Proteus output can be triggered internally, via SCPI command, or via an external TTL signal applied to the TRG1 or TRG2 ports.

On the return side, the device features two inputs which share a 5.4 GS/s analog-to-digital converter. This allows for one channel to capture data at the max sampling rate, or two channels capturing simultaneously at 2.7 GS/s. Complex data can also be captured at this rate. The captured raw data shares waveform memory space with the AWG, which means many acquisitions can be collected in a single measurement. Although raw data can be sent straight to the measurement PC for analysis, one can use the FPGA capability to perform operations on the data, including decimation, filtering, averaging, and decision making. Most importantly, the device can digitally demodulate raw data using the phase of the NCO output as a reference. Once again, the digital nature of this process eliminates the need for external down-conversion, resulting in highly coherent phase detection throughout the measurement. The Proteus digitizer can be triggered manually, externally, or automatically by the waveform playback of the AWG.

3.3 Electron spin control

The maximum possible DAC sampling rate for the Proteus is 9 GS/s, and thus the first (second) Nyquist zone extends up to 4.5 GHz (9.0 GHz). However, production of microwave signals in the third Nyquist zone (9-13.5 GHz) is also possible, at the cost of output power. This is accomplished by setting the numerically controlled oscillator (NCO) to 4.9 GHz and generating an image frequency in the higher Nyquist zone. To offset the lower microwave power, an amplifier (Tabor Electronics, model 3202) is slotted into the PXI chassis next to the AWG, allowing for two cascading stages of amplification resulting in a total gain of up to +25 dB. The means that in addition to having superb NMR capabilities, the Proteus is also suitable for X-band electron paramagnetic resonance (EPR) and dynamic nuclear polarization (DNP) applications.

As an example of the microwave capabilities of the Proteus, we will demonstrate a DNP sequence which uses the optical properties of NV centers to hyperpolarize the local ^{13}C nuclei. A chirp waveform, which consists of a linear frequency sweep from 3.755 GHz to 3.795 GHz at a rate of 750 sweeps per second is calculated and downloaded to the instrument, which is then digitally up-converted to 3.775 GHz $\pm$ 20 MHz via the NCO. This frequency is determined by the splitting of the NV spin sublevels at a given DC magnetic field, 36 mT in this case. The chirp is then sent through a high-gain amplifier to pump the sample, in conjunction with a 532nm green laser. Using the Proteus task table, as described in the section below, the chirp waveform can be applied to the diamond sample for an arbitrary length of time, typically 60-120s in this case. Although individual waveforms written to the instrument can be extremely long, proper use of the task table can help alleviate AWG

AWG Properties	
Num. Channels	4
Max sampling rate	9 GS/s
Amplitude	1mV to 1.1Vpp
Resolution	16-bit
Inst. bandwidth	1.25 GHz
Num. segments	32k
Task Table Properties	
Max length	64k tasks/ch
Max task loops	1M
Max subsequences	32k
Max sequence loops	1M
Digitizer Properties	
Channels	1 / 2
Max sampling rate	5.4 / 2.7 GHz
Frequency range	< 9 GHz
Input voltage range	0.5 Vpp
Resolution	12 bits

Table 3.1 Key specifications for Proteus P9484M AWT. High sampling rates and memory capacity are competitive with state-of-the-art commercially available AWG's and digitizers.

memory usage and reserve most of the memory for data acquisition.

The Proteus task table is a core function of the instrument's operation. It not only makes the implementation of both NMR and DNP sequences much simpler to program, but conserves memory to use instead for lengthy data acquisitions. As waveforms are written to the AWG memory, they are assigned a segment number by the user. The task table allows these segments to be played back in any order, for any number of repetitions, to skip to any other segment, and to both trigger and be triggered by other mechanisms in the device. A "task" on the table is a block of information containing this another pieces of information which are laid out in the chart below.

When all the task instructions have been specified, this information is written to the device to allow for seamless transitions between tasks during the execution. This allows for an extraordinary amount of customization and depth in the pulse and DNP sequences without high memory consumption. Decision making and task jumping can also be made on the fly using the FPGA programming blocks, for example playing a different waveform based on the input level to the device at the ADC.

In the DNP example given above, one chirp sequence can be written to the instrument

Task Parameter	Options
Task number	any integer N
Segment to play	1 to N_{seg}
Number of loops	1 to 1M
Trigger digitizer	Binary
Wait for trigger	None, Int, Ext, CPU
Subsequence	Start, middle, end
Next task	Any task number

Table 3.2 Task table functionality for the AWT. Flexibility in sequence and subsequence tasks permits a wide range of NMR pulse sequences to be implemented.

channel. To change the length of the microwave pumping without rewriting the waveform, then the amount of playback time can be increased by simply increasing the number of repetitions of the segment, which only requires overwriting the task table. Moreover, the DNP sequence can be made more complex by writing a second chirp pulse to the instrument, which sweeps the frequency in the opposite direction. These two segments can be alternated in the task table and applied to the sample for any amount of time, allowing for positive and negative polarization sequences of the ^{13}C nuclei.

3.4 Construction of NMR spectrometer

The Proteus AWG produces 75 MHz control pulses by direct digital synthesis. Figure 3.3 (A) shows the time-domain measurements of pulses directly output (before amplification) by the AWG, including (i) rectangular, (ii) Gaussian, (iii) secant, and (iv) Hermite pulses. Figure 3.3 (B) shows the Fourier transform of the four shaped pulses in (A) show high spectral purity of the AWG output. Figure 3.2 (C) shows a schematic of the home-built transmit-receive RF circuit. The Proteus provides signal generation and digitization capabilities. Transmit pulses are amplified through a 55 dBm Hurley traveling wave tube amplifier, and receive NMR signals and amplified through two gain stages of ARR very low noise amplifiers. The duplexer consists of a Tecmag cross-diode connected to a 75 MHz quarter-wave wire which ensures that the sensitive amplifiers in the receive circuit do not see the amplified pulses intended for the probe. The probe circuit consists of an inductor and two variable capacitors to tune the detection frequency and match impedance with the rest of the circuit.

Detection of the Larmor precession signal amplitude and phase is a key element of the NMR spectrometer. Sample raw data is shown in Figure 3.4 (A) for the commercial system. The commercial spectrometer used analog hardware to heterodyne the 75 MHz ^{13}C signal to 20 MHz. The digitizer then sampled the signal at 1 GS/s, about 50 points per period

of Larmor precession, as seen in. The whole acquisition window of 32 us is then Fourier transformed to find the amplitude of the 20 MHz peak. Due to the commercial hardware's heterodyne process, the NMR signal's phase is difficult to recover, limiting its use in experiment, especially ones with many successive pulse-acquisition windows. Figure 3.4 (B) shows a window of raw data from the homebuilt system with fully digital heterodyning which simplifies the data acquisition process. The 75 MHz signal is converted to DC using digital down conversion (DDC) with a numerically controlled oscillator (NCO). The real component of the complex data points are shown in the 32 us window with a zoom-in. Fourier transformation would show a zero-frequency peak corresponding to the NMR signal, and peaks at 75 MHz which are an artifact of the NCO. In our experimental setup, readout of the NMR signal is accomplished by averaging the real and imaginary components of the raw data from the acquisition window, then calculating the complex norm and angle to give us the signal amplitude and phase.

The performance of the home-built spectrometer can be benchmarked against the commercial system by looking at signal-to-noise ratio. This is done by swapping out individual components to see the impact on SNR. Figure 3.5 (A) shows the hyperpolarized pulsed spin-lock ^{13}C signal as described in [30] using pulse sequence (inset) is used as the benchmark experiment. The pulsed spin-lock allows us to measure the precession signal in a series of windows every 100 us for 60 seconds. Shown is the amplitude plotted as a function of time, acquired by the homebuilt spectrometer. Figure 3.5 (B) displays the Fourier transform of the spin-lock decay signal obtained from (i) the commercial pulse sequencer and T/R circuit, (ii) the commercial pulse sequencer with the home-built T/R circuit, and (iii) the Proteus pulse sequencer with the home-built T/R circuit. In each case, the signal is normalized to 1, and the noise is measured by averaging the 10,000 points at the wing of the power spectrum (indicated by dotted lines). This gives a measure of SNR which for the commercial system is 2.9e5. When the home-built T/R circuit is swapped in (keeping the commercial pulse sequencer), the new SNR is 3.2e5, or a modest 1.1x improvement over the full commercial system. This shows that the homebuilt circuit performs at least reasonably well compared with the commercial circuit. When the commercial pulse sequencer was then replaced by the Proteus AWG pulse sequencer, the SNR jumped to 7.0e5, representing a significant 2.2x improvement when considering just the effect of the high-fidelity Proteus pulses (or 2.4x improvement compared to the fully commercial system). The boost in SNR can likely be attributed to the high spectral purity of the 75 MHz pulses generated by the Proteus AWG.

3.5 Application to hyperpolarized NMR

The Proteus AWG and digitizer play a central role in all parts of the hyperpolarizer and NMR spectrometer, providing dual electron and nuclear spin control. Figure 3.6 displays the full schematic of the hyperpolarized NMR experiment including the roles of both electron and nuclear spin control. During hyperpolarization with 532nm laser pumping, the first channel of the AWG provides microwave chirped waveforms to perform the solid-effect DNP

enhancement of the ^{13}C NMR signal. After hyperpolarization, the waveform stops playing and the sample is shuttled to the 7T superconducting magnet. At this higher field, the second channel of the AWG creates NMR pulses of arbitrary shape and frequency. The resulting ^{13}C NMR signals are then sampled by the digitizer. The RF pulse sequence in the diagram starts with a multiple-pulse spin-lock for 1000 pulses along x. It then continues with a discrete time crystal (DTC) pulse sequence which was recently demonstrated in Ref. [28] The Proteus comes with a software package that easily implements a modular, nested pulse sequence such as the one shown in Figure 3.6.

Representative single-shot decay curve measured using the DTC pulse sequence is shown in Figure 3.7. The I_x and I_y expectation values are measured after every x pulse. Figure 3.7 (A) shows the I_x expectation for each acquisition window throughout the experiment duration. The first 1000 pulses show the ^{13}C spin system locked along the x direction. Then, the spins are periodically kicked with a $\sim \pi$-pulse along y, flipping the sign of I_x from positive to negative. One measure of the system's stability is the measured angle $\varphi = \arctan(I_y/I_x)$, or the phase of the ^{13}C signal in the I_x-I_y plane. As shown in Figure 3.7 (B), the phase switches between 0 and π with every π y-pulse. This is clearly visible in the zoomed-in sections of data in Figure 3.7 (A) (ii) and Figure 3.7 (B) (ii). As explained in Ref. [28], the significance of this experiment is the stability of this particular dipolar coupled ^{13}C spin system under this pulse sequence. Our hyperpolarizer and spectrometer is capable of measuring a full such decay curve in a single-shot, due to the unique properties of solid-state NMR systems as well as the high speed and high memory capacity of the Proteus AWT.

3.6 Outlook

In conclusion, we demonstrate a high-speed, high-memory NMR spectrometer and hyperpolarizer. Leveraging the capabilities of the Tabor Proteus P9484M arbitrary waveform transceiver, this instrument offers a versatile platform for integrated electron-nuclear spin control and dynamic nuclear polarization. Through its rapid sampling rate, substantial memory capacity, and efficient data transfer capabilities, the spectrometer enables precise NMR pulse synthesis, flexible signal reception, and phase-sensitive detection with improved signal-to-noise ratio (SNR). Additionally, its compact design and cost-effectiveness make it a valuable tool for researchers exploring innovative NMR methodologies.

Looking ahead, the capabilities of this instrument pave the way for future research directions. High-frequency pulsed DNP holds promise for enhancing sensitivity and resolution in NMR experiments. Electron decoupling techniques can further improve spectral quality and enable the investigation of complex spin systems with greater precision. Moreover, the integration of feedback spin control mechanisms using advanced FPGA engineering opens up possibilities for real-time optimization and manipulation of nuclear spins.

Overall, the high-speed, high-memory NMR spectrometer and hyperpolarizer presented in this study represents an opportunity to advance NMR instrumentation, with potential applications in quantum sensing and materials science. Continued advancements in NMR

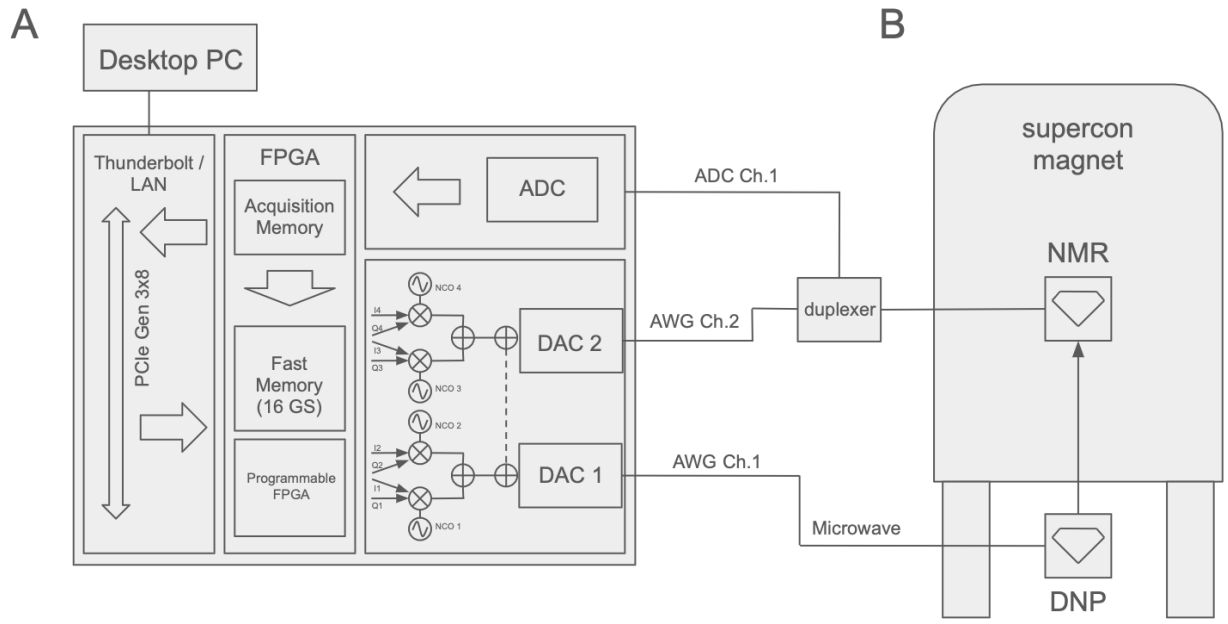

Figure 3.1 **AWT and spectrometer schematic.** Block diagram of Proteus unit and sample NMR experimental setup. (A) The Proteus is connected to a measurement PC via thunderbolt or LAN. The baseband waveforms are written to the FPGA memory and digitally upconverted via one of two NCOs on each channel, before being converted at a rate of up to 9 GS/s. (B) From this point the generated waveforms assist in optical hyperpolarization of a diamond sample implanted with NV centers. After hyperpolarization, the sample is shuttled to a high-field magnet. The analog NMR signal is then digitized at a rate of 5.4 GS/s, and the data can then be manipulated by the FPGA before being written to the module memory.

technology, coupled with innovations in RF and microwave electronics, promise to drive further progress in our understanding of complex electron-nuclear magnetic spin systems.

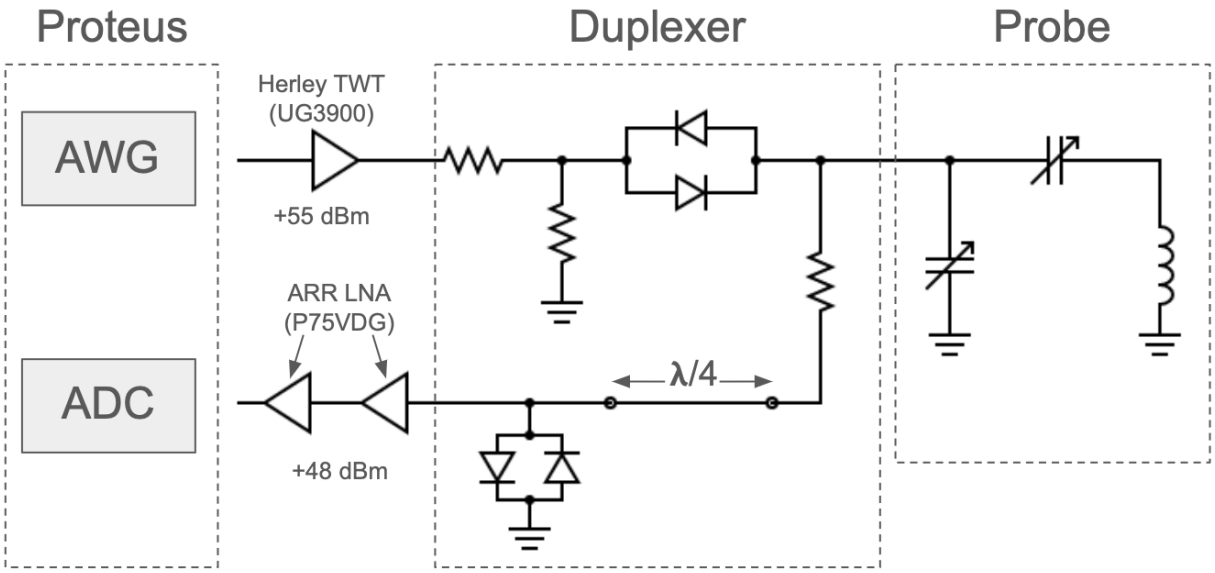

Figure 3.2 **Transmit-receive circuit diagram.** (A) The transmit-receive circuit begins with a signal generated by the ADC at 75 MHz with amplitude 1.2 Vpp. The pulse is passed through a TWT amplifier. Since the architecture of the duplexer isolates the transmit and receive circuits, the large-amplitude pulse is then transmitted to the probe. The resulting NMR signal detected by the probe is then received by the digitizer.

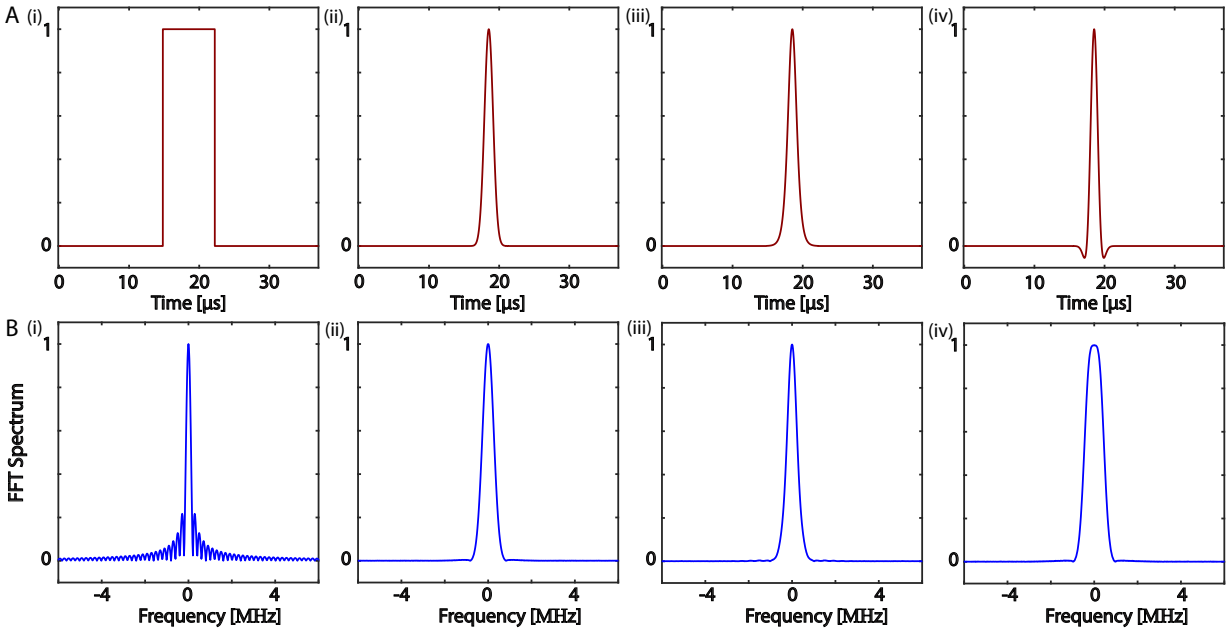

Figure 3.3 **Pulse shaping.** Time-domain functions of the shaped pulses drawn by the AWG are shown. They consist of (i) rectangular, (ii) Gaussian, (iii) secant, and (iv) Hermite pulses. (C) Fourier transforms of the digital captures of the corresponding pulses.

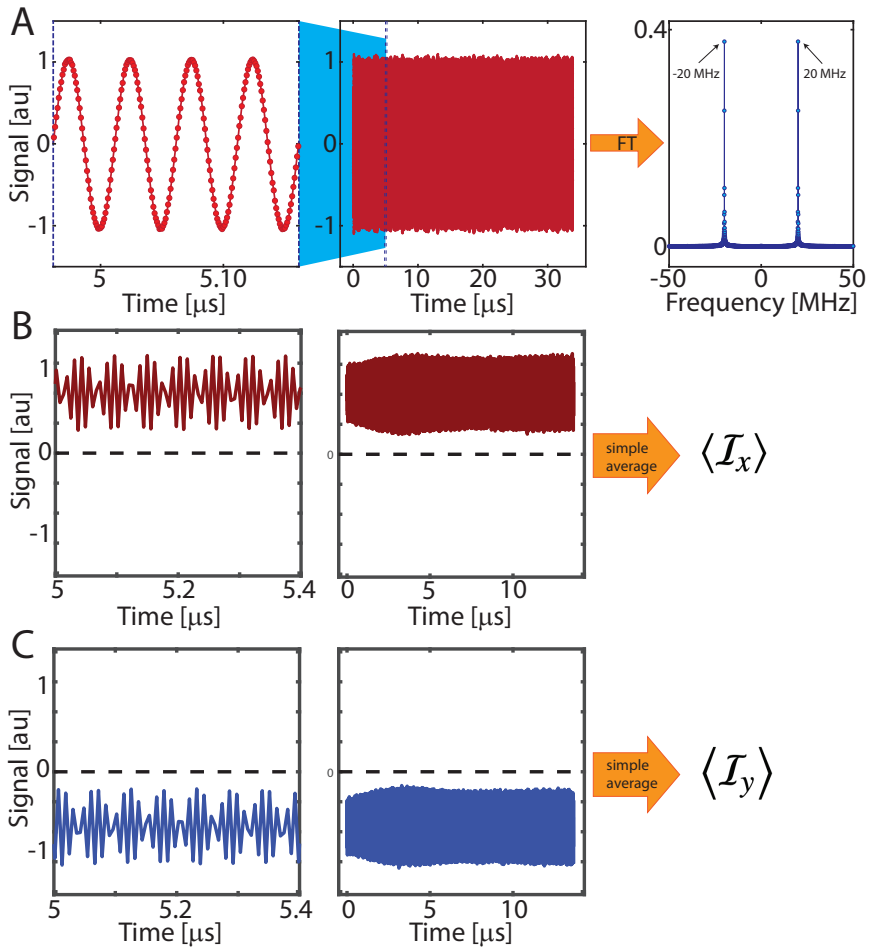

Figure 3.4 **Digital down-conversion for phase-sensitive detection.** (A) Using a commercial system, the Larmor precession signal is heterodyned down to 20 MHz. A separate digitizer can be used to sample the signal and quantify the NMR signal amplitude, but the phase information is lost due to the commercial hardware. A window of 32us of signal capture is shown here, with a zoom-in showing clear oscillations. The Fourier transform shows the strong 20 MHz peak. (B-C) Using a home-built spectrometer, the signal amplitude and phase can be recovered more simply. The NCO-assisted digitizer captures the in-phase I (B) and quadrature, Q (C) portions of the signal at each sampling point. Windows of 12us of signal capture for I and Q are shown. The 75 MHz NCO mixed the Larmor precession signal down to DC, meaning that a simple average gives the I_x and I_y polarization components.

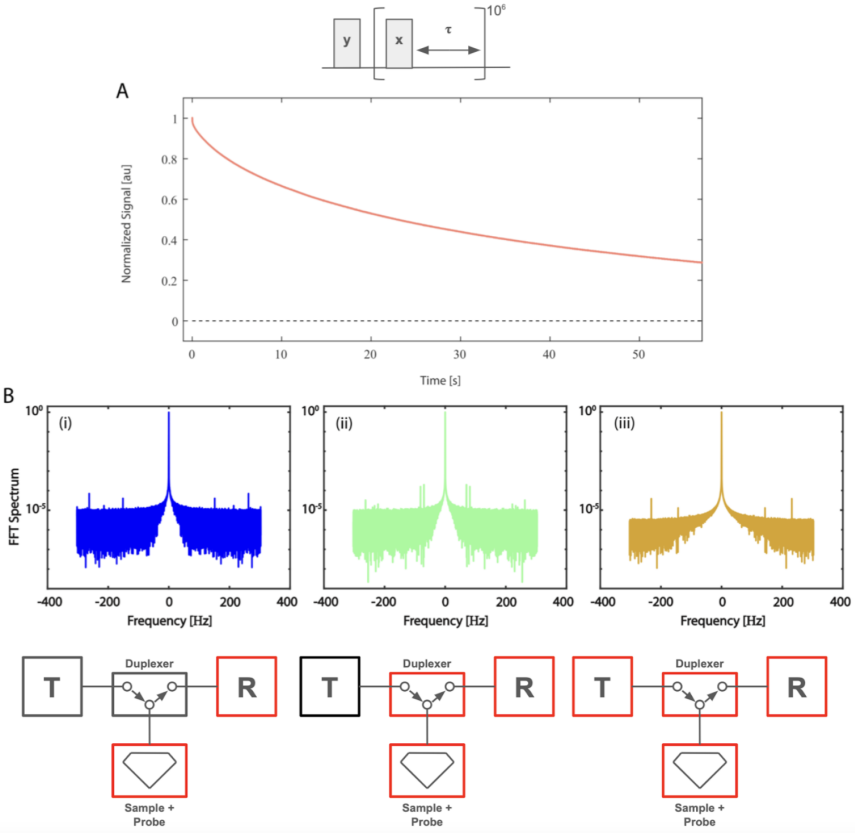

Figure 3.5 **SNR comparison.** To quantify the hardware performance of our home-built spectrometer relative to the commercial one, we measured representative ^{13}C pulsed spin-lock decay curves. (A) The pulse sequence is shown in (i). A representative one-shot decay curve acquired using the home-built spectrometer is shown in (ii). Each data point ($>$ 700000 total points) on this curve is obtained with the data processing scheme in Fig. 3. (B) Fourier transforms of the spin-lock decay curves for (i) the commercially available spectrometer system, (ii) the commercial system with the home-built transmit-receive circuit replaced, and (iii) the fully-home-built spectrometer with pulses generated by and digitized by the Proteus.

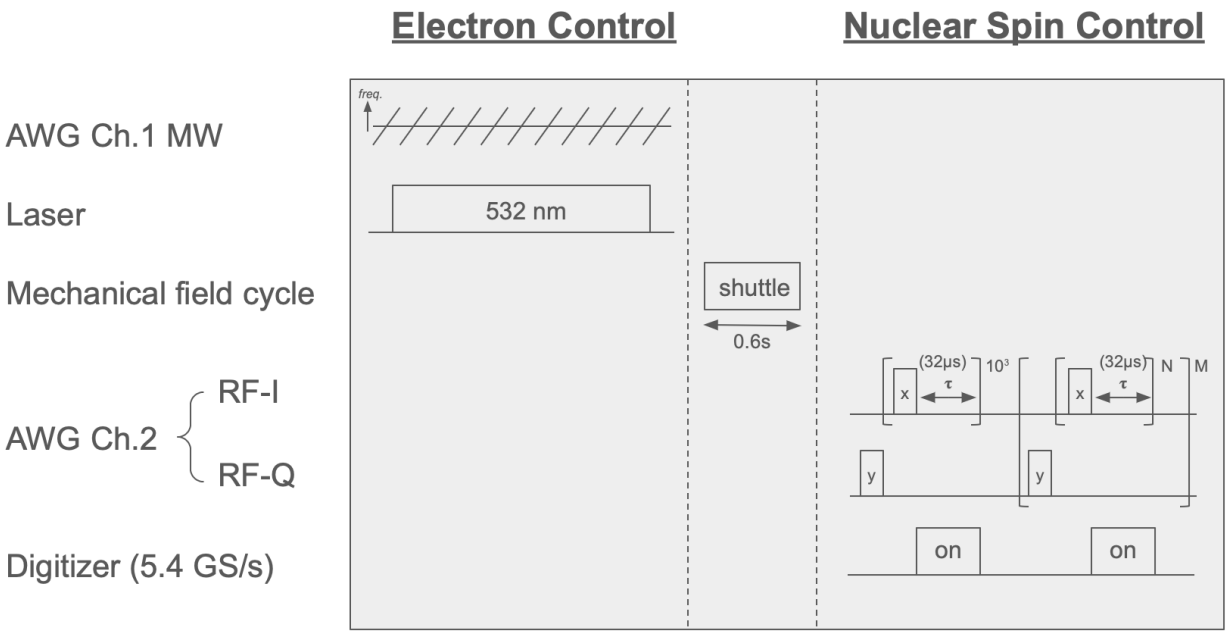

Figure 3.6 **Dual electron and nuclear spin control.** Schematic of an experiment involving both hyperpolarization (electron spin control) and NMR (nuclear spin control). At low field 36mT, the diamond sample is irradiated with 15W of 532nm laser and microwave chirps. After hyperpolarization, the sample is mechanically shuttled to high field 7T and the NMR control sequence is performed. Shown here is the a sequence that begins with multiple-pulse spin-locking until the spin signal transient has settled into a constant value. Then, the modular pulse sequence is introduced, with an off-phase y-pulse every N=300 x-pulses.

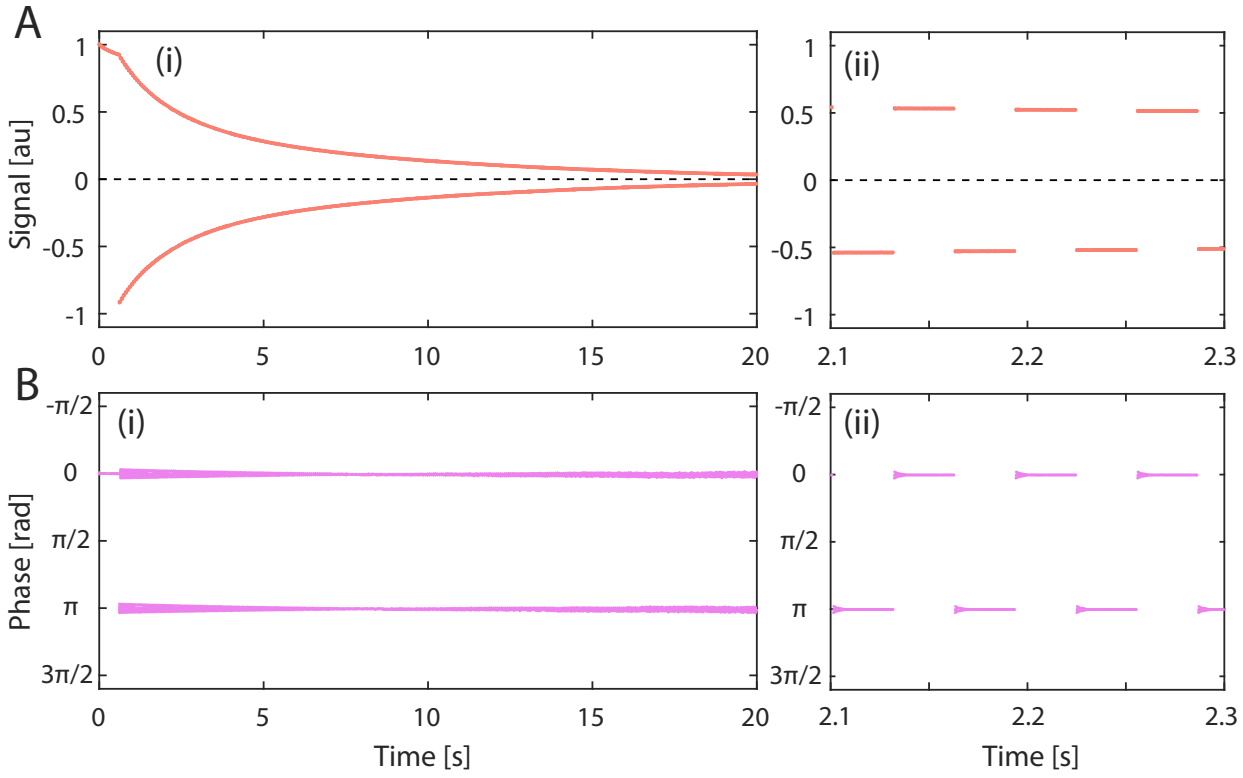

Figure 3.7 **DTC demonstration and utility of modular pulse sequence.** Single-shot measurement of DTC experiment shows a 1/e lifetime of 4.1 seconds. (A) The I_x polarization value and (B) the phase φ in the x-y plane are plotted vs the time axis. The first 1000 pulses represent the initial spin-lock along +x. Then the spins are flipped every 300 pulses for the rest of the curve. (ii) Zoom-ins show the polarization and phase clearly switching periodically in a 0.2s window of the larger curve.

Chapter 4

Floquet Prethermalization with Lifetime Exceeding 90 s in a Bulk Hyperpolarized Solid

4.1 Introduction

Systems pulled away from thermal equilibrium can exhibit unusual phenomena non-existent or difficult to achieve at equilibrium [146]. For instance, periodically driven quantum systems can display long-lived prethermal lifetimes due to the emergence of approximately conserved quantities under the effective time-independent Hamiltonian describing the drive [42, 58, 36, 8, 96]. For sufficiently large driving frequencies ω, much higher than the intrinsic energy scales in the system Hamiltonian (hereafter J), these prethermal lifetimes scale exponentially with ω [91, 37, 9, 164, 103]. Ultimately, however, the system absorbs energy and "heats up" to a featureless infinite temperature state.

The long-lived prethermal plateau and its stability against perturbations in the drive portends applications for the engineering of quantum states [58, 36, 149]. Fundamentally, the control afforded by periodically driven systems opens avenues to study non-equilibrium phenomena and explore novel dynamic phases of matter, some of which have no equilibrium counterparts [49, 85]. A flurry of theoretical work has recognized Floquet prethermalization under random driving [176], in driven linear chains [164], and even in the classical limit [72]. Experimentally, Floquet prethermalization has been observed recently in cold-atom [139, 161, 158] and NMR systems [120, 174, 136]. They demonstrated a characteristic exponential suppression of heating rates with Floquet driving. Even before the current resurgence of interest, decades-old NMR experiments had observed certain signatures of prethermalization, then referred to as "quasi-equilibrium" [111, 110, 143, 144, 163, 35].

In this Letter, we report observation of Floquet prethermal states with lifetimes exceeding 90s at room temperature in a dipolar-coupled ensemble of ^{13}C nuclei in diamond (see Figure 4.1A). These nuclear spins, *randomly* positioned at 1% concentration in the lattice,

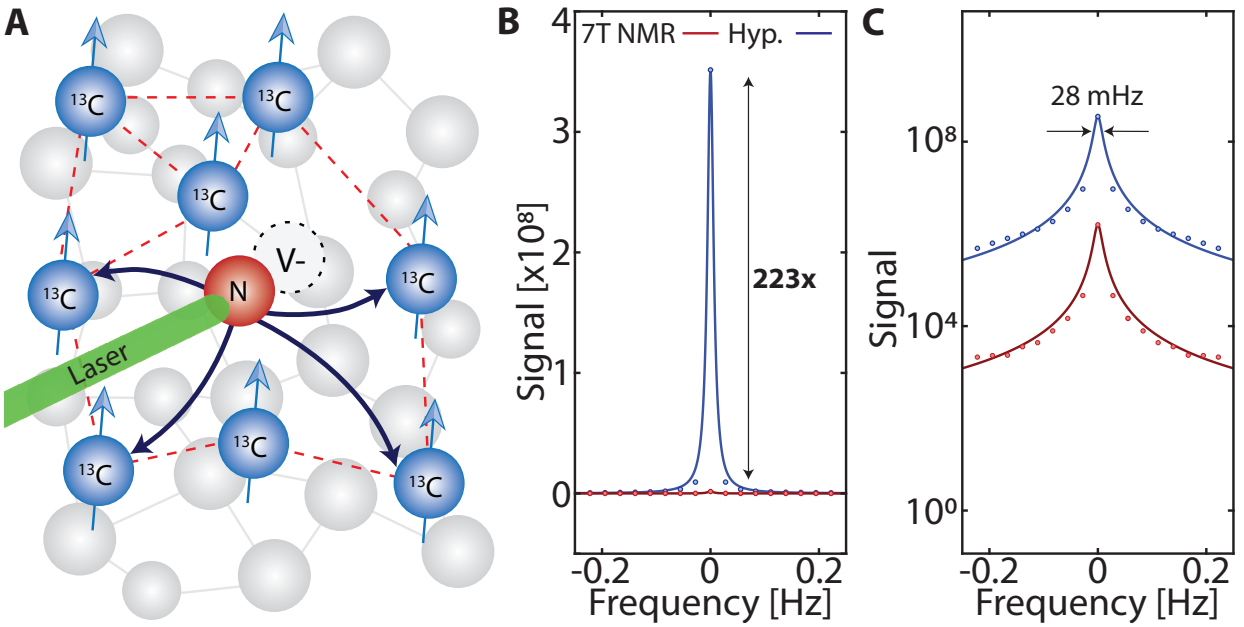

Figure 4.1 **System.** (A) Dipolar lattice of ^{13}C nuclei in diamond. Optically pumped NV centers are employed to hyperpolarize the ^{13}C nuclei (blue arrows). (B-C) *Signal gains from hyperpolarization*, demonstrated by comparing *single-shot* ^{13}C NMR spectra to conventional 7T (thermal) NMR. Data is shown in (B) linear and (C) log scales; line is a fit. Here, optical pumping was for 2min at 36mT, and thermal measurement was taken after 4hrs in the magnet.

are optically hyperpolarized by interactions with NV defect centers, which enhances their polarization ε=223-fold with respect to the thermal limit (Figure 4.1B). When placed in a Bloch transverse state $\hat{\mathbf{x}}$ in the absence of periodic driving, these precessing nuclei naturally dephase with free induction decay lifetime $T_2^*\approx$1.5ms and measured observables decay to zero. Under rapid pulsed spin-lock driving, however, we are able to effect a significant improvement; the observed lifetimes $T_2'\approx$90.9s constitute a >60,000-fold extension over T_2^*. Moreover, with a drive consisting of ≈5.8M pulses, we are able to continuously probe the thermalization process for up to 573s with high fidelity. This corresponds to $>10^{10}$ precession cycles of the nuclear spins. Both with respect to the number of pulses applied, and the ultimate transverse spin lifetimes, these values are amongst the largest reported in literature [93, 45]. Our work therefore suggests interesting opportunities for Floquet control afforded in hyperpolarizable spin networks consisting of dilute low-gyromagnetic ratio nuclei [44].

A primary contribution in this work is the ability to probe the system thermalization dynamics with unprecedented signal-to-noise (SNR). Integrated SNR (see Figure 4.1B-C) exceeds 10^9 per shot, arising from a combination of hyperpolarization and continuous spin readout in our experiments. This permits a view into the thermalization process with a high degree of clarity, in a manner not directly accessible in previous experiments. We

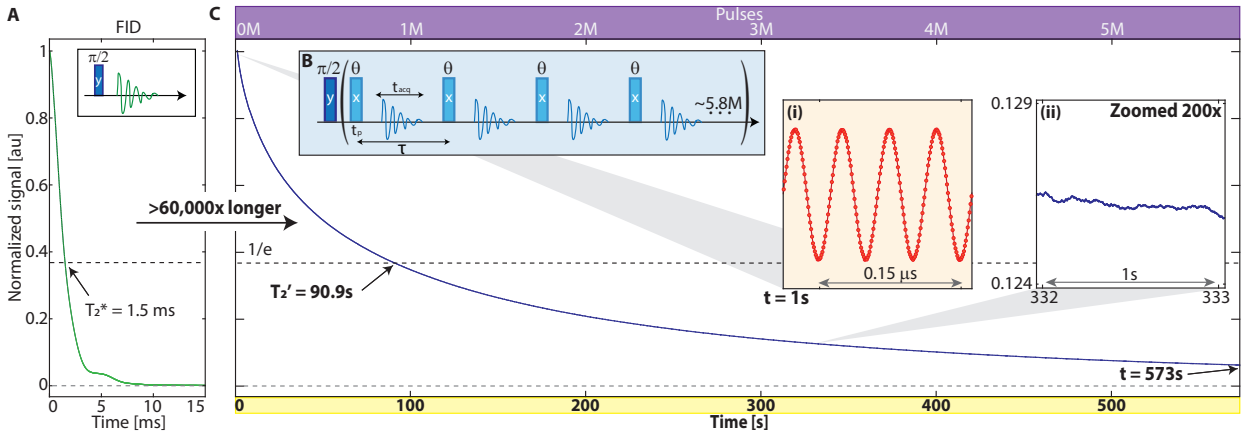

Figure 4.2 **Floquet driving and lifetime extension.** (A) Conventional ^{13}C free induction decay with $T_2^*{\approx}1.5$ms. (B) *Floquet drive* consists of a train of θ-pulses applied spin-locked with the ^{13}C nuclei. Spins are interrogated in t_{acq} windows between the pulses (blue lines), the nuclear precession is sampled every 1ns. Pulse repetition rate $\omega = \tau^{-1}$, and sequence not drawn to scale. (C) *Minutes-long lifetimes* of the transverse state result from the Floquet sequence ($\theta{\approx}\pi/2$). Data (blue points) shows *single-shot* measurement of survival probability in the state ρ_I, and line is a fit to a sum of five exponentials. Here $t_{\text{acq}}{=}2\mu$s, $t_p{=}40\mu$s and $\tau{=}99.28\mu$s, and the 573s period corresponds to ≈5.8M pulses (upper axis). We neglect here the first 100ms for clarity (see Figure 4.3A). *Inset (i)*: Raw data showing measurement of the ^{13}C spin precession, here at 1s into the decay. *Inset (ii)*: Data zoomed 200x in a 1s window. Using a $1/e$-proxy yields $T_2'{\approx}90.9$s. This corresponds to a >60,000-fold extension compared to the FID.

are able to identify the four smoothly transitioning thermalization regimes that confirm theoretical predictions [56] — an initial transient to the prethermal plateau, the crossover to unconstrained thermalization and, ultimately, infinite temperature. High measurement SNR also allows characterization of heating rates over a wide range of drive frequencies. We observe system heating scaling $\propto \exp(-t^{1/2})$ at high drive frequency ω. Simultaneously, the transient system response unveils interesting harmonic behavior while establishing the prethermal plateau.

4.2 System

In a magnetic field $\mathbf{B}_0$, the ^{13}C nuclei interact by the dipolar Hamiltonian,

$$\mathcal{H}_{dd} = \sum_{j<k} d_{jk}^{\text{CC}}(3I_{jz}I_{kz} - \vec{I}_j \cdot \vec{I}_k), \tag{4.1}$$

with a coupling strength

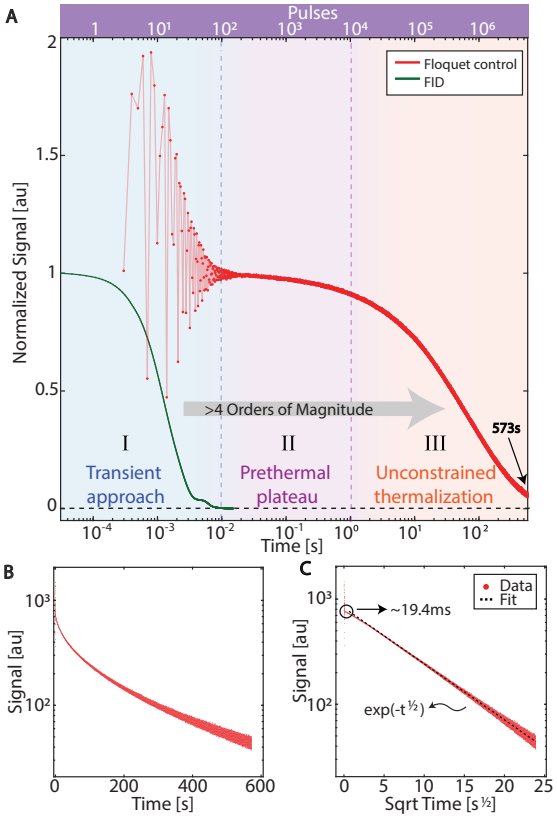

Figure 4.3 **Floquet thermalization regimes.** (A) *Log-scale* visualization of the full data in Figure 4.2C. Points are experiment, there are ≈5.8M data points here. Lines are carried out in two segments with solid and dashed lines referring to a stretched exponential with α=0.55 and α=0.5 respectively. Upper axis denotes number of pulses applied, here $J\tau$ ≈0.066. Green points are the FID. We observe distinct, yet smoothly transitioning (shaded), thermalization regimes (**I-IV**): a ≈10ms oscillatory approach **(I)** to the Floquet prethermal plateau (**II**), followed by unconstrained thermalization (**III**). Infinite temperature regime **(IV)** is not reached in these measurements up to 573s. (B) *Semi-log* plot of the experimental data (red points) in regime **II-III** shows a dynamic change of thermalization rate. Moving averaging is applied here every 0.1s. Blue line is a fit to a sum of five exponentials. (C) *Semi-log plot against* $\sqrt{t}$ yields an approximately linear dependence (dashed line) for ∼500s. Cusp (marked) at ≈9.2ms marks transition to the prethermal plateau (regime **II**, see also Figure 4.9).

$$d_{jk}^{\mathrm{CC}} = \frac{\mu_0}{4\pi}\hbar\gamma_n^2(3\cos^2\beta_{jk} - 1)\frac{1}{r_{jk}^3}, \tag{4.2}$$

where I refer to spin-1/2 Pauli matrices, γ_n=10.7MHz/T is the gyromagnetic ratio, and

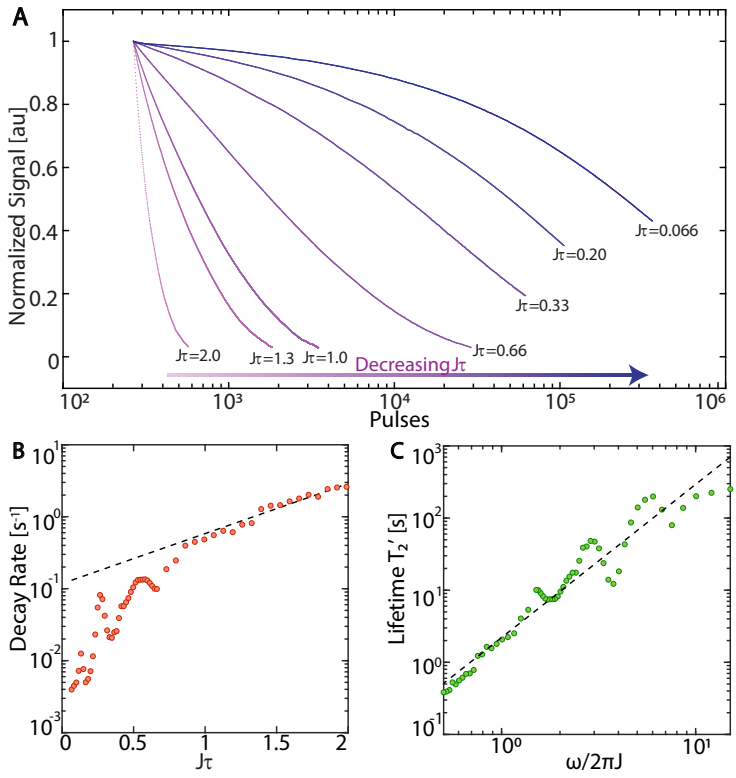

Figure 4.4 **Exponential dependence of Floquet prethermal lifetimes.** (A) *Variation with* $J\tau$. Data (points) shows measured signal probing thermalization dynamics in regime **II-III** for representative $J\tau$ values (colorbar). Here $\theta{\approx}\pi/2$ and t_{acq}=32μs and there are a high number ($\sim 10^3$-10^6) points per line [27]. Data is normalized at the transition points to the prethermal plateau (following Figure 4.3C). The Floquet prethermal decay rates reduce considerably with decreasing $J\tau$. See full data at Ref. [1]. *Inset:* Zoom-in (on semilog scale). (B) *Extracted decay rates* focusing on the region where decay follows $\sim\exp(-t^{1/2})$. Plotted in a semi-log scale against ω/J, the dashed line reveals an approximately exponential scaling of the decay rates at low drive frequencies ω (dashed line is a linear fit). At high ω we observe sharp narrow features in the prethermal decay rates. (C) *Plotted against* $J\tau$, showing exponential scaling at higher drive frequency (dashed line). Narrow features in the decay rates superimposed on the exponential background are more emphasized here. (D) *Log-scale plot* of the extracted T_2' lifetimes against ω. Dashed line is a linear fit.

$\beta_{jk} = \cos^{-1}\left(\frac{\mathbf{r}_{jk}\cdot\mathbf{B}_0}{r_{jk}B_0}\right)$ is the angle of the internuclear vector $\mathbf{r}_{jk}$ to the magnetic field. The sample is oriented with $\mathbf{B}_0||[100]$, such that nearest neighbor (NN) ^{13}C sites are decoupled. Ultimately, the median dipolar coupling is $J = \left\langle d_{jk}^{\text{CC}}\right\rangle \approx$0.66kHz (Figure 4.2A). The random ^{13}C distribution leads to a long tailed distribution in the coupling values, effectively rendering the interaction Hamiltonian *disordered*. In addition, the nuclei are subject to on-site disorder,

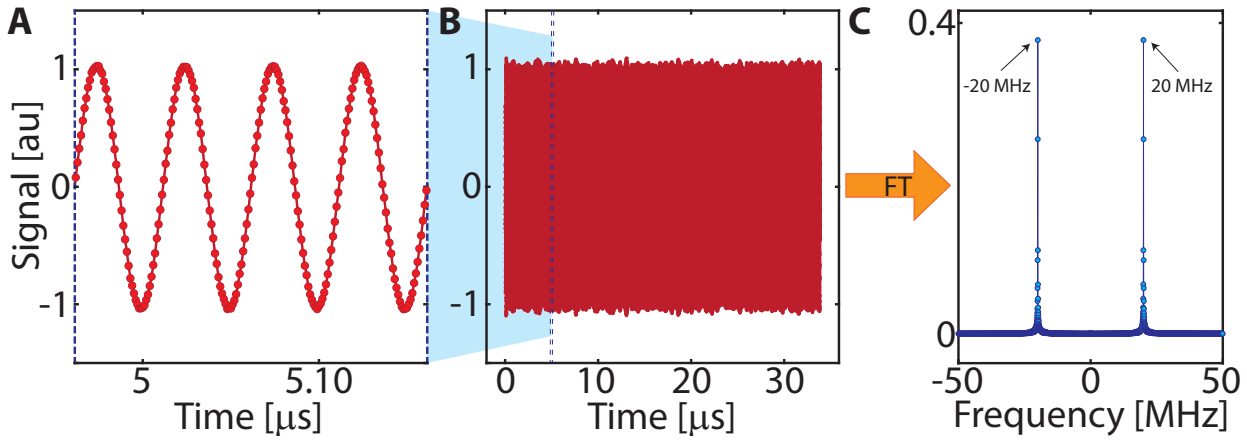

Figure 4.5 **Data processing chain.** (A) Raw data of ^{13}C nuclear precession measured inductively, here heterodyned from 75MHz (Larmor frequency) to 20MHz. The window shown is a 150ns part of the larger acquisition window. (B) Raw data corresponding to one complete acquisition period between the pulses, here t_{acq}=32μs. (C) Fourier transformation reveals characteristic peaks at the heterodyning frequency $\pm$20MHz. This amplitude forms the primary data that is plotted in Figure 4.2. We therefore obtain one data point per acquisition window, and in Figure 4.2C a total of $\approx$5.8M data points.

i.e. local dephasing fields, $\mathcal{H}_z = \sum_j c_j I_{jz}$, arising from interactions with paramagnetic impurities (e.g. P1 centers) [131]. At typical 20ppm P1 concentrations, $\langle c_j^2 \rangle \approx 0.4[\mathrm{kHz}]^2$ [17]. In the rotating frame of the Floquet drive, the ^{13}C Hamiltonian is therefore $\mathcal{H} = \mathcal{H}_{dd} + \mathcal{H}_z$.

Compared to previous NMR experiments, our work introduces some special features leveraging nuclear hyperpolarization [143, 144]. The vast preponderance of NMR experiments have been limited to high-γ_n and dense (100% abundant) nuclei such as ^{19}F, ^{31}P, and ^{1}H [136, 120]. Instead, we focus attention to dilute networks of insensitive nuclei (^{13}C). This provides a combination of factors critical to establishing Floquet control for long periods — *(i)* a relatively low $\|\mathcal{H}_{\mathrm{dd}}\|$ compared to networks constructed from sensitive (high-γ_n) nuclei, scaling as $\eta^{1/2}\gamma_n^2$, where η is the nuclear enrichment, *(ii)* a long tailed distribution in couplings, and *(iii)* long nuclear T_1 (here $\approx$25 min), significantly higher than many experimental systems, sets a long memory time for the nuclear states.

Indeed, these very factors, while attractive for Floquet control [45], usually make experiments challenging on account of poor sensitivity. Inductively measured nuclear signals scale $\propto \gamma_n^2$, with a measurement repetition rate set by T_1^{-1}, making obtaining reasonable SNR a challenge [70]. We mitigate these difficulties by a combination of hyperpolarization and instrumental advances (allowing continuous sampling). Hyperpolarization is carried out at B_{pol}=36mT through a method previously described [21, 15]. Measurement throughput is accelerated by $\approx\frac{1}{2}\varepsilon^2 \left[T_1(B_0)/T_1(B_{\mathrm{pol}})\right]^2 \frac{T_2'}{T_2^*} \gtrsim 10^{10}$ over conventional high-field (FID-based) NMR readout.

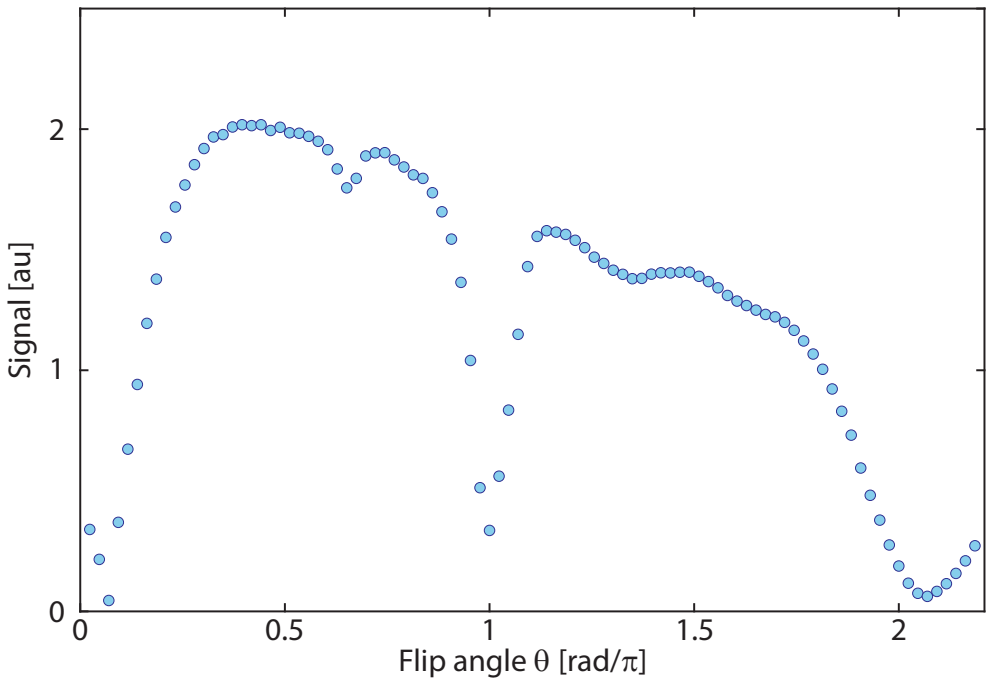

Figure 4.6 **Signal dependence on flip angle θ.** Panel shows the net signal obtained upon application of a train of θ-pulses following the initial $\pi/2$ pulse. We identify clear signal dips at $\theta \approx \{\pi, 2\pi\}$ corresponding to rapid decay due to evolution under the dipolar Hamiltonian (see [14]). In these experiments t_{acq}=32μs and pulse spacing τ=100μs.

4.3 Floquet control and measurement

The driving protocol is described in Figure 4.2B [118, 133, 132]. Post polarization, the ^{13}C nuclei are rotated to transverse axis $\hat{\mathbf{x}}$ on the Bloch sphere, placing them in an initial state $\rho_I \sim \varepsilon I_x$. The Floquet drive consists of an equally spaced train of pulses of flip angle θ. The center-to-center pulse separation is $\tau\,[=(\omega/2\pi)^{-1}]$. After N pulses, the unitary operator describing its action in the rotating frame can be written as, $U(N\tau) = [\exp(i\theta I_x)\exp(i\mathcal{H}\tau)]^N$, where we have made a simplifying assumption of δ-pulses. The data is sampled after every pulse, t_j=$j\tau$, and the evolution can be described by the operation $U(t) = \prod_{j=1}^{N}\exp(i\mathcal{H}^{(j)}\tau)$, where we refer to the toggling frame Hamiltonians after every pulse [59], $\mathcal{H}^{(j)} = \exp(ij\theta I_x)\mathcal{H}\exp(-ij\theta I_x)$. This evolution can be recast as, $U(t) = \exp(i\mathcal{H}_F N\tau)$, where H_F is the Floquet Hamiltonian that captures the system dynamics under the drive. $\mathcal{H}_F$ can be expanded in a Floquet-Magnus expansion [106, 166, 31] to leading order in the parameter ζ=$2\pi J/\omega$, and in the regime $\zeta \ll 1$, yields a time independent Hamiltonian,

$$\mathcal{H}_F^{(0)} = \sum_{j=1}^{N}\mathcal{H}^{(j)} \approx \sum_{j<k} d_{jk}^{\text{CC}}\left(\frac{3}{2}\mathcal{H}_{\text{ff}} - \vec{I}_j\cdot\vec{I}_k\right), \tag{4.3}$$

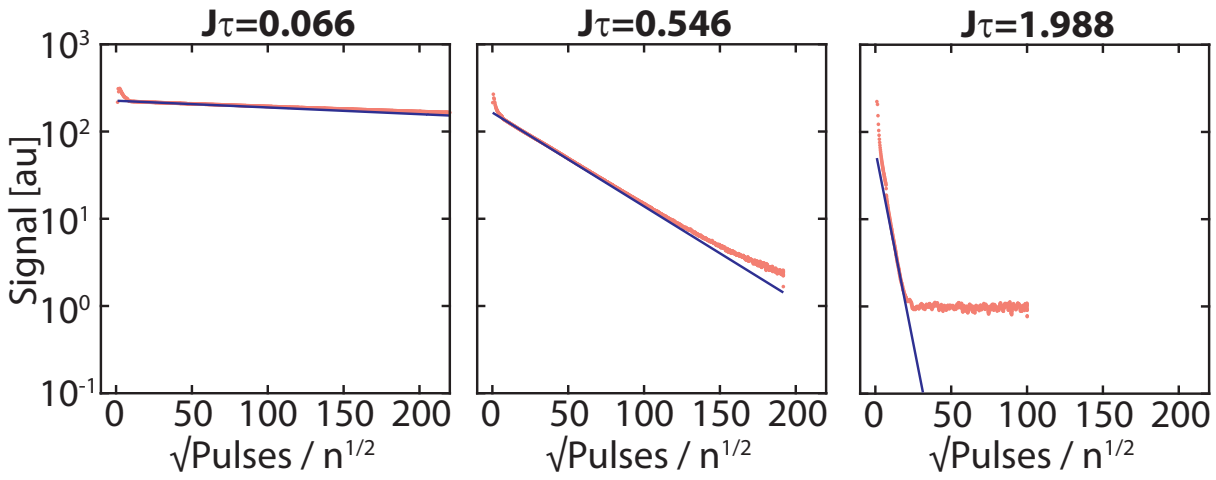

Figure 4.7 **Raw data corresponding to Figure 4.4.** Movie (see at YouTube here:[1]) shows signal plotted on a semi-log scale against $\sqrt{t}$. Data are red points, while the blue line is a fit taken in the region where $\alpha \approx 1/2$. The extracted rates are plotted as points in the lower panels of Figure 4.4.

with the flip-flop Hamiltonian, $\mathcal{H}_{\rm ff} = I_{jz}I_{kz} + I_{jy}I_{ky}$ [14]. The $\mathcal{H}_z$ dephasing fields are filtered out in $\mathcal{H}_F^{(0)}$. For sufficiently small ζ, Eq. (4.3) holds irrespective of the flip-angle θ, except for certain special values ($\theta \approx \pi, 2\pi$). We note that this constitutes a key difference with respect to conventional dynamical decoupling control (CPMG [40]), wherein the interspin couplings are retained and result in rapid ^{13}C decay [14]. The higher order terms in the Magnus expansion are progressively smaller, but contribute to long time system dynamics [166, 53]. Importantly, the initial transverse magnetized state ρ_I is a conserved quantity under $\mathcal{H}_F^{(0)}$, since $[\rho_I, \mathcal{H}_F^{(0)}]=0$. This leads to prethermal lifetimes that depend exponentially on the drive frequency ω. Ultimately, the divergence of the expansion manifests in the system heating to infinite temperature.

Figure 4.2C shows the measured survival probability $F(N\tau)$ of the state ρ_I under the applied Floquet drive. This can be expressed as, $F(N\tau) = \frac{1}{2}\mathrm{Tr}\left\{\rho_I U(N\tau)^\dagger \rho_I U(N\tau)\right\}$. We have neglected the first 100ms here for clarity (see Figure 4.3A for full data). Data shows significant extension in the transverse state lifetimes. Points in Figure 4.2C are the experimental data while the line is a fit to a sum of five exponentials (zoomed in Figure 4.2C *(ii)*); the high measurement SNR is evident in the zoomed data. The product $J\tau$ is a convenient metric to label the Floquet regime of operation, and in these measurements $J\tau$=0.066. The $\theta \approx \pi/2$ pulses here are applied every $\tau \approx 100\mu$s, and the 573s period encapsulates ≈5.8M pulses. For comparison, the conventional ^{13}C free induction decay [102] in the absence of Floquet driving is shown in Figure 4.2A, where decay occurs in $T_2^* \approx 1.5$ms on account of internuclear couplings and static field disorder. High SNR and continuous weak measurement readout allows us to recognize (see Figure 4.3B) a dynamic change in the decay rate constant along the

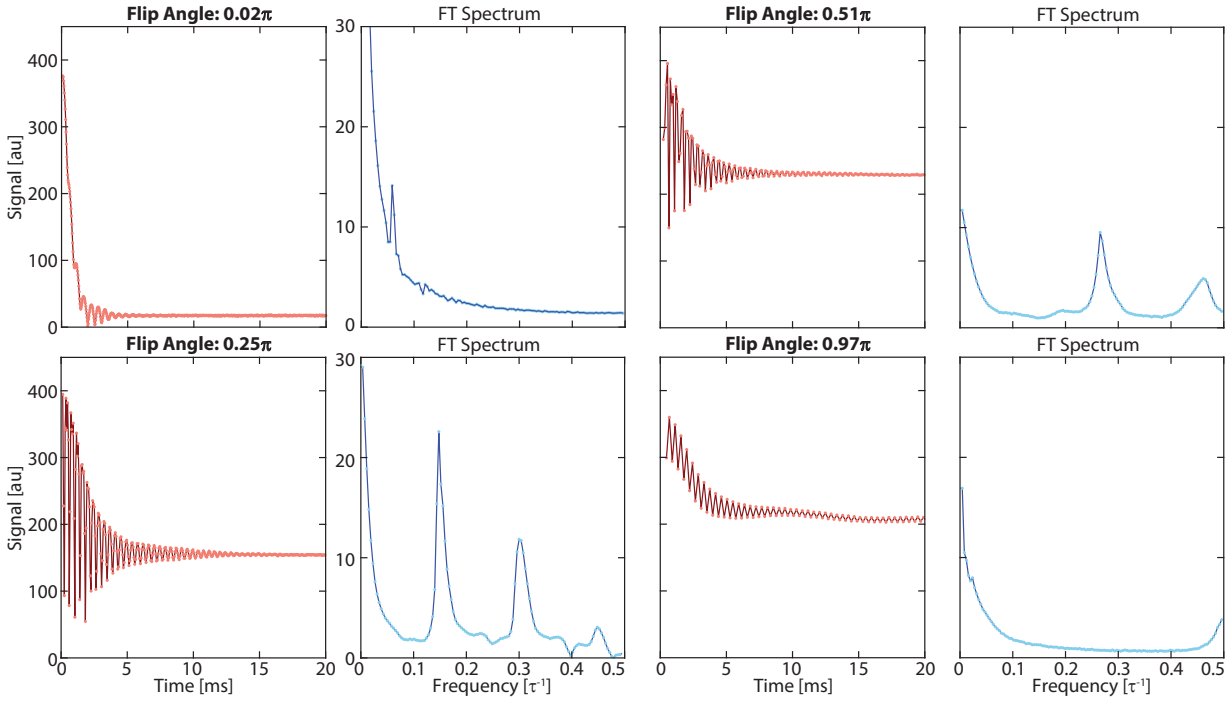

Figure 4.8 **Raw data corresponding to Figure 4.9.** Movie (see at YouTube here:[2]) shows frames corresponding to the transient approach to prethermal plateau for different flip angles θ. Panels show the transient approach and Fourier transform of the oscillations showing characteristic frequencies.

curve, making it difficult to quantify the decay rate by a single number. The data especially past 100ms is found to fit well to the stretched exponential $\sim \exp\left[-(t/T_2')^{1/2}\right]$, from where we extract $T_2'\approx$353s. Alternatively, using a $1/e$- intersection (dashed line in Figure 4.2C) as a convenient proxy yields, T_2'=90.9s. The extension leads to substantial line-narrowing of the ^{13}C NMR spectrum ($\sim$28mHz in Figure 4.1C).

The measurement procedure for Figure 4.2C is detailed as follows. The signal is sampled every 1ns in $t_{\rm acq}$ windows between the pulses (see Figure 4.2B). Such continuous readout (akin to weak measurement [122]) yields significant SNR advantages over point-by-point stroboscopic measurements. Rapid data sampling throughput (at f_s=τ^{-1}) also allows further filtering to be applied when the dynamics are slow compared to f_s. With this, we obtain a single-shot SNR $>10^3$ per measurement point, and $\approx 4\times10^9$ for the integrated signal (see Figure 4.1C).

4.4 Data Processing

We now present details of the data processing employed in this manuscript. Figure 4.5 describes the chain of steps involved in obtaining decay curves such as Figure 4.2C. We readout the NMR signal continuously in $t_{\rm acq}$ periods between the pulses, and the pulses are spaced apart by τ=100μs. A representative such acquisition window is shown in Figure 4.5B, in this case $t_{\rm acq}$=32μs. The data here (taken 1s into the decay) is sampled at 1Gs/s (Δt=1ns). A zoom in (Figure 4.5A) reveals high SNR oscillations corresponding to the precession of the hyperpolarized nuclei; the frequency here is 20MHz (heterodyned from the 75MHz Larmor frequency). For each such window, we take a Fourier transform (Figure 4.5C), and extract the 20MHz peak. This corresponds effectively to digital bandpass filtering with a filter linewidth of $\sim t_{\rm acq}^{-1}$. Each such point is then plotted to create the decay curves in Figure 4.2C, Figure 4.3 and Figure 4.4. Since the measurements are carried out after every pulse, we obtain a data point in Figure 4.5D every τ=100μs. Over the 573s decay period, this corresponds to $\approx$5.8 million measurement points. However, the data itself is slowly varying (except in regime **I**), and can be thought of as being effectively oversampled by the measurement points. Moving average filtering thus increases SNR further, acting as a low-pass filter to suppress higher frequency variations. We typically employ a moving average filter size of 0.1s.

4.5 Materials and Methods

The sample used in these experiments consists of a CVD fabricated single crystal of diamond with $\sim$1ppm of NV centers. The sample is placed flat, i.e. with its [100] face pointing parallel to the hyperpolarization and interrogation magnetic fields (36mT and 7T respectively). In this configuration, the internuclear vector between ^{13}C nuclei at NN sites on the lattice are positioned at the magic angle, and hence are suppressed.

For hyperpolarization, we employ continuous optical pumping and swept microwave irradiation for $\sim$40s through a technique described previously. Hyperpolarization is carried out at low field, the sample is shuttled to high field, and the Floquet sequence in Figure 4.2B is then applied. NV-^{13}C polarization transfer occurs via biased Landau-Zener traversals in the rotating frame; spin diffusion serves to transfer polarization to bulk ^{13}C nuclei in the diamond lattice.

Figure 4.6 shows the variation of the integrated signal as a function of the flip angle θ employed in the pulse sequence. We refer the reader to Ref. [14] for a more detailed exposition of the observed trend. For experiments Figure 4.2 and Figure 4.3 of this Chapter, we employ a pulse duty cycle of $\sim$50%, where the measured SNR is highest.

The figure movie Figure 4.7 (accessible in Ref. [1]) shows the full dataset corresponding to Figure 4.4. Similar to Figure 4.4B, we plot the data against $\sqrt{t}$ in a semi-log axis. Here the value $J\tau$ is varied by altering the spacing between the pulses in Figure 4.4B. The blue straight lines in the movie show the fit to α=1/2 region. These decay rates, corresponding to the slope of the blue lines in Ref. [1], are plotted in the lower panels of Figure 4.4.

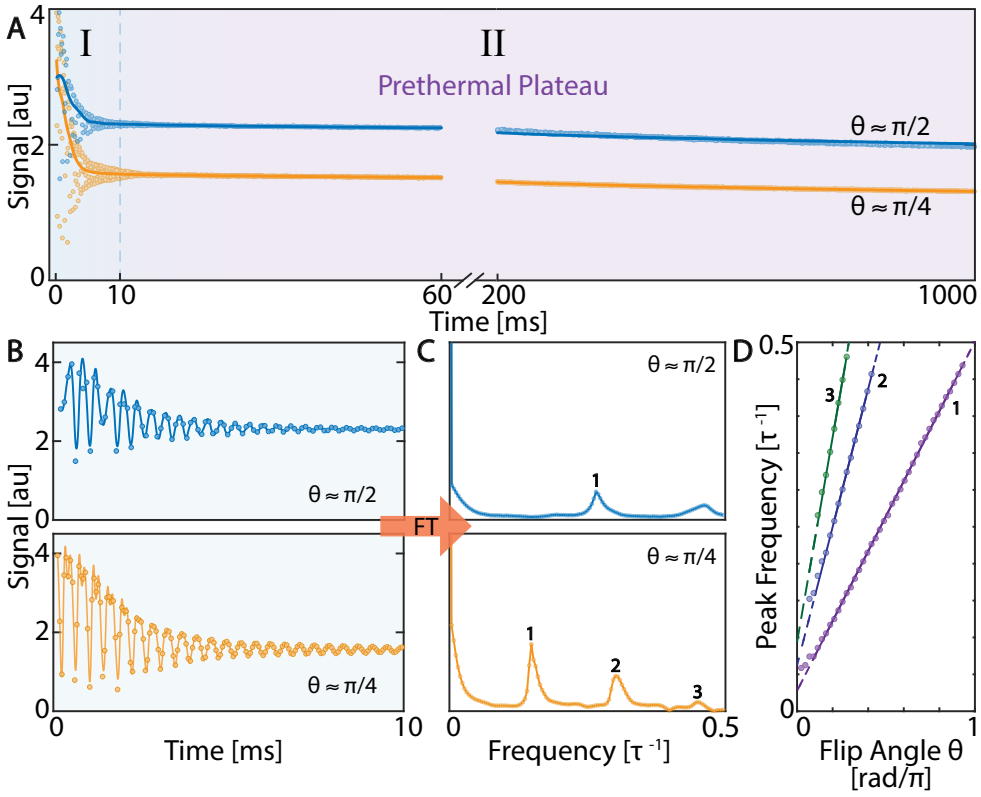

Figure 4.9 **Transient approach to prethermal plateau.** (A) *Oscillations in the approach to prethermal plateau* seen for data zooming in on region **I**, in a 1s long window (see Figure 4.3A). Data (points) corresponds to $\theta{\approx}\{\pi/2, \pi/4\}$ respectively. Solid line is data with moving average filtering applied over the entire region (see Figure 4.3B). (B) *Zoom in* to region **I** shows the transient approach with high SNR. It is evident that the oscillations are at higher frequency for $\theta{\approx}\pi/2$. Solid line is a spline fit to guide the eye. (C) *Fourier transforms* of panels in B allows identification of the frequency components constituting the oscillations as a function of $\omega{=}\tau^{-1}$. Harmonics are represented by numbers. It is clear that primary oscillation frequency is higher for $\theta{\approx}\pi/2$, where we extract the primary harmonic position at $\approx 0.26\tau^{-1}$. (D) *Variation with flip angle* θ. Data shows the position of the oscillation frequency for the primary and higher harmonics (numbered). See full data at Ref. [2]. Solid lines are linear fits, while dashed line is an extrapolation. Slopes are in the ratio expected.

Similarly, the figure movie Figure 4.8 (accessible in Ref. [2]) shows the full dataset corresponding to Figure 4.9, describing the approach to the Floquet prethermal plateau for different values of the flip angle θ.

4.6 Floquet Prethermalization

To better illustrate thermalization dynamics of the spins, Figure 4.3A shows the full data on a logarithmic time scale. The FID is also shown, and lifetime extension is evident from the shift in the curves. Points are experimental data with no moving average applied, and the solid and dashed lines are stretched exponential fits. We identify distinct, albeit smoothly transitioning, regimes in the thermalization process (shaded in Figure 4.3A). Following Ref. [42], we refer to them as: **(I)** an initial regime of constrained thermalization ($0<t<20$ms), where we observe oscillatory behavior with a harmonic frequency response of the Floquet drive frequency ω, (**II**) the prethermal plateau, leading into (**III**) unconstrained thermalization towards the (**IV**) infinite temperature state (not reached in these experiments).

Let us first focus our attention to the dynamics in regimes **II** and **III**. Figure 4.3B-C shows two complementary visualizations after moving average filter is applied over the entire data. Figure 4.3B, plotted on a semi-log scale, makes evident that the decay rate constant changes over the entire thermalization period. The high SNR and rapid sampling rate, however, allows us to unravel the exact rate change behavior in a manner not accessible in previous experiments. It is easiest seen when re-plotted against $\sqrt{t}$ in Figure 4.3C, where we obtain an approximately linear trend (dashed line) over a long period ($\sim$500s). The prethermal dynamics is therefore $\sim\exp(-t^{\alpha})$ with exponent $\alpha\approx 1/2$. Decades-old NMR experiments had observed a similar trend in paramagnetic impurity rich solids [157, 100]. We emphasize however the high SNR of the data in Figure 4.3, proffering insights into, and deviations from, this behavior. At higher $J\tau$ values, for instance, we observe a dynamic decrease in α away from 1/2 in regime **III** (movie available at Ref. [1]). The turning point (cusp) in data in Figure 4.3C, obtained after moving average filtering over the oscillations in regime **I**, also allows a convenient means to quantify the exact point of transition to prethermal plateau. The length of this period ($\approx$10-20ms) closely mirrors the period over which the FID completely decays (see Figure 4.3A).

To study the scaling of the prethermal lifetimes with the frequency of the Floquet drive ω, Figure 4.4A shows similar data at a range of $J\tau$ values. This is carried out by varying the inter-pulse spacing τ in Figure 4.2B. The full dataset (shown in Supplementary Information) consists of measurements at 57 such $J\tau$ values, but we show a restricted set here for clarity. Again, there is a high density of data points in each experimental line. To restrict attention to regions **II-III**, we normalize the data at the transition points to the prethermal plateau, identified from the cusps as in Figure 4.3C. The data show thermalization proceeding more slowly for lower values of $J\tau$. The dynamic change of rate coefficient makes plotting a single graph that encapsulates the full long-time behavior difficult. Instead, we extract the decay rates focusing on regime **II**, where decay (similar to Figure 4.3C) follows an exponent $\alpha\approx 1/2$.

This is presented in two complementary viewpoints in Figure 4.4B-C. First, in Figure 4.4B plotted on a semi-log scale with respect to the drive period τ, we see a linear trend in the decay rates, especially at high τ (dashed line). This points to an approximately exponential scaling of the state preservation lifetimes with drive frequency, one of the signatures of Floquet prethermalization. At low τ however, we observe a flatter slope with sharp features

in the decay rates. Figure 4.4C shows an alternate view instead in terms of ω. Extracting the transverse state lifetimes T_2' on the log-log plot, we find a slope of 2.1 ± 0.1 at low-frequency suggesting a Fermi's Golden Rule scaling with drive frequency [54].

The sharp peaks in the decay rates in the high ω regime in Figure 4.4B-C are intriguing. We believe this is a manifestation of quantum sensing — the ^{13}C nuclei see an enhanced decay rate when subjected to environmental magnetic fields at a fixed frequency $f_{\rm ac}$ matched in periodicity (resonant) with the pulse sequence, at $f_{\rm ac}{=}\theta/(2\pi\tau)$. The first two peaks are observed at $f_{\rm ac}{\approx}2.5$kHz and $f_{\rm ac}{\approx}5.0$kHz. This is possible because the pulsed spin-lock sequence exhibits dynamical decoupling properties similar to quantum sensing protocols [44]. The exact origin of these fields in Figure 4.4B-C are unclear and beyond the scope of the current manuscript. A more detailed exposition on exploiting Floquet prethermal states for quantum sensing will be presented elsewhere.

4.7 Approach to prethermal plateau

Finally, let us elucidate how the nuclear spins approach the Floquet prethermal plateau [61], focusing attention on regime **I** of Figure 4.3A. We observe transients in the survival probability leading into the plateau; this is shown for two choices of the flip-angle θ in Figure 4.9A ($\theta{\approx}\pi/2$ and $\theta{\approx}\pi/4$) respectively. High SNR allows us to track the oscillatory dynamics after every pulse, providing a window into how the approximately time-independent Hamiltonian is established. Moreover, the prethermal plateau level is itself dependent on θ.

The transients last for $t{\approx}10$ms, which is approximately the total lifetime for the original FID, and is of the order of magnitude of $\|\mathcal{H}_{dd}\|^{-1}$ (see Figure 4.3A). As Figure 4.9B indicates, the oscillation periodicity is closely related to the flip angle employed; for $\theta{\approx}\pi/2$, for instance, the oscillations occur at a fourth of the frequency of the Floquet drive ω. To see this more clearly, Figure 4.9C shows the respective Fourier transforms in a 10ms region. Plotted against ω, we identify harmonics of the oscillatory dynamics (numbers). For $\theta{\approx}\pi/4$ (lower panels in Figure 4.9B-C), we recognize a primary harmonic and higher harmonics at $\approx n\omega/8$, where n is an integer.

Intuitively, this characteristic periodicity can be thought of as arising from the number of pulses N_k required to return the Floquet unitary to a prior configuration; *i.e.* such that the toggling frame Hamiltonian after $2N_k$ pulses is equivalent to that after N_k, $\mathcal{H}^{(2N_k)}{=}\mathcal{H}^{(N_k)}$. This corresponds to effectively completing a 2π rotation of the Hamiltonian in the toggling frame. Four pulses are therefore needed for $\theta{=}\pi/2$ in Figure 4.9A. In general, the primary harmonic frequency is expected to be at frequency $f{=}\theta/(2\pi\tau)$. Experiments confirm this picture; we extract the oscillation frequencies in regime **I** as a function of θ, and they fall neatly onto three straight lines for the three harmonics (see Figure 4.9D). We hypothesize that the higher harmonics arise from bilinear and trilinear terms in the density matrix produced by dipolar evolution. The experimentally measured slopes are in the ratio 1:1.98:2.93, close to the 1:2:3 pattern expected.

4.8 Conclusion

In conclusion, we have observed Floquet prethermalization of dipolar-coupled nuclear spins in a bulk solid at room temperature. The observed >90s-long prethermal lifetimes in diamond ^{13}C nuclei are over four orders of magnitude longer than free induction decay times, and significantly longer than in other systems. Our measurements unveil regimes of thermalization with a degree of clarity not accessible in previous NMR studies. Apart from fundamental insights, our work points to attractive opportunities possible via Floquet control in hyperpolarizable, dilute and low-γ_n nuclear networks. Protection and continuous interrogation of spins along a Bloch transverse axis for $\sim$10min periods opens avenues for high-sensitivity magnetometers, gyroscopes [20, 97], and spin sensors [11] constructed out of hyperpolarized prethermal ^{13}C nuclei.

Part III

Discrete Time Crystal and Echo Phenomena

Chapter 5

Utilizing the Floquet Engineering Toolbox

Recent interest has surged in periodically driven (Floquet) quantum systems as a means to explore new phases of matter that exist far from thermal equilibrium. A compelling example is discrete time crystals (DTCs), which are non-equilibrium phases of matter that persist indefinitely and are characterized by the dynamic disruption of time-translation symmetry. Recent studies have demonstrated the emergence of DTC phases supported by many-body localization. Yet, significant experimental challenges persist. These include the complete characterization of the DTC phase diagram and understanding the dynamics of its structural stability and thermalization processes toward infinite temperature—crucial endeavors for leveraging these non-equilibrium phases in quantum science applications. These tasks have, until now, been elusive in experimental settings.

In Chapter 6 we demonstrate a new approach for exciting and observing DTCs, in a manner which permits measuring their phase diagram with an unprecedentedly high resolution. We focus here on "prethermal" DTCs (PDTCs) — long-lived non-equilibrium states characterized by a robust subharmonic response that harnesses the phenomenon "Floquet prethermalization". Our approach yields an acceleration in the observation of the DTC phase by over a factor of 10^5 with respect to contemporary experiments, thereby constituting a breakthrough in the ability to excite characterize the emergent prethermal DTC order. Our observed PDTCs, observable quasi-continuously for more than 14s, are amongst the longest ever observed. In Chapter 7 we expand on this study to validate our findings.

Our experiments utilize a three-dimensional disordered lattice of interacting ^{13}C nuclear spins in diamond at room temperature. We introduce a novel "two-frequency" Floquet driving technique, where the spins are initially driven to a prethermal state by a rapid drive and subsequently subjected to periodic disruptions by a slower drive. A distinctive feature of our method is the continuous observation of the spins without collapsing the quantum state, enabling us to monitor the entire process of the formation and dissolution of the DTC phase in a single experimental run. Unlike previous point-by-point measurements, our single-shot detection approach increases throughput by $10^5 - 10^7$. This breakthrough permits the first

comprehensive experimental mapping of the PDTC phase diagram, fulfilling a long-term objective of the research community. Furthermore, we present the first real-time movies of PDTCs, included as ancillary files in our submission. Our experiments delineate the boundaries of the PDTC phase with exceptional detail and accuracy, revealing new insights into its structural stability and the dynamics of its transition.

Noteworthy also is the extent of quantum control we are able to apply the system. We apply a record 135,000 pulses to the quantum system, and are able to observe rigid DTC behavior for > 450 Floquet cycles, corresponding to a total period of $> 14s$. At the same time, we are able to continuously track the full system dynamics for this entire period, opening new perspectives into the thermalization dynamics that we explain through detailed theoretical and numerical analysis.

Our measurements align remarkably well with exact numerical simulations, which are constrained by small system sizes, and with theoretical predictions concerning the lifetime of PDTCs under a two-frequency drive. Consequently, we show that ^{13}C nuclear spins are apt for simulating nonequilibrium dynamics in systems approximately three orders of magnitude larger than those manageable in current numerical simulations. In such large systems, unlike in today's numerical models, many-body effects including phase transitions and thermalization can be studied with greater reliability.

The methodology presented in this study extends traditional Floquet driving techniques. We illustrate the ability to dynamically create (i) an emergent quasi-conserved quantity that supports non-equilibrium order and (ii) simultaneously induces DTC order, which disrupts a second, concurrent drive-induced spatiotemporal symmetry. It's important to note that conventional PDTCs do not manifest above the critical temperature required for symmetry breaking. Nevertheless, the Floquet-engineered quasi-conserved quantities we introduce enable the stabilization of PDTC order for a controlled duration. Thus, our findings enrich the toolkit of Floquet engineering and make significant contributions to the fields of AMO-based quantum simulation, quantum dynamics, and condensed matter physics. They suggest the use of multi-frequency concatenated drives to activate and maintain interacting quantum matter in far-from-equilibrium states. Additionally, our approach facilitates the detection of PDTCs with stable fractional subharmonic responses and the exploration of topological prethermal states maintained by quasi-periodic driving, which lack equilibrium analogs. We foresee these techniques being applied in quantum simulation and quantum sensing, utilizing hyperpolarized prethermal spins on solid-state and AMO platforms.

In Chapters 8 and 9 we entertain diversions into studies of echo phenomena related to the DTC.

Chapter 6

Critical Prethermal Discrete Time Crystal Created by Two-Frequency Driving

6.1 Introduction

Periodically driven (Floquet) quantum systems enable the realization of novel phases of matter far from thermal equilibrium. An interesting example are discrete time crystals (DTC) [141, 83, 52] – infinitely long-lived non-equilibrium phases of matter characterized by the dynamical breaking of time-translation symmetry [140, 84, 50, 82, 170, 68, 99], and stabilized by many-body localization, signatures of which were observed in recent experiments [41, 175, 119, 152, 137, 128, 113]. In the absence of localization and at high drive frequencies, energy absorption in Floquet systems is suppressed to exceedingly long times – a phenomenon known as *"Floquet prethermalization"* [150, 138, 121], wherein the periodically driven many-body state has a lifetime (T_2') that is significantly enhanced with respect to the natural system free induction decay time T_2^*. The heating rate $\propto (T_2')^{-1}$ is exponentially suppressed for sufficiently local interactions and large driving frequencies $\omega_f \gg J$, where J is the intrinsic spin coupling strength [10, 115, 105]. Recently, it has been suggested that Floquet drives can yield prethermal discrete time crystals (PDTCs) [51], non-equilibrium metastable states characterized by a robust subharmonic response in the drive frequency, and with a parametrically long lifetime that harnesses prethermalization. This has also inspired extensions of time crystal phenomena to classical systems [123, 173, 172]. Nevertheless, characterizing the full phase diagram of the emergent prethermal DTC order, rigidity, and elucidating its thermalization dynamics towards infinite temperature, remains a challenging task [136, 92]. At the same time, this is critical for advancing our fundamental understanding of non-equilibrium order, and for leveraging such collective phenomena in applications, such as in quantum simulation and sensing.

In this Chapter, we report on a novel experimental approach for the high-throughput

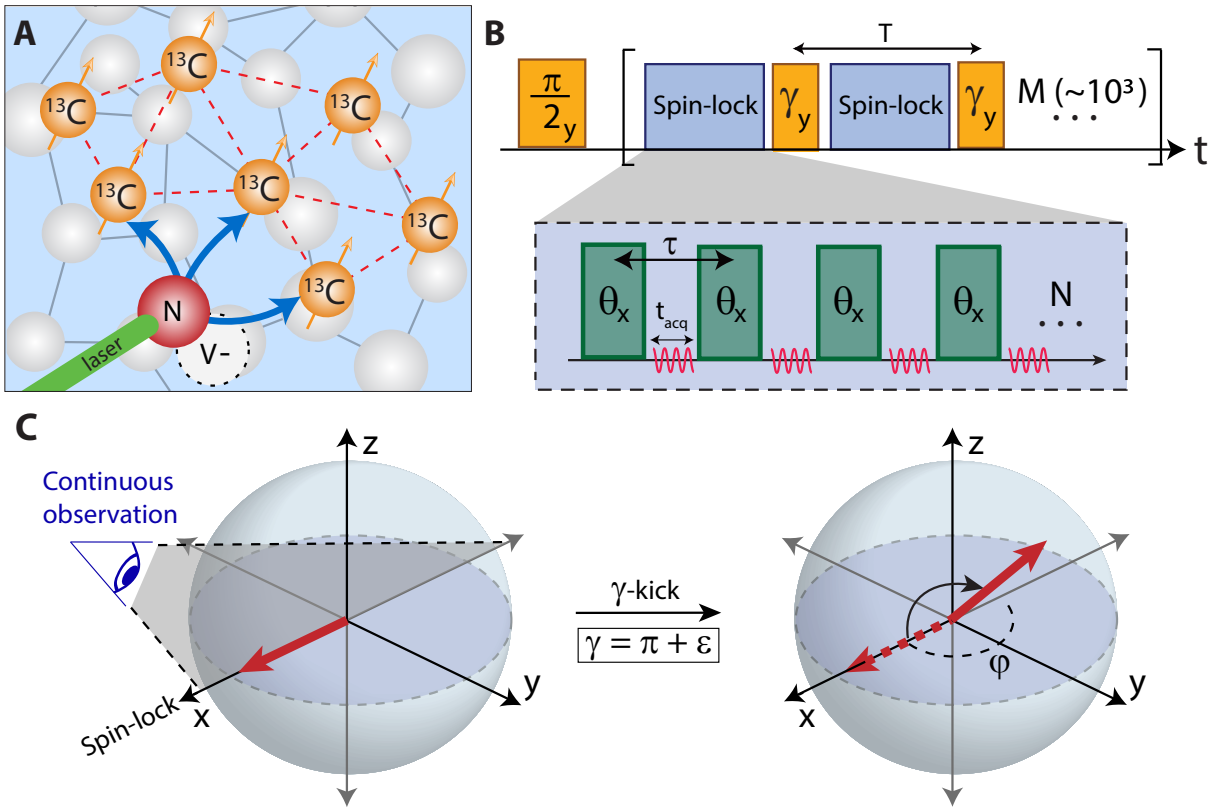

Figure 6.1 **Experimental Implementation.** (A) *System.* Dipolar lattice of ^{13}C nuclei in diamond. Dashed lines display representative interspin couplings. Optically pumped NV centers hyperpolarize the ^{13}C nuclei (blue arrows). (B) *Concatenated Floquet drive* at 7T consists of interleaved application of a fast-drive (blue) along $\hat{\mathbf{x}}$ and slow kicks (yellow) along $\hat{\mathbf{y}}$ separated by period T. Fast drive is composed of a train of $\theta(\neq\pi)$ pulses (green) separated by period τ that spin-lock the nuclei along $\hat{\mathbf{x}}$. Kick interval $T{=}N\tau$, and the ratio N is tunable within the range 1-10^3. System undergoes evolution under interspin couplings in intervals between the pulses. Spins are interrogated by RF induction in $t_{\rm acq}{=}64\mu$s windows between the pulses (red zig-zag lines); Larmor precession is sampled every 1ns. This effectively yields the ability to track projections along $\hat{\mathbf{x}}$ and $\hat{\mathbf{y}}$ quasi-continuously with period τ. (C) *Schematic Bloch sphere depiction* of the reduced density matrix of a single spin in the rotating frame. Following a kick, spins prethermalize towards the quasi-stationary state along $\hat{\mathbf{x}}$. Continuous tracking of the spins in the $\hat{\mathbf{x}}$-$\hat{\mathbf{y}}$ plane during this process is highlighted. Kicks shown are for the example $\gamma{=}\pi+\varepsilon$, where a PDTC state manifests as a periodic switching of the spins between $+\hat{\mathbf{x}}$ and $-\hat{\mathbf{x}}$ between successive kicks.

characterization of the formation and melting of PDTCs, which permits measuring their phase diagram with unprecedented high resolution. Our experiments are performed on an

interacting system of driven, hyperpolarized, ^{13}C nuclear spins in diamond (Figure 6.1A), endowed with long prethermal lifetimes under Floquet driving. We propose a novel use of a *"two-frequency"* Floquet drive [1] applied to the ^{13}C nuclei (see Figure 6.1B): the spins are made to prethermalize to an effective Hamiltonian $\overline{\mathcal{H}}$ (featuring a quasi-conserved $\hat{\mathbf{x}}$-magnetization [**SM**]), under a fast drive (with period τ), while also being periodically kicked away from the prethermal state by a slower drive with period T ($=N\tau$). The deviation away from the $\hat{\mathbf{x}}$ axis can be continuously monitored in periods between the fast drive, allowing a means to track the full system dynamics for long periods (¿14s), corresponding to 450 Floquet cycles or $>1.35 \times 10^5$ fast pulses, *without collapsing the quantum state*. Compared to point-by-point measurements in previous experiments, this allows a dimension reduction for mapping the PDTC phase diagram. In concert with the multiple-minute-long T_2' lifetimes of the ^{13}C nuclei, we are able to unravel the emergent prethermal DTC order with significantly higher clarity than previous measurements. The developed two-frequency drive represents a generalization of conventional Floquet driving allowing for a mutable design and the experimental realization of non-equilibrium order even beyond the paradigmatic DTC.

The two-frequency drive developed here represents a generalization of conventional Floquet driving; at once it allows the dynamical engineering of an emergent quasi-conserved quantity to stabilize non-equilibrium order at arbitrary temperatures, while simultaneously exciting the DTC order. Here we analyze the effect of driving on the long-time melting of the time-crystalline metastable state and show that the associated heating rates match well to a theoretical model. Overall therefore, this work enhances the Floquet engineering toolbox for the experimental realization and observation of non-equilibrium order beyond the paradigmatic DTC.

6.2 System

We consider a lattice of ^{13}C nuclei (Figure 6.1A) in diamond, optically hyperpolarized for $t_{\rm pol}$=60s by surrounding Nitrogen Vacancy (NV) centers [22, 16]. Hyperpolarization yields a ≈680-fold enhancement in ^{13}C magnetization over thermal equilibrium, yielding a starting density matrix $\rho_0 \sim \epsilon \mathcal{I}_z$, where ϵ=0.68% (see Methods). Here, $\mathcal{I}_\nu = \sum_j I_{j\nu}$ with $\nu \in \{x, y, z\}$ and $I_{j\nu}$ refer to spin-1/2 Pauli operators associated with nuclear spin j [47]. The natural abundance (1%) nuclei are not spatially ordered, and are coupled via dipolar interactions, $\mathcal{H}_{\rm dd} = \sum_{k<\ell} b_{k\ell}(3I_{kz}I_{\ell z} - \vec{I}_k \cdot \vec{I}_\ell)$. One can define a characteristic energy scale via the median interspin coupling, J=0.66kHz [30]. They are also subject to electron-mediated random on-site fields from surrounding NV and P1 paramagnetic defects, $\mathcal{H}_z = \sum_j c_j I_{zj}$ [130, 17]. Despite the concomitant position disorder and random on-site fields, the three-dimensional long-range nature of the interactions precludes many-body localization. The long-range interactions also make simulating the exact Floquet dynamics for a large number of spins inaccessible using classical computers.

[1] The term frequency refers to the inverse periods of the two superimposed drives, rather than their Fourier decompositions.

Figure 6.1B describes the experimental protocol — hyperpolarized ^{13}C nuclei are tipped along $\hat{\mathbf{x}}$, and subject to concatenated "fast" and "slow" Floquet drives, characterized by periods τ and $T = N\tau$ respectively. First, the fast drive, consisting of a train of $\theta(\neq l\pi)$ pulses (Figure 6.1B), engineers the internuclear Hamiltonian so that spins, initially aligned along $\hat{\mathbf{x}}$ are rendered quasi-stationary [30]. This is accomplished by arranging $\mathcal{H}_{\rm dd}\rightarrow\overline{\mathcal{H}} + d_N\mathcal{I}_x$ to leading order in the Magnus expansion, such that $[\overline{\mathcal{H}} + d_N\mathcal{I}_x, \mathcal{I}_x]$=0 (supplementary material Sec. VI). This quasi-conservation causes the spins to prethermalize along $\hat{\mathbf{x}}$ due to the nonintegrable character of $\overline{\mathcal{H}}$. By contrast, in the absence of the fast drive, evolution under $\mathcal{H}_{\rm dd}$ causes system observables to rapidly (in J^{-1}) become indistinguishable from a featureless infinite temperature state.

Interspersed at period T, the slower drive *kicks* the spins along the $\hat{\mathbf{y}}$ (or $\hat{\mathbf{z}}$) axis with angle γ (see Figure 6.1B). The spins are allowed to prethermalize back along $\hat{\mathbf{x}}$ between successive kicks (see Figure 6.2A). Figure 6.1C shows this visually on the Bloch sphere (in the rotating frame) for a kick of angle γ=π+ε. Therefore, in the prethermal plateau, the system is governed by an effective Hamiltonian obtained through an inverse frequency expansion (supplementary material Sec. VI). For γ=$\{0, \pi\}$, although the slow $\hat{\mathbf{y}}$-kicks do not cause any extra heating, they give rise to non-equilibrium ordered states. At γ=π the two-cycle time-evolution operator, U_F^2=$\exp[-i2T\overline{\mathcal{H}}]$, is governed by the $\mathbb{Z}_2$ symmetric many-body Hamiltonian $\overline{\mathcal{H}}$, where the $\mathbb{Z}_2$ symmetry is implemented by flipping the $\hat{\mathbf{x}}$-direction of all spins. This drive-induced symmetry of U_F^2, together with the discrete time-translation invariance, creates a *spatio-temporal* eigenstate order in U_F. Any initial state that breaks this symmetry is forced to oscillate with period $2T$, forming a PDTC state. In the experiment, we additionally observe that interactions stabilize a finite region near γ=π, where a stable PDTC period doubling response arises, with the spins flipping from $+\hat{\mathbf{x}}$ to $-\hat{\mathbf{x}}$ between successive kicks (Figure 6.1C).

A distinguishing feature of our experiments is the ability to quasi-continuously track the prethermalization dynamics after each kick. The spins are *non-destructively* interrogated by Nuclear Magnetic Resonance (NMR) in $t_{\rm acq}(>0.6\tau)$ windows between the fast pulses (Figure 6.1B). The magnitude and phase of the ^{13}C Larmor precession is sampled every 1ns, allowing one to reconstruct the instantaneous projections $\langle\mathcal{I}_x(t)\rangle$, as well as the phase $\varphi(t)$ of the spin vector in the $\hat{\mathbf{x}}$-$\hat{\mathbf{y}}$ plane (see Methods). In reality, the quasi-continuous time variable t is discretized in units of τ. Hyperpolarization enables high signal-to-noise (SNR$\gtrsim$10^2) signal acquisition per measurement point.

It is worth emphasizing that, although rotating-frame DTCs are also observable in our system under a suitable single-frequency drive, either no continuous measurement can be performed or the spins rapidly decay to infinite temperature near the DTC point $\theta = \pi$ (supplementary material Sec. VI). Two-frequency driving circumvents this problem since θ can be arbitrarily chosen (except for θ=$\{0, \pi\}$) and DTCs instead appear conditioned on γ. Concatenated driving, therefore, engineers a separation between the interaction driven spin-dynamics and breaking of a discrete spatio-temporal symmetry (supplementary material Sec. VII). Additionally, the ratio N=T/τ is tunable, affording flexibility in exploring dynamical regimes at small and large N. In typical experiments, NM>1.35×10^5 fast pulses

are applied, corresponding to M>450 Floquet cycles. Our approach portends observing the long-time and intra-period time-crystalline dynamics continuously and without state reinitialization. This constitutes a vast improvement in throughput with respect to contemporary experiments, (see supplementary *movie* files), with a resulting measurement speedup of at least NM>10^5; compared to experiments probing lab-frame ($\hat{\mathbf{z}}$) DTCs [136], these gains could be as much as $NM(T_1/t_{\rm pol})\sim10^7$.

6.3 Prethermalization and discrete time crystals

Figure 6.2A first clarifies the prethermalization process during the spin kicks, essential to ultimately generate the PDTCs. Shown is a single-shot trace plotting $\langle\mathcal{I}_x\rangle$ after every fast pulse. We display the Floquet cycle number M on the lower $\hat{\mathbf{x}}$-axis and absolute time on the upper $\hat{\mathbf{x}}$-axis for an exemplary 165ms window. Here θ=$\pi/2$, and the γ-kicks are applied every 50.7ms (denoted by the dashed lines). Each γ-kick is associated with transient dynamics of the coupled ^{13}C nuclei as they prethermalize along $\hat{\mathbf{x}}$, producing the flat plateau-like regions shown. The inset Figure 6.2A*(i)* zooms into one representative transient; the oscillation period here is set approximately by the number of fast pulses required to complete a 2π rotation. The high temporal resolution revealed by the high SNR, and the ability of the ^{13}C nuclear system to sustain a large number of γ-kicks (see also Figure 6.3A) allows us to track the kicked prethermalization dynamics for long periods.

Employing an exemplary choice of flip-angle γ=0.97π slightly away from the perfect DTC point, Figure 6.2B demonstrates generation of stable DTC order, exhibiting period doubling in $\langle\mathcal{I}_x(t)\rangle$ during the application of M>450 γ-kicks (see Figure 6.3A for full data). The data were collected in a single run of the experiment. Red (blue) colors here represent odd (even) γ-kicks respectively, and prethermal plateaus separate successive kicks. These data comprise $>1.35\times10^5$ fast pulses, and *rigid* DTC behavior is observable for >14s (see also Figure 6.3A). The decay of the signal is approximately mono-exponential with a 1/e lifetime t≈4.68s (corresponding to M_e≈149 Floquet cycles at γ=0.97π), making it amongst the longest DTCs observed in the literature. Moreover, the Jt≈10^4 value here is considerably beyond state-of-art for systems exhibiting DTC order [175, 41, 128, 113, 92], demonstrating an ability to probe long-time dynamics in our system. This long-time stability can be attributed to the emergent quasi-conservation of $\hat{\mathbf{x}}$-magnetization under the evolution engineered by the two-frequency drive. In particular, our driving protocol allows the formation and observation of DTC order, even if temperature in the prethermal plateau is infinite [104], but also at room temperature, which may be well above the critical temperature associated with symmetry breaking (supplementary material Sec. VII). The long-range nature of the spin-spin interaction suggests critical DTC order [68]. On the other hand, the lifetime of the DTC order is parametrically controlled by the frequency (of switching) of the employed drives (see sec. 6.4 and supplementary material Sec. VII). Thus, the observed DTC order corresponds to a *critical prethermal* DTC.

Continuous observation yields an insightful view into the thermalization dynamics away

from the stable points, a challenging task in other experimental systems. This is demonstrated in data focusing on the instantaneous phase $\varphi(t)=\tan^{-1}(\langle\mathcal{I}_y\rangle\,/\,\langle\mathcal{I}_x\rangle)$ of the spins in the $\hat{\mathbf{x}}$-$\hat{\mathbf{y}}$ plane after every fast pulse. This is captured by the points in Figure 6.2C for the full 14s experiment, and considering four representative constant-γ values (see Figure 6.3A for full data). When γ=0.01π, the spins are locked at $\varphi\approx$0, reflecting prethermalization along $\hat{\mathbf{x}}$. A slight deviation γ=0.06π, reveals transient oscillations in φ with every γ-kick but no sign inversion. The transients result in the observed data spreading around φ=0. Figure 6.2C(ii) therefore permits visualization of the "melting" of the prethermal $\hat{\mathbf{x}}$-magnetization order to infinite temperature, where φ becomes random; this is observable at $t\gtrsim$10s. Analogously, the PDTC order (Figure 6.2C(iii)), here at γ=1.01π, is visible as characteristic π-phase switching between successive kicks. The last panel (Figure 6.2C(iv)) denotes γ=1.08π, when again PDTC melting can be observed via the phase randomization at long times.

Collating 285 such data traces while varying angle $\gamma\in([-1.1\pi, 1.1\pi])$, it is possible to construct a movie of the kicked prethermalizing spins (see ancillary .gif files in the supplementary material). The result is plotted in Figure 6.3A, where we display $\langle\mathcal{I}_x\rangle$ (cf. colorbar), with each vertical slice corresponding to measurement data as in Figure 6.2B. Left and right vertical axes here refer to the Floquet cycle number M and absolute time, respectively, on a logarithmic scale. The data highlight the almost three decades in the slow drive kicks, for which we observe the PDTC order, indicated by a regular switching of the magnetization from $\hat{\mathbf{x}}$ to -$\hat{\mathbf{x}}$ with every slow kick (here 300 fast pulses). The transition into and out of the finite PDTC regions is clearly evident, and not easily accessible in other experiments, allowing to precisely characterize the heating dynamics (see Figure 6.4). and map the entire non-equilibrium phase diagram. Interestingly, we observe very similar heating dynamics in the prethermal regime around γ=0 and the PDTC regime around $\gamma=\pi$ even though both regimes are associated with completely different non-equilibrium order. Near γ=0, we observe a suppression of heating due to the emergent drive-induced quasiconservation of the $\hat{\mathbf{x}}$-magnetization; the low-frequency kicks approximately wrap to the identity, and the effective Hamiltonian $\mathcal{H}_{\text{eff}}\approx\overline{\mathcal{H}}$ is built solely from the high-frequency $\hat{\mathbf{x}}$-drive. Instead, near $\gamma=\pm\pi$, we observe a region corresponding to PDTC order, where there is a regular switching of the magnetization from $\hat{\mathbf{x}}$ to -$\hat{\mathbf{x}}$ with every slow kick (here 300 fast pulses), a signature of period doubling response. Interspin interactions play a crucial role to preserve a uniform switching frequency away from $\gamma=\pi$.

The insets (Figure 6.3A *(i)* and *(ii)*) show zooms into PDTC regions in a 1.05s window at t=3.15s and t=11.55s respectively.We plot them here on a linear scale with time for clarity. While faint, the stable periodic DTC response is markedly clear even in Figure 6.3A *(ii)*, highlighting the high SNR in the experiment.

A complementary view of Figure 6.3A is presented in Figure 6.3B, where we consider the Fourier transform of $\langle\mathcal{I}_x(M)\rangle$, the mean signal value between successive γ-kicks for each value of γ (vertical slices in Figure 6.3A). Plotted is the corresponding Fourier intensity on logarithmic scale, where a span to six orders of magnitude is visible. The PDTC response appears as a sharp period-doubling peak in frequency at $(\gamma,\omega)=(\pm\pi,\pi)$. Using a 20% magnitude threshold, we estimate the finite γ-extent of the rigid PDTC regions to $\Delta\varepsilon=\pm$

0.2π about $\gamma = \pm\,\pi$. Similarly, the long-lived prethermal phase at γ=0 appears as a sharp peak at $(\gamma, \omega) = (0, 0)$. For comparison, the dark regions correspond to rapid state decay near $\gamma = \pm\,\pi/2$, where the effective Hamiltonian no longer features a quasi-conserved $\hat{\mathbf{x}}$-magnetization (supplementary material Sec. VI). The dashed lines in Figure 6.3B indicate the expected position of the Fourier peaks in the absence of interactions, J=0. In this diagram, the peak positions trace a rhombic pattern (dashed lines). The difference in the experimental data is evident, which indicates the role played by interactions in our system.

Comparing the experimental measurements to corresponding numerical simulations (see supplementary material Secs. V, VII, VIII and IX), we find an excellent qualitative agreement: In Figure 6.3C-D we display the exact simulation results matching experimental conditions in the data in Figure 6.3A-B. Interestingly, we observe that the long-range interactions, together with the random spin positions, induce a self-averaging effect in the simulations so that reliable theoretical results can already be obtained for moderately small system sizes (here L=14 spins). By contrast, the experimental platform comprises a cluster of about $L{\sim}10^4$ interacting spins [17] which outcompetes the numerically reachable system sizes by three orders of magnitude. The presence of a large number of interacting degrees of freedom is crucial for experimentally observing collective statistical mechanics phenomena such as symmetry breaking and thermalization. Thus, our results indicate that Floquet-engineered ^{13}C nuclei can serve as a competitive quantum simulator of thermalizing spin dynamics.

The observed PDTC behavior is also insensitive to the initial state. While we lack microscopic control over the initial state, different and highly non-trivial initial states can be obtained from letting the initial hyperpolarized density matrix ρ_0 evolve under the system Hamiltonian $\mathcal{H}_{\mathrm{dd}} + \mathcal{H}_z$ up to times $\sim J^{-1}$. For a set of such states we find comparable results between experiment and simulation (supplementary material Sec. VII). Our system thus satisfies all required landmarks of PDTCs: a parametrically long lived prethermal window featuring spatio-temporal symmetry breaking, which is rigid over a finite γ-region, and insensitive to fine-tuned initial states.

6.4 Melting of prethermal order

To quantify the stability of the PDTC order away from the stable point at $\gamma{=}\pi$, we investigate the influence of finite ε on its lifetime, which we define as the 1/e decay time of the signal. In turn, the inverse lifetime defines the associated heating rate. The long-range character of the dipolar interactions leads to a logarithmically divergent total energy of the system in three dimensions that, when combined with the lack of Lieb-Robinson bounds , makes the theoretical analysis of the heating rates for large systems difficult. For these reasons, to quantify the heating rates of the two-frequency drive, we perform a series of numerical simulations, and compare the results against experimental observations (supplementary material Sec. VIII).

Note that, even at $\gamma{=}\pi$ (where the slow drive does not contribute to heating) the system slowly heats up due to energy absorption resulting from the fast (spin-locking) $\hat{\mathbf{x}}$-drive.

This provides a lower bound for relevant heating rates, $\Gamma_{\min}(\tau)$, which we find scales as a power-law of the $\hat{\mathbf{x}}$-drive period, $\Gamma_{\min} \propto (J\tau)^2$ [30]. Finite ε opens an additional channel for the system to absorb energy and, eventually, the heating rates of both drives conspire to yield a combined overall heating rate $\Gamma(\tau, \varepsilon)$. In Figure 6.4 we extract the heating rates associated to finite ε, where we display $\Gamma - \Gamma_{\min}$ for $|\langle \mathcal{I}_x(t) \rangle|$ away from the stable points ($\gamma = \{0, \pi\}$) obtained from Figure 6.3A-B, and plotted on a logarithmic scale with respect to both heating rate and deviation ε. The curves indicate a parametrically controllable power-law heating with an exponent ≈ 2.21, consistent with Fermi's Golden rule. Intriguingly, we observe that the power law heating rates are close to identical for both stable points $\gamma = \{0, \pi\}$, where the relevant timescales are governed by a Lorentzian $\Gamma^{-1} \propto [g\varepsilon^2 + \Gamma_{\min}]^{-1}$ for some system-dependent constant g; this behavior is also borne out in numerical simulations (see supplementary material Sec. VIII, Fig. S14).

For the observed prethermal DTC lifetime to be *controllable*, relevant life-times are expected to increase with increasing drive frequencies. Indeed, the heating time in units of Floquet cycles Γ^{-1}/N depends sensitively on the frequency of the Floquet drive $\omega_F = 2\pi/(N\tau)$. In particular, at $\varepsilon = 0$ our model predicts $\Gamma^{-1}/N \sim 1/(NJ\tau^2)$. Increasing the frequency of switching by tuning N (τ), is expected to lead to a linear (quadratic) increase of Γ^{-1}/N, which we have confirmed numerically for our system (supplementary material Sec. VIII, Fig. S15). In Figure 6.4C-D we display experimental measurements of the dependence of Γ^{-1}/N as a function of N and τ, for finite ε. Although a crisp $1/N$ dependence is washed out in the presence of finite ε, we observe a clear increase in the lifetime. For sufficiently large τ in the timescale-separated regime $T/\tau \gg 1$, $\Gamma^{-1}(\tau)/N$ as a function of τ agrees well with a power law with an exponent close to -2, while at very small τ the DTC lifetime increase comes to a halt. This is to be expected for fixed ε, since decreasing the value of τ reduces the many-body nature of the effective Hamiltonian (see supplementary material Sec. VI). Note that DTC order is a many-body effect that relies on spontaneous spatio-temporal symmetry breaking in interacting systems. Thus, when the many-body nature gets gradually reduced, the stability and rigidity of the DTC order are expected to decline accordingly.

6.5 Two-frequency Floquet engineering

When the condition $N = T/\tau \gg 1$ is not met, time-scale separation between the slow and the fast drive is violated, and a complex interplay between the two drives emerges In this regime, the two drives cannot be treated independently of one another; instead, they mutually influence each other leading to novel effective Hamiltonians that sensitively depend on N. Consequently, the corresponding heating diagrams exhibit significant differences, as compared to the time-scale separated case, but also for different values of N. In Figure 6.5 we show the time-evolution of the $\hat{\mathbf{x}}$-magnetization as a function of γ for $N = 8$ and $N = 9$. Three features are particularly noteworthy: (i) in contrast to the timescale separated case, the heating dynamics around $\gamma = \pi$ differs significantly from that around $\gamma = 0$. In particular, (ii) far away from $\gamma = \pi$, heating depends sensitively on the specific value of N, where

even a minimal change (in N) can induce completely different heating behaviours (compare Figure 6.5A-B). These features can be explained by the different effective Hamiltonians (see supplementary material Sec. IX) forming at different N, γ, respectively. (iii) Even though interference effects induce new effective Hamiltonians with case-specific heating properties, the formation of time-crystalline order is stable against these deformations (Figure 6.5C-D). However, the relevant lifetimes and regimes of rigidity depend sensitively on N (supplementary material Sec. IX): changing $N = 8$ into $N = 9$ amounts in a (late) lifetime increase from 270 to 396 Floquet cycles (cf. Figure 6.5C-D)). These results provide a proof-of-principle example for the fine interplay between the two drives which offers a versatile tool to engineer new kinds of effective Hamiltonians with orchestrated physical properties, such as DTC order and beyond.

6.6 Conclusions and Outlook

Summarizing, we have observed critical prethermal discrete time crystals in dipolar-coupled nuclear spins in a bulk three-dimensional solid. We developed a novel protocol to excite and observe the PDTC formation and melting using a concatenated two-frequency Floquet drive. Parametric control over both drive frequencies allows us to reach PDTC lifetimes up to 396 Floquet cycles, observable in a single run of the experiment. This experimental advance unveils properties of the PDTC with a high degree of clarity, including its rigidity and melting characteristics, and to map the entire prethermal phase diagram of the system. Our measurements are in excellent agreement with numerical simulations, and approximate theoretical predictions.

Our study greatly expands the Floquet engineering toolkit: it portends multi-frequency concatenated drives to excite and stabilize novel types of quantum matter far from equilibrium by engineering emergent quasi-conservation laws that offer protection against immediate high-temperature melting. The novel Floquet driving protocol paves the way to experimentally realizing intriguing non-equilibrium states, potentially including PDTCs with a stable fractional subharmonic response or PDTCs and topological prethermal states stabilized by quasiperiodic driving . An extension of this work to multi-frequency driving is well within the scope of present-day experimental capability, and can be used to introduce more degrees of freedom to Floquet engineering. We envision application of these ideas in quantum simulation and sensing in AMO platforms as well as with hyperpolarized prethermal spins in solid-state systems.

6.7 Methods

1. Sample and hyperpolarization methodology: Here we employ a CVD grown single crystal of diamond with a defect density of 1ppm NV centers and natural abundance ^{13}C. The sample is placed with its [100] face parallel to the hyperpolarization and readout mag-

netic fields (38mT and 7T respectively). ^{13}C nuclei are hyperpolarized via the NV centers via a protocol described in Ref. [30] involving continuous optical pumping and swept microwave (MW) irradiation. Polarization is transferred from the NV electrons to proximal ^{13}C nuclei via a spin-ratchet mechanism that involves traversals of Landau-Zener anticrossings in the rotating frame of the swept MWs. The traversal probabilities are nuclear spin-state selective and are biased towards one nuclear spin orientation; this results in hyperpolarization. Spin diffusion serves to transfer this polarization to nuclear spins in the bulk lattice. Typical bulk polarization levels reached are about 0.6%.

2. Data collection and processing: The data processing pipeline follows a similar approach as described in Ref. [30]. The NMR signal is sampled continuously in $t_{\rm acq}$ windows between the fast spin-lock pulses, at a sampling rate of 1GS/s via a Tabor Proteus arbitrary waveform transceiver. Continuous observation exploits the fact that the NMR coil produces no backaction on the spins. In typical experiments, the pulses are spaced apart by τ=105 μs and the acquisition windows are $t_{\rm acq}$=64 μs. The ^{13}C Larmor precession (at $\approx$75MHz) is heterodyned to 20MHz prior to digitization. For each $t_{\rm acq}$ acquisition window, we take a Fourier transform and extract the magnitude and phase of the 20MHz peak. This corresponds to the application of a digital bandpass filter with a linewidth of $t_{\rm acq}^{-1}\approx$31.2kHz. Fast digitization hence yields signal-to-noise (SNR) gains, and typical SNR per point (detection window) is $\gtrsim 10^2$. For the 14s long acquisition in the Chapter, there are $\sim$135k such data collection windows.

3. Extraction of amplitude and phase in Figure 6.2 and Figure 6.3: The magnitude and phase of the Fourier transform of the heterodyned precession in each $t_{\rm acq}$ readout window report respectively on the magnitude and phase of the spin vector in the $\hat{\mathbf{x}}$-$\hat{\mathbf{y}}$ plane in the lab frame. This corresponds to magnitude $S_L=[\langle\mathcal{I}_x^2\rangle + \langle\mathcal{I}_y^2\rangle]^{1/2}$, and phase $\varphi_L=\langle\mathcal{I}_y\rangle\,/\,\langle\mathcal{I}_x\rangle$, where subscript L here refers to the lab frame. It is more convenient to to instead obtain the phase of the spins $\varphi_R=\varphi$ in the rotating frame. To do this, we note that the phase values φ_L obtained in successive $t_{\rm acq}$ windows just differ by the (trivial) phase accrued during the t_p spin-locking pulse. Subtracting this global phase allows us to extract φ, which in combination with the magnitude signal then allows us to extract the survival probability along the $\hat{\mathbf{x}}$ direction in the rotating frame, $\langle\mathcal{I}_x(t)\rangle$ that we display in Figure 6.2 and Figure 6.3 of the main text.

4. Numerical simulations: To numerically simulate the many-body dynamics of dipolar interacting ^{13}C nuclei, we design random graphs of L=14 and L=16 interacting spins-1/2 and perform exact time evolution with up to 10^6 $\hat{\mathbf{x}}$-kicks (corresponding to $\approx 10^3$ $\hat{\mathbf{y}}$-kicks) based on an OMP-parallelized Krylov method using the open-source python package QuSpin [165]. For further details we refer the reader to Sec. IV of the supplementary material.

5. Comparison with previous work: To date DTC order has been studied in vari-

ous systems ranging from cold atoms [175, 92] over superconducting qubits [113] to systems based on NV centers [41, 128]. The DTC order observed in these works can be separated into two groups: many-body localized DTCs and prethermal DTCs. While many-body localized DTCs are assumed to be infinitely long-lived in the absence of decoherence, prethermal DTCs, as in our experiments, are ultimately limited by the lifetime of the prethermal plateau. However, in reality also many-body localized DTCs are subject to decoherence due to technical limitations. Remarkably, even though our DTC order is of different physical origin, we find comparable lifetimes to state-of-the-art many-body-localized DTCs. Moreover, our lifetimes exceed those reported for prethermal DTCs, both, in units of Floquet cycles as well as absolute time.
Apart from these benchmark parameters, our system shares ingredients with the systems investigated in Refs. [41] and [128]. Like in our work, these works investigate systems based on NV centers: Reference [128] examines a quasi one-dimensional system of 9 dipolar coupled ^{13}C nuclear spins in the many-body localized regime, while in Ref. [41] effective two-level systems of electronic states in NV centers are used to implement DTC order. In contrast, our (three-dimensional) system consists of $10^3 - 10^4$ dipolar coupled ^{13}C *nuclear* spins. In particular, in comparison to Ref. [41] the normalized interaction strength $\langle J \rangle / \gamma_n^2$ in our system is increased by a factor 4.5×10^4 [here $\gamma_{e/n}$ denotes the gyromagnetic ratio of electronic/nuclear spins]; moreover, at comparable normalized driving strength, we obtain an improvement of normalized spin lifetimes by a factor of 5.7×10^2 (see also Sec. III of the supplementary material for a detailed table of relevant system parameters). Induced by the two-frequency drive, the DTC order we observe is prethermal, i.e., our DTC lifetime is parametrically controlled by the drive frequency, while no such feature is present in Ref. [41] where a single-frequency drive is used.

5. Data availability: Data from experiments and simulations displayed in the main text are available in Zenodo with the identifier `https://doi.org/10.5281/zenodo.7301638`. All other data from the Supplementary Information are available from the authors upon reasonable request.

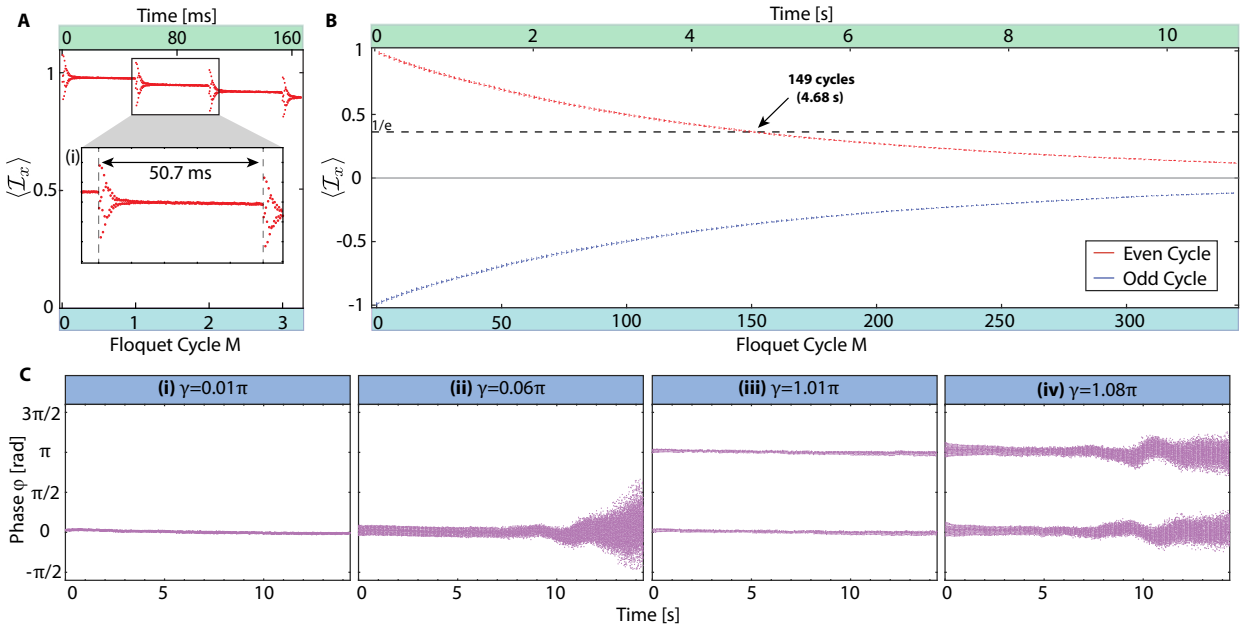

Figure 6.2 **Continuously observed prethermalization and PDTC.** (A) *Floquet prethermalization* of the kicked ^{13}C spins, shown for $\theta{=}\pi/2, \tau{=}169\mu$s, $N{=}301$, and $\gamma{=}0.08\pi$. Data (points) depict single-shot measurement of $\langle \mathcal{I}_x \rangle$, for four kicks (165ms). Oscillations depict transient approach to prethermal plateaus (flat regions). Here, we normalize the signal upon reaching the initial prethermal state. Due to a slight frequency offset in the pulses applied, the spin-lock axis is slightly tilted from $\hat{\mathbf{x}}$ and deviation from it results in the signal being apparently greater than unity during the transient. Upper axis denotes time t, while lower axis denotes Floquet cycle number M. *Inset:* Zoom into region between two kicks (dashed lines) separated by 50.7ms. First kick is preceded by a 1s-long prethermalization along $\hat{\mathbf{x}}$ (not shown). For movie of full dataset, see ref. [3] for link. (B) *Single-shot PDTC measurement* for $\theta{=}\pi/2, \tau{=}105\mu$s, $N{=}300$, and $\gamma{=}0.97\pi$. Panel shows the signal $\langle \mathcal{I}_x \rangle$; signals from alternate kicks are depicted by red and blue points. Total time here corresponds to 1.35×10^5 periods of the fast drive, and ∼400 slow kicks (see Figure 6.3A for full data). PTDC decay envelope is approximately monoexponential with 1/e time constant ≈4.68s (dashed line). For movie of full dataset, see ref. [4] for link. (C) *PDTC phase response.* For characteristic vertical slices in Figure 6.3(A), we plot the phase of the spins φ on the Bloch sphere (see Figure 6.1C) for the entire 14s period. *(i)* Phase response at $\gamma{=}0.01\pi$ showing the quasi-equilibrium of the spins along $\hat{\mathbf{x}}$. *(ii).* At slight deviations, $\gamma{=}0.06\pi$, the spins start leaving the prethermal axis $\hat{\mathbf{x}}$, and undergo heating, manifesting in the randomization of their phase at long times (here $t \gtrsim 10$s). *(iii)* PDTC response at $\gamma{=}1.01\pi$ showing stable period doubled oscillations, represented by the π-phase shift between successive γ-kicks. *(iv)* Melting of the PDTC order at $\gamma{=}1.08\pi$, observable by the randomization of the phase at long times.

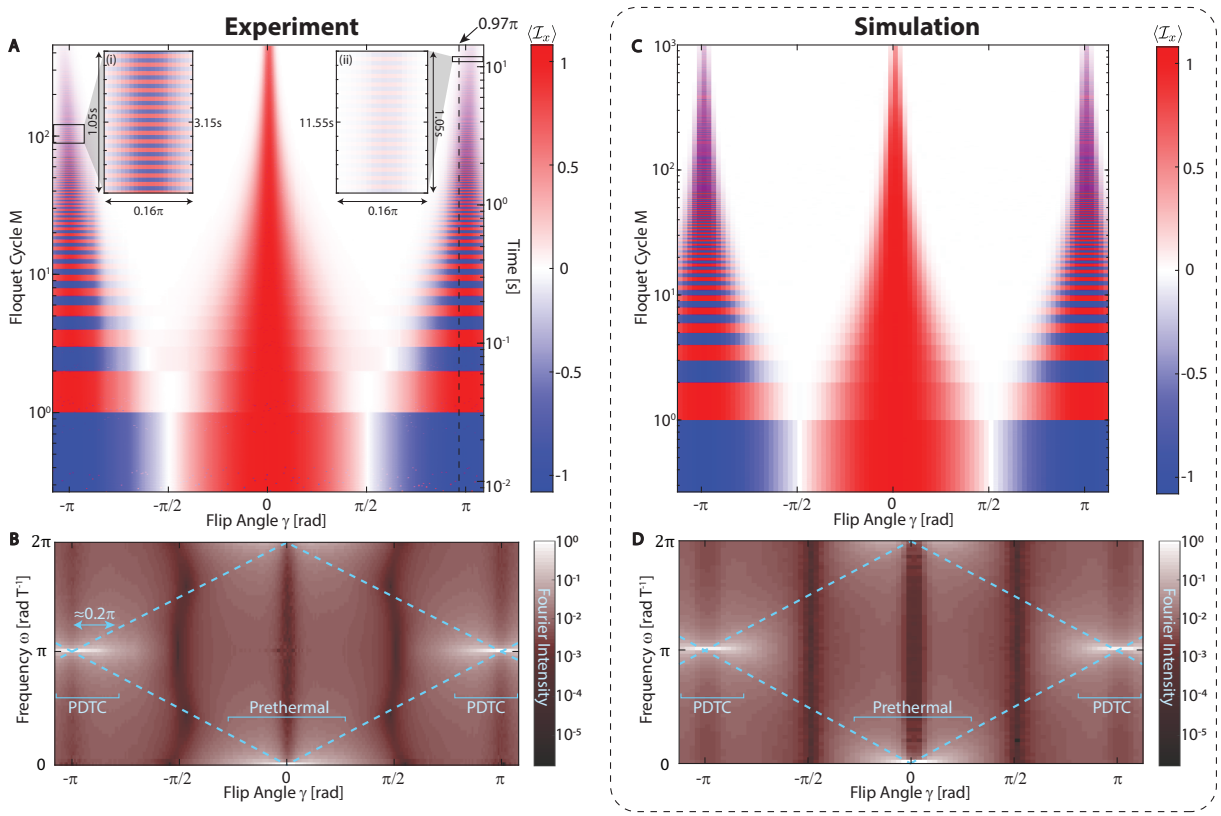

Figure 6.3 **Prethermal DTC phase diagram.** (A) *Movie* showing emergence of prethermal DTCs. 285 traces similar to Figure 6.2B are plotted stacked for different values of kick angle γ in $[-1.1\pi, 1.1\pi]$. Colors represent signal $\langle \mathcal{I}_x \rangle$ (see colorbar). Time $N\tau$ and Floquet cycle number M run vertically and are plotted on a logarithmic scale. Data are taken to 14s (M=450 cycles). Central feature (near γ=0) shows stabilization of long-time spin survival as a result of drive-induced quasiconservation of $\hat{\mathbf{x}}$-magnetization due to Floquet prethermalization. PDTC response (striped regions) are visible near $\gamma = \pm\pi$. Striped signal denotes spins inverting between $\hat{\mathbf{x}}$ and $-\hat{\mathbf{x}}$ in a period-doubled fashion. Spins flip every N=300 fast pulses, and rigid PDTC response (peaks) persist to three decades of the fast drive. *Inset:* Zoom into PDTC response in two 1s-windows centered at t=3.15s, and t=11.55s respectively plotted on a linear scale. Rigid DTC behavior is observable for over 14s, even at γ=0.97π. See ref. [4] for movie version of same dataset. (B) *Fourier transform* of the data in (A), plotted with respect to the inverse period of the slow drive $\omega = 2\pi\ T^{-1}$ radians. Colors represent strength of Fourier peak intensity spanning six orders of magnitude (colorbar). PDTC (period-doubled) order is evident by the extended white peaks at $(\gamma, \omega) = (\pm\pi, \pi)$, while the trivial (prethermal) phase arises for $(\gamma, \omega) = (0, 0)$. Dashed lines indicate expected Fourier peak pattern in the absence of interactions. (C-D) *Numerical simulations* analogous to the experiments in A-B for L=14 interacting spins on a pseudo random-graph with $J\tau = 0.07$ and $N = 300$.

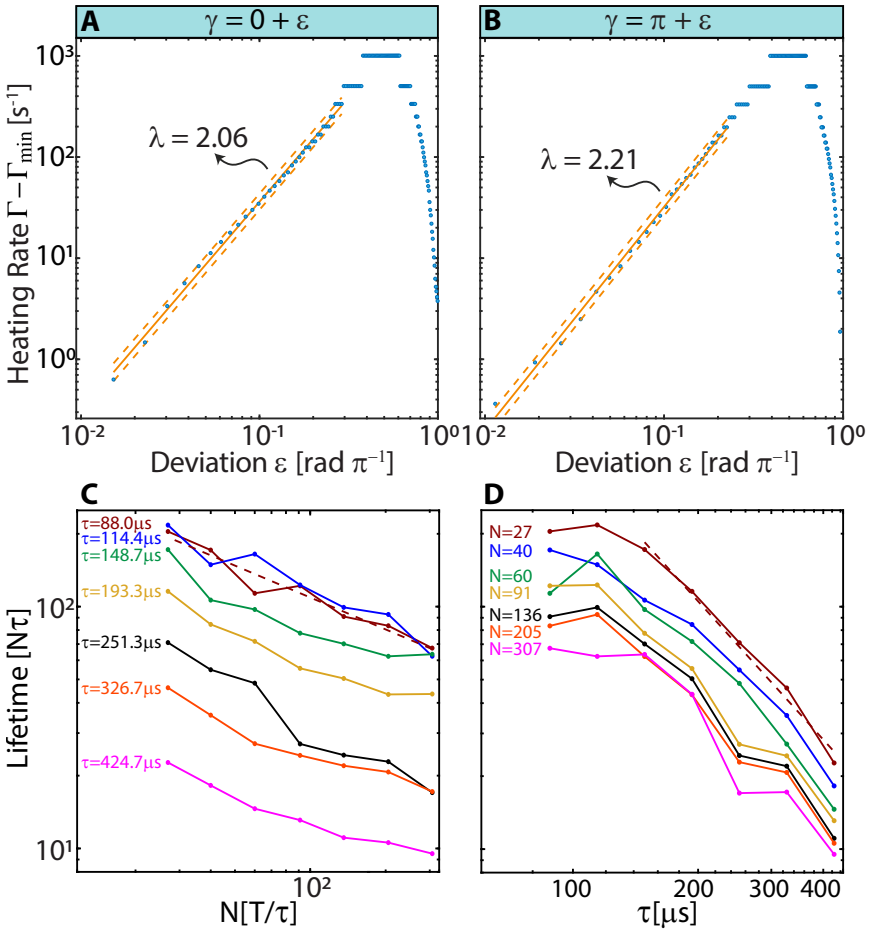

Figure 6.4 **Experimental characterization of PDTC rigidity and prethermal lifetimes.** (A-B) *System heating rates* estimated by the inverse of a 1/e-threshold lifetime. We observe the heating rates follow a power law $\Gamma \propto g\epsilon^{\lambda} + \Gamma_{\min}$ [see text], with an exponent λ=2.06 for prethermal phase (A) and λ=2.21 for PDTC phase (B), agreeing well with numerical simulations (supplementary material Sec. VIII). Solid line is a fit and dashed lines are error bars at two standard deviations. (C-D) *Prethermal lifetimes* for different values of N and τ. Dashed lines correspond to power-law fits with exponents -0.44 (C) and -1.90 (D). Increasing the drive frequency leads to an increase in lifetime of the prethermal DTC state.

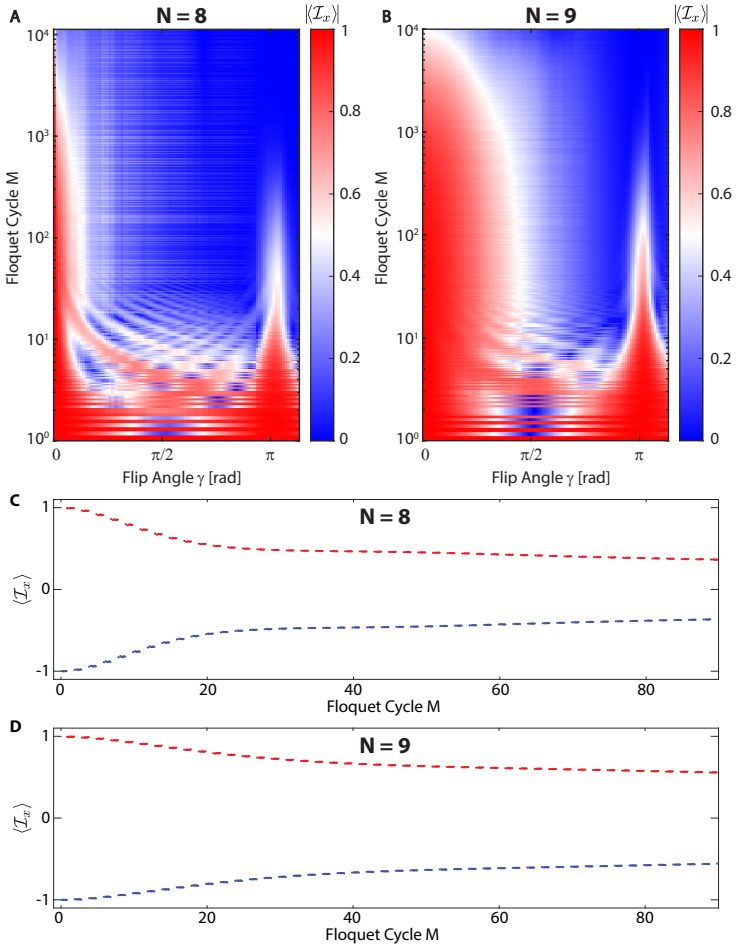

Figure 6.5 **Experimental characterization of the heating dynamics at small N.** Complex interplay between the fast and slow periodic drives is seen when the condition $N = T/\tau \gg 1$ is not met. (A) Movie showing time-series data from 103 experiments with different values of flip angle γ in $[0, 1.1\pi]$ and $N = 8$ $\hat{\mathbf{x}}$-pulses between $\hat{\mathbf{y}}$-pulses. Colors represent absolute value of signal $|\langle \mathcal{I}_x \rangle|$ (see colorbar). Floquet cycle number M runs vertically on a logarithmic scale. Data are taken past 10^4 Floquet cycles. (B) Movie similar to (A) but with $N = 9$ $\hat{\mathbf{x}}$-pulses between the $\hat{\mathbf{y}}$-pulses. In both movies (A) and (B), $\hat{\mathbf{x}}$-pulse flip angle was calibrated to $\theta = \pi/2$. (C-D) Line cut of (A-B), respectively, at $\gamma = 1.011\pi$, shows a clear DTC signal with even (odd) cycles shown in red (blue). Late lifetimes (measured starting from Floquet cycle 100, after the initial transient regime) are 270 Floquet cycles for $N = 8$ (C) and 396 Floquet cycles for $N = 9$ (D). Due to the complexity of signal processing we plot absolute values in (A-B) and unwrap the phase information only for the line cuts shown in (C-D).

Chapter 7

Experiment and Numerical Simulation Details for PDTC Study

7.1 Introduction

In this supplementary material we provide additional experimental and theoretical details for the chapter *"Critical prethermal discrete time crystal created by two-frequency driving"*. In Sec. 7.2, we briefly introduce the Hamiltonian of the system. We continue with motivating the employed driving scheme in Sec. 7.3, details on the experimental implementation (Sec. 7.4) and numerical simulations (Sec. 7.5). Section 7.6 provides additional experimental data backed up by numerics that studies the thermalization behavior under $\hat{\mathbf{z}}$ kicks, and also proves the equivalence of $\hat{\mathbf{z}}$ and $\hat{\mathbf{y}}$ slow kicks. Throughout the text, we compare our theoretical predictions against observed experimental data.

7.2 Model

In this section, we analyze the dynamics of the Floquet drive built out of two superimposed step drives, that we use in Chapter 6. Since the periods of repetition, N and M, of the two step drives may vary independently, we refer to this protocol as a "two-frequency" drive. Note that the term frequency here refers to the inverse periods of the two superimposed drives, rather than the support of their Fourier decompositions. Discrete [86, 167] and continuous [38] versions of such two-frequency drives have been previously used for dynamical decoupling protocols and Hamiltonian engineering [65].

We investigate a hyperpolarized lattice of ^{13}C nuclei in diamond [22, 16]. In the high-field (secular) approximation, the physics of the interactions in the system is captured by the dipolar spin Hamiltonian,

$$\mathcal{H}_{\mathrm{dd}} = \sum_{j<k}^{L} b_{jk} \left(3 I_{jz} I_{kz} - \vec{I}_j \cdot \vec{I}_k \right), \tag{7.1}$$

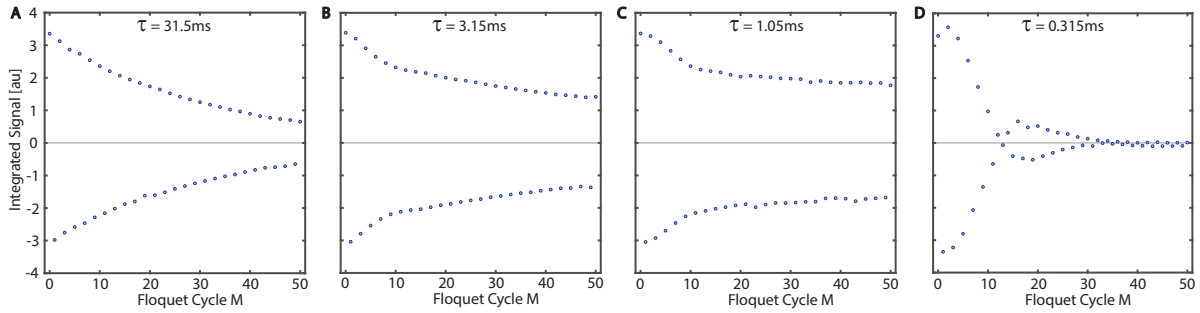

Figure 7.1 **Single-frequency driving PDTC.** Experimental data showing PDTC with traditional single-frequency driving after initializing the spins with a polarization along $\hat{\mathbf{z}}$. Each data point represents the integrated signal $\langle \mathcal{I}_z \rangle$, readout by multiple-pulse spin-locking after the application of M pulses with flip angle $\gamma = 0.97\pi$ and period $\tau = 31.5\text{ms}, 3.15\text{ms}, 1.05\text{ms}, 0.315\text{ms}$ (A-D). For $\tau = 31.5ms$ (A), the DTC response persists for less than 30 Floquet cycles before reaching 1/e signal decay. The optimal PDTC lifetime is found for $\tau = 1.05\text{ms}$ (C) where the system sees a quick decay during the first 10 Floquet cycles followed by a long plateau. When driving is too fast, the Floquet Hamiltonian becomes effectively single-particle [cf. Eq. (**??**)] and a split beat pattern emerges, quickly destroying the DTC response (see (D), $\tau = 0.315\text{ms}$). These data motivate the use of a two-frequency in our system which enables the observation of long-lived PDTC order.

where $b_{jk} = \frac{\mu_0}{4\pi}\hbar\gamma_n^2(3\cos^2\alpha_{jk} - 1)\frac{1}{|\vec{r}_{jk}|^3}$ with the gyromagnetic ratio $\gamma_n = 10.7\text{MHz/T}$; the angle of the interspin vector $\vec{r}_{jk}$ and the external magnetic field $\vec{B}_0$, is $\alpha_{jk} = \cos^{-1}\left(\frac{\vec{r}_{jk}\cdot\vec{B}_0}{|\vec{r}_{jk}||\vec{B}_0|}\right)$. $I_{j\mu}$ describes a spin-1/2 operator in direction μ at some spatial position j. The number of spins in the system is L. In Chapter 6, we had introduced the coupling strength $J = \langle b_{jk} \rangle$.

^{13}C spins located near paramagnetic impurities, such as NV-centers or other lattice paramagnetic defects (e.g., P1 centers), experience a hyperfine-mediated magnetic field localized from the defect site. Since this field falls off as $1/r^3$, different ^{13}C atoms experience a different shift, based on their location and the distance to the nearest paramagnetic impurity. This effect can be approximately modeled by introducing an additional term in the Hamiltonian,

$$\mathcal{H}_z = \sum_{j=1}^{L} c_j I_{jz}, \tag{7.2}$$

where we assume that c_j are Gaussian distributed random numbers with a standard-deviation on the order of the relevant energy scales in Eq. (7.1) [17].

The total system Hamiltonian in the laboratory frame is composed of $\mathcal{H}_{\text{dd}}$, $\mathcal{H}_z$ and the trivial Zeeman Hamiltonian. Assuming the pulses applied are on-resonance, however, the system is conveniently described in the rotating frame by the Hamiltonian,

$$\mathcal{H} = \mathcal{H}_{\text{dd}} + \mathcal{H}_z. \tag{7.3}$$

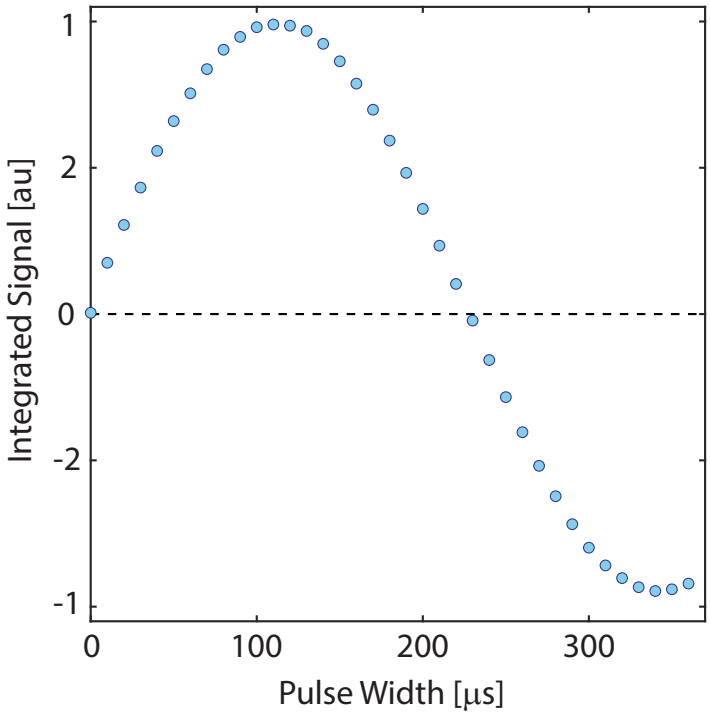

Figure 7.2 **Calibration of flip angle.** Experimental data points represent integrated signal readout via spin-locking following initial excitation pulse of finite width. Experiments were performed for different pulse widths and plot represents a Rabi oscillation, with flip angle π being calibrated to the zero-crossing and the rest of the flip angles scaling linearly with pulse width.

Next, we additionally subject the system to a two-step periodic drive created by two independent external fields applied along (i) the $\hat{\mathbf{x}}$ direction, U_x, and (ii) the $\hat{\mathbf{z}}$-direction, U_z, [in the theoretical analysis below, we consider $\hat{\mathbf{z}}$ kicks, but in experiments $\hat{\mathbf{y}}$-kicks are used as they are easier to implement]. The physical system, which generates the time evolution $U_{\mathcal{H}}$, is exposed to a rapid periodic application of the $\hat{\mathbf{x}}$-drive; every N repetitions of the $\hat{\mathbf{x}}$-drive, we apply the $\hat{\mathbf{z}}$-field U_z once, which completes one Floquet period (or cycle). We note that the two constituent drives used here have commensurate periods. The entire evolution over one driving cycle is then described by the Floquet unitary U_F:

$$\begin{aligned} U_F &= (U_x U_{\mathcal{H}})^N U_z, \\ U_z &= \mathrm{e}^{-i\gamma \mathcal{I}_z}, \quad U_x = \mathrm{e}^{-i\theta \mathcal{I}_x}, \quad U_{\mathcal{H}} = \mathrm{e}^{-i\tau \mathcal{H}}, \end{aligned} \tag{7.4}$$

where we defined the net spin operator $\mathcal{I}_\nu = \sum_j I_{j\nu}$ with $\nu \in \{x, y, z\}$. Note here we have assumed that the pulse action can be described as instantaneous rotations (δ-pulse approximation). The angles of the $\hat{\mathbf{x}}$ and $\hat{\mathbf{z}}$ rotations are denoted θ and γ, respectively [Fig **??**].

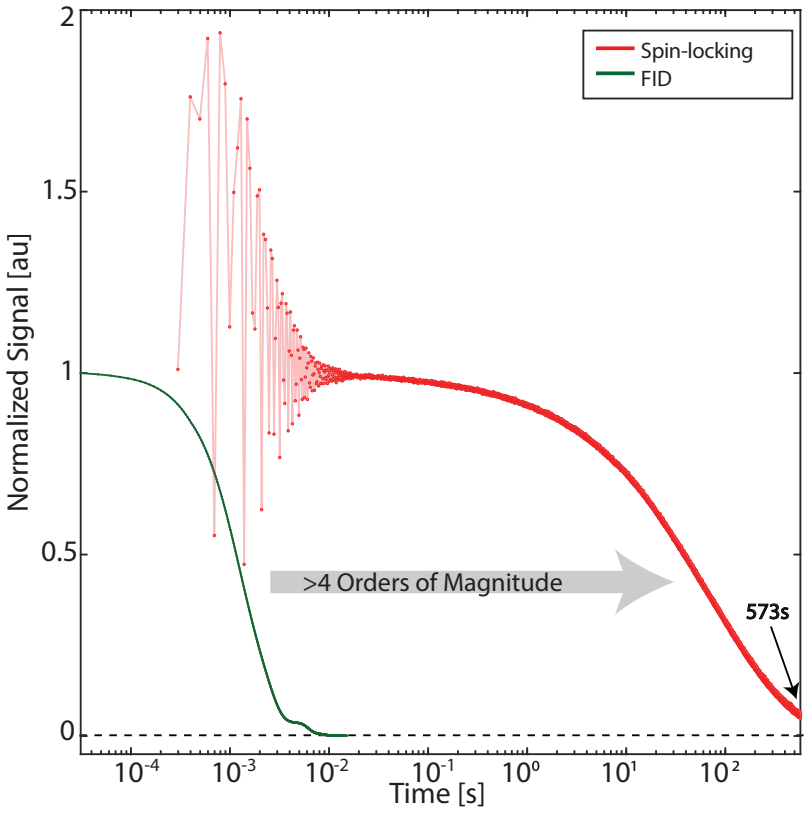

Figure 7.3 **Free induction decay and pulsed spin-lock data.** Measurements shown for free induction decay (green line and points) and for pulsed spin-locking Floquet control (red line and points). Free induction decay lifetime $T_2^* = 1.5$ms is extended with high-frequency pulsing by over 5 orders of magnitude, $T_2' = 90.9$s. Adapated from Ref. [30].

The stroboscopic dynamics of any initial state $|\psi_0\rangle$ is thus determined by successive applications of U_F

$$|\psi(M)\rangle = U_F^M |\psi_0\rangle = \left[(U_x U_{\mathcal{H}})^N U_z \right]^M |\psi_0\rangle, \tag{7.5}$$

where M denotes the stroboscopic Floquet cycle, and similarly for mixed initial states.

7.3 Motivation for using a two-frequency drive

Let us now elucidate upon the experimental and theoretical motivation for using the two-frequency drive in this work. We begin by noting that the ^{13}C nuclei are dipolar coupled with the Hamiltonian $\mathcal{H}_{\rm dd}$ above, and when prepared in an initial state $\rho_0 \propto \mathcal{I}_x$, undergo dipolar

Parameter	Value
Inter-spin spacing	1nm
Initial state $\hat{\mathbf{x}}$-polarization ϵ	0.68%
Median interaction strength $\langle J \rangle$	0.66kHz
Drive strength Ω	7.6kHz
Total spin lifetime T_2'	90.9s
Normalized interaction strength $\langle J \rangle / \gamma_n^2$	5.8×10^{-12}HzT^2
Normalized drive strength Ω/γ_n	$7.1 \times 10^{-}4$T
Normalized spin lifetime $\gamma_n T_2'$	9.7×10^{-8}T^{-1}
Sampling rate	$(0.105\text{ms})^{-1}$
Number of measured points per kick	299
Total observation time	14s
Signal to noise ratio per point	$> 10^2$

Table 7.1 Summary of experimentally relevant system and drive parameters.

evolution under it. This results in the rapid free induction decay, with a time constant $T_2^* \sim 1.5$ms.

Consider now the application of a single frequency drive, consisting of a train of θ-pulses spin locked with the ^{13}C nuclei. While the resulting spin decay lifetimes T_2' can be far in excess of T_2^*, the fastest signal decay occurs for $\theta = \{0, \pi, 2\pi\}$. This stems from the fact that the dipolar interaction is invariant under rotations by π; this yields an average Hamiltonian under the Floquet drive, $\bar{\mathcal{H}}^{(0)} = \mathcal{H}_{\text{dd}}$. For other angles of θ, it is easy to show instead that the dipolar interaction is effectively engineered to a form that commutes with the initial state. This fast decay at $\theta = \pi$ would normally prevent observation of a PDTC in the rotating frame with a single frequency drive alone. In our work, this problem is essentially circumvented by the use of the two frequency drive.

We note that it is still possible to observe the DTC-like behavior in the laboratory frame with a single frequency drive. This is shown experimentally in Fig. 7.1. However, obtaining data similar to Fig. 7.5 then has to be constructed in a point-by-point fashion, and the experiment has to be re-initialized between successive measurement kicks. This makes observation of the formation and melting of the PDTC order at high resolution extremely challenging. In summary, our two-frequency drive approach allows the ability to excite the PDTC order while it simultaneously permits the tracking of the spin thermalization

continuously, yielding a unique means to observe the driven interacting spin dynamics away from equilibrium.

From the theoretical perspective, multi-frequency drives are especially interesting as they allow to Floquet engineer novel kinds of effective Hamiltonians and non-equilibrium ordered states that might be inaccessible with single-frequency drives. To illustrate this idea, let us assume a two-step (i.e., single-frequency) drive composed of the Hamiltonians H_1 and H_2 repeatedly applied with amplitudes J and θ such that time evolution over one Floquet period is given by

$$U_F = \exp\left(-iJH_1\right)\exp\left(-i\theta H_2\right). \tag{7.6}$$

Provided $||JH_1|| \sim ||\theta H_2|| \ll 1$, the Baker-Campbell-Hausdorff expansion predicts a Floquet Hamiltonian of the form $H_F = (JH_1 + \theta H_2)/(J+\theta) + \mathcal{O}(T')$ with $T' \sim J, \theta$. Although, H_F might provide a new effective Hamiltonian that mixes the properties of H_1 and H_2, there is only a limited amount of flexibility: the lowest order effective Hamiltonian will always be given by the average Hamiltonian of JH_1 and θH_2. In contrast, a much more interesting regime is found when $||JH_1|| \ll 1$ but $||\theta H_2|| \sim 1$. In this case, the standard Baker-Campbell-Hausdorff expansion leads to an infinite series of terms $\propto J$ (i.e., terms $\propto J\theta, J\theta^2, J\theta^3$, etc.), and more sophisticated techniques are required to find closed form expressions [159]. Eventually, the series resummation leads to new types of (interaction) terms which can depend on θ in a non-linear way (see also Sec. **??**). This ansatz allows us to engineer new effective Hamiltonians with case-specific properties beyond the average Hamiltonian: for instance, in this work, we engineer a many-body effective Hamiltonian with an emergent $U(1)$ and $\mathbb{Z}_2$ symmetry, which is subject to a second drive to implement non-equilibrium order – in our case a prethermal discrete time-crystalline order – in the system.

7.4 Details of the experimental implementation

Pulse calibration and parameter regime

The flip angles (θ, γ) in the experiments are calibrated using a ^{13}C nuclear Rabi oscillation. The first tipping pulse (to be calibrated) is followed by a $\theta{\approx}\pi/2$ spin-lock train. We plot the integrated signal in Fig. 7.2. The SNR is very good because of the long resulting rotating frame lifetimes T_2'. Furthermore, in order to make the experiments less susceptible to precise calibration of the first $\pi/2$ pulse (that tips the spins onto the $\hat{\mathbf{x}}$-$\hat{\mathbf{y}}$ plane), we apply the first phase γ-kick to the spins after a period of 1s, so that the spins have already prethermalized along $\hat{\mathbf{x}}$ before the γ-kicks are applied. This ensures that the initial state of the spins in the experiment is exactly $\rho_0 \propto \epsilon\mathcal{I}_x$, with the experimentally measured value $\epsilon = 0.68\%$. Fig. 7.3 shows experimental data for the system's natural free induction decay time and maximum possible lifetime extension under Floquet control. Further relevant system and drive parameters are collected in Tab. 7.1.

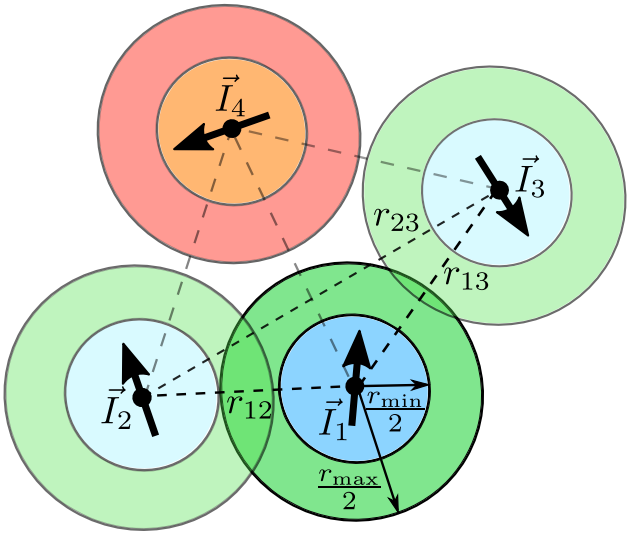

Figure 7.4 **Schematic for the generation of a pseudo-random graph.** Starting off with a spin $\vec{I}_1$ in some random position, we propose a new position for the next spin $\vec{I}_2$ [see text]. Since $r_{\min} < r_{12} < r_{\max}$ we accept $\vec{I}_2$ and add it to the graph. Next, we propose $\vec{I}_3$, which also satisfies all requirements since all inter-spin vectors $r_{13}, r_{23} > r_{\min}$, while $r_{13} < r_{\max}$. Hence, we also accept $\vec{I}_3$. The next proposal, $\vec{I}_4$, only has inter-spin vectors which are all larger than $r_{\max}$ and, thus, constitutes an invalid choice; hence, it is discarded. If we aim to simulate $L = 4$ spins (or more) we would have to continue proposing new spins until a valid fourth spin position is found and added to the graph. Figure prepared by Christoph Fleckenstein.

7.5 Details of the numerical simulations

Random graph design

We perform exact numerical simulations of the system with L ^{13}C nuclear spins, placed on a pseudo-random graph. In creating the lattice graph, we respect two conditions: (i) we ensure a certain average spin density at the system size L; (ii) we avoid isolated spin positions ('outliers'), that would not contribute to the many-body dynamics as their coupling constant becomes negligible in comparison to their "bulk" spins counterparts due to the spatial decay of the dipolar interactions.

To iteratively generate the spin positions on the graph, we apply the following rule: first, we randomly generate a new spin position, and we check if it has a minimum distance $r_{\min}$ to all other spins. In addition, we also require that at least one of the mutual interspin vectors satisfies $|\vec{r}_{jk}| < r_{\max}$ [cf. Fig. 7.4]. If these conditions are met, we accept the new spin position and add it to the list of spins on the graph. Otherwise we discard the proposed spin position and start over with a new proposal. In Chapter 6 we use $r_{\min} = 0.7$, $r_{\max} = 0.8$,

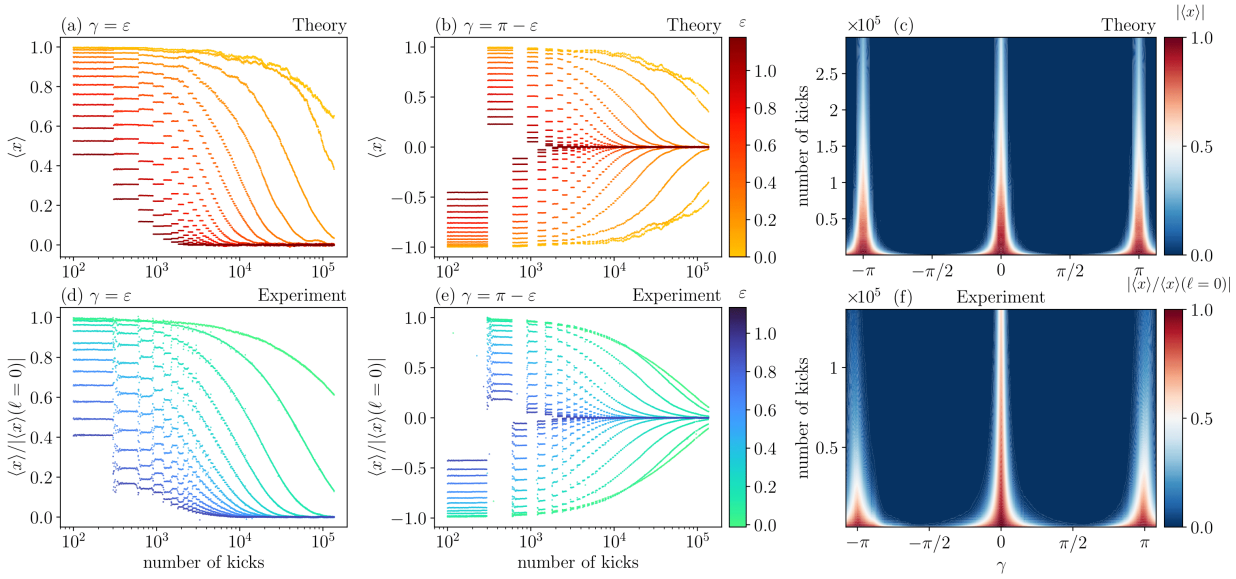

Figure 7.5 **Comparison of numerical simulation and experiment. (a)-(b)** Time evolution of the $\hat{\mathbf{x}}$-polarized initial state under the drive generated by Eq. (7.4) at $\gamma = \varepsilon$ (a) and $\gamma = \pi + \varepsilon$ (b) for different values of ε: we plot the expectation value of the $\hat{\mathbf{x}}$-magnetization, $\langle x \rangle = \frac{2}{L}\langle \mathcal{I}_x \rangle$, vs. time given in number of kicks. **(c)** $|\langle x \rangle|$ as a function of the $\hat{\mathbf{z}}$-kick angle γ and number of kicks. To generate the random graph of spins we used $r_{\min} = 0.7$, $r_{\max} = 0.8$ (in units of $\sqrt[3]{\mu_0 \hbar \gamma_n^2}$) with $L = 14$. The single particle energies c_j are normally distributed random numbers with mean $\langle c_j \rangle = \overline{b_{jk}}$ and standard deviation $\sigma_c = 10 \times \overline{b_{jk}}$, where $\overline{b_{jk}}$ is the median of all coupling constants of the graph. Simulations and figure prepared by Christoph Fleckenstein. **(d)-(f)** experimental data corresponding to (a) and (b) and (c) respectively. Parameters are as in Fig. 7.3. In all panels, we plot logarithmically many points in the number of kicks. $N = 300$ and $\tau J = 0.07$ for all figures.

both in units of $\sqrt[3]{\mu_0 \hbar \gamma_n^2}$.

Time evolution and initial state

In the numerical simulations using this pseudo-random graph of spins, unless stated explicitly otherwise, we initialize the system in the $\hat{\mathbf{x}}$-polarized pure product state $|\psi_0\rangle = \bigotimes_{j=1}^{L} \frac{1}{\sqrt{2}} (|\uparrow_j\rangle + |\downarrow_j\rangle)$, and perform numerically exact time evolution according to the protocol given in Eq. (7.4). While most of our results are based on this initial state, we also show that the effects we observe are qualitatively initial-state independent [cf. Fig. 7.7].

Since the interaction is long-range and the positions of the nuclei are not spatially ordered, the characteristic energy scale of the model is not immediately obvious, and needs to be

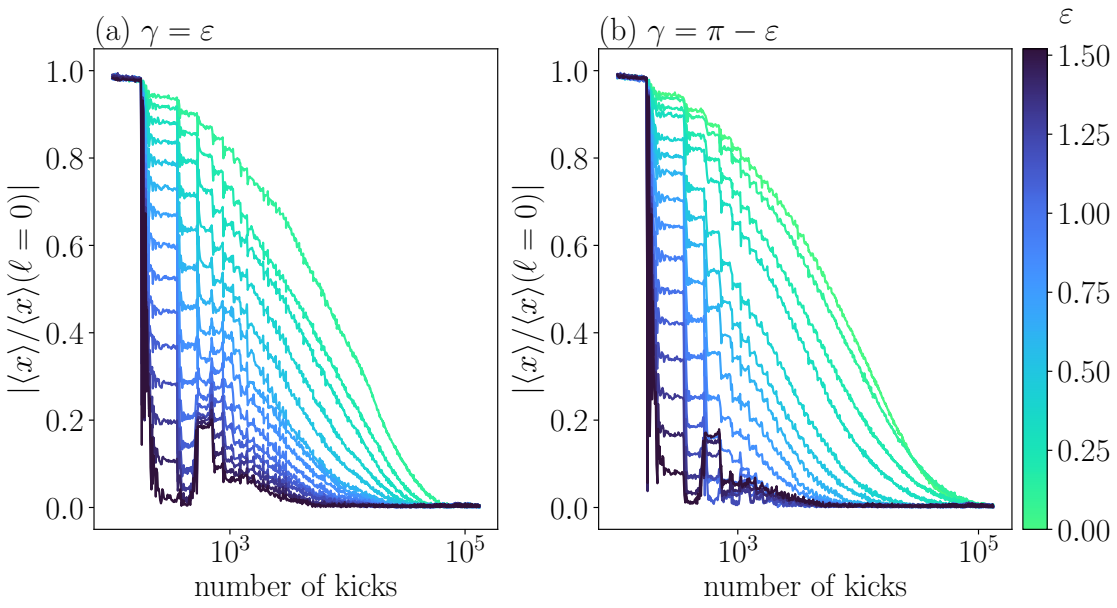

Figure 7.6 **Equivalence of $\hat{\mathbf{z}}$ and $\hat{\mathbf{y}}$ kicks.** Experimental results analogous to the dataset shown in Fig. 7.5, except here the low-frequency driving consists of composite pulses along $\hat{\mathbf{z}}$-axis rather than simple $\hat{\mathbf{y}}$-pulses (see Fig. **??** for driving protocol). NMR signal $\langle \mathcal{I}_x \rangle$ is measured between fast pulses and composite $\hat{\mathbf{z}}$-rotation is applied between every $N = 176$ fast pulses. Single-shot experiment yields one line, and experiment is repeated for different values of γ in $[0, \pi]$. Just as with the experiment with $\hat{\mathbf{y}}$-pulses, the dynamics show long lifetimes for small flip angle deviations ε, $\gamma = \varepsilon$ (a) and $\gamma = \pi + \varepsilon$ (b).

extracted from the dynamics. To this end, we define a characteristic energy $J = 1/\tau_d$, where τ_d is the timescale on which single-particle observables decay by a factor of 1/e, as they approach their equilibrium value when evolved under $U_{\mathcal{H}}$. We note in passing that J may vary depending on the initial state, i.e., different values might be obtained for J when probed with other initial states than $|\psi_0\rangle$. Therefore, the value of J only serves as a rough estimate of relevant energy scales.

To further increase the ergodicity of the drive and diminish finite-size effects in the dynamics, we add a small uniformly distributed random "noise" $\delta\tau \in [-0.05\tau, 0.05\tau]$ to the duration τ for which we apply $\mathcal{H}$, i.e. $\tau \to \tilde{\tau} = \tau + \delta\tau$ so that $\tilde{\tau}$ is slightly different in each cycle of $(U_x U_{\mathcal{H}})$ [55, 57]. After each application of U_x, U_z, respectively, we compute the expectation value of single particle observables

$$\langle x\rangle = \frac{2}{L}\langle \mathcal{I}_x\rangle, \quad \langle y\rangle = \frac{2}{L}\langle \mathcal{I}_y\rangle, \quad \text{and} \quad \langle z\rangle = \frac{2}{L}\langle \mathcal{I}_z\rangle.$$

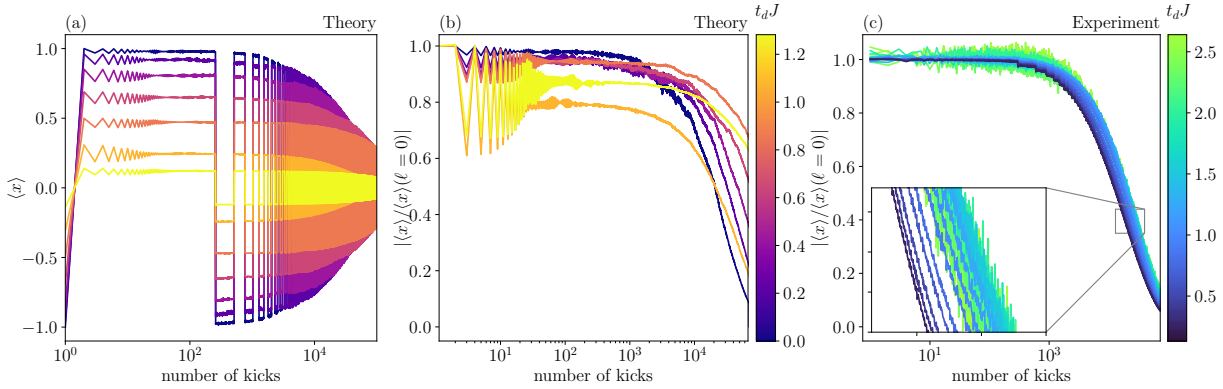

Figure 7.7 **Numerical Simulation. (a)-(b)** Time evolution of different initial states $|\psi\rangle_i^{t_d}$ prepared by evolving the fully polarized state for a time t_d with $\mathcal{H}$: $|\psi\rangle_i^{t_d} = \mathrm{e}^{-it_d\mathcal{H}} \bigotimes_{j=1}^{L} \frac{1}{\sqrt{2}} (|\uparrow_j\rangle - |\downarrow_j\rangle)$. In (b) we display the absolute value of the $\hat{\mathbf{x}}$-magnetization using the data from (a), normalized to its initial magnitude. The simulation parameters are $L = 16$, $N = 255$, $\gamma = \pi + 0.02$, $J\tau = 0.2$, and the remaining parameters are the same as in Fig. 7.5. Simulations and figure prepared by Christoph Fleckenstein. **Experiment: (c)** Corresponding experimental time-evolution curves for different initial states obtained using the same procedure: the initially prepared density matrix (see Chapter 6) is evolved with the bare dipolar Hamiltonian $\mathcal{H}$ up to time t_d before the two-frequency drive is started. The inset provides a zoom in of the marked region to visualize individual curves. The parameters of the experiment are the same as in Figure 6.3, and $\gamma = 0.96\pi$.

7.6 Thermalizing dynamics: simulation versus experiment

We now elucidate in greater detail the thermalization dynamics of the spins in a comparison between theory and experiment. Figure 7.5 displays the dynamics of the system, obtained numerically ((a)-(c)) and in the experiment ((d)-(f)). In the numerical simulations, the initial state $|\psi_0\rangle$ is evolved in time up to 5×10^4 kicks for $N = 300$ [throughout the supplementary material, we also show results for a few more values of N]. Note that here we treat $\hat{\mathbf{x}}$-kicks and $\hat{\mathbf{z}}$-kicks on equal footing: each application of U_x, U_z, respectively, adds $+1$ to the total number of kicks. We show the simulated time evolution curves for $\gamma = 0 + \varepsilon$ (a) and $\gamma = \pi - \varepsilon$ (b), where different curves correspond to different values of ε (see colorbar): with an increasing value of ε the heating time gets gradually reduced until no stable magnetization is visible anymore when $\varepsilon \to \pi/2$.

In the experiment, the initial state after the $\pi/2$-pulse about the y-axis [see Fig. 7.1] is the mixed state $\rho_0 \propto \epsilon \mathcal{I}_x$. The time evolution of the $\hat{\mathbf{x}}$-magnetization shown Fig. 7.5 (d) and (e) is measured in the experiment. Despite the different initial states, the curves are thoroughly comparable on a qualitative basis, with the notable difference that the experimental curves

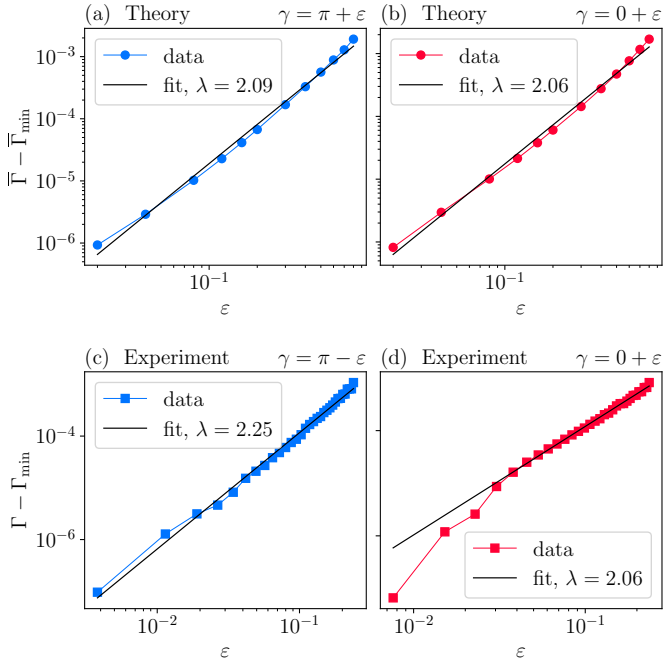

Figure 7.8 **Comparison of scaling behaviour in theory and experiment. (a)-(b) Numerical simulation** – Numerically extracted heating times averaged over 20 graph realizations, $\overline{\Gamma}^{-1} = N_{\text{seed}}^{-1} \sum_{s=1}^{N_{\text{seed}}} \Gamma_s^{-1}$ with $N_{\text{seed}} = 20$, as function of ε at $\gamma = \pi + \varepsilon$ (a) and $\gamma = 0 + \varepsilon$ (b). We plot $\overline{\Gamma} - \overline{\Gamma}_{\min}$ on the y axis to check for corresponding scaling. $\overline{\Gamma}_{\min}^{-1}$ is defined as the heating time at $\varepsilon = 0$: $\overline{\Gamma}_{\min}^{-1} \equiv \overline{\Gamma}^{-1}(\varepsilon = 0)$. We fit the data to $\overline{\Gamma} = g/N\varepsilon^{\lambda} + \overline{\Gamma}_{\min}$. (fit values of (a): $g = 0.56$, $\overline{\Gamma}_{\min} = 3.67 \times 10^{-5}$, fit values of (b): $g = 0.52$, $\overline{\Gamma}_{\min} = 3.40 \times 10^{-5}$). The simulation parameters are $L = 16$, $N = 255$, $J\tau = 0.2$. Remaining parameters are as in Fig. 7.5. Simulations and figure prepared by Christoph Fleckenstein. **(c)-(d) Experiment** – Corresponding heating rates extracted from experimental data for $\gamma = \pi - \varepsilon$ (c) and $\gamma = \varepsilon$ (d). In (d) the three smallest data points are not included in the fit since these curves did not reach the 1/e-threshold. We fit the data to $\Gamma = g/N\varepsilon^{\lambda} + \Gamma_{\min}$ (fit parameters of (c): $g = 6.15$, $\Gamma_{\min} = 1.75 \times 10^{-5}$, fit parameters of (d): $g = 4.17$, $\Gamma_{\min} = 7.34 \times 10^{-6}$). The remaining parameters are the same as in Figure 6.3.

yield much cleaner results in the small ε regime. This can be traced back to large differences in the system size in experiment ($L \sim \mathcal{O}(10^4)$) and theory ($L \sim \mathcal{O}(10^1)$).

In Fig. 7.5 (c) (Fig. 7.5 (f)) we display theoretical (experimental) results of the absolute value of the $\hat{\mathbf{x}}$-magnetization, $|\langle x \rangle|$, for a wide range of γ-values. In both panels, we can distinguish between three overall regimes: around $\gamma = 0$ ($\gamma = 2\pi$) heating is suppressed as U_z almost wraps up to the identity so that the slow-frequency $\hat{\mathbf{z}}$-kicks become ineffective,

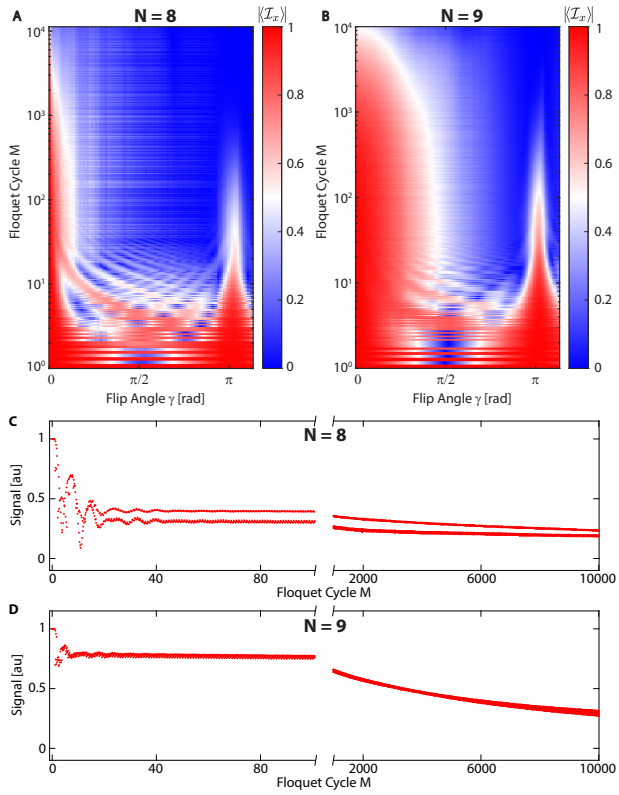

Figure 7.9 **Experimental characterisation of the heating dynamics at small N.** Complex interplay between the fast and slow periodic drives is seen when the condition $N = T/\tau \gg 1$ is not met. (A) Movie showing time-series data from 103 experiments with different values of flip angle γ in $[0, 1.1\pi]$ and $N = 8$ $\hat{\mathbf{x}}$-pulses between $\hat{\mathbf{y}}$-pulses. Colors represent absolute value of signal $|\langle \mathcal{I}_x \rangle|$ (see colorbar). Floquet cycle number M runs vertically on a logarithmic scale. Data are taken past 10^4 Floquet cycles. (B) Movie similar to (A) but with $N = 9$ $\hat{\mathbf{x}}$-pulses between the $\hat{\mathbf{y}}$-pulses. In both movies (A) and (B), $\hat{\mathbf{x}}$-pulse flip angle was calibrated to $\theta = \pi/2$. (C-D) Line cut of (A), (B), respectively, at $\gamma = 0.244\pi$. In (C), different plateaus correspond to micromotion within a Floquet cycle. The data shown in (A) and (B) is identical to the data shown in Figure 6.5.

and the effective Hamiltonian is engineered solely from the high-frequency $\hat{\mathbf{x}}$-drive. Around $\gamma = \pi$, we observe a similar behaviour; there, the formation of the PDTC leads to slow thermalization dynamics. In between these regimes the $\hat{\mathbf{z}}$-kicks lead to rapid thermalization to infinite temperature resulting in a decay of the signal within very few cycles (cf. Fig. 7.3).

We note further that quantitatively identical results are obtained using a $\hat{\mathbf{z}}$-kick to the spins instead of a $\hat{\mathbf{y}}$-kick. In the experiment, however, this requires each kick to be constructed out of a composite rotations along the $\hat{\mathbf{x}}$ and $\hat{\mathbf{y}}$ axes. Data corresponding to such $\hat{\mathbf{z}}$-kicks are shown in Fig. 7.6 around the two stable points, $\gamma = \epsilon$ and $\gamma = \pi - \epsilon$.

In order to claim validity of prethermal discrete time crystalline behavior, we should check that the dynamics are present for initial states other than the polarized state. Although the system does not grant local control of spin states, we can utilize the native dipolar interactions already present. To validate our conclusion numerically, we initialize the system in various different states by time-evolving the $\hat{\mathbf{x}}$-polarized state for some transient time t_d with $\mathcal{H}$, i.e. $|\psi\rangle_i^{t_d} = \mathrm{e}^{-it_d\mathcal{H}} \bigotimes_{j=1}^{L} |\leftarrow_j\rangle$. In that way we obtain experimentally accessible, yet highly non-trivial, initial states with non-zero $\hat{\mathbf{x}}$-magnetization, provided $t_d J \lesssim 1$. The results are displayed in Fig. 7.7 (a) and (b). We plot the absolute value of the signal $|\langle x\rangle|$ for clarity. All chosen initial states lead to long-lived subharmonic oscillations of the signal; yet, we find differences in their lifetime: while states with large initial $\hat{\mathbf{x}}$-magnetization tend to increase their lifetime with increasing t_d, at small initial $\hat{\mathbf{x}}$-magnetization, the lifetime behavior becomes less systematic. For values very close to zero initial $\hat{\mathbf{x}}$-magnetization we observe no PDTC order (data not shown).

Experimentally, we pursue the same strategy. We create different initial states by evolving the rotated starting density matrix ρ_0 (see Chapter 6) with the bare Hamiltonian $\mathcal{H}$ for different times t_d to obtain a set of different and highly non-trivial initial states, which are subsequently subject to two-frequency driving. Each state corresponds to a different run of the experiment. We display the results in Fig. 7.7 (c). We show only absolute values, yet all tested initial states create persistent (in time) and rigid (in ε) subharmonic oscillations with similar heating times. This is a notable difference to the data obtained using numerical simulations, where different initial states can induce considerably different heating times. We hypothesize that the difference in the heating behavior of various initial states is related to the relatively small system sizes that can be reached in the numerical simulations.

7.7 Heating timescales and duration of the prethermal plateau

The lifetime of a PDTC, like that of any prethermal order, is predominantly determined by the amount of energy absorbed from the nonequilibrium drive. To quantify this energy absorption, we define the heating time empirically, as follows. Given the time evolution curve of some observable O, the heating time is the time required to reach 1/e of the initial value of that observable. In principle, one would have to define the heating time with respect to the *prethermal* value of a given observable. However, since we only investigate the quasi-conserved $\hat{\mathbf{x}}$-magnetization, the initial and prethermal expectation values coincide.

The concatenated two-frequency drive offers two obvious mechanisms for the system to heat up to infinite temperature: the slow and fast drives independently cause energy absorption, each with a potentially different rate corresponding to its own timescale. Numerically and experimentally, we observe an interplay of both timescales. However, theoretically we can disentangle them and analyze each effect separately. To this end, in what follows, we discuss the influence of heating caused by the slow $\hat{\mathbf{z}}$-drive, and then the fast $\hat{\mathbf{x}}$-drive, before we conclude with the general case for the two-frequency drive.

Heating timescales associated with the slow $\hat{\mathbf{z}}$-drive

To analyze heating caused by the slow drive, we assume the (approximate) effective Hamiltonian emerging from the fast drive,

$$U_0 U_x^N \;\equiv\; U_{0x} = \exp\left[-iT\overline{\mathcal{H}} - \frac{i\pi}{2}\,(N \bmod 8)\,\mathcal{I}_x \right]. \tag{7.7}$$

, to be exact. This allows us to numerically study a periodic drive of the form:

$$U_F \approx \mathrm{e}^{-iT\overline{\mathcal{H}}} U_x^N U_z = U_0 U_x^N U_z, \quad U_0 = \mathrm{e}^{-iT\overline{\mathcal{H}}}. \tag{7.8}$$

We further increase the ergodicity of the relatively small systems accessible in our simulations and diminish the related finite-size effects by adding a small uniformly distributed noise δ to the driving period [55, 57]

$$U_F = \mathrm{e}^{-iN(\tau+\delta\tau)\overline{\mathcal{H}}} U_z, \tag{7.9}$$

where δ takes a different value in each Floquet cycle.

We then evolve the fully $\hat{\mathbf{x}}$-polarized initial state under Eq. (7.9) up to 5×10^4 kicks. The results are displayed in Fig. 7.10. We find a clear power-law scaling of the heating times Γ_z^{-1} which is close to a Fermi-golden-rule scaling, $\Gamma_z^{-1} \sim \varepsilon^{-2}$. This can be understood as the $\hat{\mathbf{z}}$-drive is effectively operating in the low-frequency regime for $N \gg 1$ [the short-range interacting exponential suppression typically occurs in the high-frequency regime]. Note that, at $\varepsilon = 0$, although the energies of many-body states can differ by multiples of the drive frequency, heating is suppressed by the complete absence of matrix elements between these states. Finite $\varepsilon > 0$ induces finite matrix elements which in turn results in intense energy absorption according to Fermi's Golden rule. Note that we observe approximately the same golden rule ε-scaling for different values of N (Fig. 7.10a-b).

The power-law suppressed heating in our system, causes the finite stable regions around $\gamma = 0, \pi$ to shrink much faster, as compared to the exponential suppression of heating at high-frequencies. However, in practice the timescales are still parametrically controlled by ε and the prethermal physics is governed by the effective Hamiltonian. In fact, the experimentally observed lifetimes for our PDTC readily exceed state-of-art lifetimes of PDTCs in the high-frequency regime [136, 92].

We note in passing that finite noise δ in the driving protocol has no influence on the scaling of heating times, but it is capable of removing long-time finite size synchronization effects [55, 57]. This can be seen in Fig. 7.10 where finite δ causes more points to align on the straight line without changing its slope, whereas points that are already in-line remain unchanged.

Heating timescales associated with the fast $\hat{\mathbf{x}}$-drive

The physics of the thermalization dynamics associated with the fast $\hat{\mathbf{x}}$-drive only, is not immediately obvious due to the interplay between three effects: (i) the power of the dipolar

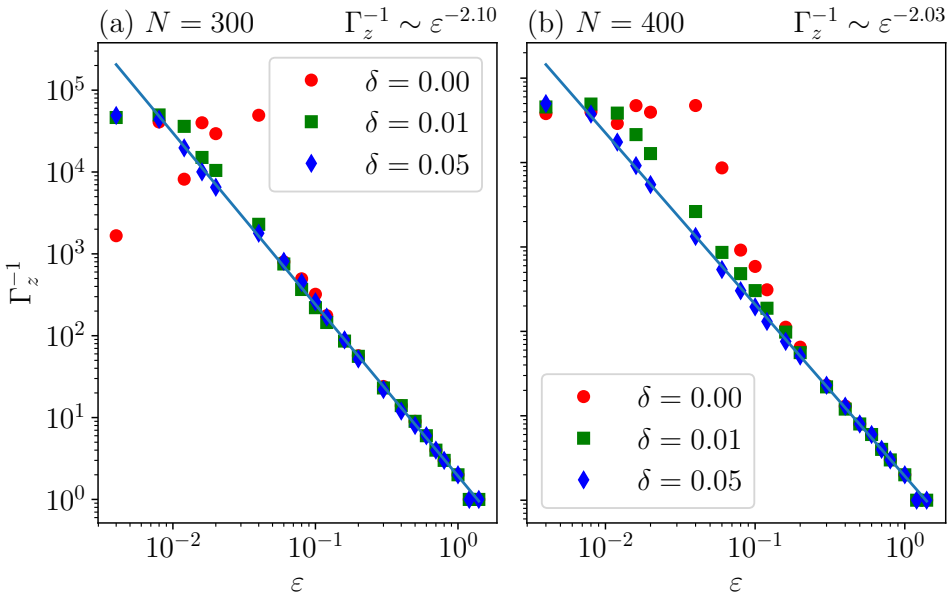

Figure 7.10 **Numerical simulation.** ε dependence of the heating timescales Γ_z^{-1} associated with the slow $\hat{\mathbf{z}}$-drive: (a) $N = 300$, (b) $N = 400$ around $\gamma = \pi + \varepsilon$. The system size is $L = 14$, and $J\tau = 0.2$. Further simulation parameters are the same as in Fig. 7.5. Simulations and figure prepared by Christoph Fleckenstein.

interaction term is critical in three dimensions, which implies a logarithmic divergence of the total energy in the thermodynamic limit. (ii) In the limit $\tau \to 0$, the effective Hamiltonian of the system approaches an integrable model, for which the notion of thermalization itself is not well-defined. Integrability breaking, though, occurs at order $\mathcal{O}(\tau)$ in the effective Hamiltonian, although its not pronounced at the accessible system sizes in the numerical simulations. (iii) Even when $J\tau \ll 1$, we still have $\theta \sim \mathcal{O}(1)$ so that the high-frequency regime ($\theta \ll 1$ and $J\tau \ll 1$) is practically inaccessible.

For these reasons, it is difficult to make predictions for rigorous bounds on the heating rates, given the above properties of the model [105]. Nonetheless, it is possible to study the energy absorption numerically. To this end, we investigate the drive generated by the repeated application of $U_x U_{\mathcal{H}}$ at $\gamma = 0$ with fixed $\theta = \pi/2$ for different values of $J\tau$. From the time-evolution curves we extract the heating times $\Gamma_{\min}^{-1}(J\tau)$ and display them as a function of τ in Fig. 7.11 for different random graph realizations. We find that – similar to the slow $\hat{\mathbf{z}}$-drive – the fast $\hat{\mathbf{x}}$-drive shows a power-law scaling, $\Gamma_{\min}^{-1} \propto (J\tau)^{\kappa}$ with a Golden-rule exponent $\kappa \approx -2$. This result is in agreement with recent experimental measurements reported in Ref. [30].

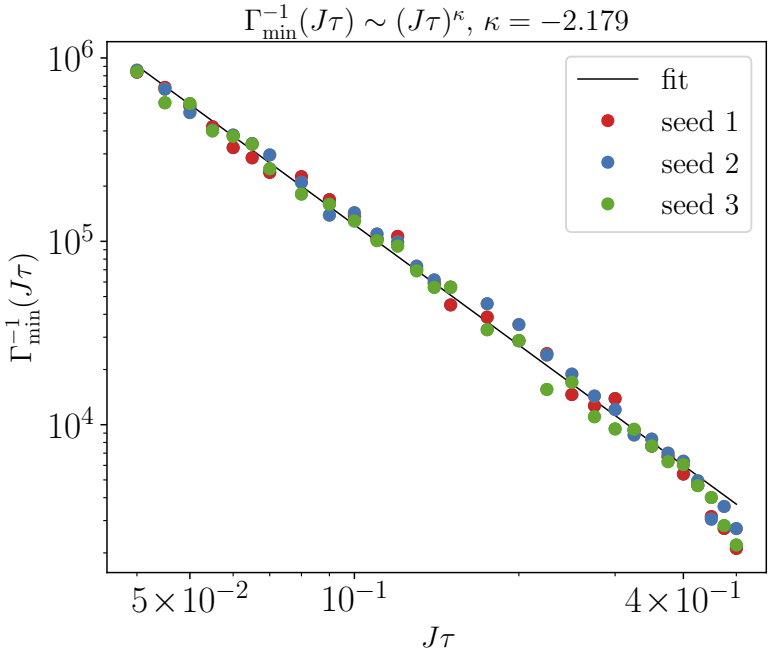

Figure 7.11 **Numerical simulation.** Heating times $\Gamma_{\min}^{-1}(J\tau)$ associated with the fast $\hat{\mathbf{x}}$-drive, extracted from corresponding time-evolution curves (data not shown), as a function of $J\tau$. Different colors (red, green and blue) correspond to different random graph realizations. The system size is $L = 14$. The remaining simulation parameters are the same as in Fig. 7.5. Simulations and figure prepared by Christoph Fleckenstein.

Heating model for the concatenated two-frequency drive

Now that we have analyzed the fast and slow drives independently, we can move on with the discussion of the heating rates of the more complex concatenated two-frequency drive.

To understand the combined heating timescales we deploy a simple model: assuming that there are no correlation effects between the different drives (which applies in the time-scale separated regime $N \gg 1$), a simple model that approximates the dynamics of the magnetization decay can be formulated using a discretized-in-time rate equation that captures the influence of the MN-th kick on the magnetization:

$$\langle x\rangle((MN+1)\tau) - \langle x\rangle(MN\tau) = -\left[\frac{\Gamma_z(\varepsilon)}{N} + \Gamma_{\min}(J\tau)\right]\langle x\rangle(MN\tau). \tag{7.10}$$

Here we denote the heating rates of the slow $\hat{\mathbf{z}}$-drive and the fast $\hat{\mathbf{x}}$-drive by $\Gamma_z(\varepsilon)$ and $\Gamma_{\min}(J\tau)$, respectively. Recalling that N and M are the repetition numbers of the $\hat{\mathbf{x}}$- and $\hat{\mathbf{z}}$-drives, Eq. (7.10) has the simple solution

$$\langle x\rangle(MN\tau) = \exp\left[-\left(\frac{\Gamma_z(\varepsilon)}{N} + \Gamma_{\min}(J\tau)\right) MN\tau\right].$$

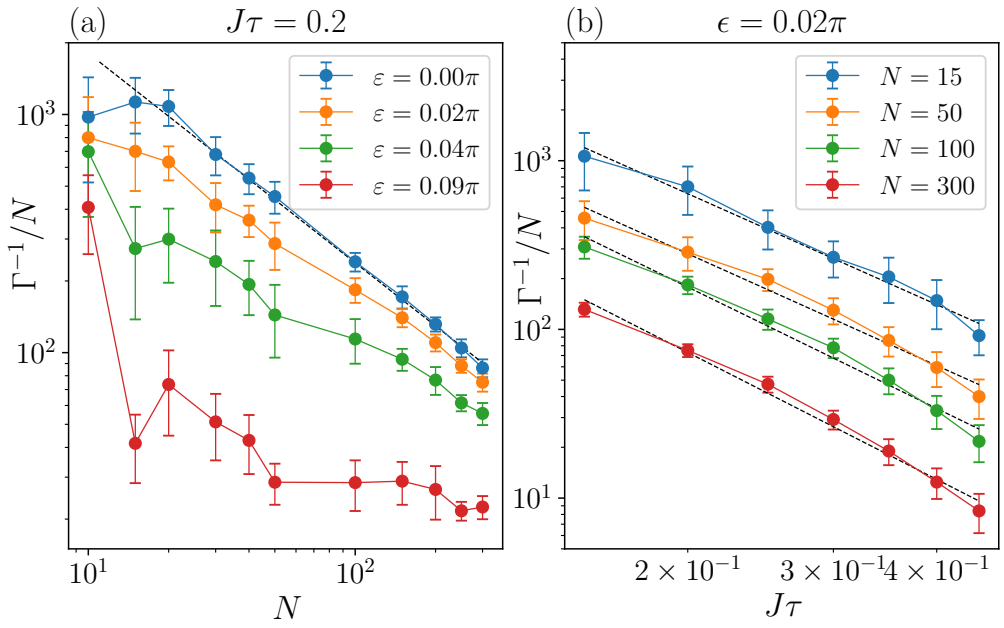

Figure 7.12 **Numerical simulation.** (a) N-dependence of the heating time Γ^{-1} in units of Floquet cycles for 4 different values of ε. The dashed lines correspond to a least-square fit. We find a scaling of $\Gamma^{-1}/N \sim N^{-0.88}$ (b) $J\tau$-dependence of the heating time Γ^{-1} in units of Floquet cycles for 4 different N. In both panels all points are averaged over 10 random graph realizations.Error bars represent the standard deviation from the mean value. Dashed lines correspond to least-square fits: we find a scaling of We find a scaling of $\Gamma^{-1}/N \sim (J\tau)^{-\alpha}$ with $\alpha = 2.18$ ($N = 15$), $\alpha = 2.20$ ($N = 50$), $\alpha = 2.39$ ($N = 100$) and $\alpha = 2.50$ ($N = 300$). The system size is $L = 16$. Remaining parameters are as in Fig. 7.5. Simulations and figure prepared by Christoph Fleckenstein.

Notice that the exact functional form of the true time-dependence of the magnetization may not resemble a simple exponential. However, if we are only interested in heating timescales and taking into account the experimentally observed mono-exponential behavior, Eq. (7.10) provides a valid approximation, since the time required to reach a value of 1/e is exactly given by $\Gamma^{-1} = [\Gamma_z(\varepsilon)/N + \Gamma_{\min}(J\tau)]^{-1}$. At $\varepsilon = 0$ the slow drive is ineffective so that $\Gamma^{-1}|_{\varepsilon=0} = \Gamma^{-1}_{\min}(J\tau)$, and we recover the heating rate of the fast drive. For a fixed fast-drive frequency, we can thus identify the minimum heating rate as $\Gamma_{\min}(J\tau)$. Together with the conclusions from Sec. 7.7 we, therefore, expect a scaling approximately given by

$$\Gamma^{-1} = \frac{1}{\frac{g}{N}\varepsilon^2 + \Gamma_{\min}(J\tau)}, \tag{7.11}$$

with some numerical constant g. Rearranging this expression as $\Gamma = g/N\varepsilon^\lambda + \Gamma_{\min}$ we fit a straight line on a log-log plot to both numerical and experimental data, with fitting

parameters g, λ, and $\Gamma_{\min}$.

In Fig. 7.8 we present fits of the heating times extracted from both numerical simulations (Fig. 7.8 (a)-(b)) and experimental data (Fig. 7.8 (c)-(d)). The left (right) columns in the figure show data taken in the vicinity of $\gamma = \pi$ ($\gamma = 0$). The axes are chosen such that a straight line indicates scaling according to Eq. (7.11). For all datasets we see a straight line over at least two decades, which renders the fit results trustworthy, and in agreement with our simplified theoretical model. That said, in the simulated data, we observe a slight upward bending in the small ε-regime. This is to be expected as Eq. (7.10) constitutes only a minimal approximate model, which completely disregards the interplay between the two constituent drives that are likely to contribute an additional ε dependence. However, these interplay effects are expected to fade away as time-scale separation becomes more pronounced in the limit $N \gg 1$. This behavior is corroborated by the experimental data in Fig. 7.8 (c) and (d) obtained with $N = 300$, where almost no bending is visible anymore. A few experimental data points for small ε in (d) were left out of consideration when computing the fitting line, since the corresponding time-traces did not reach the 1/e threshold by the time the experiment ended. Overall, simulation and experimental data yield very similar heating rates, described by a power-law with an exponent close to 2, consistent with our theoretical analysis.

Overall, the excellent qualitative agreement between theory and experiment is remarkable considering the three orders of magnitude difference in the system size between the two. From a theory perspective, this justifies the results obtained using exact simulation of the dynamics in the modelled system, and indicates that these numerical techniques can be used to make reliable predictions about experimental systems. Nonetheless, the experiment covers system sizes that are infeasible to reach on any classical computer in the foreseeable future. Therefore, the experiment remains indispensable for probing statistical mechanics concepts related to collective phenomena, such as thermalization dynamics or symmetry breaking, which are only well-defined in the thermodynamic limit.

Chapter 8

Solid Echo in the Rotating Frame

8.1 Introduction

The *spin echo* or *Hahn echo* was accidentally discovered by Erwin Hahn in 1949 while performing experiments on nuclear spin coherence relaxation [60]. He observed that, by applying a π-pulse after an excitation pulse, he could reverse the evolution of the spins under any interaction proportional to $\widehat{I}_z$. Consequently, the relative phases accumulated by the spins that cause the signal to decay are refocused and an *echo* is observed. In the early 1960s, Powles and Mansfield [125, 107, 108] discovered what is now known as the *solid echo*, consisting of the equivalent of the Hahn echo but for the dipolar interaction, whose dephasing part is $\propto \widehat{I}_{1z}\widehat{I}_{2z}$. However, due to the nature of the dipolar interaction, the echo pulse angle must to be $\pi/2$ instead of π, and its phase aligned to the original magnetization in the rotating frame (see Chapter 4 of [88]). Therefore, considering two spins $\widehat{I}_1$ and $\widehat{I}_2$ coupled with a dipolar Hamiltonian $\widehat{\mathcal{H}}_{DC} = d_{CC}(3\widehat{I}_{1z}\widehat{I}_{2z} - \widehat{\mathbf{I}}_1\widehat{\mathbf{I}}_2)$ and an initial density matrix $\widehat{\rho}_I = \widehat{I}_x = (\widehat{I}_{1x} + \widehat{I}_{2x})/\sqrt{2}$, we can refocus the evolution of $\widehat{\rho}$ under $\widehat{\mathcal{H}}_{DC}$ by applying the sequence $\tau - (\pi/2)_x - \tau$.

Spin echo phenomena and their numerous derivatives are now part of the base foundations of the NMR ecosystem and have been incorporated into countless NMR pulse sequences. Consequently, it is even more surprising to find that these phenomena can still harbor some mysteries and occur in unexpected contexts. For instance, Barrett et al. showed that a train of π-pulse could generate solid echoes in a dilute dipolar solid [barrett]. In this chapter, we report the observation of the solid echo of a Floquet Hamiltonian engineered by a strong spin-lock on a dipolar solid nuclear spin system. We identified this phenomenon as an analogy of the solid-echo that occurs in the rotating frame. We discovered this phenomenon accidentally while studying discrete time crystals [28], when we observed that the transient oscillations were being refocused when one of the pulses was tuned near $\pi/2$. Thus, we identified this phenomenon as an analogue of the solid-echo sequence. The analogy comes into play because rather than refocusing free evolution under the dipolar interaction, our sequence instead refocuses a Floquet Hamiltonian engineered by rapidly pulsing dipolar-

interacting spins. We provide an analytical form for this *rotating-frame* solid echo by making analogy to the *classic* solid-echo. To support our interpretation, we show that it is possible to recreate the qualitative features with numerical simulation and using a relatively simple model.

NB: Much of the formal analysis and experimental data in this Chapter was taken with the help of collaborator Quentin Reynard-Feytis, and reproduced with his permission here. The manuscript is still in preparation, so it has not been published yet. Quentin Reynard-Feytis retains the right to use this work as his intellectual property.

8.2 System

The experimental system is composed of a ^{13}C nuclear spins lattice (Fig. 8.1A) in natural abundance diamonds, optically hyperpolarized using Nitrogen Vacancy (NV) centers [21, 15]. Hyperpolarization time lasts $t_{pol} = 40s$, which results in an enhancement $\epsilon \approx 223$ compared to thermal equilibrium. The magnetically active ^{13}C are spatially disordered and are coupled by the dipolar coupling interaction $\widehat{\mathcal{H}}_{DC} = \sum_{i<j} \widehat{\mathcal{H}}^{ij}_{DC}$ with $\widehat{\mathcal{H}}^{ij}_{DC} = d^{CC}_{ij}(3\widehat{I}_{iz}\widehat{I}_{jz} - \widehat{\mathbf{I}}_i\widehat{\mathbf{I}}_j)$. The coupling strength is defined by $d^{CC}_{ij} = (\mu_0/4\pi)\hbar\gamma_n^2(3\cos^2\beta_{ij} - 1)r_{ij}^{-3}$, where $\gamma_n = 10.74$ MHz/T is the gyromagnetic ratio and β_{ij} is the angle between the internuclear vector and the external magnetic field. The general pulse sequence we used is shown in Fig. 8.1.B. We start with $(\pi/2)_y$ excitation pulse to place the magnetization along x and apply a period of pulsed spin-locking along this axis. The pulsed spin-lock, extensively detailed in Chapter 3 [30], consists of the repetition of *Floquet cycles* which are composed of a $(\vartheta)_x$-pulse and an acquisition period $\tau_{\text{acq}} = 85\mu s$. Therefore, for each Floquet cycle, we sample the Larmor precession signal which is then Fourier transformed and gives a single amplitude/phase point for a given time t. The amplitude taken over each Floquet cycle results in the curve shown in Fig. 8.1C. For any $\vartheta \neq n\pi$, the pulsed spin-lock engineers an average dipolar Hamiltonian 8.1 that commutes with the part of the density matrix which is $\propto \widehat{I}_x$ with $\widehat{I}_\nu = \sum_i I_{i\nu}$.

$$\bar{\mathcal{H}}^0_F = \sum_{j=1}^{N} \bar{\mathcal{H}}^j \approx \sum_{j<k} d^{CC}_{jk}\left(\frac{3}{2}(\widehat{I}_{jz}\widehat{I}_{kz} + \widehat{I}_{jx}\widehat{I}_{kx}) - \widehat{\mathbf{I}}_j.\widehat{\mathbf{I}}_k\right) \tag{8.1}$$

The consequence is that the $\widehat{I}_x$-component of the density matrix decays with a $T_2' = 90s$, providing it a 60,000-fold extended lifetime with respect to the FID lifetime $T_2^* = 1.5ms$. The magnetization is called *quasi-conserved* and it leads to the first regime represented in figure 8.1.C, which is called *prethermal plateau* **(a)** where the detected signal appears constant within a relatively short time scale. After the system is stabilized at this plateau, we then apply a second $(\pi/2)_y$-pulse that kicks the magnetization out of the x axis, in the $y-z$-plane, and we apply a second period of spin-lock pulsing. This leads to the second regime shown in figure 8.1.C, where the magnetization then precesses along the x-axis. Since the magnetization no longer commutes with the Floquet Hamiltonian 8.1, it rapidly vanishes

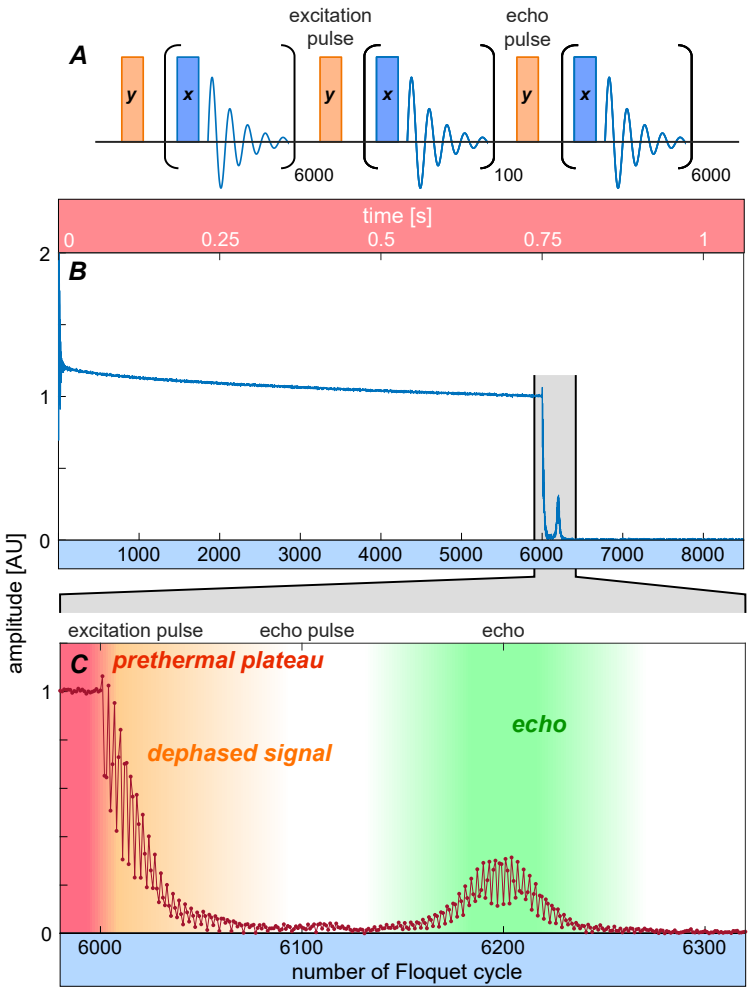

Figure 8.1 **Pulse sequence and echo observation. A.** ***Sequence.*** Representation of the general pulse sequence. It starts with a first $(\pi/2)_y$-pulse to bring the magnetization among $\widehat{x}$ followed by a period of Floquet driven and detection. Afterwards, we apply another $(\pi/2)_y$-pulse followed by another period of Floquet driving/detection. The Floquet driving/detection protocol is detailed, it consists of the repetition of Floquet cycles composed of a $(\pi/2)_x$-pulse and a period of detection. For each fid acquired, we Fourier transform it to obtain its amplitude and its phase at a given time t, which overall will form the resulting amplitude curve. **B-C.** ***Results.*** Representation of the obtained curve.

within $\simeq$ 10 ms **(b)**. We can draw a parallel to classic NMR experiments, where the *conserved* quantities are along z due to the static magnetic field B_0 and its associated Zeeman interaction. In this case, known as the laboratory frame, the magnetization is dephased by the Zeeman truncated dipolar Hamiltonian $\sum_{i<j} \widehat{I_i z} \widehat{I_j z}$ when it is put in the $x-y$-plane. In our case, we can say that we "mimic" the classical NMR experiment in the rotating frame.

8.3 Observation of the solid echo

The rotating-frame solid echo protocol is shown in figure 8.2A and the experimental curve showing the echo for $\tau = 100$ pulses is shown in figure 8.2B. We start by waiting for the system stabilizes on the prethermal plateau and we apply an excitation $(\pi/2)_y$ pulse that kicks the magnetization out of the x-axis where the magnetization was quasi-conserved, leading to the *dephased signal*. After the delay τ, we apply a second $(\pi/2)_y$ pulse and continue measuring the spins between pulses. The echo is observed after the same delay τ from the echo pulse. We quantified the echo maximum intensity as a function of the delay between the excitation pulse and the echo 2τ and noted that it followed a stretched exponential decay with a $T_2' = 14ms$.

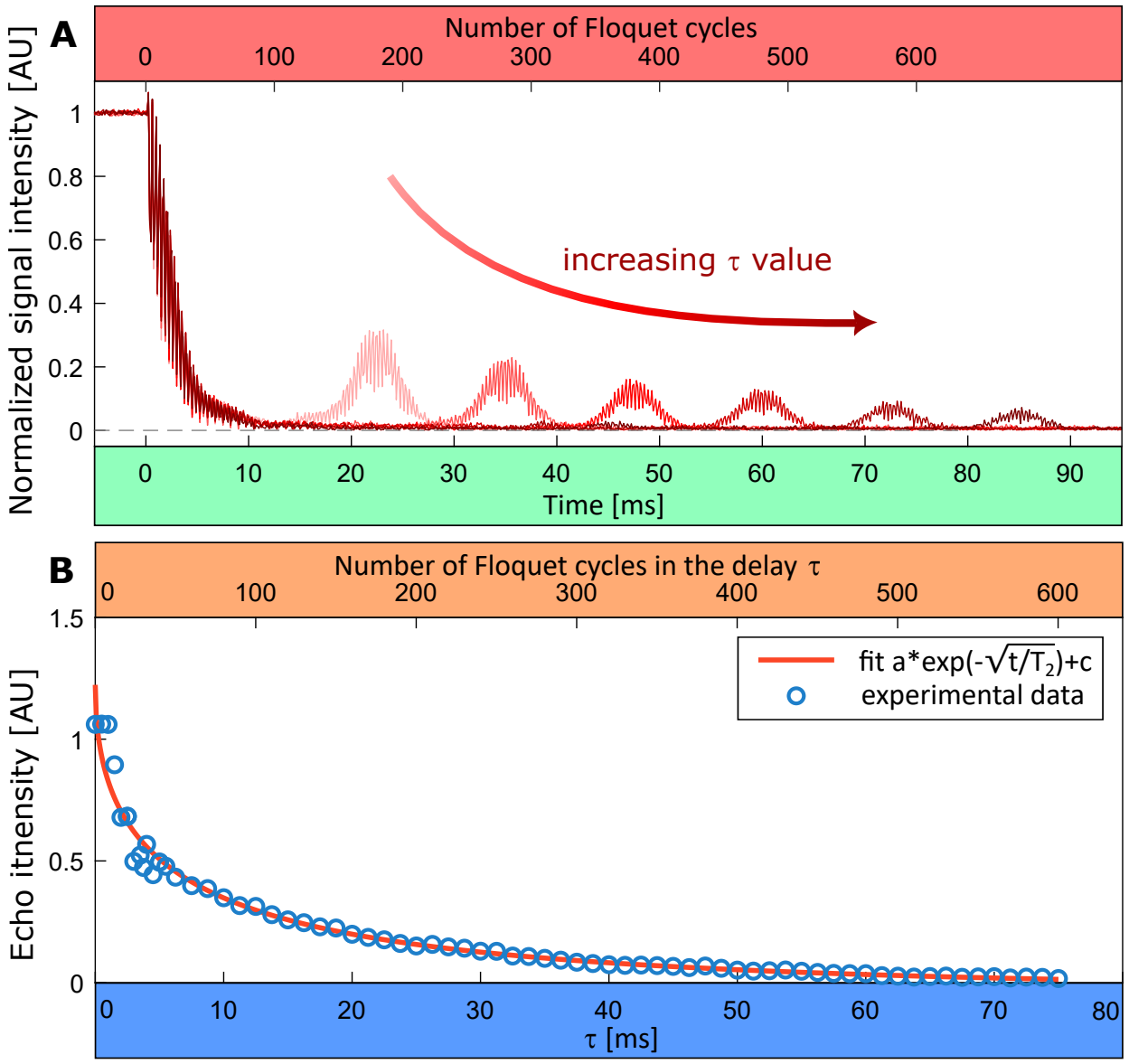

Figure 8.2 **Observation of the rotating frame solid echo.** (A) General protocol, we let the system stabilizing on the prethermal plateau and we apply a first excitation $(\pi/2)_y$ pulse that kicks out the magnetization from the Floquet driving axis and we apply the Floquet driving for a length τ before we apply a second $(\pi/2)_y$ pulse. We then observe the spin for a longer delay and observe that part of the signal is being refocused. (B) Resulting decay curve showing the Floquet rotating frame solid echo for $\tau = 100FC$. We also represented the intensity of the echo as a function of the delay τ and fit it with a stretched exponential model obtaining a $T_2' = 14$ ms.

When we first observed this echo, it was unclear what kind of interaction we were refocus-

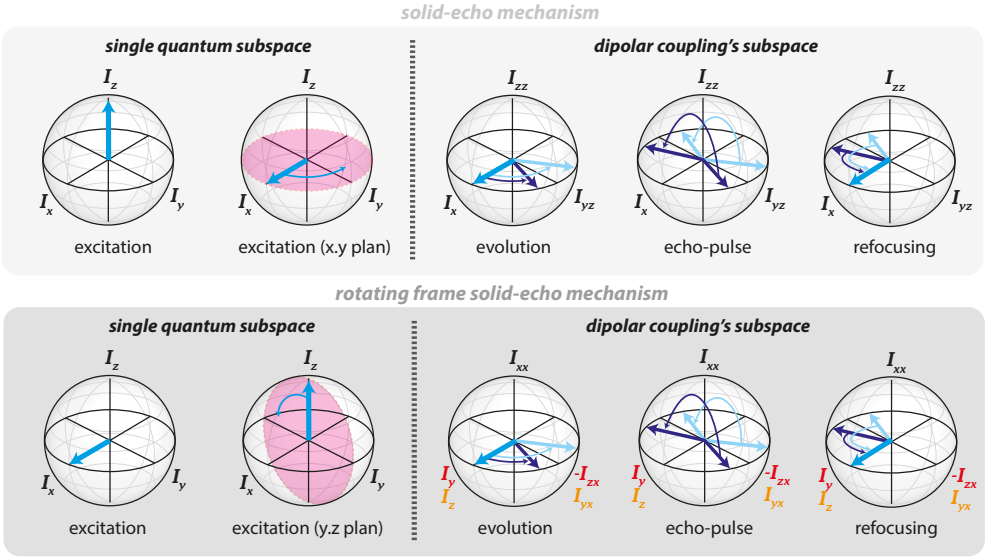

Figure 8.3 **Laboratory-frame (classic) vs. rotating-frame solid echo.** Figure prepared by Quentin Reynard-Feytis.

ing. It was only when we realized that the echo intensity was at its peak when the refocusing pulse was $\simeq \pi/2$ that we deduced that we were refocusing the dipolar interaction *felt* by the spin under the spin-locking. It is interesting to note that the observed phenomenon still presented some unclear features that strongly differ from the classic solid echo. First of all, the phase of the *excitation* and *echo* pulse are the same, which shouldn't be the case since solid-echo only occurs if the two pulses are dephased by $\pi/2$. We also measured the T_2' of the system in this context by measuring the intensity of the echo as a function of the delay τ and noted that it was surprisingly short. Nonetheless, these surprising features can be explained theoretically and computationally.

8.4 Theory analysis

When considering a single pair of spins $\mathbf{I}_1$ and $\mathbf{I}_2$, a normal solid-echo consists of the refocusing of their evolution under a dipolar Hamiltonian

$$\widehat{\mathcal{H}}_{DC} = d_{cc}(3\widehat{I}_{1z}\widehat{I}_{2z} - \widehat{\mathbf{I}}_1\widehat{\mathbf{I}}_2) \tag{8.2}$$

Essentially, as explained in figure 8.3, the classic solid-echo occurs when, from equilibrium, the conserved magnetization along z which commutes with the Zeeman Hamiltonian, is placed along the $x-y$-plane. In the laboratory frame, the magnetization precesses along the

z-axis, however it remains fixed in the rotating frame, in which the dipolar Hamiltonian for two spins $\mathbf{I}_1$ and $\mathbf{I}_2$ can be written

Since the $\widehat{\mathbf{I}}_1\widehat{\mathbf{I}}_2$ commutes with the density matrix, we can only consider the evolution of the density matrix under $\widehat{I}_{1z}\widehat{I}_{2z} \rightarrow \widehat{I}_{zz}$. The evolution of the density matrix under the dipolar coupling Hamiltonian for a time τ can be written

$$\widehat{I}_x \xrightarrow[\tau]{3d_{cc}\widehat{I}_{zz}} cos(3d_{cc}\tau)\widehat{I}_x + sin(3d_{cc}\tau)\left(\widehat{I}_{1y}\widehat{I}_{2z} + \widehat{I}_{2z}\widehat{I}_{1y}\right) = cos(3d_{cc}\tau)\widehat{I}_x + sin(3d_{cc}\tau)\widehat{I}_{yz} \quad (8.3)$$

As shown in figure 8.3, the evolution of the density matrix under the dipolar coupling can be represented in the dipolar coupling associated subspace. Therefore, the mechanism of the solid-echo appears as clear as the Hahn echo: if a $(\pi/2)$ pulse is applied along x, the starting axis, it will invert the $\widehat{I}_{yz}$ part while keeping the $\widehat{I}_x$ part unchanged. Thus, after a similar evolution time τ, the spin pairs with different d_{cc} values will be refocused among $\widehat{I}_x$, giving rise to an echo. A similar picture can be used to describe how the transient signal echo is happening. As mentioned previously, the system presents *quasi-conserved*, quantities under the pulse spin-lock which are in our case the magnetization along x. The magnetization in the $y-z$-plane precesses along x and gives rise to the transient oscillations.

Under the pulsed spin-locking, our system experiences a Floquet Hamiltonian whose first order expression in equation 8.1 can be rewritten

$$\widehat{\mathcal{H}}_F^0 = \sum_{j<k} d_{jk}^{CC}\left(\frac{1}{2}\widehat{\mathbf{I}}_j.\widehat{\mathbf{I}}_k - \frac{3}{2}\widehat{I}_{jx}\widehat{I}_{kx}\right) \quad (8.4)$$

With the same reasoning as before, we can see that the non-commuting part that leads to the dephasing of the transient signal is the $\widehat{I}_{1x}\widehat{I}_{2x} \rightarrow \widehat{I}_{xx}$ part. Similarly to the classic solid-echo, it is possible to represent the evolution of the density matrix under the average dipolar Hamiltonian of the magnetization precessing in the $y-z$-plane under the Floquet driving. The main difference remaining between the classic and rotating-frame solidecho is that the pulse spin-locking constantly drive the densitiy matrix through the terms $\widehat{I}_y \circlearrowleft \widehat{I}_z$ and their associated term in the dipolar coupling's subspace $\widehat{I}_{zx} \circlearrowleft \widehat{I}_{yx}$. Since the echo pulse is performed along y, it is obvious that only the part of the density matrix among $\widehat{I}_y$ and $\widehat{I}_{zx}$ will be refocused. This quantity depends on the number of Floquet cycles during the delay τ and the value of the pulsing angle ϑ.

8.5 Numerical simulations

To further our understanding of this phenomenon and to test our model, we used a toy model to qualitatively reproduce the results. For this, we considered a group of independent spin

pairs coupled with different dipolar coupling constants within a given range and distribution. This model, in addition to being relatively light to compute, seemed particularly well-adapted to our system considering that it is composed of diluted ^{13}C nuclei. In the figure 8.4, we show the result when the pulse value was exactly 90°. We are then able to reproduce the echo phenomenon we observed. When we zoom over a dozen pulse cycles and observe the evolution of the terms $\widehat{I}_y$, $\widehat{I}_z$, $\widehat{I}_{xy}$, $\widehat{I}_{xz}$, we can see that the density matrix evolution is a succession of cycles during which the $\widehat{I}_y$ term evolves under the actual dipolar Hamiltonian $\widehat{I}_{zz}$ and is mixed with $\widehat{I}_{xz}$ and Floquet cycles during which the terms are converted into $\widehat{I}_y$ and $\widehat{I}_{xy}$ respectively. Since the latter terms do not commute with the density matrix, they are conserved through the cycle. Therefore, the simulation reveals more of a step-wise solid-echo mechanism. However, this is actually the same as the result that we are expecting. It is just that in our theoretical approach, we considered the average Hamiltonian, and here we took the exact Hamiltonian and analyzed it over time (just as happens in the experiment). In both cases, the evolution in the associated dipolar coupling subspace corresponds to an effective dipolar coupling constant with a factor 1/2.

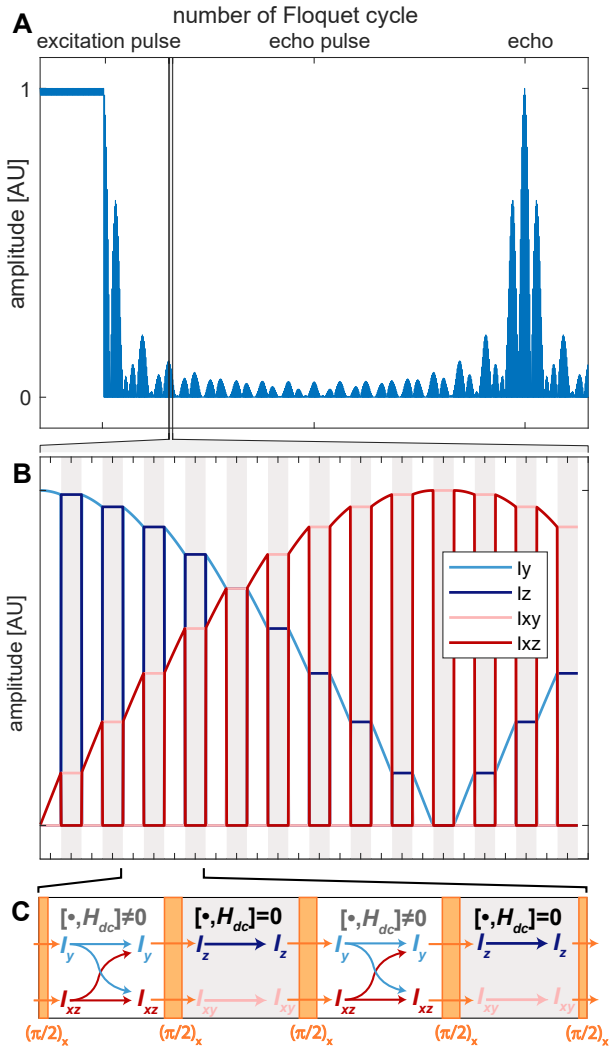

Figure 8.4 **Simulation of the rotating frame solid-echo of a group of spin pairs with a given range of dipolar coupling constant..** A. Reproduction of the general experiment with the excitation pulse, echo pulse and the observed echo, under the Floquet driving. B. Zoom on $\simeq 20$ Floquet cycles with the evolution of the different terms of the density matrix for each pair of spins, assuming that the Floquet driving pulse angle is exactly $\pi/2$. During the odd Floquet cycles, the system evolve under the dipolar coupling Hamiltonian while, during the even Floquet cycles, it is conserved through DQCs terms that commute with $\widehat{\mathcal{H}}_{DC}$. C. Schema of the mixing between all the density matrix terms for 4 Floquet cycles, showing the succession of commuting/non-commuting free-evolution period. Analysis and figure prepared by Quentin Reynard-Feytis.

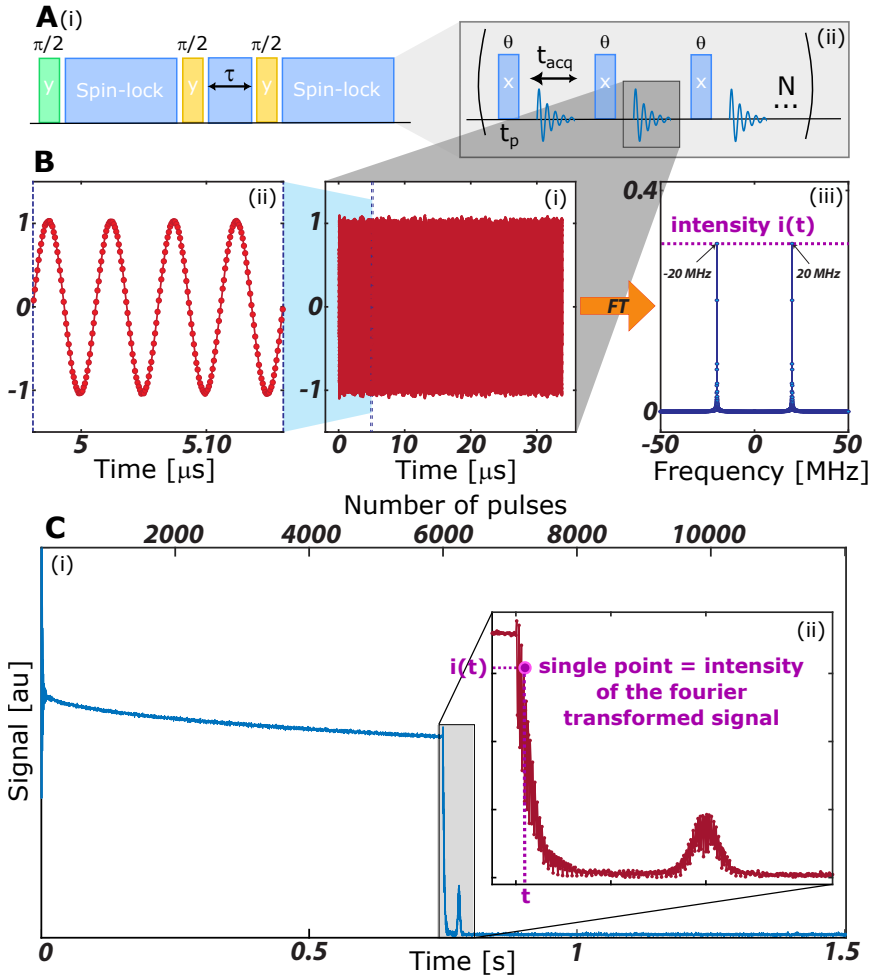

Figure 8.5 **Data acquisition and processing chain.** (A) General (i) pulse and acquisition sequence of the echo experiment, with a detailed representation of the spin-lock procedure (ii). (Bi) Raw data of ^{13}C nuclear precession measured inductively, here heterodyned from 75MHz (Larmor frequency) to 20MHz. The window shown is a 150ns part of the larger acquisition window. (Bii) Raw data corresponding to one complete acquisition period between the pulses, here t_{acq}=32μs. (Biii) Fourier transformation reveals characteristic peaks at the heterodyning frequency $\pm$20MHz.

8.6 Data Acquisition

The data processing chain is described in Figure 8.5. Figure 8.5A(i) shows the previously presented protocol for the rotating-frame solid-echo observation, where we start with an excitation pulse to kick the magnetization along the x-axis, followed by a general spin-lock procedure to reach the Floquet prethermal plateau. After 6000 pulse cycle, we apply an excitation pulse that kicks the magnetization out of the spin-lock axis, a delay τ of spin-

lock followed by an echo pulse and another 6000 pulse cycles of spin-locking. The spin-lock procedure is also detailed in Figure 8.5A(ii) where we can see the repetition of Floquet cycles composed of a ϑ-pulse along x which last $t_p = 85\mu s$ and a detection period of $t_{acq} = 85\mu s$ during which the data are readout with a sampling rate of 1Gs/s, giving a resulting FID represented on Figure 8.5B(i). A zoom in Figure 8.5B(ii) shows high SNR oscillations which corresponds to the oscillations of hyperpolarized nuclei. Thus, for every Floquet cycle, we have a corresponding fid on which we can perform a Fourier transform to obtain a spectrum as represented on Figure 8.5B(iii). For each spectrum, we extract the 20 MHz peak and its amplitude, that will lead to a single point on the the decay curve represented on the figure Figure 8.5C, which then presents one point for every Floquet cycle.

8.7 Materials and Methods

The sample used in these experiments consists of a CVD fabricated single crystal of diamond with ∼1ppm of NV centers. The sample is placed flat, i.e. with its [100] face pointing parallel to the hyperpolarization and interrogation magnetic fields (36mT and 7T respectively). In this configuration, the internuclear vector between ^{13}C nuclei at nearest-neighbor sites on the lattice are positioned at the magic angle, and hence are suppressed.

For hyperpolarization, we employ continuous optical pumping and swept microwave irradiation for ∼40s through a technique described previously. Hyperpolarization is carried out at low field, the sample is shuttled to high field, and the Floquet sequence in Figure **??**B is then applied. NV-^{13}C polarization transfer occurs via biased Landau-Zener traversals in the rotating frame; spin diffusion serves to transfer polarization to bulk ^{13}C nuclei in the diamond lattice.

8.8 Physics of the solid echo in the rotating frame using the product operator formalism

In this Chapter, we described the rotating-frame solid-echo phenomenon by taking the propagator and the average Hamiltonian and looking at its commutation properties with the starting density operator. Although this might be a better insight of what is happening in our system, it is definitely not the clearer way of explaining an echo phenomenon.

In the general case, when it comes to explain "basic" spin physic such as Hahn echoes, one tends to use the product operator formalism. The latter consists in the use of the commutation relationships between the operators of the Hamiltonian and the components of the density matrix to express its evolution under various Hamiltonians.

$$\text{if } [\mathcal{A}, \mathcal{B}] = i\mathcal{C} \text{ then } \mathcal{A} \overset{\omega\mathcal{B} \text{ for } \tau}{\longrightarrow} cos(\omega\tau)\mathcal{A} + sin(\omega\tau)\mathcal{C} \tag{8.5}$$

In this part, we will then use this formalism to explain the rotating-frame solid-echo phenomenon and show the similarities and differences with a classic solid-echo to give to the

lecturer a good picture of this phenomenon. We will consider an homonuclear 2 spin system I_1 and I_2 coupled by a dipolar interaction truncated over the Zeeman Hamiltonian $\widehat{\mathcal{H}}_{DC} = d_{CC}(3\widehat{I}_{1z}\widehat{I}_{2z} - \widehat{\mathbf{I}}_1\widehat{\mathbf{I}}_2)$ and an initial state $\widehat{\rho}_0 = \widehat{I}_x = (\widehat{I}_{2x} + \widehat{I}_{1x})/2$. In all the equations, the terms coming from $\widehat{\mathbf{I}}_{1x}$ will be in b blue and the terms coming from $\widehat{\mathbf{I}}_2$ will be in r red. To simplify the equations, we will use the notations $cos(\beta) = c\beta$ and $\sin(\beta) = s\beta$ and the factor $1/2$ in the density matrix.

classic solid-echo description – In this case, we'll consider the sequence $\tau - (\pi/2)_x - \tau$. As we are in the rotating frame we can only consider the dipolar Hamiltonian. In addition, the fact that the $\widehat{\mathbf{I}}_1\widehat{\mathbf{I}}_2$ term commutes with $\widehat{\rho}_0$ permits us to only consider the Hamiltonian $\widehat{\mathcal{H}}'_{DC} = 3d_{CC}\widehat{I}_{1z}\widehat{I}_{2z}$.
The first delay τ give us

$$a\widehat{I}_{1x} + a\widehat{I}_{2x} \xrightarrow{\tau} rc\beta\widehat{I}_{1x} + s\beta\widehat{I}_{1y}\widehat{I}_{2z} + rc\beta\widehat{I}_{2x} + s\beta\widehat{I}_{1z}\widehat{I}_{2y} = c\beta(a\widehat{I}_{1x} + a\widehat{I}_{2x}) + s\beta(a\widehat{I}_{1y}\widehat{I}_{2z} + a\widehat{I}_{1z}\widehat{I}_{2y}) \quad (8.6)$$

under the pulse $(\pi/2)_x$, it gives

$$c\beta(a\widehat{I}_{1x} + a\widehat{I}_{2x}) + s\beta(a\widehat{I}_{1y}\widehat{I}_{2z} + a\widehat{I}_{1z}\widehat{I}_{2y}) \xrightarrow{(\pi/2)_x} c\beta(\widehat{I}_{1x} + a\widehat{I}_{2x}) - s\beta(a\widehat{I}_{1z}\widehat{I}_{2y} + a\widehat{I}_{1y}\widehat{I}_{2z}) \quad (8.7)$$

we can constat that the $(\pi/2)_x$ pulse invert the product of the first delay τ, which is the main principle of such phenomenon such as the Hahn echo. Therefore, the second delay τ gives, after some rearrangements

$$\begin{aligned} c\beta(\widehat{I}_{1x} + \widehat{I}_{2x}) - s\beta(\widehat{I}_{1z}\widehat{I}_{2y} - \widehat{I}_{1y}\widehat{I}_{2z}) \xrightarrow{\tau} & c\beta^2(\widehat{I}_{1x} + \widehat{I}_{2x}) \\ & + s\beta c\beta(\widehat{I}_{1y}\widehat{I}_{2z} + \widehat{I}_{1z}\widehat{I}_{2y}) - c\beta s\beta(\widehat{I}_{1z}\widehat{I}_{2y} + \widehat{I}_{1y}\widehat{I}_{2z}) + s\beta^2(\widehat{I}_{2x} + \widehat{I}_{1x}) \\ & = \widehat{I}_{1x} + \widehat{I}_{2x} \end{aligned} \quad (8.8)$$

Thus, as an analogy to the Hahn echo, we can see that the evolution of the density matrix $\widehat{\rho}_0 = \widehat{I}_x$ is reversed by the $(\pi/2)_x$ pulse. In the figure Figure 8.6, we represent the classic solid-echo spin evolution in an adequate subspace, which permit to get almost the same picture than the Hahn echo. We represent the spin evolution under the Hamiltonian $\widehat{I}_{1z}\widehat{I}_{2z}$ of two pairs of coupled spin with respective dipolar coupling constant d_1 and d_2. We thus can see how the $(\pi/2)_x$ echo pulse reverse the evolution of the density matrix under this Hamiltonian and permits, in fine, to refocus the signal among the x-axis.

8.9 Rotatating frame solid echo description

Now that we have described the classic solid-echo phenomenon by using the product operator formalism, we can do the same for the case that we observed in our experiment. The main

differences are that we don't consider the dipolar coupling Hamiltonian directly but, the engineered average dipolar Hamiltonian by the Floquet driving. Then, we can directly see its influence through the period of Floquet driving without considering every pulses. As mentioned in the Chapter, the latter has the form

$$\widehat{\mathcal{H}}_F^0 \approx d_{12}^{CC}\left(\frac{1}{2}\widehat{\mathbf{I}}_1.\widehat{\mathbf{I}}_2 - \frac{3}{2}\widehat{I}_{1x}\widehat{I}_{2x}\right) \tag{8.9}$$

Thus, during the Floquet driving, we will consider that the system is only evolving under this average Hamiltonian. One can note that, similarly to the dipolar coupling Hamiltonian, the $\widehat{\mathbf{I}}_j.\widehat{\mathbf{I}}_k$ commutes with the density matrix as long as the spins are on resonance and we can thus only consider the $\widehat{I}_{1x}\widehat{I}_{2x}$ part of the Hamiltonian for the echo phenomenon. The sequence we want to analyze is $\tau - (\pi/2)_y - \tau$ and we'll admit that the initial state is $\rho_0 = -\widehat{I}_{1y} - \widehat{I}_{2y}$. This point is subtle we will discuss about it later. By equivalent calculations than the classic solid-echo, we have:

$$\begin{aligned} a\widehat{I}_{1y} + a\widehat{I}_{2y} \xrightarrow{\tau} rc\beta\widehat{I}_{1y} + s\beta\widehat{I}_{1z}\widehat{I}_{2x} + rc\beta\widehat{I}_{2y} + s\beta\widehat{I}_{1x}\widehat{I}_{2z} \\ = c\beta(a\widehat{I}_{1y} + a\widehat{I}_{2y}) + s\beta(a\widehat{I}_{1z}\widehat{I}_{2x} + a\widehat{I}_{1x}\widehat{I}_{2z}) \end{aligned} \tag{8.10}$$

under the pulse $(\pi/2)_y$, it gives

$$\begin{aligned} c\beta(a\widehat{I}_{1y} + a\widehat{I}_{2y}) + s\beta(a\widehat{I}_{1z}\widehat{I}_{2x} + a\widehat{I}_{1x}\widehat{I}_{2z}) \xrightarrow{(\pi/2)_y} \\ c\beta(a\widehat{I}_{1x} + a\widehat{I}_{2x}) - s\beta(a\widehat{I}_{1x}\widehat{I}_{2z} + a\widehat{I}_{1z}\widehat{I}_{2x}) \end{aligned} \tag{8.11}$$

And then, similarly to the normal solid-echo, we finally obtain

$$\begin{aligned} c\beta(a\widehat{I}_{1y} + a\widehat{I}_{2y}) - s\beta(a\widehat{I}_{1x}\widehat{I}_{2z} - a\widehat{I}_{1z}\widehat{I}_{2x}) \xrightarrow{\tau} c\beta^2(a\widehat{I}_{1y} + a\widehat{I}_{2y}) \\ + s\beta c\beta(a\widehat{I}_{1z}\widehat{I}_{2x} + a\widehat{I}_{1x}\widehat{I}_{2z}) - c\beta s\beta(a\widehat{I}_{1x}\widehat{I}_{2z} + a\widehat{I}_{1z}\widehat{I}_{2x}) + s\beta^2(\widehat{I}_{2y} + a\widehat{I}_{1y}) \\ = \widehat{I}_{1y} + \widehat{I}_{2y} \end{aligned} \tag{8.12}$$

Therefore, by using tho product operator formalism, we can see why we observe this rotating frame solid-echo that distinguish itself from the classic solid-echo by being the refocusing of an average Hamiltonian instead of the Hamiltonian of an interaction. An important point we have omitted here is to explain why we start with the initial state $\rho_0 = -\widehat{I}_{1y} - \widehat{I}_{2y}$ and not $\rho_0 = -\widehat{I}_{2z} - \widehat{I}_{2z}$. Effectively, when we take the classic solid-echo phenomenon, the echo pulse phase should be aligned with the starting magnetization. The reason is that if you want to invert the rotation under the dipolar Hamiltonian in the adequate subspace described on figure ..... the only pulse you can apply to do so is a pulse among the x-axis. The same conditions looks necessary in our equation to explain the rotating frame solid-echo. Then, if we start with $\rho_0 = -\widehat{I}_{1y} - \widehat{I}_{2y}$, the echo requires a $(\pi/2)_y$ pulse, while a $(\pi/2)_z$ pulse will only refocused an initial state $\rho_0 = -\widehat{I}_{1z} - \widehat{I}_{2z}$.

8.10 Influence of the excitation and refocusing pulse width on the echo signal intensity

When we first discovered this echo phenomenon, it wasn't really straightforward that this could be a rotating-frame solid echo and after isolating this echo phenomenon, we wanted to identify what interaction was actually refocused in our system. Therefore, we did a bi-dimensional parameters sweep varying both the excitation and the refocusing pulse width. We then measured the relative intensity of the echo signal, taking in count only the refocused part and removing the quasiconserved quantities (invariant signal after the echo) and normalizing it by the signal intensity just before the excitation pulse. The resulting results are presented on the figure 8.7. We can clearly identify that the optimal excitation pulse value is the $\pi/2$ value, which means that the echo phenomenon is due to the magnetization kicked away from the x-axis in the y-z-plane. For the optimal refocusing pulse value, the $\pi/2$ value also seems to be the best value in the general case, however we can observe that when the excitation pulse is close to $\pi/2$, the optimal refocusing pulse value is slightly under $\pi/2$.

8.11 Influence of the delay τ in the CPMG-like experiment in the rotating frame

When we implemented the CPMG-like experiment, we were interested to see if there were any differences between the results depending on how we set the delay τ between the refocusing pulses. We thus used two different τ value of 100µs and 125µs and measure the intensity of each echo. The results are shown on the figure 8.8. However it is difficult to say whether there is an actual influence of the value of the delay τ with only two experiments even if the difference between the two experiments here seems to be insignificant.

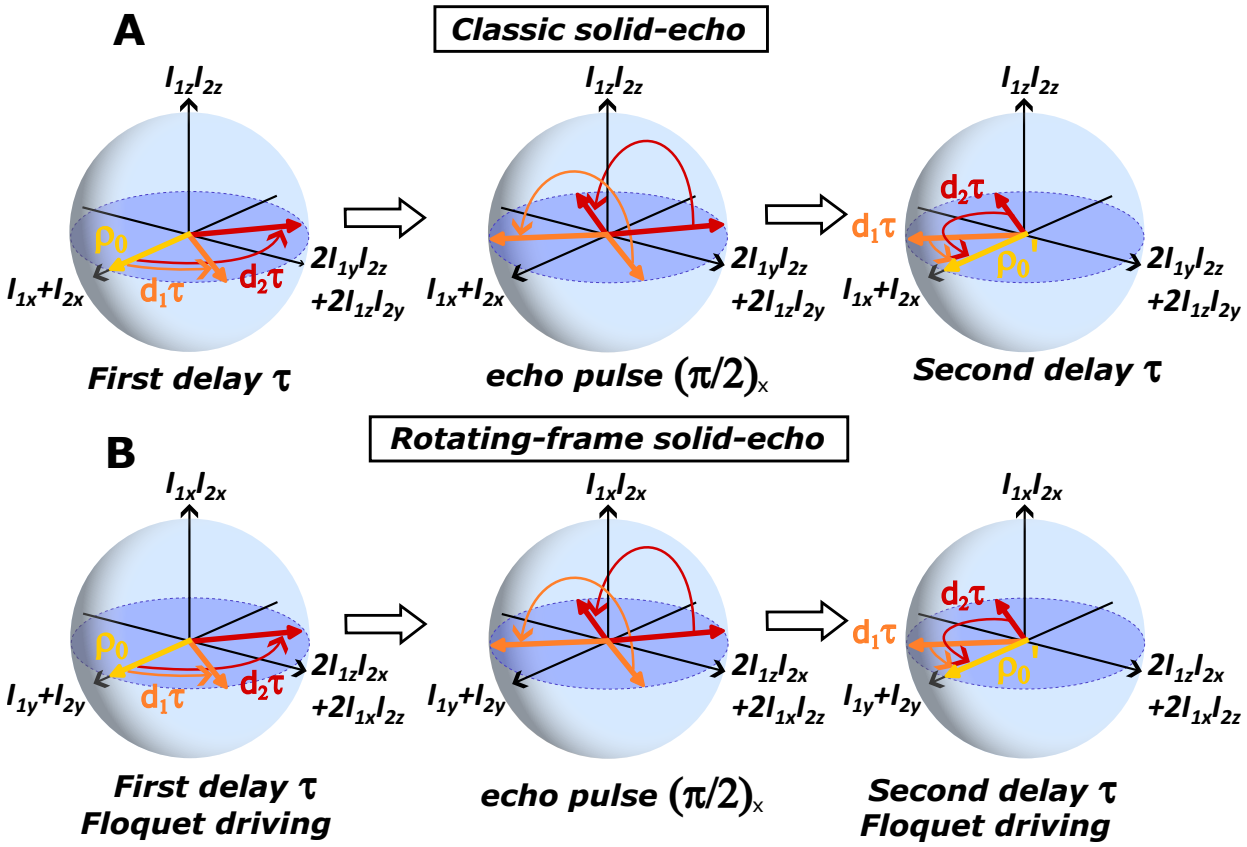

Figure 8.6 **Illustration of the classic solid-echo and rotating-frame solid echo mechanism.** The spin mechanism is illustrated in the subspace resulting of the interaction between the density matrix and the Hamiltonian at every step of the solid-echo. We represent two pairs of spins coupled by two different dipolar coupling constant d_1 and d_2 respectively. (A) Classic solid-echo where the magnetization is defocused under the influence of the dipolar coupling term $\widehat{I}_{1z}\widehat{I}_{2z}$ (B) Rotating-frame solid-echo where the magnetization is defocused under the influence of the average dipolar Hamiltonian coupling term $\widehat{I}_{1x}\widehat{I}_{2x}$.

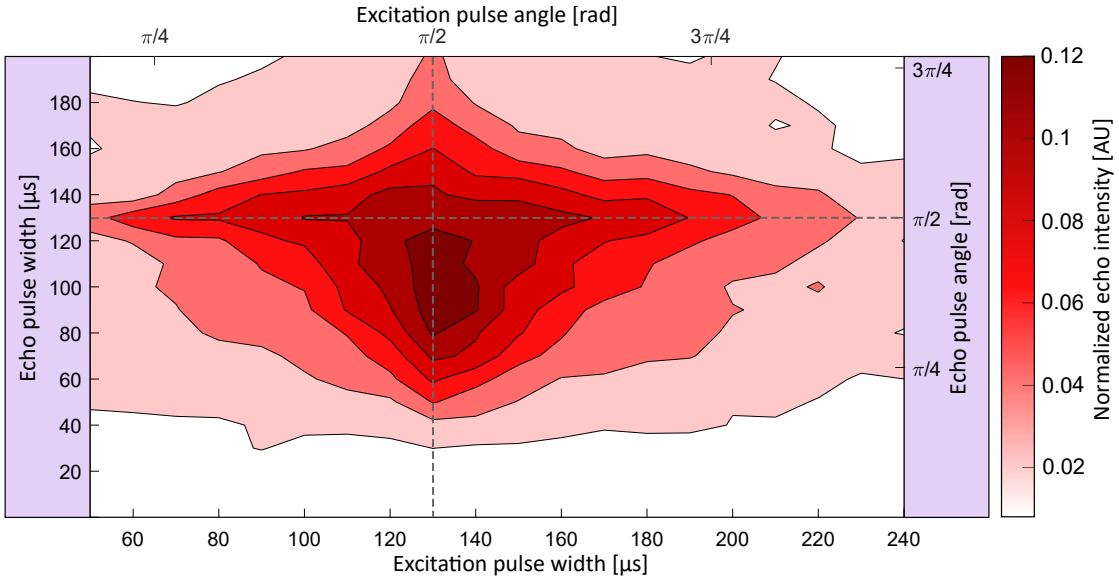

Figure 8.7 **Heat map.** Maximum measured echo intensity normalized by the signal intensity before the excitation pulse as a function of excitation pulse angle (horizontal axis) and echo pulse angle (vertical axis). The dashed lines represent the $\pi/2$ values for each pulse which seems to be the optimal conditions in the general case. Interestingly, we can point out that when the excitation pulse is around $\pi/2$, we have a slightly better echo when the the echo pulse is slightly lower than $\pi/2$, which is not the case otherwise where we can clearly see that $\pi/2$ corresponds to the optimal value. The delay τ used was 200 pulse cycles (corresponding to 25 ms), the excitation pulse follows a spin-lock period of 6000 pulse cycles.

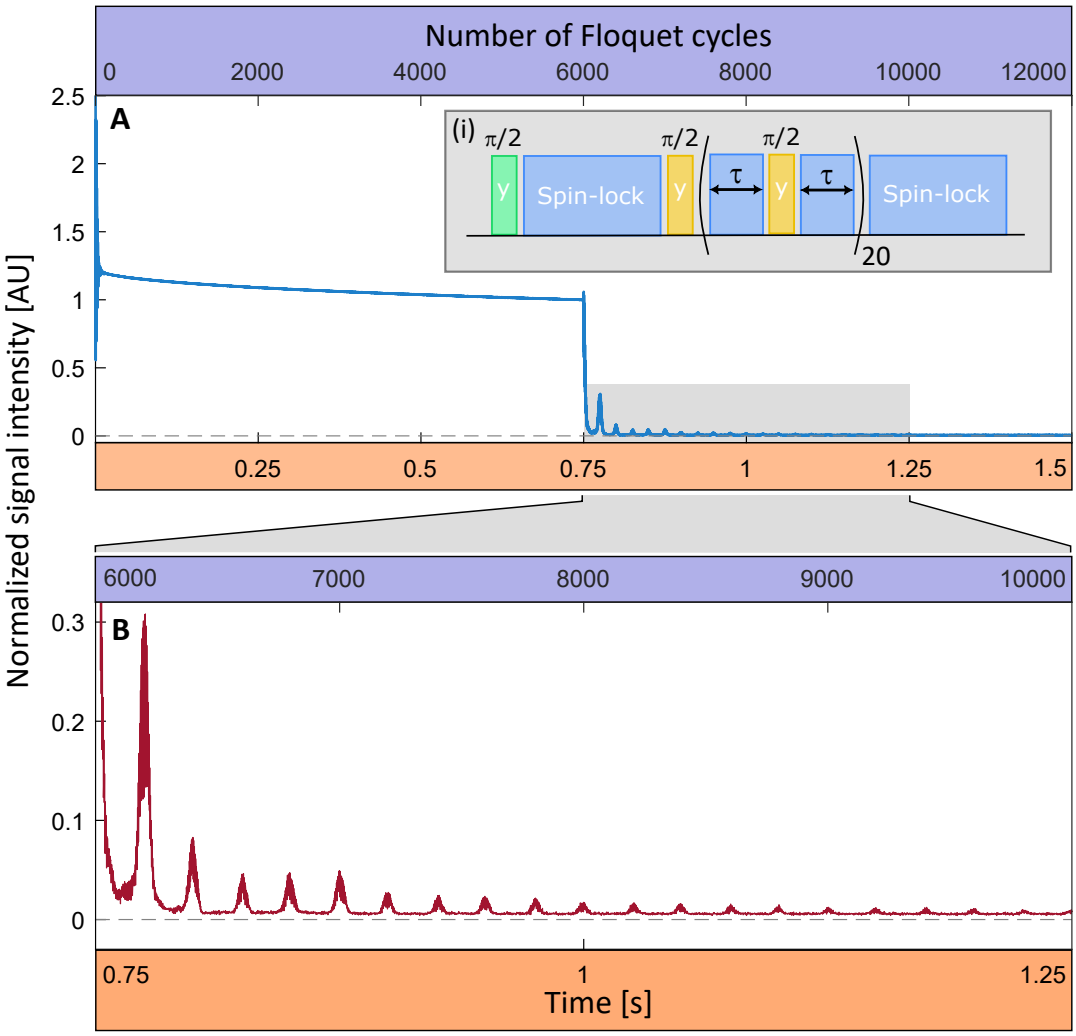

Figure 8.8 **Rotating-frame analogue of CPMG experiment.**

Chapter 9

Loschmidt Echo as an Experimental Probe of Time-Crystalline Dynamics

9.1 Introduction

Interacting many-body spin systems that resist thermalization are of interest to the condensed matter physics and quantum information communities. One dynamical system of interest is the critical discrete time crystal which can be formed by periodic applications of global spin rotations interleaved with free evolution under dipolar interactions. We implement a time crystal experiment in an ensemble of hyperpolarized ^{13}C nuclear spins using magnetic resonance instrumentation. By negating the dipolar interaction Hamiltonian, we demonstrate time-reversal of the coherent dipolar evolution – a form of the Loschmidt echo technique. Lastly, we insert a perturbation between the forward and reverse evolution periods. The next step in these experiments will be to measure the Loschmidt echo decay rate as a function of perturbation strength, the scaling of which can give insight into system dynamics. Equipped with a better understanding of the system's slow thermalization processes, the application will be to develop a highly coherent quantum sensor leveraging the interacting network of spins.

Open quantum systems will generically relax to thermal equilibrium due to its coupling to the environment. The inevitable restoration to equilibrium however erases the rich array of information present in the coherent evolution of non-equilibrium populations. This means that a high level of coherent control over a non-equilibrium system can be highly desirable [162]. Consider the example of designing a sensor: an ideal system for this purpose is one that is highly sensitive to the signal(s) of interest, and highly insensitive to all other signals. A real-world implementation may require us to sort through several signal sources and filter out information that is deemed irrelevant.

The Loschmidt echo can implement a signal filter using the technique of time reversal [43]. In principle, it is possible to implement time reversal in a closed quantum system that does not relax to thermal equilibrium [171]. Since the dynamics are fully unitary, the backward

time evolution propagator can be applied by simply negating each term in the system Hamiltonian and evolving for an amount of time equal to the original forward evolution. If the experimentalist can control various terms in the system Hamiltonian separately, they might selectively negate some terms in the Hamiltonian while leaving others untouched [112]. In this scenario, one can effectively decouple interactions at will. These interactions are said to be echoed out; selective time reversal acts as a physical signal filter. This is the principle of the Loschmidt echo – reversing the evolution under certain Hamiltonian terms to isolate certain effects on a system [74].

The first experiments implementing time reversal were nuclear magnetic resonance spectroscopy. In 1950, Hahn demonstrated the "spin echo" which revived the NMR signal decay resulting from magnetic field inhomogeneity [60]. The term in the Hamiltonian looks like a distribution of Zeeman energy offsets. Each spin sees a slightly different magnetic field strength δI_z that dephases it from other spins. During precession, the spin populations are inverted with a resonant π pulse around any axis in the transverse plane. Applying a frame transformation with respect to the action of this pulse, the Hamiltonian sees a sign change, $-\delta I_z$ inverting the frequency offset that each spin sees. By stepping the echo delay time τ and tracking the characteristic decay time, the spin echo can be used to measure T_2 relaxation times. This is more accurate than the simple free induction decay time T_2^* which includes effects from field inhomogeneity [53]. The same principle has been applied to dynamical decoupling [14, 24] – sequences of π pulses designed to minimize single-qubit errors due to terms that look like field inhomogeneity.

As useful as the spin echo is, the dynamics can be explained using a single-body picture. When interactions are introduced into a many-body system, the dynamics become considerably more complex. The first reported time-reversal of many-body interactions was by Rhim, Pines and Waugh in 1970 in a system of dipolar-coupled nuclear spins [135]. One simple illustration of the working principle is through the "magic echo" experiment [151]. At high magnetic field, the dipolar interaction retains only the secular terms, giving the form:

$$\mathcal{H}_{zz} = \sum_{j<k} d_{jk}^{\mathrm{CC}}(3I_{jz}I_{kz} - \vec{I_j}\cdot\vec{I_k}) \tag{9.1}$$

where d_{jk} is the coupling strength between spins j and k, and I_v are nuclear spin operators. Driving the system with a strong spin-lock along I_x re-arranges the $\mathcal{H}_{zz}$ term to give:

$$-\frac{1}{2}\mathcal{H}_{xx} = -\frac{1}{2}\sum_{j<k} d_{jk}^{\mathrm{CC}}(3I_{jx}I_{kx} - \vec{I_j}\cdot\vec{I_k}) \tag{9.2}$$

which can be transformed to $-\frac{1}{2}\mathcal{H}_{zz}$ by conjugating the spin-lock with $\frac{\pi}{2}$ pulses along I_y. Thus we have a negative form of the original Hamiltonian (scaled by $\frac{1}{2}$) that can be re-scaled by holding the spin-lock for twice as long as the original dipolar evolution period τ.

Making use of these techniques, I will show preliminary results characterizing the dynamics of a discrete time crystal (DTC). The DTC is the first stable non-equilibrium phase

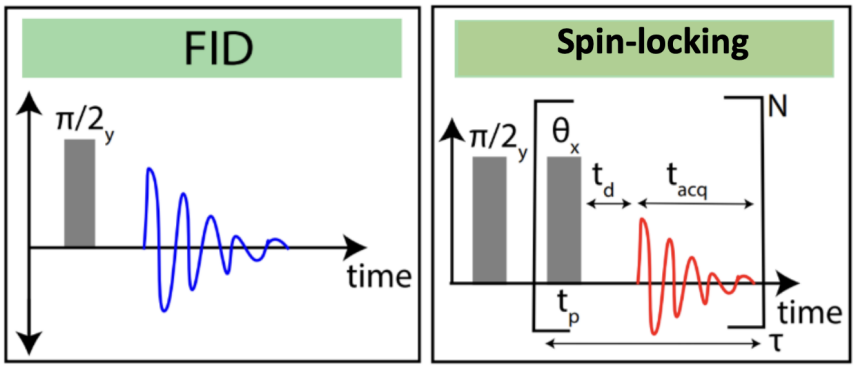

Figure 9.1 **Free induction decay (left) and multiple-pulse spin-locking (right) readout pulse sequences.** In our experiment, the flip angle ϑ is $\frac{\pi}{2}$, pulse width $t_p = 45\mu s$, acquisition time $t_{acq} = 32\mu s$, inter-pulse spacing $\tau = 88\mu s$, number of pulse duty cycles N=113636 (for a total experiment measurement time of 10s).

of matter, characterized by the spontaneous breaking of discrete time-translation symmetry [170, 41]. DTCs are recently attracting attention in the fields of condensed matter physics and quantum information [128, 113]. Experimental realization of a long-lived many-body interacting system robust to perturbations can be the platform for quantum sensing and possibly also serve as a benchmarking tool for quantum computers [52].

9.2 Experimental methods

Sample and hyperpolarization – NMR experiments were performed on a 4mm single-crystal diamond (natural abundance ^{13}C) doped with 1ppm nitrogen vacancy (NV) defect centers. While the thermal polarization of ^{13}C nuclear spins at 7T (inside the superconducting magnet) and room temperature is only 6ppm, the presence of NV centers enables us to initialize the nuclei at a much higher polarization, 10^2 times greater than thermal levels [30]. There are a macroscopic number of spins across the full sample, but the system can be viewed as an ensemble of NV central spins each surrounded by a bath of 10^2-10^3 ^{13}C spins. This is a helpful perspective because the hyperpolarization is generated locally around the NV centers before slowly diffusing away toward the bulk [29]. Since the hyperpolarized nuclei contribute the large majority of the observed NMR signal, we will consider our system to be an ensemble of 10^2-10^3 dipolar-interacting nuclear spins.

Signal measurement – Readout of global spin polarization for each experiment was done with a multiple-pulse spin-locking sequence. Single-shot free induction decay measurement is limited by the dipolar interactions which generate multiple-quantum coherences causing the observable global polarization signal to decay within a time constant $T_2^* = 1.5$ms. Our system is equipped with a fast digitizer (1GS/s) which can sample the coherent Larmor precession during free evolution periods between RF pulses.

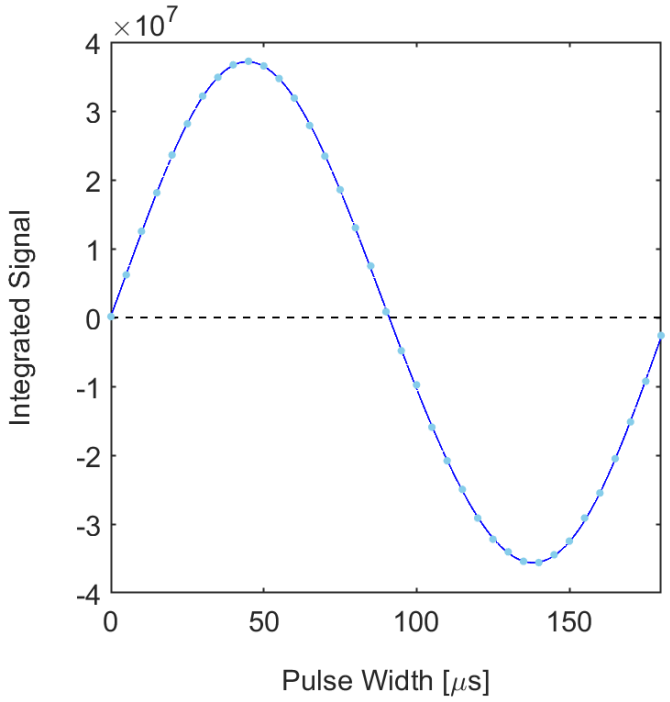

Figure 9.2 **Calibration of Rabi frequency.** Data points show integrated signal $< I_x >$ readout via spin-locking following initial excitation pulse of finite width. Each point shows a single-shot experiment for different pulse widths and plot represents one full period of a Rabi oscillation, with flip angle π being calibrated to the zero-crossing and the rest of the flip angles scaling linearly with pulse width.

Accelerated readout by spin-locking – This vast acceleration in measurement can be considered in terms of the total number of Larmor precession cycles measured in a single-shot experiment. For FID readout, the T_2^* decay timescale permits (1.5ms)*(75MHz) = **112,500 precession cycles** before the signal reaches 1/e of the original maximum. By contrast, spin-lock readout can increase the decay timescale up to 90.9s [30]. Since we cannot measure during the pulsing time, this leaves us with 32μs measurement windows to detect spin precession. In these experiments, the inter-pulse spacing was 88μs, leaving us with 90.9s / 88μs $\approx$ 1 million windows in principle to work with. In practice, we measured each shot for 10s, which leaves 113,600 windows. Considering that we perform this in a single-shot experiment, spin-locking allows us to effectively view the polarization for (113,600 windows)*(32μs/window)=3.64s, which is equivalent to (3.64s)*(75MHz) $\approx$ **273**

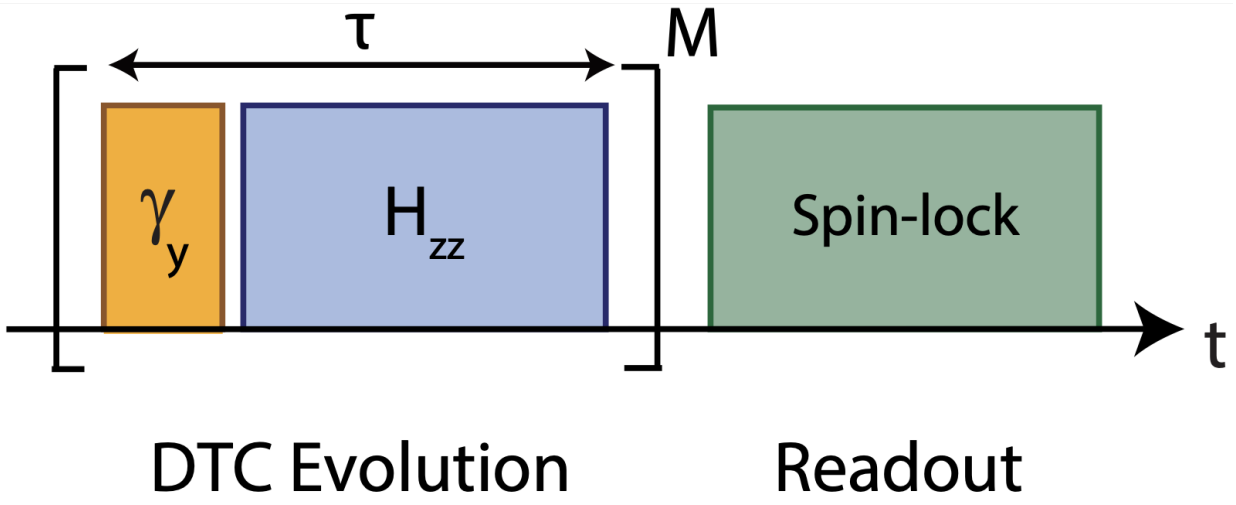

Figure 9.3 **Pulse sequence diagram of discrete time crystal experiment.** DTC evolution consists of periodic y-pulses on all spins with a flip angle of $\gamma = 0.96\pi$ and free evolution under the secular parts of the dipolar Hamiltonian, $\mathcal{H}_{zz}$. After M cycles, $< I_z >$ is readout via multiple-pulse spin-locking.

million precession cycles before the signal drops to 1/e. Spin-locking thus accelerates measurement throughput by more than three orders of magnitude compared to FID readout. In the following experiments and throughout this Chapter, we will utilize spin-locking measurement as a way to measure total spin polarization $< I_z >$. We truncate the initial transient (20ms) and then integrate the signal under the entire time-series to gain a reliable measure for $< I_z >$. Reliable implementation also requires calibrating the RF pulse for a $\frac{\pi}{2}$ flip angle, which we address next.

Rabi frequency – Global spin rotation flip angles were calibrated by stepping the initial pulse width (at constant RF power) from 0μs to 180μs, followed by multiple-pulse spin-lock readout. This experiment essentially shows the action of the initial pulse in moving the total spin polarization away from I_z, toward I_x and then all the way around the x-z plane of the Bloch sphere.

Figure 9.2 above shows one full period of the Rabi oscillation occurring after approximately 180μs. From the zero-crossing we can determine that a pulse width of 90μs corresponds to a flip angle of π, and a pulse width of 45μs corresponds to $\frac{\pi}{2}$.

9.3 Discrete Time Crystal (DTC)

Experimental implementation – The simplest construction of a DTC requires periodic driving and pairwise interactions among the system constituents. Dipolar interacting many-body spin systems driven by radiofrequency NMR pulses suffices for this construction. Initializing

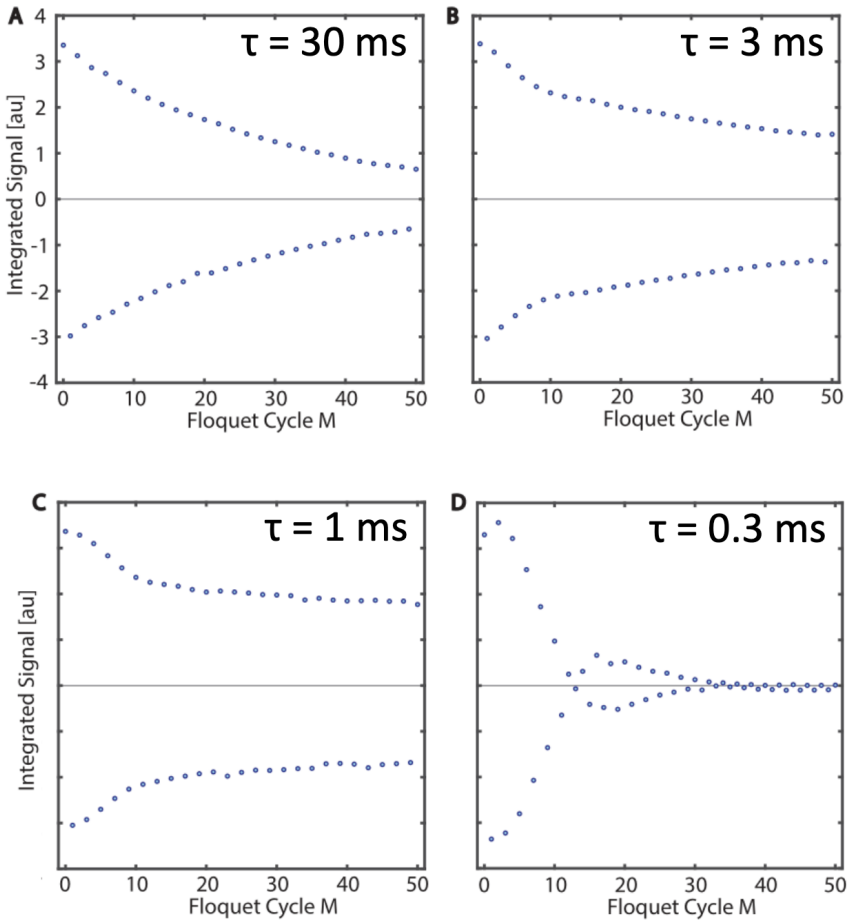

Figure 9.4 **DTC with different driving periods.** Experimental data showing DTC with traditional single-frequency driving after initializing the spins with a polarization along $< I_z >$. Each data point represents the integrated signal $< I_z >$, readout by multiple-pulse spin-locking after the application of M pulses with flip angle $\gamma = 0.96\pi$ and period τ =30ms, 3ms, 1ms, 0.3ms (A-D). For τ =30ms (A), the DTC response persists for less than 30 Floquet cycles before reaching 1/e signal decay. The optimal DTC lifetime is found for τ =1ms (C) where the system sees a quick decay during the first 10 Floquet cycles followed by a long plateau. When driving is faster than the typical dipolar coupling strength 1/T2*=1/(1.5ms), the effective dynamics become single-particle and a split beat pattern emerges, quickly destroying the DTC order (see (D), τ =0.3ms).

the system by optical hyperpolarization with a density operator

$$\rho = \frac{1}{2} I_0 + \epsilon I_z \tag{9.3}$$

where I_0 is the identity and polarization $\epsilon = 1\%$. Since the identity does not evolve in

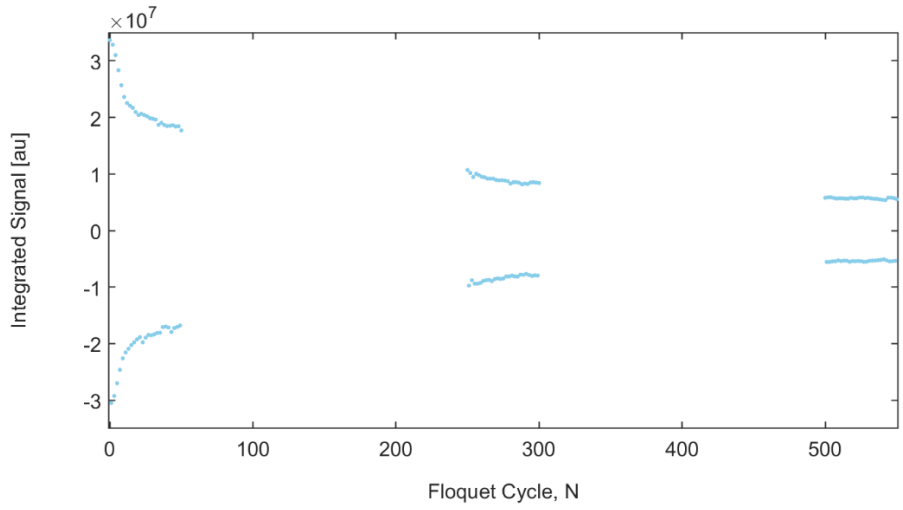

Figure 9.5 **Long-time DTC experiment with τ =1ms.** The first 50 Floquet cycles show the same data as in Figure 9.4C above. The measurements then skip ahead to the 250th Floquet cycle for 50 cycles, then again to the 500th Floquet cycle.

time, we simply consider the polarized component I_z.

According to the pulse sequence diagram shown in Figure 9.3, the DTC experiment takes place in M cycles of evolution which consist of an 'imperfect' π pulse (here with flip angle $\gamma = 0.96\pi$) followed by time for evolution under the secular dipolar interaction $\mathcal{H}_{zz}$. This experiment requires a single shot for every value of M, since the spin-locking measurement ultimately disrupts the polarization $< I_z >$.

Dependence on drive frequency – Since the flip angle γ is not exactly π, the spin polarization will not show period-doubling response in the absence of interactions. The single-particle case is illustrated in the experimental data shown in Figure 9.4D below. With the interaction time $\tau < T_2^*$ not enough for dipolar evolution to take place between pulses, the pulse errors build on one another and ultimately form a beat pattern. As one can see in Figure 9.4A-C, the system shows a longer-lasting period-doubling response when the interaction time $\tau > T_2^*$ is long enough for dipolar evolution to significantly act on the system. Increasing the drive period beyond 1ms, we see that slower relaxation process eventually cause the period-doubling to decay more quickly. We see an optimal drive period at $\tau = 1ms$, with Figure 9.4C showing an initial decay followed by a long plateau.

Long lifetime of DTC with optimal drive frequency – Since each data point requires a single shot experiment, I skipped ahead hundreds of cycles to get a view into the long-time DTC behavior of the ^{13}C system. From the 50th to the 300th cycle, the polarization signal drops by about 50%, and the same drop occurs from the 300th to the 550th cycle.

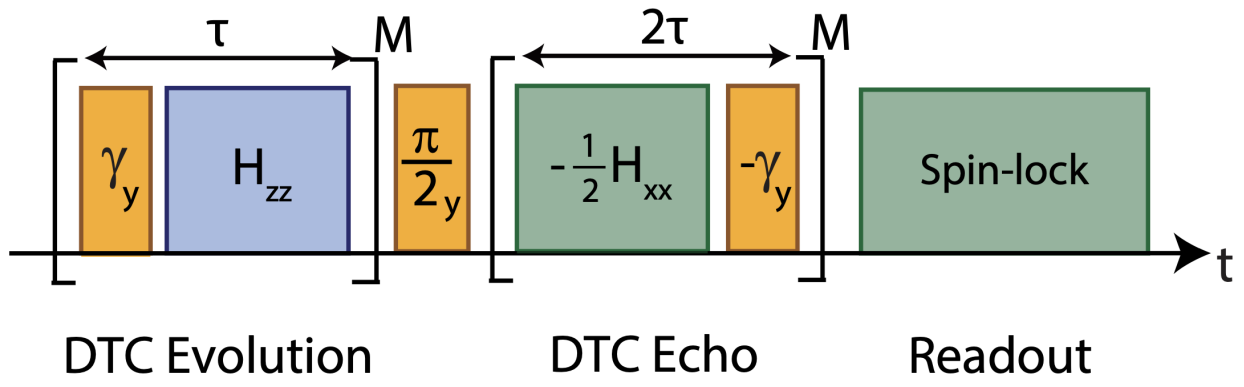

Figure 9.6 **Pulse sequence diagram for DTC Echo experiment.** After application of M cycles of DTC evolution, the polarization is brought into the transverse plane by a $\frac{\pi}{2}$-pulse along I_y. Then, the coherent forward evolution is un-done by applying M cycles of reverse evolution. Note that the negation of the dipolar Hamiltonian in the rotating frame is accomplished by continuous-wave spin-locking along I_x.

Qualitatively, this means that the long-time decay of the plateau follows an approximately exponential decay envelope with a half-life of 250 cycles.

9.4 DTC Echo

Experimental implementation – Echoing out the coherent DTC evolution requires us to re-create the inverse of the unitary representing one cycle of forward evolution. The first part, a global y-pulse with angle γ, is inverted by negating the flip angle (or equivalently negating the phase from y to -y). The second part involves dipolar evolution, and so we must employ the magic echo. As explained in the Introduction section above, we re-quantize the spin system along the x-axis with a $\frac{\pi}{2}$ y-pulse and continuous-wave spin-lock along x-axis. The spin-lock generates the Hamiltonian $-\frac{1}{2}\mathcal{H}_{xx}$, which we apply for 2τ, twice as long as the forward evolution cycle. Additionally, a frame transformation with respect to the $\frac{\pi}{2}$ y-pulse transforms $\mathcal{H}_{xx}$ to $\mathcal{H}_{yy}$. Note that this particular protocol was first employed in solid-state NMR experiments by Rovny et al. in 2018 (see ref. [136]) and then repeated on superconducting qubits by Mi et al. in 2022 (see ref. [113]).

Results – After performing the experiment for some number of forward and backward evolution cycles and measuring the polarization each time by spin-lock readout, we are left with a time series. This data represents the 'leftover' polarization after 3τ of evolution. If the coherent evolution is perfectly re-focused, then the resulting decay is a result of dissipation to the environment. Since we want to look at what happened during each of the first 50 cycles, we take the cube root of the time series, giving us the auto-correlation showing the system coherence.

Sources of error – The main error in the DTC Echo experiment arises from the fact that the backward evolution is not perfectly implemented. That is, the continuous-wave spin-lock does not apply $-\frac{1}{2}\mathcal{H}_{xx}$ exactly. If the transmitted spin-lock is strong enough, this will be a good first-order approximation. However, there are still higher-order terms in the average Hamiltonian that may cause coherent loss of polarization. Related, the assumption that the autocorrelation in Figure 9.7 represents only dissipation to the environment does not necessarily hold. Since the cube root step relied on this assumption, there may be additional effects contributing to the decay.

9.5 DTC Mixing

Experimental implementation – Now that we have demonstrated a Loschmidt echo of the DTC experiment, a logical next step is to intentionally perturb the system between forward and backward evolution periods. It may be interesting to investigate the action of global pulses in this place, but here we decided to take advantage of the dipolar dephasing that occurs during the system's free induction decay. The FID time of 1.5ms indicates how long it takes for dipolar evolution to reduce the observable polarization to 1/e of its starting value. For this perturbation, we chose a 1ms decay time during which we know the spin states are coherently scrambled.

Preliminary results – Figure 9.9 shows the results from this first experiment. The same procedure of extracting the time-series and autocorrelation was followed as in the Figure 9.7 Loschmidt DTC Echo data. Qualitatively, the initial smooth decay seen in the first 10 cycles (more noticeable in Figure 9.5 but also visible in Figure 9.7) is not present here. The autocorrelation decays to 0.71 in the 50 cycles shown here. We notice this is slightly more decayed than the DTC Echo data, which only fell to 0.75 after 50 cycles.

Interpretation – The number of Floquet cycles in Figure 9.9 represents the mixing time observed for the perturbed system, showing the effect of the 1ms decay throughout the time crystal's evolution. The extracted autocorrelation thus represents the effect of the perturbation spreading throughout the course of the experiment (in addition to the effects of environmental dissipation and imperfect echos). The fact that the correlation remains almost as strong in the DTC Mixing experiment (0.71) as it is in DTC Echo experiment (0.75) after 50 cycles shows that the extra perturbation only minimally added to the decay of polarization. Since the action of the perturbation is to scramble the system's many-body spin state (under dipolar evolution), we can interpret the DTC behavior as relatively state-independent. That is, the polarization trajectory remains unchanged when the system state is scrambled. We can investigate further by repeating the experiment for different perturbation strengths (by varying the perturbation decay time) and comparing the resulting decay rates of the autocorrelation.

9.6 Conclusions

In this experimental study, we investigated the many-body dynamics of a large spin system. Hyperpolarization and spin-locking measurement readout allow us to access the global polarization quickly and accurately as our main observable. NMR control pulses periodically drive the system with intermittent periods of interaction. Discrete time crystalline behavior is demonstrated when the global polarization shows persistent period-doubling. We then implemented a DTC Echo experiment through symmetries in the secular dipolar Hamiltonian accessible by a hard spin-lock drive. The observed revival of polarization indicates successful refocusing of coherent evolution, even if not perfect.

We showed a preliminary study in which the spin states were scrambled under the dipolar Hamiltonian between forward and backward DTC evolution. The results show that the polarization is remarkably stable under this perturbation, suggesting that the DTC behavior is independent of spin state. The next experiments may include different types of perturbations. The main limitation in this system is the lack of local control or measurement – for both transmitting pulses and receiving signal, we only have global access.

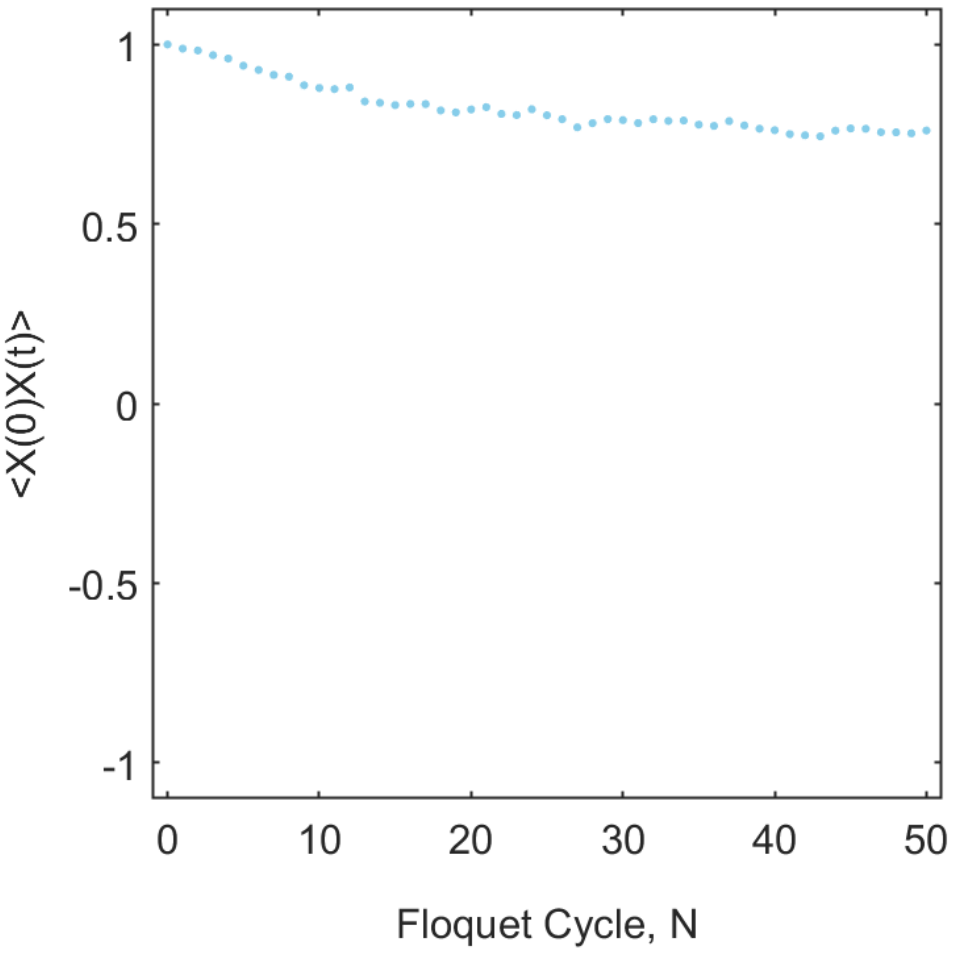

Figure 9.7 **Extracted autocorrelation of coherent polarization dynamics.** Each data point represents an experiment with N cycles of forward DTC evolution followed by exactly N cycles of reverse DTC echo. The signal was readout by spin-locking, and the autocorrelation extracted by normalizing to N=0 and then taking the cube root of the time series.

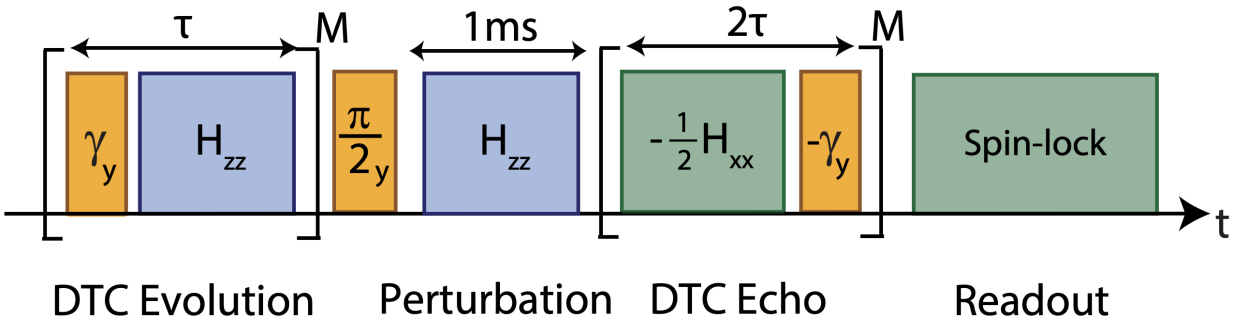

Figure 9.8 **Pulse sequence diagram of the DTC Mixing experiment.** The spin state is perturbed between the forward and reverse evolution sections of the DTC Echo experiment. This is accomplished by adding a delay of 1ms during which the spins undergo dipolar dephasing, similar to the free induction decay.

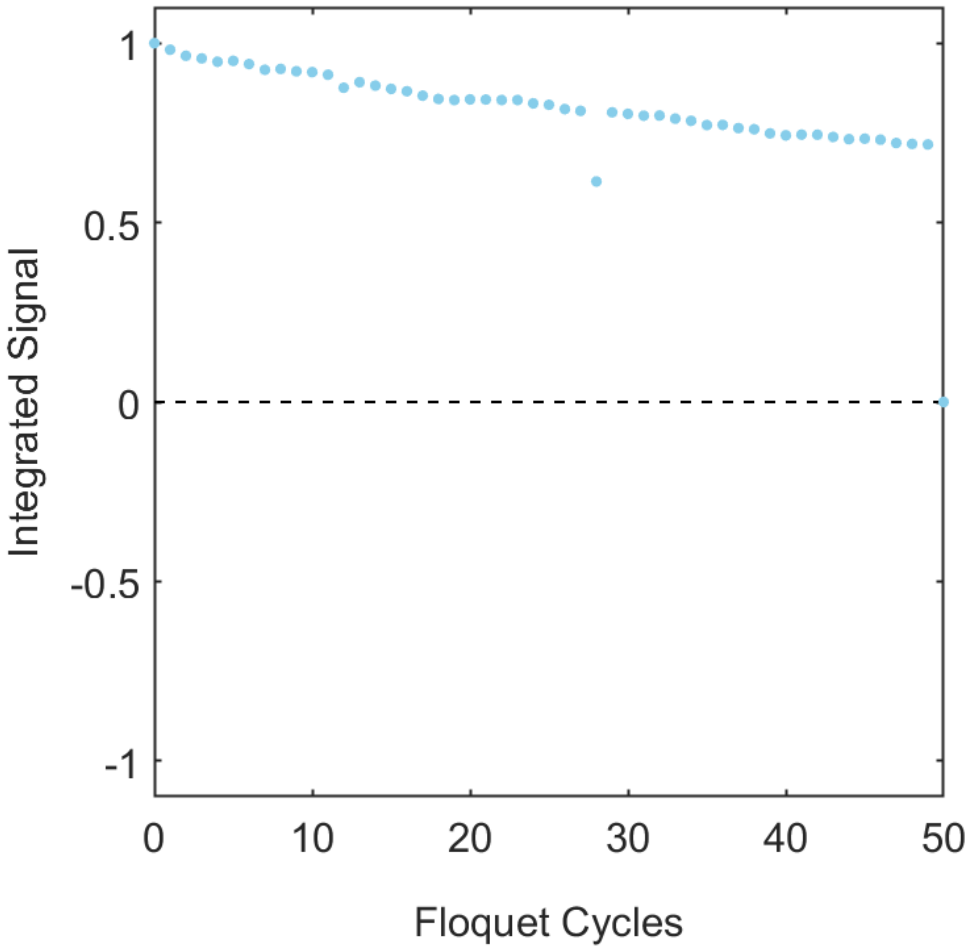

Figure 9.9 **Preliminary results for DTC mixing.** A perturbation of 1ms decay under dipolar interactions was inserted between the forward and reverse evolution sections of the DTC echo experiment.

Part IV

Bulk Transport of Hyperpolarization

Chapter 10

Toward Nanoscale Imaging

In Chapter 11 we employ relaxometry to try to answer an engineering question relevant to the fields of quantum information science and dynamic nuclear polarization (DNP). The study primarily focuses on how electronic spins, characterized by their rapid relaxation rates, influence the relaxation processes of nearby nuclear spins. The spin diffusion barrier has been identified as a central engineering challenge for generating bulk levels of nuclear spin hyperpolarization from a central paramagnetic spin species.

We are able to directly observe the slow evolution of the polarization through the nuclear spin bath using the multiple-pulse spin-lock protocol described in previous sections. This allows for high-resolution monitoring of nuclear magnetization and reveals that the ensemble-averaged nuclear lifetimes increase with the duration of hyperpolarization, thus indicating the significant role of electronic spins in nuclear spin relaxation. Surprisingly, the study finds that nuclear spin relaxation can actually be modulated by adjusting the polarization time, a feature that appears surprising at face value.

However, numerical simulations show that spin diffusion can account for this observation. During hyperpolarization, spin diffusion allows the polarization to build up further from the NV centers, which ultimately increases the nuclear spin lifetime at the beginning of the NMR experiment. This finding highlights the nuanced role of electronic spins in influencing nuclear spin dynamics.

In Chapter 12 we extend this result to create non-trivial spin textures using both dissipation and coherent control. The sign of the nuclear spin hyperpolarization generated during the experiment can be change on-demand. Thus as positive polarization is diffusing outward, a small "shell" of negative polarization can be quickly injected before starting the NMR experiment. Additionally, by tuning the pulsed spin-lock sequence near the sensitive flip angle of π, we select a specific "shell" of spins around the NV center with high spatial accuracy. Thus we demonstrate control over the initial state as well as the equation of motion in the nanoscale system to generate interesting spin textures.

Chapter 11

Electron Induced Nanoscale Nuclear Spin Relaxation Probed by Hyperpolarization Injection

11.1 Introduction

Coupled electron-nuclear spin systems are highly relevant in quantum information science [126, 94, 44] and dynamic nuclear polarization (DNP) [12]. Consider an electronic spin centrally located (position r=0) in a bath of nuclear spins within a magnetic field B_0 (see Figure 11.1A-B). The electrons are fast-relaxing (short T_{1e}), and can serve as a relaxation source for the nuclear spins [168, 33, 34] (schematically shown in Figure 11.1C). Such electron induced nuclear relaxation is an important consideration for applications in quantum registers, memories, and sensors constructed out of nuclear spins [62, 129, 116]. It also plays a key role in determining rates of polarization transfer in DNP [148, 145, 147]. However, probing such relaxation influences, particularly in a spatially defined manner, is challenging. This is because experiments typically have very restricted access to spins in the bath, limiting the possibility of spatially distinguishing them [34, 157, 69, 154, 127]. Previous nanoscale quantum sensing experiments have, for instance, been limited to proximal central spin relaxation effects in small (<20) spin networks [46, 11].

In this Chapter, we report on experiments that study the effects of an electronic spin on nuclei over wider length scales, spanning several nanometers and involving several hundred nuclei. Our strategy (Figure 11.1D) exploits controllable hyperpolarized spin injection from the electron to the nuclear bath. The hyperpolarization time τ is employed as a knob to tune length scales in the bath being probed; the polarization is carried over longer distances with increasing τ. Simultaneously, the nuclei are subject to a RF driving protocol that permits continuously tracking their magnetization over minute long periods with high signal-to-noise (SNR) [142]. The measurements reveal, surprisingly, that ensemble-averaged nuclear lifetimes T_2' in the rotating frame increase dramatically with increasing polarization time τ.

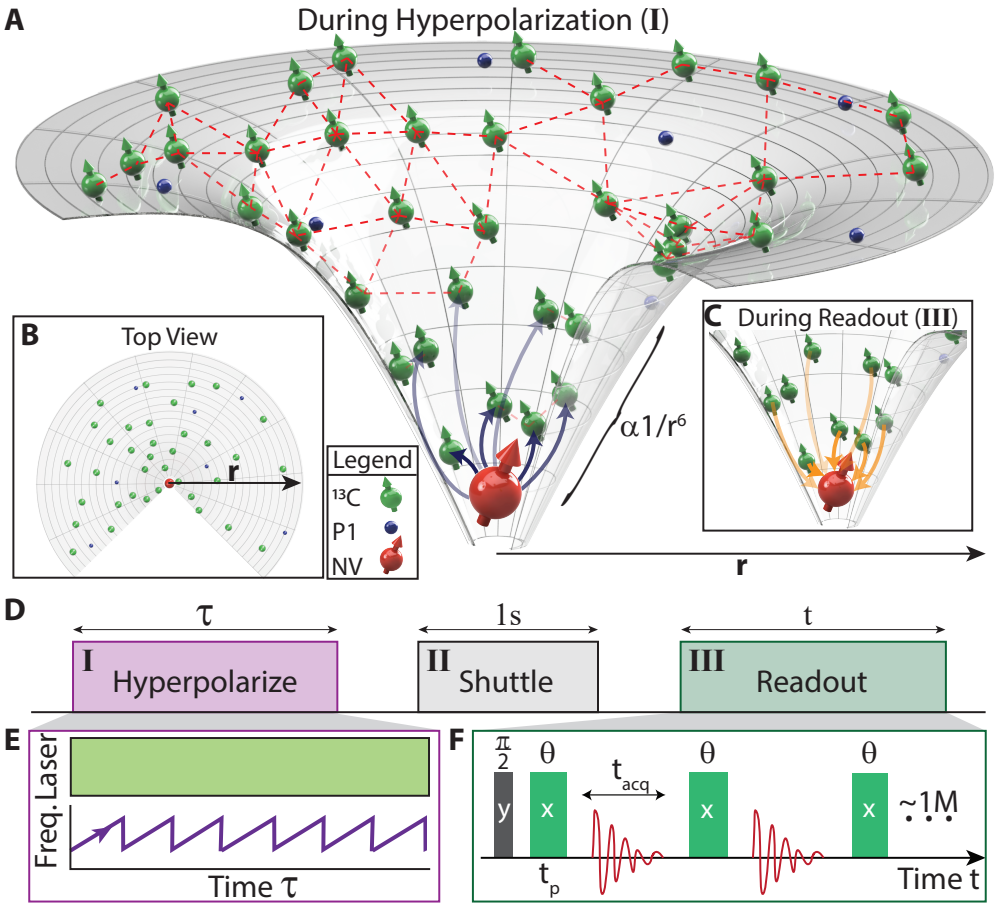

Figure 11.1 **System and protocol.** (A-C) *System* consists of central NV electron (red), and ^{13}C nuclei (green) and P1 centers (blue) at distance r. Dashed lines are inter-nuclear dipolar couplings. Profile denotes $1/r^6$ NV-mediated relaxation effect. (A,C) NV acts as polarization source and relaxation sink respectively, during different experimental regimes. (D) *Experiment schematic:* **(I)** NV$\rightarrow^{13}$C hyperpolarization for period τ at 36mT, **(II)** transport to high field and **(III)** ^{13}C readout for time t at 7T. (E) *Hyperpolarization* (**I**) involves MW chirps [22, 16]. (F) *Measurement* (**III**) comprises a train of spin-locking θ-pulses with interrogation in $t_{\rm acq}$ inter-pulse intervals [30]. *Note*: Time τ describes hyperpolarization time and time t describes readout time.

This constitutes a direct experimental signature of electron induced nuclear spin relaxation, allowing us to quantify its influence over several nanometers.

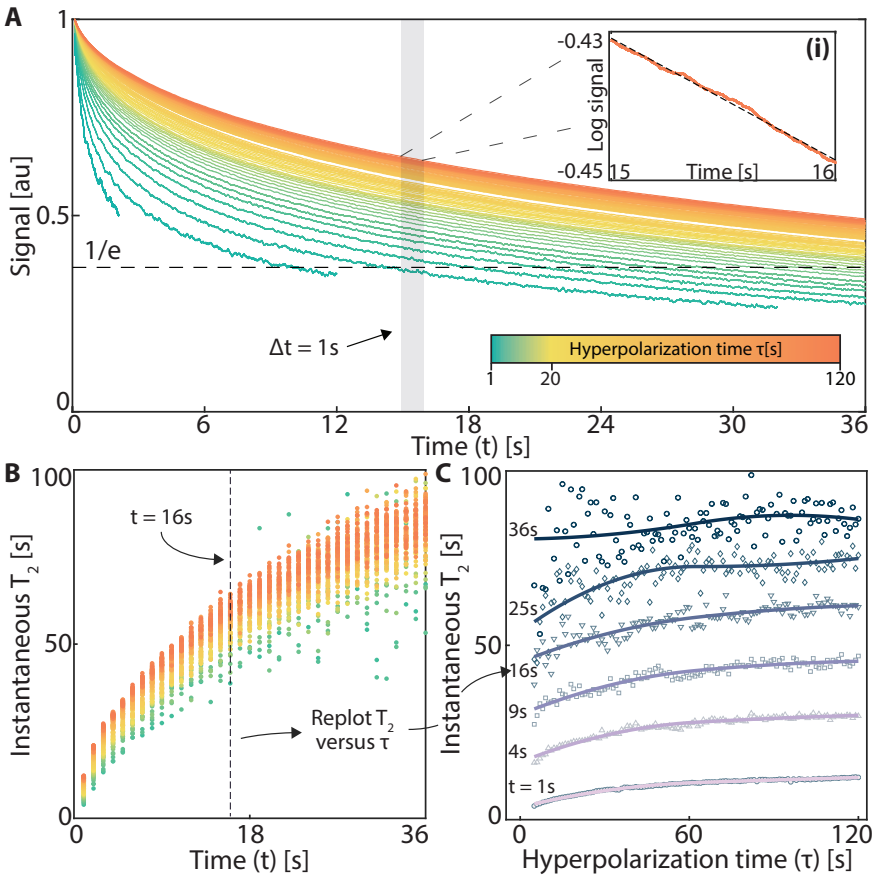

Figure 11.2 **Effect of increasing hyperpolarization time τ.** (A) *Spin-lock decays* for different hyperpolarization times τ corresponding to colorbar (regime **I** in Figure 11.1D). Single-shot data (obtained with t_{acq}=32μs and $\theta\approx\pi/2$ in Figure 11.1F) is boxcar averaged over 97ms, and normalized after truncation at t=9.7ms. Dashed line represents $1/e$ intercept. *Inset (i):* Zoom into representative 1s segment (gray window in (A)). Dashed line is a fitted piecewise monoexponential. (B) *Instantaneous lifetime* T_2 measured along decay curve, extracted from slopes as in A(i). Color bar (see (A)) represents τ. Dashed line shows exemplary segment ending at 16s (gray window in (A)). (C) *Instantaneous* T_2 plotted against τ. Points show T_2 lifetimes from (B) for exemplary 1s segments ending at labeled t values. Lines are spline fits.

11.2 System and Protocol

Experiments are carried out in diamond, with central NV [77, 109] electronic spins surrounded by ^{13}C nuclei (Figure 11.1A-B). NV centers (≈1ppm) are separated by ≈12nm and ^{13}C nuclei appear with lattice density ≈0.92 spins/nm^3, yielding a relative NV:^{13}C ratio ∼1:10^4 [17, 160]. In addition, the lattice hosts randomly positioned paramagnetic impurities

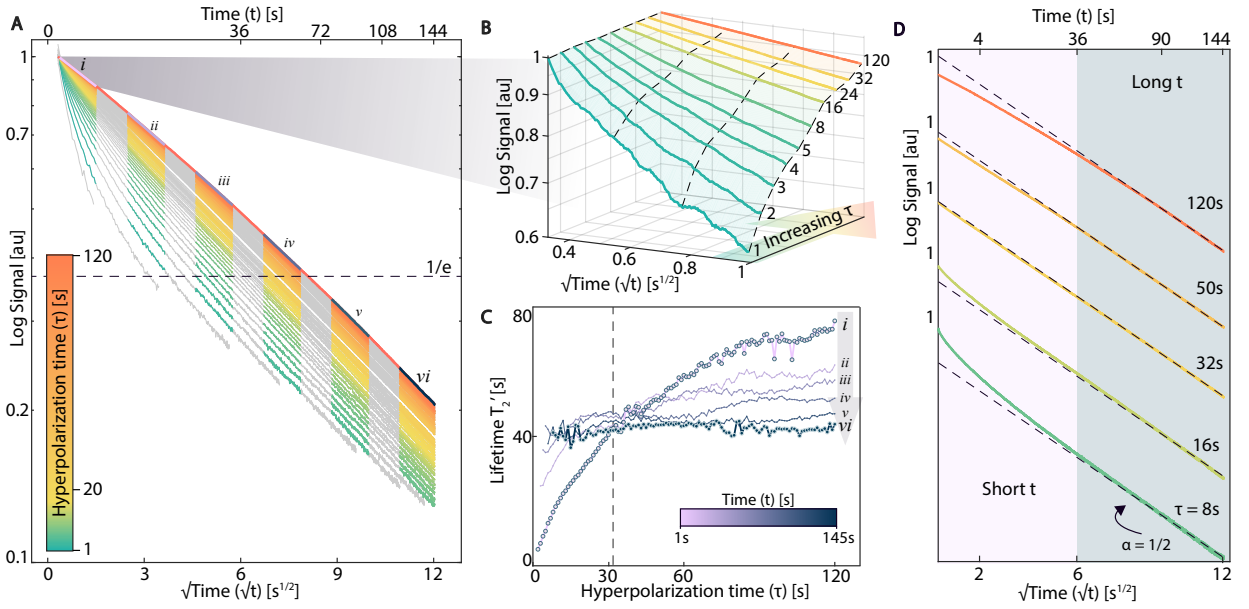

Figure 11.3 **Quantifying instantaneous decay rates.** (A) *Full data* in Figure 11.2 plotted on a log scale with respect to $\sqrt{t}$ for different τ (color bar). Traces extending to t=144s have $\sim 10^6$ points. Upper axis shows time t. Six equally sized (in $\sqrt{t}$) segments (labeled *(i)*-*(vi)*) are selected. (B) *Zoom into segment (i)* (sampled every ≈5ms) for representative marked τ values (same colorbar as (A)). Dashed lines are at equally spaced $\sqrt{t}$ values to guide the eye. (C) *Extracted time constants* T_2' from slopes of the corresponding segments in (A). Segment *(i)* shows a steep increase in T_2' with τ; subsequent segments show progressively flatter profiles (gray arrow). Crossover of early and late segments occurs at $\tau \approx 32$s (dashed line). (D) *Variations in short and long time decay* behavior with τ. At long t, decay closely follows α=1/2 (dashed lines, extracted from segment *(vi)*), while short times t show a transition from convex to concave behavior at $\tau \approx 32s$ (similar to Figure 11.3C). Upper axis represents time t.

(P1 centers) at a concentration >20ppm, which can also serve as relaxation sources.

Experiments are conducted in three regimes (indicated in Figure 11.1D): **(I)** optically induced NV→^{13}C spin injection for period τ at low-field (B_{pol}=36mT), **(II)** rapid transport to high field, and **(III)** ^{13}C interrogation for time t at B_0=7T. For hyperpolarization (Figure 11.1E), we exploit a mechanism previously described in Refs. [22, 16, 23]. Distant spins are polarized by spin diffusion driven by the internuclear dipolar Hamiltonian [127, 80, 71], $\mathcal{H}_{\text{dd}} = \sum_{j<k} d_{jk}^{\text{CC}}(3I_{jz}I_{kz} - \vec{I_j}\cdot\vec{I_k})$, where I_j refer to j^{th} spin-1/2 operators, and coupling strengths $d_{jk}^{\text{CC}} \propto \gamma_n^2/r^3$, with magnetogyric ratio γ_n=10.7MHz/T, and r being the inter-nuclear distance. Bulk averaged ^{13}C hyperpolarization under maximal conditions is $\varepsilon \approx 0.3\%$.

Sample transport (regime **II**) occurs in $t_s \approx 1\text{s} \ll T_{1n}$, adiabatic with respect to the instantaneous ^{13}C Larmor frequency, thereby preserving hyperpolarization [19]. Conversely,

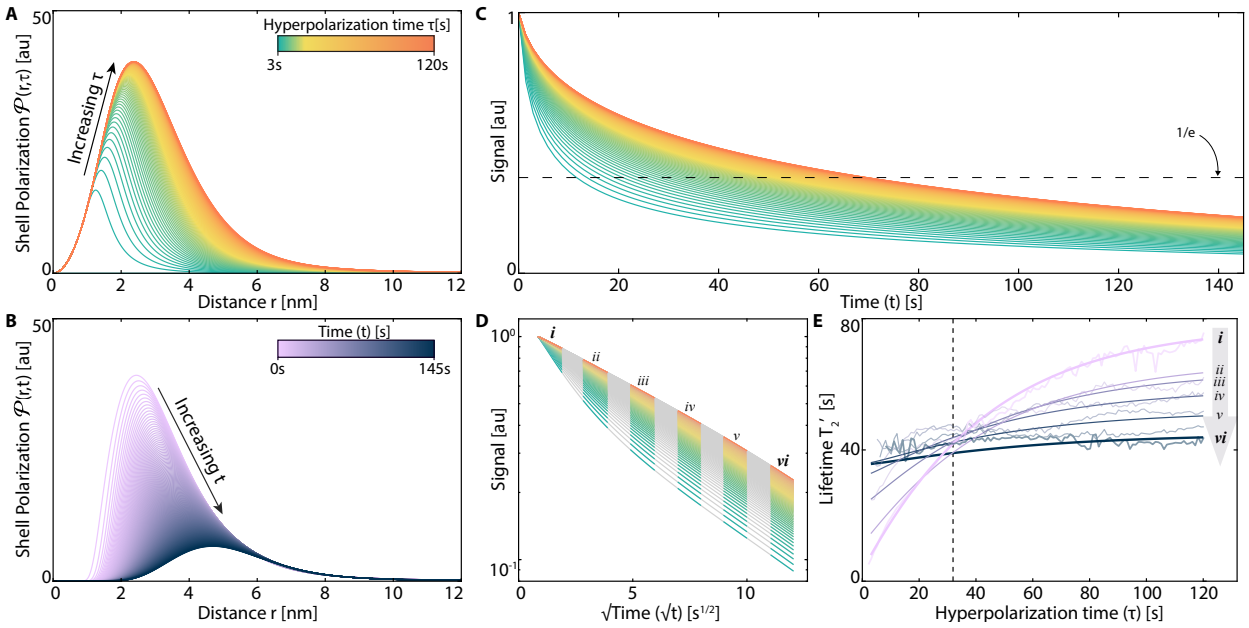

Figure 11.4 **Simulations of polarization evolution in time and space.** (A) *Spatial polarization build-up* with τ (colorbar) plotting polarization $\mathcal{P}(r,\tau)$ in a shell at distance r from the central NV center (during regime **I** in Figure 11.1D). (B) *Polarization distribution during readout* period t (colorbar) in regime **III** of Figure 11.1D. Here, we set the initial condition to be the τ=120s polarization distribution in panel (A). (C) *Simulated NMR signals* following panels (A-B) for different hyperpolarization times τ similar to Figure 11.2A. Data reveals T_2' increase with τ, in agreement with the experimental data in Figure 11.2 (see (A) for colorbar). (D) *Stretched exponential decay dynamics.* Analogous to Figure 11.3A, data from (C) is plotted on a logarithmic scale with respect to $\sqrt{t}$. Stretched exponential behavior qualitatively matches data in Figure 11.3A. Segments labeled *(i)-(vi)* are used to extract T_2' decay constants. (E) *Extracted T_2' decay constants* for representative segments *(i)-(vi)* show qualitative agreement with Figure 11.3C. Here, dark lines are simulation and light lines are experimental data. Dashed line marks crossover at $\tau\sim$32s.

since $t_s \gg T_{1e}\sim$1ms [124, 75], the NV center rapidly loses hyperpolarization and ultimately returns to thermal levels ($\approx$3%) in regime **III** (Figure 11.1F). Subsequently, the NV center predominantly serves as a point relaxation source for the nuclear bath (Figure 11.1C).

Ensemble ^{13}C readout (regime **III**) employs a protocol described in Refs. [18, 30]. ^{13}C spins are prepared along the transverse axis $\hat{\mathbf{x}}$ ($\rho_I = \varepsilon \sum_j I_{jx}$) on the Bloch sphere, and a train of spin-locking θ-pulses are applied [133, 134]. ^{13}C nuclei are interrogated between pulses, allowing continuous tracking with high SNR [27]. Signal obtained corresponds to measuring the survival probability in the $\hat{\mathbf{x}}$-$\hat{\mathbf{y}}$ plane. The sequence operation can be described by the unitary $U(t)$. For sufficiently rapid pulsing duty cycle, $U(t) \approx \exp(i\mathcal{H}_F^{(0)} t)$, such that the inter-nuclear Hamiltonian is engineered to leading order in the Magnus expansion to

$\mathcal{H}_F^{(0)} \approx \sum_{j<k} d_{jk}^{CC} \left(\frac{3}{2}\mathcal{H}_{ff} - \vec{I}_j \cdot \vec{I}_k \right)$, where $\mathcal{H}_{ff}=I_{jz}I_{kz} + I_{jy}I_{ky}$ is a flip-flop Hamiltonian [30]. Since $[\rho_I,\mathcal{H}_F^{(0)}]=0$ commutes with the initial state, dipolar evolution is suppressed to leading order. As a result, ^{13}C free induction decay lifetimes $T_2^* \sim 1.5$ms are significantly extended, here to $T_2' \gtrsim 65.5$s (see Figure 11.2A).

11.3 Results

Figure 11.2A describes our primary experimental result (see movie [5]), showing ^{13}C NMR signal measured employing differing hyperpolarization periods τ (varied every one second from τ=1s to τ=120s). Each 36s trace consists of $\sim$369,000 pulses (see Figure 11.3 for full data), and the ^{13}C nuclei are interrogated after every pulse (Figure 11.1F). Surprisingly, we observe that the signals decay *more slowly* with increasing τ. Normalization of the signal profiles allows the ability to unravel the *relative* changes in the decay time constant T_2', estimated from the $1/e$ intercept (horizontal dashed line in Figure 11.2A). For example, comparing τ=2s and τ=120s in Figure 11.2A, we observe a $\approx$6.42-fold increase in T_2' (from 10.2s to 65.5s).

The $1/e$-intercept is blind to the instantaneous change of the decay profile and therefore provides only limited information. To more clearly observe the decay dynamics, we divide the curves in Figure 11.2A into 36 segments of width Δt=1s, with one such segment shown in the gray window in Figure 11.2A. We fit the decay in each segment to a monoexponential (as in inset (i)) and extract the *instantaneous* time constants $T_2(t)$, which are plotted in Figure 11.2B. The notation T_2 (as opposed to T_2') emphasizes that these are monoexponential constants. For each trace, the signals decay markedly slower with increasing time t (see also Figure 11.3). Ultimately, the T_2 times are remarkably long ($T_2 \approx$100s) at large τ. Increasing polarization time τ makes the overall decay slower for any selected segment. Indeed, for the segment ending at t=16s (vertical dashed line in Figure 11.2B), the T_2 value is increased by 1.66-fold. To now emphasize the relative change in the T_2 values for different segments, Figure 11.2C shows the T_2 lifetimes plotted against τ, where data corresponding to each segment in Figure 11.2A-B forms the lines. Figure 11.2C makes clear that the instantaneous T_2 increases for each segment with increasing t and within each segment with increasing τ. The maximum relative change occurs for short τ and at early t.

A clearer view of data in Figure 11.2 can be obtained by noting that the decays approximately follow a stretched exponential of the form $\exp\left[-(t/T_2')^{\alpha}\right]$ with $\alpha \approx 1/2$ (see Figure 11.3 and movies [6, 7]). While similar behavior has been alluded to before [101, 64, 66], high SNR and rapid data collection here allows an unprecedentedly clear view. Figure 11.3A shows data from Figure 11.2 plotted on a logarithmic scale with respect to $\sqrt{t}$. The signals then manifest as approximately straight lines, demonstrating stretched exponential character. T_2' lifetimes can now be extracted conveniently from the instantaneous slopes s, as $T_2'=1/s^2$. High SNR and rapid data collection rates allow the unique ability to continuously observe the stretched exponential dynamics. We now focus attention to six segments along the decay

curves (labeled *(i)-(vi)* in Figure 11.3A). Data reveals that the decay in segment i deviates from the stretched exponential behavior (especially for low hyperpolarization time τ), as evidenced by the nonlinear traces in the log vs $\sqrt{t}$ representation. In contrast, the traces at long time t are observed to be independent of τ (evident from the approximately parallel profiles in segment *(vi)*). To elucidate this further, segment *(i)* is zoomed in Figure 11.3B on the same log scale for representative values of τ. The panel makes clear the apparent change in T_2' with τ (due to deviation from stretched exponential decay at short t and τ).

Figure 11.3C shows extracted T_2' values for six segments ($i-vi$). $T_2'^{(i)}$ apparently grows significantly with increasing time τ, while $T_2'^{(vi)}$ is flat and almost independent of τ. Additionally, the extracted T_2' values for the different segments cross over at $\tau\approx$32s. Finally, Figure 11.3D offers insight into variation from exact α=1/2 stretched exponential behavior with changing τ. At long times t, the behavior follows a *universal* α=1/2 dependence (dashed lines). However, in the short time region ($t\lesssim$36s), there is a transition from convex to concave behavior around α=1/2. Cross-over occurs at $\tau\approx$32s, similar to Figure 11.3C.

11.4 Theory

To describe the experimental observations, we construct a semi-quantitative model for nuclear polarization $p(r,t)$ at coordinate r and time t. We assume centrosymmetry, a good approximation given the ensemble average in our experiments. We then model the dynamics using the differential equation,

$$\frac{\partial}{\partial t}p(r,t) = \frac{P_0}{r^6} - \frac{\kappa_0}{r^6}p(r,t) - \frac{1}{T_1}p(r,t) + D\nabla^2 p(r,t) \tag{11.1}$$

following the Bloembergen model in non-conducting solids [32]. Here P_0 denotes the rate of hyperpolarization injection and κ_0 is the strength of spatially dependent relaxation due to the central NV center. The $1/r^6$ scaling of the P_0 term in Eq. 11.1 does not yield qualitatively different behavior compared to a $1/r^3$ scaling but makes the equation better conditioned near r=0. In any case, the $r\to$0 region and associated frozen core is not observable due to the relatively small ^{13}C detection bandwidth ($\approx$32kHz) employed. In contrast to the NV center (at r=0), we assume that the relatively dense P1 centers serve as contributors to *background* relaxation of the ^{13}C nuclei independent of their position; this is captured by the T_1 term in Eq. 11.1. Finally, the last term denotes spin diffusion which we assume to be Fickian and Gaussian with a single constant D at all locations. This is a good approximation given the large number of ^{13}C nuclei around every NV center [127]; e.g. a sphere of radius 4nm contains $\approx$247 nuclear spins.

We solve Eq. 11.1 separately in the three regimes of the experiment (Figure 11.1D), with the solution for one regime setting the initial conditions for the next. Obtaining a precise estimate of the parameters in Eq. 11.1 is challenging and outside the scope of this Chapter. We therefore make some simplifying assumptions. In regime **I**, we assume P_0/κ_0=1. D in regimes **I** and **III** are assumed to differ by a factor of 2. We employ T_1=$q^{-1}T_{1,\mathrm{LF}}$

and T_1=$q^{-1}T_{1,\mathrm{HF}}$ in regime **I** and **III** respectively, where $T_{1,\mathrm{LF}}$=283s and $T_{1,\mathrm{HF}}$=1520s are measured low and high-field bulk ^{13}C lifetimes at τ=60s [27], and q is a scaling factor employed as a free parameter in the fits. For Figure 11.4, we find good agreement with q=6.75. The latter assumption can be rationalized by the fact that (1) contributions from P1 centers to T_1 relaxation are hard to separate in the bulk T_1 measurements; (2) we measure longitudinal $T_{1,\mathrm{HF}}$ which only approximates transverse T_1 in Eq. 11.1; and (3) $T_{1,\mathrm{LF}}$ is measured under dark conditions, but the corresponding T_1 in regime **I** is measured under optical illumination.

With these assumptions, Figure 11.4A-B shows the simulated system dynamics, where we plot the polarization contained in a shell at radius r, $\mathcal{P}$=$4\pi r^2 p$. Figure 11.4A first shows $\mathcal{P}(r,\tau)$ with increasing hyperpolarization time τ in regime **I**, assuming a 1s shuttling period in regime **II**. Simulation parameters are set to obtain good qualitative agreement with experiment (here D=0.0135nm^2/s and P_0=6.75s^{-1}). With increasing τ, spin diffusion leads to a spread of polarization; this is evidenced by the movement of the "centroid" of $\mathcal{P}(r,\tau)$ with increasing τ towards greater r in Figure 11.4A. Notably however, replenishment of polarization from the NV in regime **I** makes $\mathcal{P}(r,\tau)$ skew towards the left. In a complementary manner, Figure 11.4B elucidates $\mathcal{P}(r,t)$ during regime **III**, starting with the τ=120s distribution in Figure 11.4A. The strong relaxing effect of the NV center yields the polarization "hole" close to r=0, and manifests as the steep wall of growing polarization in Figure 11.4B. Additionally, the centroid of $\mathcal{P}(r,t)$ moves towards larger r and homogenizes as t increases; the shift with r is greater here because there is no polarization replenishment and relaxation is slower for larger r.

Figure 11.4C displays the net polarization $\int\mathcal{P}(r,t)dr$ during the readout period (from trajectories as in Figure 11.4B), but for varying τ. Normalizing the traces shows that relaxation is slower with increasing τ, matching experiments in Figure 11.2A. This arises because the shifting centroid of $\mathcal{P}$ makes electron mediated relaxation less effective. Interestingly, we find that the decays in Figure 11.4C also follow an α=1/2 stretched exponential. This is shown by again plotting the data on a log vs $\sqrt{t}$ scale in Figure 11.4D, where we observe a behavior similar to experiments in Figure 11.3A. We hypothesize that the stretched exponential decay at long times t results from the relatively flat distribution of polarization across shells. However, we again see a deviation from stretched exponential decay at short times t and τ (also observed experimentally). We attribute this early time behavior to relaxation from NV centers: the deviation is larger at low t and τ when the polarization is localized near the NV centers than at long t and τ when the centroid of $\mathcal{P}$ is further from the NVs (verified by distributions in Figure 11.4A-B). The emergence of a stretched exponential distribution from a large sum of individually monoexponential decays is verified numerically.

As shown in experiments in Figure 11.3, the relaxation profile is independent of τ at long readout periods t (evidenced by the approximately parallel traces in segment *(vi)* of Figure 11.4D); Figure 11.4B allows us to verify that this is indeed because the polarization has spread far from the NV center and the decay is instead predominantly due to background $1/T_1$ relaxation. Indeed, as shown in Figure 11.4E, upon taking segments *(i)-(vi)* along the decay curves in Figure 11.4D and extracting their T_2' values, we observe a progressive

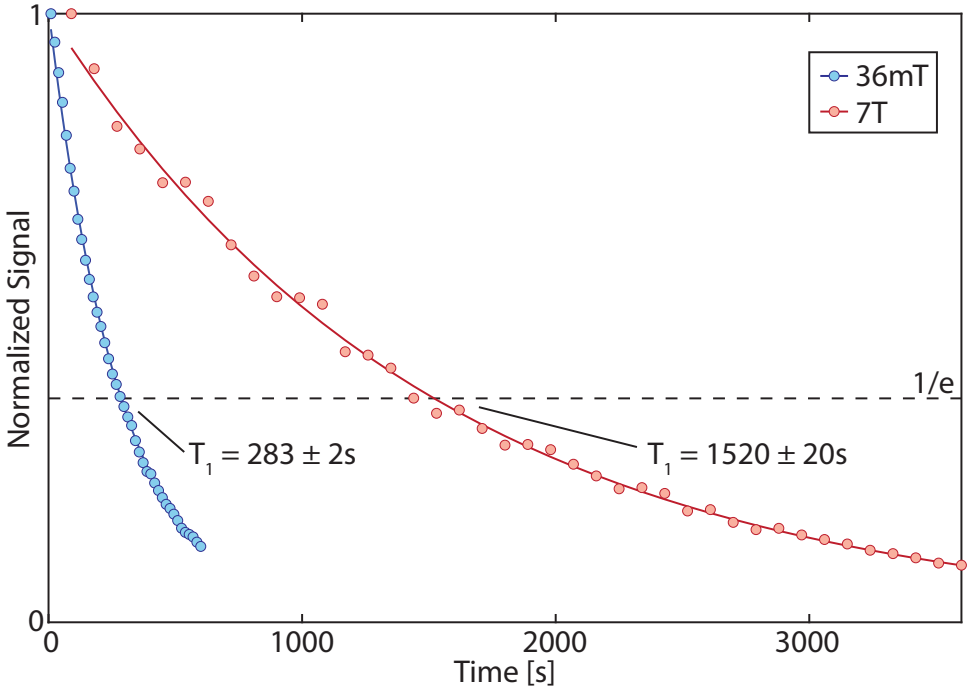

Figure 11.5 T_1 **measurements.** *Sample* T_1 at low-field (36mT, blue) and high-field (7T, red) at τ=60s. Points are data and solid lines are monoexponential fits. Dashed line denotes $1/e$, and intersections give a low-field T_1 of 283±2s and a high field T_1 of 1520s±20s.

flattening of the T_2' values with increasing τ, agreeing with experimental data in Figure 11.3C (overlapped here).

11.5 Outlook

Figure 11.4 suggests that spin-lock control enables the ability to peer into nuclear polarization localized at different positions r with respect to the central electron. Moving through time t in the decay curve corresponds to shifting the sensitive region in the lattice being probed. This suggests a (nonlinear) means to map from t to an effective r coordinate, suggesting a method of discriminating nuclei in the electronic environment. Furthermore, Figure 11.3 indicates that nuclear spins can probe electronic relaxation processes, potentially offering a view into the phonon density of states that dominate these relaxation mechanisms [75, 155, 76, 98]. This is relevant to molecular systems [26, 67, 156, 117], and in DNP, wherein the concentration and identity of electron spins can vastly affect nuclear polarization levels [95, 39].

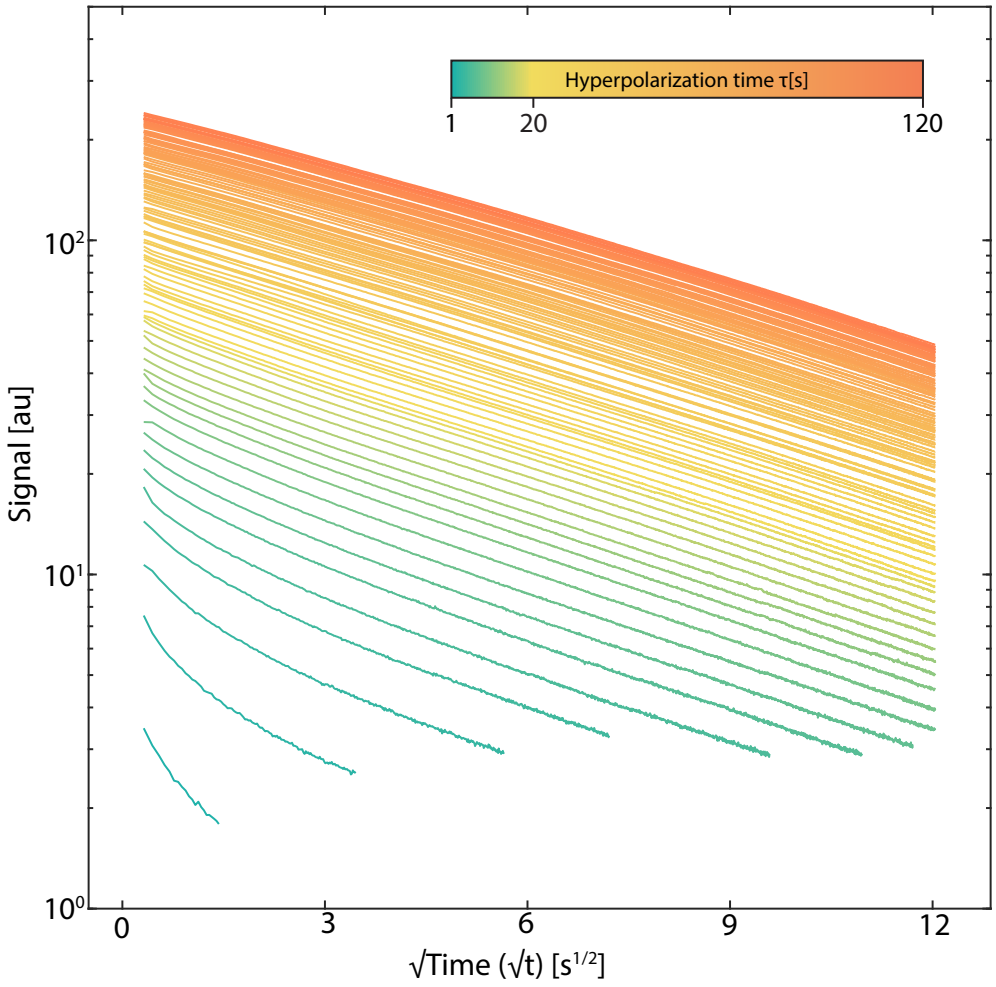

Figure 11.6 **Polarization buildup with hyperpolarization period τ.** Panel shows the unnormalized data corresponding to Figure 11.3A. The different curves are the ^{13}C pulsed spin-lock decays obtained under varying hyperpolarization time τ (see colorbar). This data is also shown as a movie in Ref. [7].

11.6 T_1 measurements at low and high field

Figure 11.5 considers the measurement of the T_1 of the ^{13}C nuclear spins at the polarizing field (B_{pol}=36mT) and the readout field (B_0=7T) respectively. For these measurements, the sample is first hyperpolarized, and is subsequently carried to the field of interest (B_{pol} or B_0) for a waiting period t_0. Finally, the sample is transported to B_0 where spin-lock readout is carried out similar to Figure 11.2, and the integrated signal is plotted. The rapid field cycling for these measurements is carried out via mechanical sample shuttling, and the experimental strategy is similar to that in Ref. [17].

Notably, varying the period t_0 allows one to discern the profile of the T_1 relaxation at both fields (see Figure 11.5). We find that the relaxation profiles closely follow monoexponential decay profiles (solid lines). From a $1/e$ intercept (dashed line) in Figure 11.5 we find the respective low and high field relaxation times as $T_{1,\mathrm{LF}}$=283±2s and $T_{1,\mathrm{HF}}$=1520 ± 20s respectively. We note that the monoexponential decays here stand in contrast to the observed stretched exponential decays that we find for the rotating frame lifetimes T_2' in Figure 11.2 and Figure 11.3.

11.7 Movies showing data in Figure 11.2 and Figure 11.3

As a complement to the graphs in this Chapter, we present movies corresponding to the data in Figure 11.2A and Figure 11.3A on Youtube (found at Refs. [5, 6]). These movies show clearly the progressive slowing down of the decay profiles upon increasing the hyperpolarization time τ in both representations. The gray lines here show fitted stretched exponential lines corresponding to the previous data for clarity, allowing a guide to the eye to track the slowing relaxation dynamics with increasing τ. Figure 11.6 shows an unnormalized plot of Figure 11.3, from where the polarization buildup dynamics as a function of τ can be extracted.

11.8 T_2^* vs T_2' lifetimes

Figure 11.7 describes the two relaxation times present in the experiments in this Chapter. In the system of ^{13}C nuclear spins we consider, free induction decay lifetime T_2^* ≈1.5ms, predominately due to strong dipolar interactions between individual spins (Figure 11.7A). Under Floquet control (described by Figure 11.7B(i)), however, T_2'= 90.9s, an extension of more than 60,000x. In fact, the signal remains substantial even at ∼600s, as shown in Figure 11.7B (here hyperpolarization time τ= 120s). This dramatic increase in lifetime is arranged for through spin-locking to a conserved axis ($\hat{\mathbf{x}}$) which is arranged collinear with the initial magnetization.

Figure 11.7C shows that the T_2' lifetime is dependent on the spin-lock pulse sequence parameters, namely the driving frequency. Here, Jρ is used as a convenient metric for describing the frequency of the drive, where J is the dipolar coupling strength and ρ is the interpulse spacing (see Figure 11.7B(i)). The traces here show that the decay is significantly slower at lower Jρ, corresponding to a higher frequency Floquet drive (this dependence is discussed in detail in Ref. [30]). Importantly, the experiments of this Chapter were performed with the Floquet drive parameters all held constant, and any variations in T_2' lifetimes are caused entirely by varying the hyperpolarization time τ.

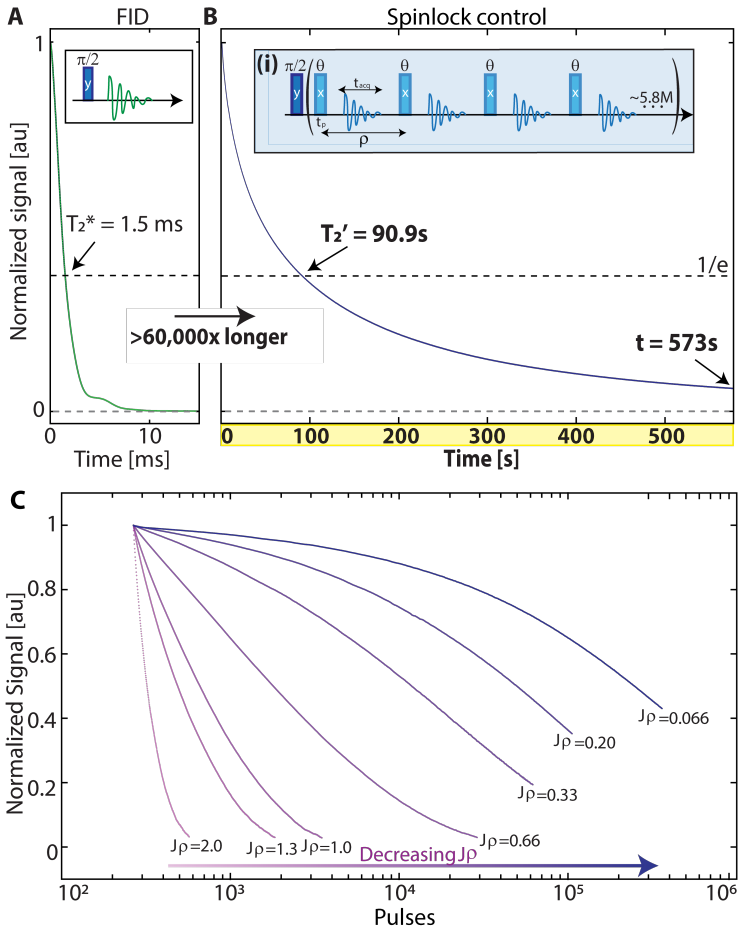

Figure 11.7 **Relaxation lifetimes under Floquet control.** (A) *Free induction decay* of ^{13}C nuclei in $T_2^* \approx 1.5$ ms due to strong dipolar coupling. (B) *Lifetime extension due to spin-locking* to T_2'= 90.9s. Floquet driving consists of a train of ϑ pulses separated by acquisition periods (inset). Here t_{acq}=2μs, t_p=40μs, and ρ=99.28μs. (C) *Spin-lock lifetime dependence on drive frequency.* Traces shows an increase in lifetime with decreasing Jρ. Here, J is the median dipolar coupling strength and ρ (the interpulse spacing in the Floquet drive) is varied. Figure adapted from Ref. [30].

11.9 Assumptions made for theoretical model in Figure 11.4

In what follows, we summarize the main assumptions made for the theoretical model utilized in this work and provide justifications of their relevance:

(1) *Uniform nuclear spin density*: we have assumed here that the ^{13}C nuclei are uniformly distributed in the lattice with a high density, hence allowing Eq. 11.1 to be written as a

continuous differential equation with respect to r. This is a good approximation in our experiments because they constitute an ensemble average over $>10^8$ NV-^{13}C systems; each with a central NV defect surrounded by $\sim 10^4$ ^{13}C nuclei. Any microscopic features arising from the discrete arrangement of the spins are washed out by the ensemble average.

(2) *Purely radial polarization distribution*: we have assumed that the polarization profile is isotropic in space and only depends on the radial position r from the NV center. This allows the diffusion equation in Eq. 11.1 to be written for a single variable r. While we expect some variability in the rate of hyperpolarization injection from the NV center based on angle theta (due to variation in the hyperfine coupling), any differences in polarization within a radial shell are rapidly homogenized by ^{13}C spin diffusion (strong for nuclei in the same shell because they are at identical r).

(3) *Absence of spin diffusion barrier*: in our model we have assumed spin diffusion between all ^{13}C nuclei ignoring the presence of a spin diffusion barrier. This simplifying assumption is valid because the finite measurement bandwidth in our experiment makes it feasible to only measure nuclei that are weakly hyperfine coupled, i.e. with $0 < —A_{zz}— <$ 30kHz. This region can be considered close to the boundary of the spin diffusion barrier, and the number of spins in this region affected by the barrier (with their diffusion suppressed) are relatively very few.

(4) *Validity of the spin diffusion model*: We have assumed purely hydrodynamic diffusion in a Bloembergen-like model [32]. This assumes that the polarization evolution can be captured by Fick's law. This is a good approximation given the spin numbers we consider; every NV center has $\sim 10^4$ ^{13}C nuclei surrounding it, and at the distance scales we consider even at short τ, >100 ^{13}C nuclei per NV center contribute to the signal. In this regime of a large number of spins, the Bloembergen diffusion model has been shown to excellently capture the spin dynamics [13, 87, 127].

(5) *Local and global relaxation*: we have assumed that the ^{13}C relaxation is set by spatially "local" and "background" sources — by the NV centers and P1 centers respectively. Given that the polarization is injected from the NV center sites, the NVs are assumed to be at the center ($r= 0$) of each of the spin systems considered in the ensemble average. On the other hand, the P1 centers are randomly distributed, and in an ensemble average occur with a fixed background density. Moreover, the inter-NV spacing is rather large (25nm), and hence each NV-^{13}C combined system can be considered to be unique with minimal overlap (for all t and τ considered in the Chapter).

Finally, the values of the various parameters employed in the simulation were set by matching the relaxation data from the experiment.

Chapter 12

Initializing and Controlling Mesoscale Spin Textures

12.1 Introduction

In both classical and quantum contexts, thermalization describes how systems evolve towards thermal equilibrium, a state characterized by maximum entropy and minimal accessible information about their past states [153]. Thermalization is the process by which isolated systems approach equilibrium [42].

This work is part of a broader endeavor to control and manipulate thermalization processes in quantum systems [105, 89]. Here we demonstrate two techniques to study these processes: controlled dissipation and Hamiltonian engineering. These techniques are applied to initialize structured mesoscopic quantum states involving hundreds of spins. By manipulating a system of interacting nuclear spins at high temperatures, we have engineered shell-like nuclear spin polarization textures. This approach leverages thermalization dynamics to achieve spatial and temporal control without needing to individually address spins, which also helps in avoiding control errors and overcoming spectral crowding of spin resonances.

Our experiments use a model system based on Nitrogen-Vacancy (NV) center defects in diamond, surrounded by ^{13}C nuclear spins. The NV centers act as polarization injectors and antennas, creating nanoscale gradients that influence nuclear spin resonance frequencies in their vicinity. The presence of this gradient hyperfine field allows for the creation of stable spin textures by controlling the thermalization process through a time-periodic drive and spatially dependent dissipation. These methodological advancements have implications for quantum memories, spintronics, and nanometer-resolved magnetic resonance imaging.

12.2 Central Spin Model

The understanding of the system dynamics in this chapter relies on the concept of the central spin model. As per the visual in Figure 12.1, this view entails a highly sensitive spin species

at the origin of the system, $r = 0$. Since there is a large ensemble of NV centers across the entire diamond sample, the presence of ^{13}C and other defect spin species approximately averages out. Thus we assume spherically symmetrical dynamics, and so the distance r of a ^{13}C species from the nearby NV center is the only relevant parameter. Please see Chapter 10 for a discussion of the assumptions made here.

12.3 State Engineering

The first method of generating spin textures involves an addition to the experiment described in Chapter 10. During the hyperpolarization pumping portion of the experiment, the sign of polarization which is injected locally from the NV center can be chosen to be positive or negative. This provides us the first critical tuning control: the system is initialized with 60 seconds of positive hyperpolarization, and then the sign of polarization is instantaneously switched to negative. Then, negative hyperpolarization continues for a variable period of time τ, followed by shuttling to high field and inductive NMR readout.

Representatives from the resulting NMR spin-lock decay curves are shown in Figure 12.2. After only a small period of negative pumping, the decay curve appears to be somewhat unchanged as expected. Then as the negative pumping time is increased further, a zero-crossing appears in the middle of the spin-lock curve. In this dataset, the zero-crossing appears when the negative pumping time $\tau \approx 40 - 45$ seconds.

To understand the origin of the zero-crossing, it is informative to inspect the frequency-domain NMR spectra from these data. As seen in Figure 12.3, the single NMR line appears unchanged before the zero-crossing appears. Then, as the zero-crossing starts to appears when $\tau = 40$s, the wings of the NMR peak start to invert negative. Throughout the zero-crossing, we see the wings of the peak fully invert, and it is not until $\tau = 47$s that we see the center of the peak distribution follow suit.

The central position of the NMR peak represents the bulk ^{13}C species that see little or no frequency shift from interaction with the central NV center. The ^{13}C species present at the wings of the peak lineshape, on the other hand, see a significant frequency shift due to the hyperfine field. Thus the peak distribution gives us a qualitative sense of spatial proximity to the central spin. Since the wings of the NMR lineshape first invert, we interpret this to mean the negative hyperolarization first arrives at the ^{13}C nuclear spins closest to the NV center. Eventually, the negative polarization diffuses outward into the bulk, causing the peak center to finally invert. All of this is consistent with Chapter 10's understanding of how hyperpolarization across the bulk sample proceeds.

Using the same model developed in Chapter 10, we can simulate the polarization evolution throughout (positive and negative) hyperpolarization and NMR measurement. The model appears as:

$$\frac{\partial}{\partial t}p(r,t) = \frac{P_0}{r^6} - \frac{\kappa_0}{r^6}p(r,t) - \frac{1}{T_1}p(r,t) + D\nabla^2 p(r,t) \tag{12.1}$$

whereas the only addition now is that the experiment starts with 60 seconds of evolution under positive hyperpolarization followed by variable time τ evolution under negative hyerpolarization. This is accounted by changing the sign of P_0 from positive to negative. The results of the numerical simulations are shown in Figure 12.4. In addition to the spin-lock curves, it is helpful to visualize the spatial distribution of polarization as time evolves. Consistent with the experimental data, we find that the negative polarization begins closest to the NV center, then spreads outward over time, giving rise to the zero-crossings in the NMR spin-lock curves.

12.4 Hamiltonian Engineering

An additional method for engineering spin textures was discovered by modifying the effective Hamiltonian during the spin-lock. The full details are investigated at length in ref. [63], but the basic picture is that when the pulse flip angle ϑ approaches the value π, the spin-lock no longer becomes effective at establishing a quasi-conservation law with respect to total polarization. Further, due to the hyperfine gradient field, the effective flip angle seen by each ^{13}C species depends on its position $r > 0$ relative to the central NV center. The effective flip angle seen by the spins is thus a distribution – and when the global angle is near π, there will be a single "shell" of spins that see exactly $\vartheta = \pi$, whereas spins closer to and farther away from the NV center will see angles $\vartheta < \pi$ or $\vartheta > \pi$. Thus the efficacy of the spin-lock greatly depends on the spin's proximity to the NV center.

In practice, this effect is seen as a dramatic zero-crossing over the course of the NMR decay curve, even with a fully positive hyperpolarization scheme. As seen in Figure 12.5, the spin-lock curve is stable over a long period of time (horizontal axis units in seconds). When the flip angle is tuned near π, the NMR signal dips near or below zero. This indicates some non-trivial spatially dependent spin texture resulting from the control sequence. Figure 12.6 shows the calculated integrated signal (blue) and 1/e lifetimes (red) in the dataset from Figure 12.5. A closer examination of the dip around $\vartheta = \pi$ with a finer step in flip angle shows the hysteretic nature of this zero-crossing. At the near side of $\vartheta < \pi$, the whole curve dips, whereas at the far side of $\vartheta > \pi$ the signal does not start to drop until progressively later times in the spin-lock. This is especially surprising given the timescale of the experiment – the effect is not noticed until several seconds into the measurement.

12.5 Conclusion

A detailed investigation into the Hamiltonian engineering mechanism is given in ref. [63], but here we simply observe that there is a hysteretic zero-crossing that occurs during the spin-lock in the region of $\vartheta \approx \pi$. We hypothesize that non-trivial spin textures are the direct cause of the signal drop, but due to the strange nature of the curves, the mechanism is quite different. The state engineering technique gives rise to smooth zero-crossings that

are entirely expected from the diffusive dynamics in the three-dimensional system surround each NV center. However, the Hamiltonian engineering technique relies on the strenght of the hyperfine field gradient emanating from the NV center.

These two distinct yet related techniques highlight an especially intriguing application of this work: nanoscale magnetic resonance imaging. Traditional MRI techniques can also use different methods to achieve results. Relaxometry can distinguish between environments with different types of noise which relax nuclear spins at different rates. This is akin to the state engineering technique, since the difference in relaxation rates due to distance $r > 0$ from the noise central NV center gives rise to curves that depend on the initial state of the polarization distribution. MRI also makes frequent use of magnetic field gradients. This is akin to the Hamiltonian engineering technique, since the native gradient imposed by the paramagnetic NV center is what gives rise to the differences in spatial distribution. An interesting future direction could be to combine these techniques to more quantitatively define the mapping from spin-lock measurement to nanometer-resolved image.

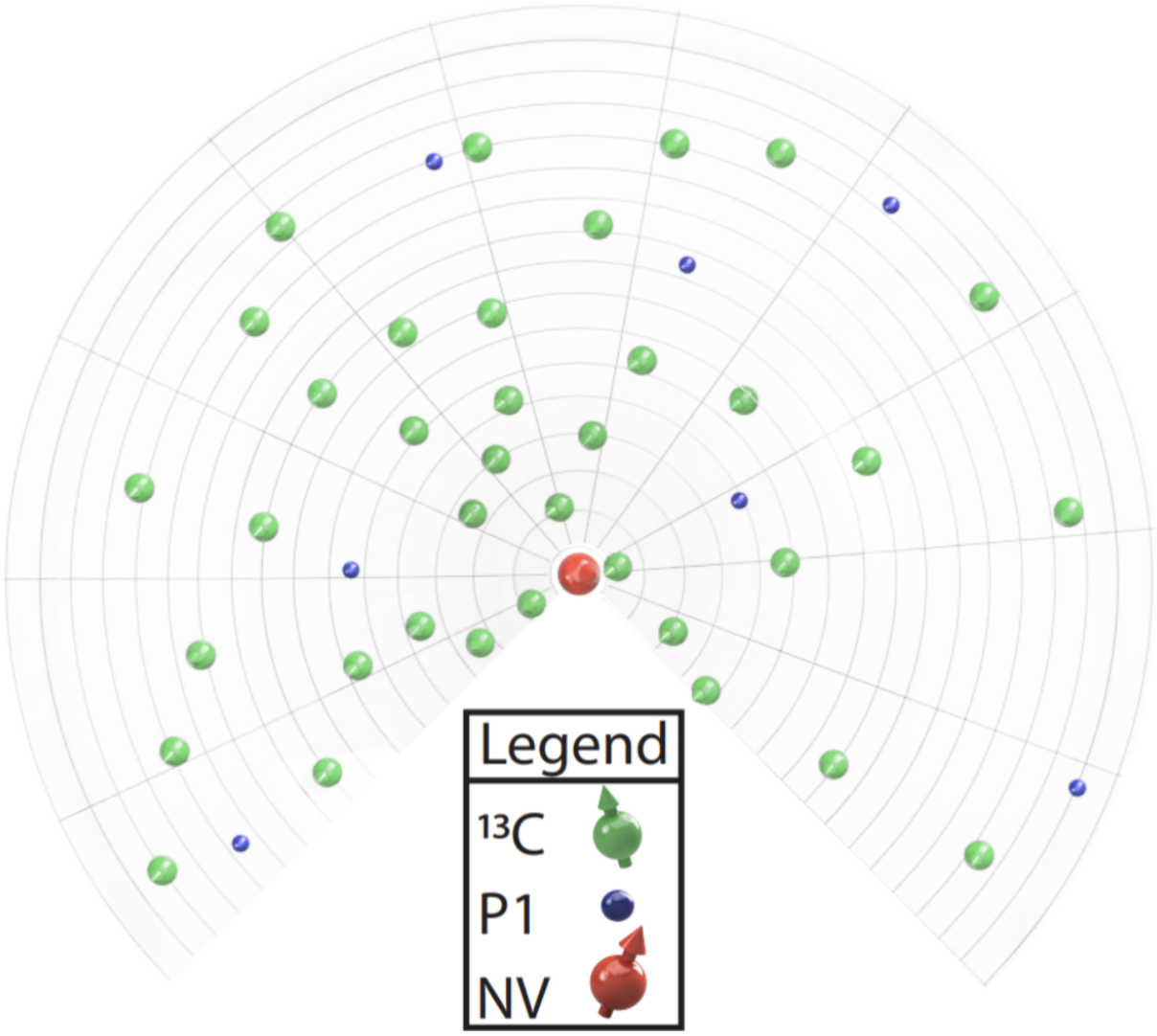

Figure 12.1 **Bird's-eye view of central spin model.**

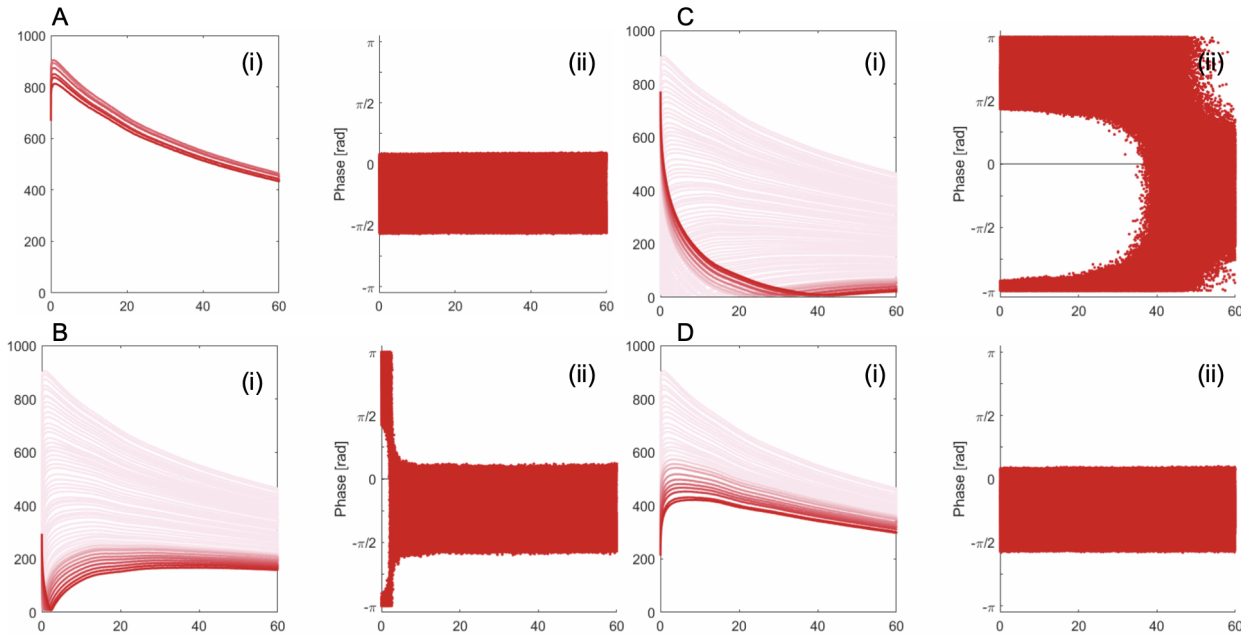

Figure 12.2 **Effect of negative pumping after positive pumping.** For each part A-D, the left graph (i) shows the NMR decay curve and the right graph (ii) shows the phase value in the x-y plane. The phase values appear jumbled due to measurement taking place in the rotating frame. Each curve was measured after 60 s of positive hyperpolarization pumping followed by a variable amount of negative polarization: (A) 30 s, (B) 35 s, (C) 40 s, and (D) 45 s. The way to interpret the phase data plots is as follows: the phase data in the $-\pi/2$-0 range indicates a positive NMR signal, whereas phase data in the $+\pi/2$-π range indicates a negative NMR signal. Thus B(ii) and C(ii) indicate experiments where the spin polarization changed from positive to negative somewhere in the middle.

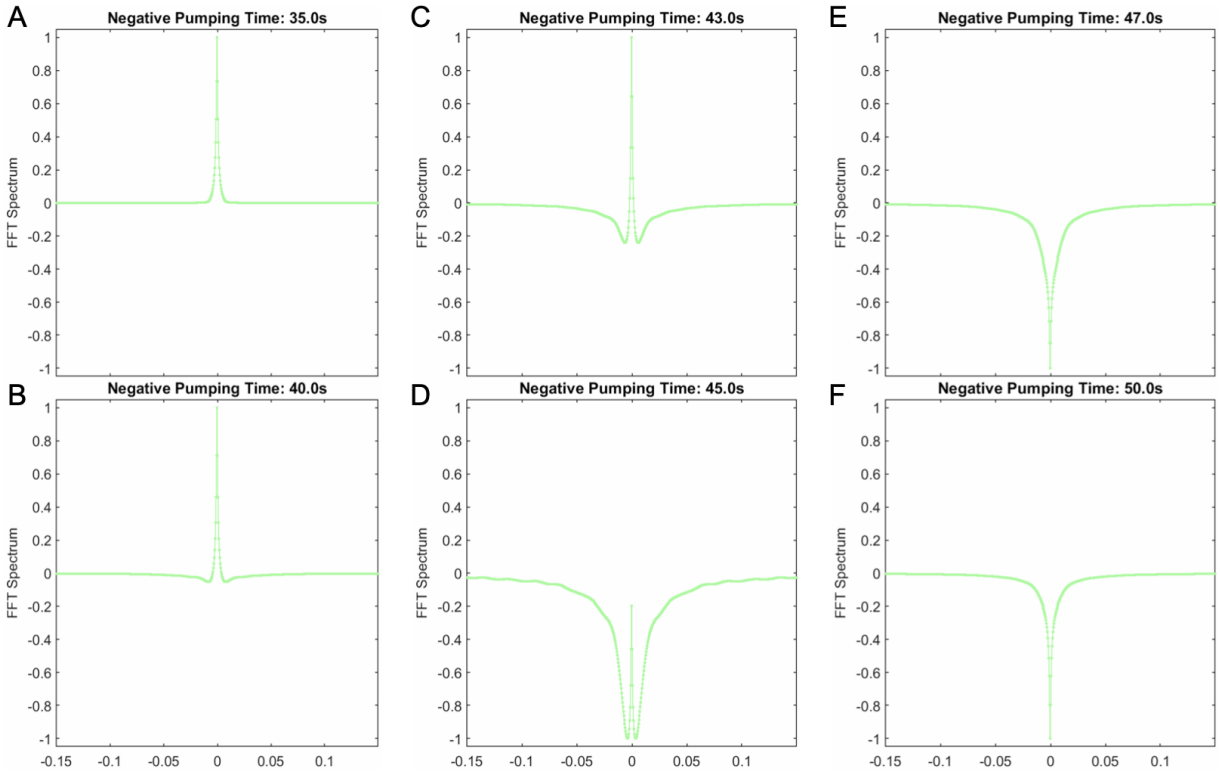

Figure 12.3 **Fast Fourier transform of the decay curves from Figure 12.2.**

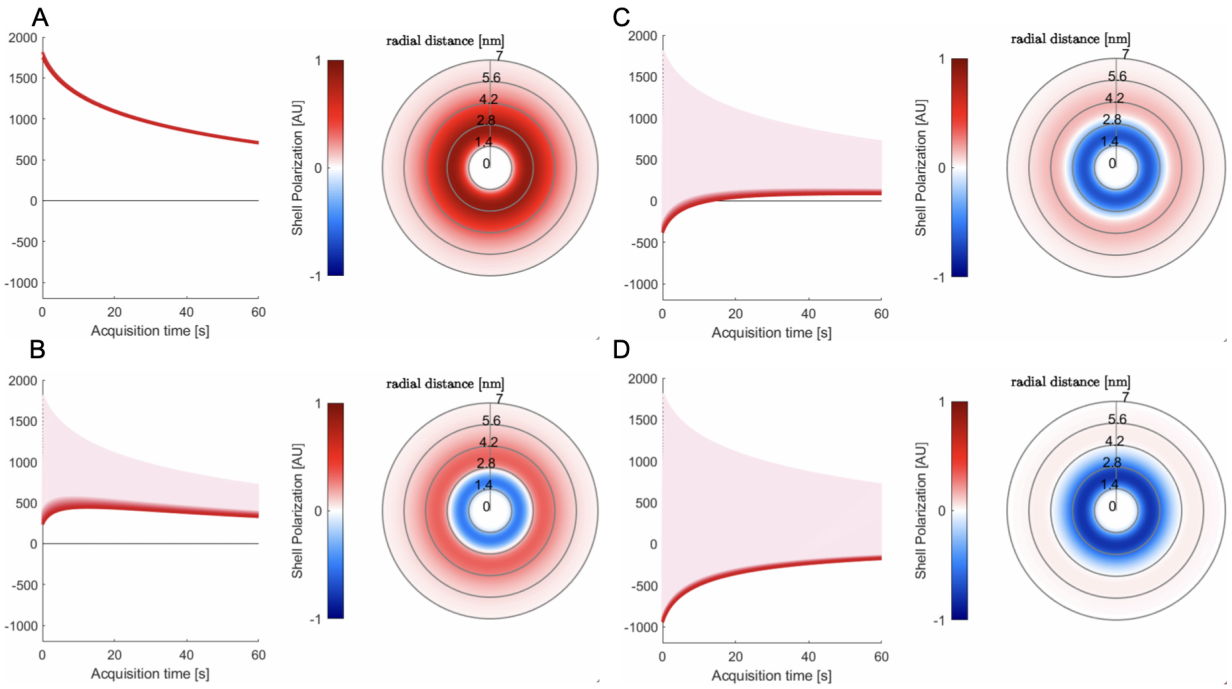

Figure 12.4 **Spin diffusion simulations.** The same model as in Chapter 10 was used to simulate these polarization distributions and resulting decay curves. Simulations and plotting performed by Quentin Reynard-Feytis and reproduced with his permission here.

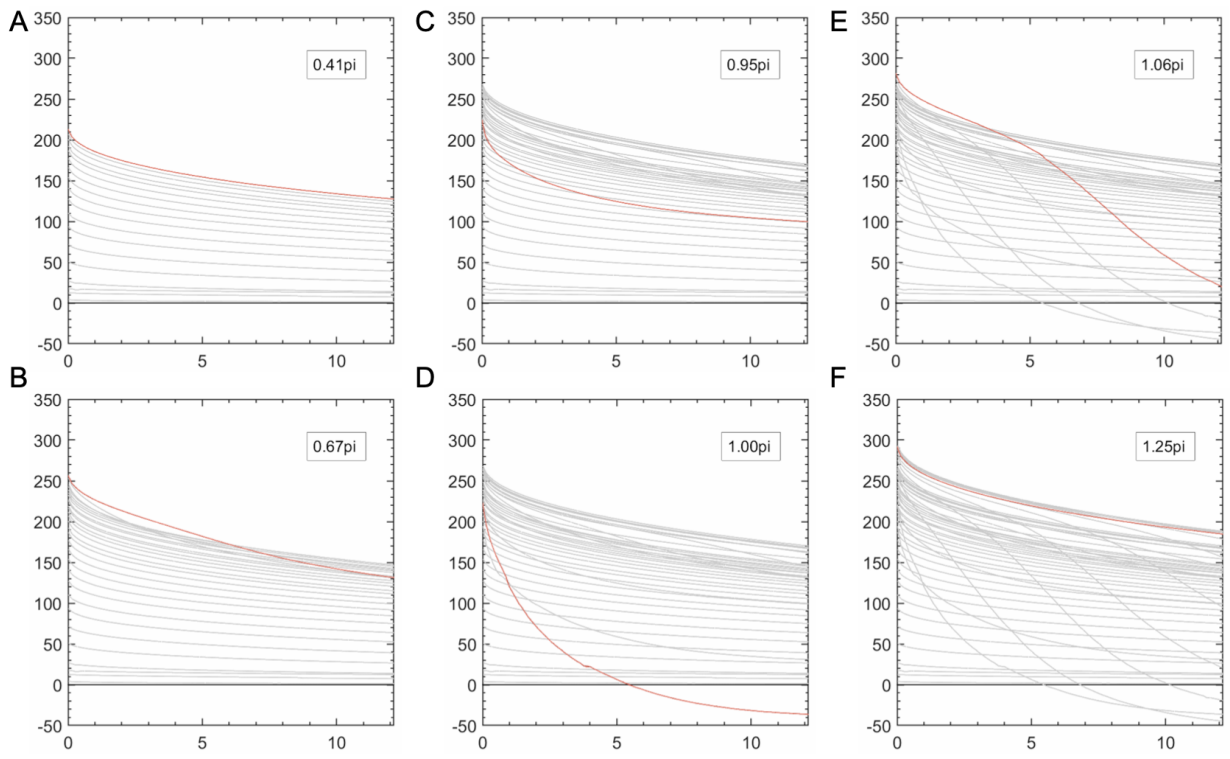

Figure 12.5 **Hamiltonian engineering.** Each graph shows a spin-lock decay curve taken after 60 s of positive hyperpolarization. The flip angles indicate the repeated ϑ pulse used in that shot. Horizontal axis units in seconds, vertical axis indicates NMR signal in arbitrary units.

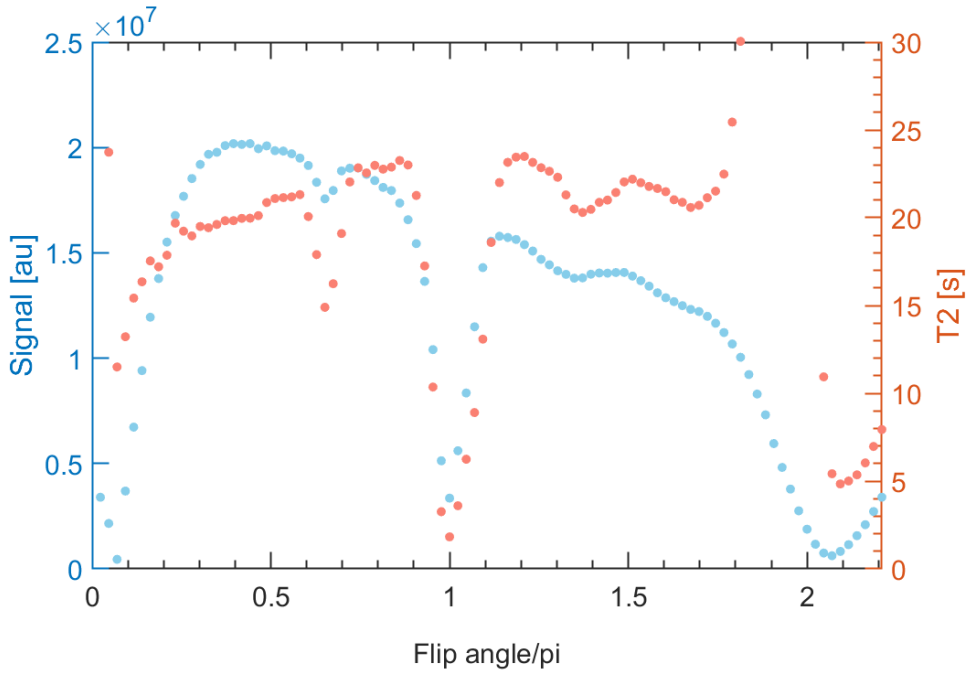

Figure 12.6 **Total signal and 1/e lifetime measured from dataset in Figure 12.5.**

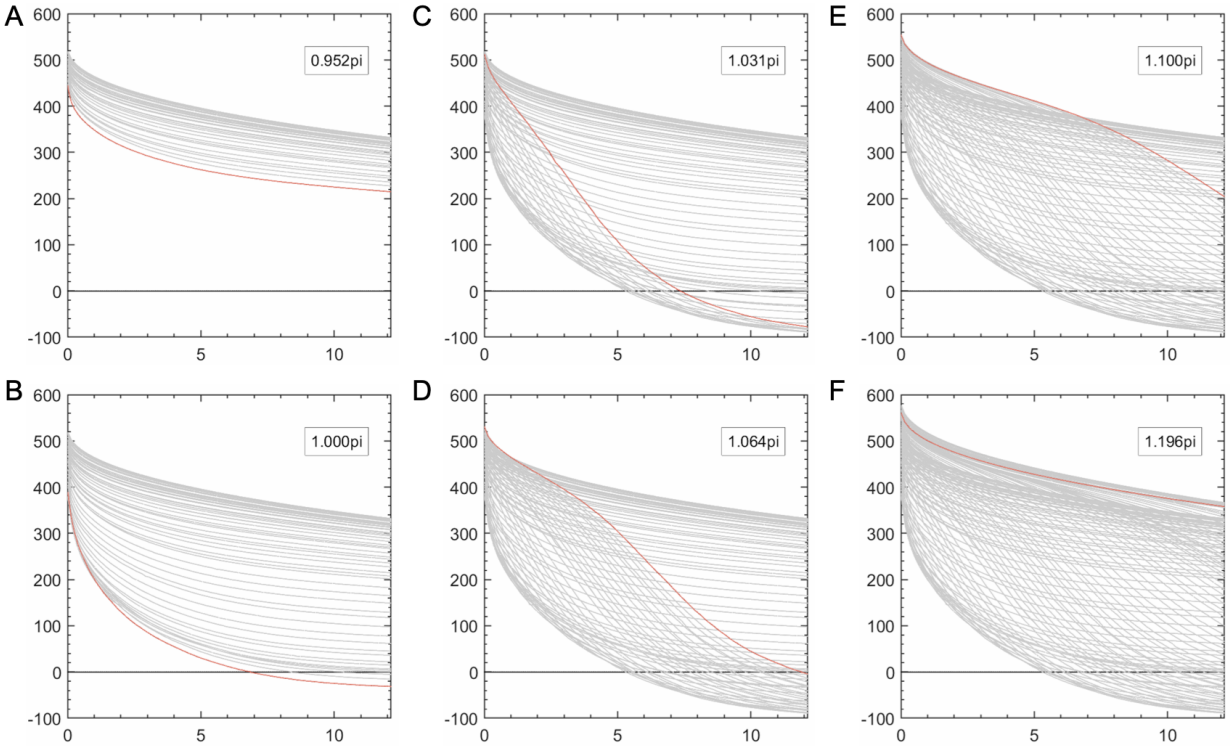

Figure 12.7 **Fine sweep of ϑ.** Analogous dataset to Figure 12.5 focusing on the dip around $\vartheta = \pi$ with a finer step. Horizontal axis units in seconds, vertical axis indicates NMR signal in arbitrary units.

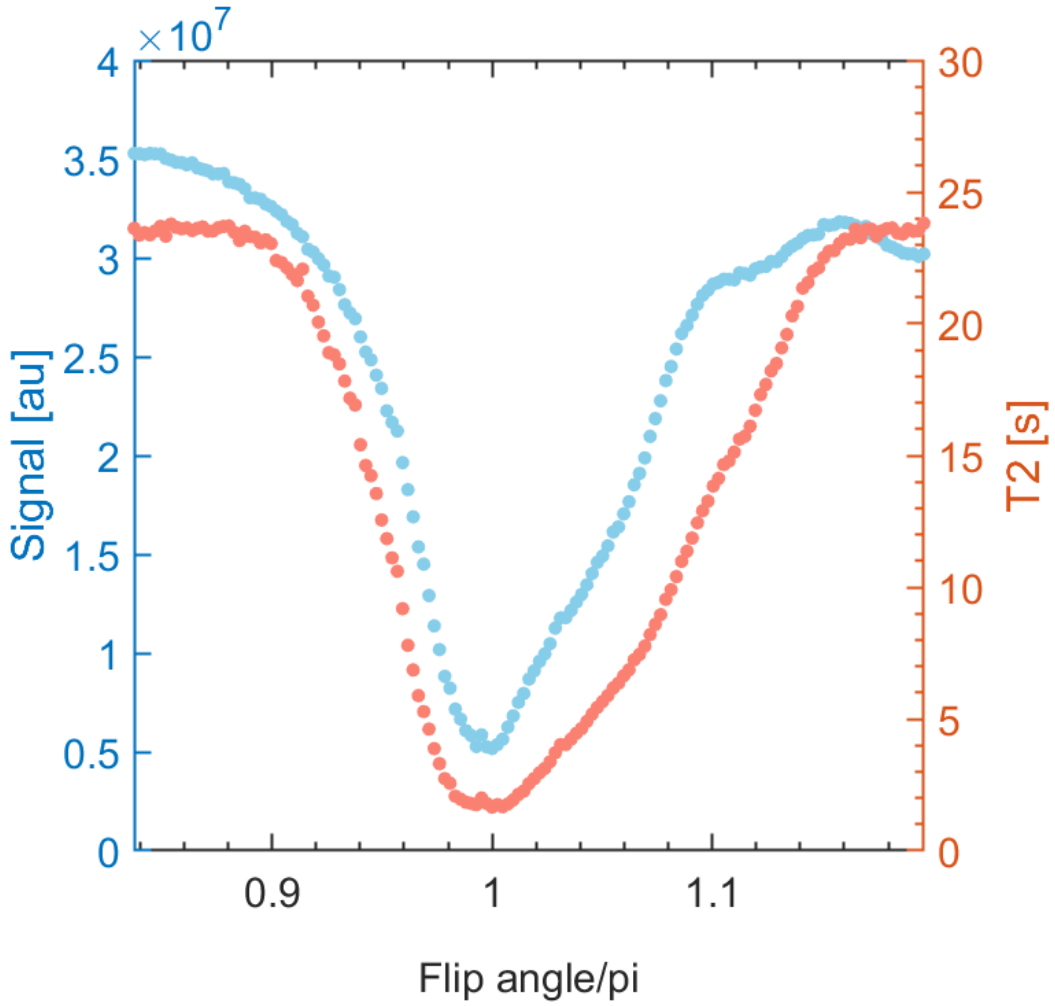

Figure 12.8 **Total signal and 1/e lifetime measured from dataset in Figure 12.7.**

Bibliography

[1] Video showing full dataset of Fig. 4: https://www.youtube.com/watch?v=uLKIR_XM_FQ. 2021.

[2] Video showing full dataset of Fig. 5: https://www.youtube.com/watch?v=8NI7Zzugi4o. 2021.

[3] Movie of full dataset from Fig. 2A of main text: https://youtu.be/61ZqLgbCuyo. 2021.

[4] Video showing first 55 Floquet cycles from full dataset of Fig. 3A: https://youtu.be/m5iASnBZ9oo. 2021.

[5] Video showing full dataset of Fig. 2A: https://www.youtube.com/watch?v=GEdVRV2cXH4. 2021.

[6] Video showing full dataset of Fig. 3A: https://www.youtube.com/watch?v=b8Be0R2etZQ. 2021.

[7] Video showing unnormalized dataset of Fig. 3A: https://www.youtube.com/watch?v=5tir0OyE4zg. 2021.

[8] Dmitry A Abanin, Wojciech De Roeck, and François Huveneers. "Exponentially slow heating in periodically driven many-body systems". In: *Physical Review Letters* 115.25 (2015), p. 256803.

[9] Dmitry A Abanin et al. "Effective Hamiltonians, prethermalization, and slow energy absorption in periodically driven many-body systems". In: *Physical Review B* 95.1 (2017), p. 014112.

[10] Dmitry A. Abanin, Wojciech De Roeck, and F. Huveneers. In: *Phys. Rev. Lett.* 115 (2015), p. 256803. URL: http://link.aps.org/doi/10.1103/PhysRevLett.115.256803.

[11] MH Abobeih et al. "Atomic-scale imaging of a 27-nuclear-spin cluster using a quantum sensor". In: *Nature* 576.7787 (2019), pp. 411–415.

[12] A Abragam and M Goldman. "Principles of Dynamic Nuclear Polarization". In: *Reports on Progress in Physics* 41.3 (1978), pp. 395–467.

[13] Anatole Abragam. *The principles of nuclear magnetism*. 32. Oxford university press, 1961.

[14] A Ajoy et al. "Dynamical decoupling in interacting systems: applications to signal-enhanced hyperpolarized readout". In: *arXiv preprint arXiv:2008.08323* (2020).

[15] A Ajoy et al. "Enhanced dynamic nuclear polarization via swept microwave frequency combs". In: *Proceedings of the National Academy of Sciences* 115.42 (2018), pp. 10576–10581.

[16] A Ajoy et al. "Enhanced dynamic nuclear polarization via swept microwave frequency combs". In: *Proceedings of the National Academy of Sciences* 115.42 (2018), pp. 10576–10581. DOI: https://doi.org/10.1073/pnas.1807125115.

[17] A Ajoy et al. "Hyperpolarized relaxometry based nuclear T 1 noise spectroscopy in diamond". In: *Nature Communications* 10.1 (2019), pp. 1–12.

[18] A. Ajoy et al. "Dynamical decoupling in interacting systems: applications to signal-enhanced hyperpolarized readout". In: *arXiv preprint arXiv:2008.08323* (2020).

[19] A. Ajoy et al. "Wide dynamic range magnetic field cycler: Harnessing quantum control at low and high fields". In: *Review of Scientific Instruments* 90.1 (2019), p. 013112. DOI: 10.1063/1.5064685. eprint: https://doi.org/10.1063/1.5064685. URL: https://doi.org/10.1063/1.5064685.

[20] Ashok Ajoy and Paola Cappellaro. "Stable three-axis nuclear-spin gyroscope in diamond". In: *Physical Review A* 86 (6 Dec. 2012), p. 062104. DOI: 10.1103/PhysRevA.86.062104. URL: http://link.aps.org/doi/10.1103/PhysRevA.86.062104.

[21] Ashok Ajoy et al. "Orientation-independent room temperature optical ¡sup¿13¡/sup¿C hyperpolarization in powdered diamond". In: *Science Advances* 4.5 (2018), eaar5492. DOI: 10.1126/sciadv.aar5492. URL: https://www.science.org/doi/abs/10.1126/sciadv.aar5492.

[22] Ashok Ajoy et al. "Orientation-independent room temperature optical 13C hyperpolarization in powdered diamond". In: *Sci. Adv.* 4.5 (2018), eaar5492. URL: http://advances.sciencemag.org/content/4/5/eaar5492.

[23] Ashok Ajoy et al. "Room temperature "optical nanodiamond hyperpolarizer": Physics, design, and operation". In: *Review of Scientific Instruments* 91.2 (2020), p. 023106.

[24] Gonzalo A. Álvarez et al. "Performance comparison of dynamical decoupling sequences for a qubit in a rapidly fluctuating spin bath". In: *Phys. Rev. A* 82 (4 2010), p. 042306. DOI: 10.1103/PhysRevA.82.042306. URL: http://link.aps.org/doi/10.1103/PhysRevA.82.042306.

[25] Atta-ur-rahman, M. Choudhary, and Atia-Tul-Wahab. "Some Key Developments in NMR Spectroscopy". In: (2016), pp. 415–429. DOI: 10.1016/B978-0-12-411589-7.00009-7.

[26] SL Bayliss et al. "Optically addressable molecular spins for quantum information processing". In: *Science* 370.6522 (2020), pp. 1309–1312.

[27] William Beatrez et al. See Supplemental Material. 2022.

[28] William Beatrez et al. "Critical Prethermal Discrete Time Crystal Created by Two Frequency Driving". In: *Nat. Phys.* 19 (Jan. 2023), pp. 407–413. DOI: 10.1038/s41567-022-01891-7. URL: https://www.nature.com/articles/s41567-022-01891-7.

[29] William Beatrez et al. "Electron Induced Nanoscale Nuclear Spin Relaxation Probed by Hyperpolarization Injection". In: *Phys. Rev. Lett.* 131 (1 July 2023), p. 010802. DOI: 10.1103/PhysRevLett.131.010802. URL: https://link.aps.org/doi/10.1103/PhysRevLett.131.010802.

[30] William Beatrez et al. "Floquet Prethermalization with Lifetime Exceeding 90 s in a Bulk Hyperpolarized Solid". In: *Phys. Rev. Lett.* 127 (17 Oct. 2021), p. 170603. DOI: 10.1103/PhysRevLett.127.170603. URL: https://link.aps.org/doi/10.1103/PhysRevLett.127.170603.

[31] S. Blanes et al. "The Magnus expansion and some of its applications". In: *Physics Reports* 470.5–6 (2009), pp. 151–238. DOI: 10.1016/j.physrep.2008.11.001.

[32] Nicolaas Bloembergen. "On the interaction of nuclear spins in a crystalline lattice". In: *Physica* 15.3-4 (1949), pp. 386–426.

[33] Nicolaas Bloembergen, EM Purcell, and RV Pound. "Nuclear magnetic relaxation". In: *Nature* 160.4066 (1947), pp. 475–476.

[34] WE Blumberg. "Nuclear spin-lattice relaxation caused by paramagnetic impurities". In: *Physical Review* 119.1 (1960), p. 79.

[35] R. Bruschweiler and R.R. Ernst. "Non-ergodic quasi-equilibria in short linear spin 12 chains". In: *Chem. Phys. Lett.* 264.3-4 (1997), pp. 393–397. ISSN: 0009-2614. DOI: 10.1016/S0009-2614(96)01310-3. URL: http://www.sciencedirect.com/science/article/pii/S0009261496013103.

[36] Marin Bukov, Luca D'Alessio, and Anatoli Polkovnikov. "Universal high-frequency behavior of periodically driven systems: from dynamical stabilization to Floquet engineering". In: *Advances in Physics* 64.2 (2015), pp. 139–226.

[37] Marin Bukov et al. "Prethermal floquet steady states and instabilities in the periodically driven, weakly interacting bose-hubbard model". In: *Physical Review Letters* 115.20 (2015), p. 205301.

[38] JM Cai et al. "Robust dynamical decoupling with concatenated continuous driving". In: *New Journal of Physics* 14.11 (2012), p. 113023. URL: https://iopscience.iop.org/article/10.1088/1367-2630/14/11/113023/meta.

[39] Andrea Capozzi et al. "Thermal annihilation of photo-induced radicals following dynamic nuclear polarization to produce transportable frozen hyperpolarized 13C-substrates". In: *Nature communications* 8.1 (2017), pp. 1–7.

[40] H. Y. Carr and E. M. Purcell. "Effects of Diffusion on Free Precession in Nuclear Magnetic Resonance Experiments". In: *Physical Review* 94.3 (1954), pp. 630–638. DOI: 10.1103/PhysRev.94.630.

[41] Soonwon Choi et al. "Observation of discrete time-crystalline order in a disordered dipolar many-body system". In: *Nature* 543.7644 (2017), pp. 221–225. DOI: https://doi.org/10.1038/nature21426.

[42] Luca D'Alessio and Marcos Rigol. "Long-time behavior of isolated periodically driven interacting lattice systems". In: *Physical Review X* 4.4 (2014), p. 041048.

[43] Emily Davis, Gregory Bentsen, and Monika Schleier-Smith. "Approaching the Heisenberg Limit without Single-Particle Detection". In: *Phys. Rev. Lett.* 116 (5 Feb. 2016), p. 053601. DOI: 10.1103/PhysRevLett.116.053601. URL: https://link.aps.org/doi/10.1103/PhysRevLett.116.053601.

[44] Christian L Degen, F Reinhard, and P Cappellaro. "Quantum sensing". In: *Reviews of Modern Physics* 89.3 (2017), p. 035002.

[45] Yanqun Dong et al. "Controlling coherence using the internal structure of hard π pulses". In: *Phys. Rev. Lett.* 100.24 (2008), p. 247601.

[46] A Dréau et al. "Probing the dynamics of a nuclear spin bath in diamond through time-resolved central spin magnetometry". In: *Physical review letters* 113.13 (2014), p. 137601.

[47] M. Duer. *Introduction to Solid-State NMR Spectroscopy*. John Wiley & Sons, 2004.

[48] James Eills et al. "Spin Hyperpolarization in Modern Magnetic Resonance". In: *Chemical Reviews* 123.4 (2023). PMID: 36701528, pp. 1417–1551. DOI: 10.1021/acs.chemrev.2c00534. eprint: https://doi.org/10.1021/acs.chemrev.2c00534. URL: https://doi.org/10.1021/acs.chemrev.2c00534.

[49] Dominic V Else and Chetan Nayak. "Classification of topological phases in periodically driven interacting systems". In: *Physical Review B* 93.20 (2016), p. 201103.

[50] Dominic V. Else, Bela Bauer, and Chetan Nayak. "Floquet Time Crystals". In: *Phys. Rev. Lett.* 117 (9 Aug. 2016), p. 090402. DOI: 10.1103/PhysRevLett.117.090402. URL: https://link.aps.org/doi/10.1103/PhysRevLett.117.090402.

[51] Dominic V. Else, Bela Bauer, and Chetan Nayak. "Prethermal Phases of Matter Protected by Time-Translation Symmetry". In: *Phys. Rev. X* 7 (1 Mar. 2017), p. 011026. DOI: 10.1103/PhysRevX.7.011026. URL: https://link.aps.org/doi/10.1103/PhysRevX.7.011026.

[52] Dominic V. Else et al. "Discrete Time Crystals". In: *Annual Review of Condensed Matter Physics* 11 (Mar. 2020), pp. 467–499. DOI: https://doi.org/10.1146/annurev-conmatphys-031119-050658.

[53] RR Ernst, G Bodenhausen, and A Wokaun. *Principles of nuclear magnetic resonance in one and two dimensions*. Clarendon Press Oxford, 1987.

[54] Christoph Fleckenstein and Marin Bukov. "Prethermalization and thermalization in periodically driven many-body systems away from the high-frequency limit". In: *Phys. Rev. B* 103 (14 Apr. 2021), p. L140302. DOI: 10.1103/PhysRevB.103.L140302. URL: https://link.aps.org/doi/10.1103/PhysRevB.103.L140302.

[55] Christoph Fleckenstein and Marin Bukov. "Prethermalization and thermalization in periodically driven many-body systems away from the high-frequency limit". In: *Phys. Rev. B* 103 (14 Apr. 2021), p. L140302. DOI: 10.1103/PhysRevB.103.L140302. URL: https://link.aps.org/doi/10.1103/PhysRevB.103.L140302.

[56] Christoph Fleckenstein and Marin Bukov. "Thermalization and prethermalization in periodically kicked quantum spin chains". In: *Phys. Rev. B* 103 (14 Apr. 2021), p. 144307. DOI: 10.1103/PhysRevB.103.144307. URL: https://link.aps.org/doi/10.1103/PhysRevB.103.144307.

[57] Christoph Fleckenstein and Marin Bukov. "Thermalization and prethermalization in periodically kicked quantum spin chains". In: *Phys. Rev. B* 103 (14 Apr. 2021), p. 144307. DOI: 10.1103/PhysRevB.103.144307. URL: https://link.aps.org/doi/10.1103/PhysRevB.103.144307.

[58] Nathan Goldman and Jean Dalibard. "Periodically driven quantum systems: effective Hamiltonians and engineered gauge fields". In: *Physical review X* 4.3 (2014), p. 031027.

[59] U. Haeberlen. *High Resolution NMR in Solids: Selective Averaging*. Academic Press Inc., New York, 1976.

[60] E. L. Hahn. "Spin Echoes". en. In: *Physical Review* 80.4 (Nov. 1950), pp. 580–594. ISSN: 0031-899X. DOI: 10.1103/PhysRev.80.580. URL: https://link.aps.org/doi/10.1103/PhysRev.80.580 (visited on 06/22/2022).

[61] Asmi Haldar, Roderich Moessner, and Arnab Das. "Onset of Floquet thermalization". In: *Physical Review B* 97.24 (2018), p. 245122.

[62] R. Hanson et al. "Coherent Dynamics of a Single Spin Interacting with an Adjustable Spin Bath". In: *Science* 320.5874 (2008), pp. 352–355. DOI: 10.1126/science.1155400.

[63] K. Harkins and et al. "Nanoscale engineering and dynamical stabilization of mesoscopic spin textures". In: *arXiv preprint arXiv:2310.05635* (2023). DOI: 10.48550/arXiv.2310.05635.

[64] J Stephen Hartman, Arjun Narayanan, and YouXiang Wang. "Spin-lattice relaxation in the 6H polytype of silicon carbide". In: *Journal of the American Chemical Society* 116.9 (1994), pp. 4019–4027.

[65] David Hayes, Steven T Flammia, and Michael J Biercuk. "Programmable quantum simulation by dynamic Hamiltonian engineering". In: *New Journal of Physics* 16.8 (2014), p. 083027. URL: https://iopscience.iop.org/article/10.1088/1367-2630/16/8/083027/meta.

[66] P Mark Henrichs and Max Linder. "Carbon-13 spin diffusion in the determination of intermolecular structure in solids". In: *Journal of Magnetic Resonance (1969)* 58.3 (1984), pp. 458–461.

[67] A Henstra and W Th Wenckebach. "Dynamic nuclear polarisation via the integrated solid effect I: theory". In: *Molecular Physics* 112.13 (2014), pp. 1761–1772.

[68] Wen Wei Ho et al. "Critical Time Crystals in Dipolar Systems". In: *Phys. Rev. Lett.* 119 (1 July 2017), p. 010602. DOI: 10.1103/PhysRevLett.119.010602. URL: https://link.aps.org/doi/10.1103/PhysRevLett.119.010602.

[69] E Philip Horvitz. "Nuclear spin diffusion induced by paramagnetic impurities in non-conducting solids". In: *Physical Review B* 3.9 (1971), p. 2868.

[70] DI Hoult. "The NMR receiver: a description and analysis of design". In: *Progress in Nuclear Magnetic Resonance Spectroscopy* 12.1 (1978), pp. 41–77.

[71] Yonatan Hovav, Akiva Feintuch, and Shimon Vega. "Theoretical aspects of dynamic nuclear polarization in the solid state–the solid effect". In: *Journal of Magnetic Resonance* 207.2 (2010), pp. 176–189.

[72] Owen Howell et al. "Asymptotic prethermalization in periodically driven classical spin chains". In: *Physical Review Letters* 122.1 (2019), p. 010602.

[73] F. Iemini, R. Fazio, and A. Sanpera. "Floquet time-crystals as sensors of AC fields". In: *arXiv preprint arXiv:2306.03927 [quant-ph]* (2023).

[74] Rodolfo A. Jalabert and Horacio M. Pastawski. "Environment-Independent Decoherence Rate in Classically Chaotic Systems". In: *Phys. Rev. Lett.* 86 (12 Mar. 2001), pp. 2490–2493. DOI: 10.1103/PhysRevLett.86.2490. URL: https://link.aps.org/doi/10.1103/PhysRevLett.86.2490.

[75] A Jarmola et al. "Temperature-and magnetic-field-dependent longitudinal spin relaxation in nitrogen-vacancy ensembles in diamond". In: *Physical review letters* 108.19 (2012), p. 197601.

[76] J-C Jaskula et al. "Cross-sensor feedback stabilization of an emulated quantum spin gyroscope". In: *Physical Review Applied* 11.5 (2019), p. 054010.

[77] F. Jelezko and J. Wrachtrup. "Single defect centres in diamond: A review". In: *Physica Status Solidi (A)* 203.13 (2006), pp. 3207–3225. DOI: 10.1002/pssa.200671403. URL: http://dx.doi.org/10.1002/pssa.200671403.

[78] I. Kaminker and Songi Han. "Amplification of Dynamic Nuclear Polarization at 200 GHz by Arbitrary Pulse Shaping of the Electron Spin Saturation Profile." In: *The journal of physical chemistry letters* 9 11 (2018), pp. 3110–3115. DOI: 10.1021/acs.jpclett.8b01413.

[79] Ilia Kaminker, Ryan Barnes, and Songi Han. "Arbitrary waveform modulated pulse EPR at 200GHz". In: *Journal of Magnetic Resonance* 279 (2017), pp. 81–90. ISSN: 1090-7807. DOI: https://doi.org/10.1016/j.jmr.2017.04.016. URL: https://www.sciencedirect.com/science/article/pii/S1090780717301167.

[80] Alexander Karabanov et al. "Dynamic nuclear polarization as kinetically constrained diffusion". In: *Physical review letters* 115.2 (2015), p. 020404.

[81] Martin RW. Kelz JI Uribe JL. "Reimagining magnetic resonance instrumentation using open maker tools and hardware as protocol". In: *J Magn Reson* 319 (2020). DOI: 10.1016/j.jmro.2021.100011.

[82] C. W. von Keyserlingk, Vedika Khemani, and S. L. Sondhi. "Absolute stability and spatiotemporal long-range order in Floquet systems". In: *Phys. Rev. B* 94 (8 Aug. 2016), p. 085112. DOI: 10.1103/PhysRevB.94.085112. URL: https://link.aps.org/doi/10.1103/PhysRevB.94.085112.

[83] Vedika Khemani, Roderich Moessner, and SL Sondhi. "A brief history of time crystals". In: *arXiv preprint arXiv:1910.10745* (2019). URL: https://arxiv.org/abs/1910.10745.

[84] Vedika Khemani et al. "Phase Structure of Driven Quantum Systems". In: *Phys. Rev. Lett.* 116 (25 June 2016), p. 250401. DOI: 10.1103/PhysRevLett.116.250401. URL: https://link.aps.org/doi/10.1103/PhysRevLett.116.250401.

[85] Vedika Khemani et al. "Phase structure of driven quantum systems". In: *Phys. Rev. Lett.* 116.25 (2016), p. 250401.

[86] K. Khodjasteh and D. A. Lidar. "Fault-Tolerant Quantum Dynamical Decoupling". In: *Phys. Rev. Lett.* 95 (18 Oct. 2005), p. 180501. DOI: 10.1103/PhysRevLett.95.180501. URL: https://link.aps.org/doi/10.1103/PhysRevLett.95.180501.

[87] Givi Razhdenovich Khutsishvili. "Spin diffusion". In: *Soviet Physics Uspekhi* 8.5 (1966), p. 743.

[88] Rainer Kimmich. *NMR: Tomography, Diffusometry, Relaxometry*. Springer Berlin, Heidelberg, 1997. DOI: 10.1007/978-3-642-60582-6.

[89] Jonathan P King et al. "Optically rewritable patterns of nuclear magnetization in gallium arsenide". In: *Nature communications* 3.1 (2012), pp. 1–7.

[90] W. Köckenberger and J. Matysik. "Hyperpolarization Methods in NMR". In: *Encyclopedia of Spectroscopy and Spectrometry (Third Edition)*. Ed. by John C. Lindon, George E. Tranter, and David W. Koppenaal. Third Edition. Oxford: Academic Press, 2017, pp. 156–162. ISBN: 978-0-12-803224-4. DOI: https://doi.org/10.1016/B978-0-12-409547-2.12203-6. URL: https://www.sciencedirect.com/science/article/pii/B9780124095472122036.

[91] Tomotaka Kuwahara, Takashi Mori, and Keiji Saito. "Floquet–Magnus theory and generic transient dynamics in periodically driven many-body quantum systems". In: *Annals of Physics* 367 (2016), pp. 96–124. ISSN: 0003-4916. DOI: https://doi.org/10.1016/j.aop.2016.01.012. URL: https://www.sciencedirect.com/science/article/pii/S0003491616000142.

[92] Antonis Kyprianidis et al. "Observation of a prethermal discrete time crystal". In: *Science* 372.6547 (2021), pp. 1192–1196. DOI: https://doi.org/10.1126/science.abg8102.

[93] T. D. Ladd et al. "Coherence time of decoupled nuclear spins in silicon". In: *Phys. Rev. B* 71 (1 Jan. 2005), p. 014401. DOI: 10.1103/PhysRevB.71.014401. URL: https://link.aps.org/doi/10.1103/PhysRevB.71.014401.

[94] TD Ladd et al. "Quantum computers". In: *Nature* 464.7285 (2010), pp. 45–53.

[95] Sascha Lange et al. "The effect of biradical concentration on the performance of DNP-MAS-NMR". In: *Journal of magnetic resonance* 216 (2012), pp. 209–212.

[96] Achilleas Lazarides, Arnab Das, and Roderich Moessner. "Equilibrium states of generic quantum systems subject to periodic driving". In: *Physical Review E* 90.1 (2014), p. 012110.

[97] MP Ledbetter et al. "Gyroscopes based on nitrogen-vacancy centers in diamond". In: *Physical Review A* 86.5 (2012), p. 052116.

[98] MP Ledbetter et al. "Gyroscopes based on nitrogen-vacancy centers in diamond". In: *Physical Review A* 86.5 (2012), p. 052116.

[99] L. Liao et al. "Dynamics of a space-time crystal in an atomic Bose-Einstein condensate". In: *Phys. Rev. A* 99 (1 Jan. 2019), p. 013625. DOI: 10.1103/PhysRevA.99.013625. URL: https://link.aps.org/doi/10.1103/PhysRevA.99.013625.

[100] Nai-an Lin and SR Hartmann. "Nuclear Spin-Lattice Relaxation in Ca F 2 via Paramagnetic Centers for Short Correlation Time when Spin Diffusion is Inhibited". In: *Physical Review B* 8.9 (1973), p. 4079.

[101] Herman Lock, Gary E Maciel, and Curtis E Johnson. "Natural-abundance 13C dynamic nuclear polarization experiments on chemical vapor deposited diamond film". In: *Journal of materials research* 7.10 (1992), pp. 2791–2797.

[102] IJ Lowe. "Free induction decays of rotating solids". In: *Physical Review Letters* 2.7 (1959), p. 285.

[103] David J Luitz et al. "Prethermalization without temperature". In: *Physical Review X* 10.2 (2020), p. 021046.

[104] David J. Luitz et al. "Prethermalization without Temperature". In: *Phys. Rev. X* 10 (2 May 2020), p. 021046. DOI: 10.1103/PhysRevX.10.021046. URL: https://link.aps.org/doi/10.1103/PhysRevX.10.021046.

[105] Francisco Machado et al. "Long-Range Prethermal Phases of Nonequilibrium Matter". In: *Phys. Rev. X* 10 (1 Feb. 2020), p. 011043. DOI: 10.1103/PhysRevX.10.011043. URL: https://link.aps.org/doi/10.1103/PhysRevX.10.011043.

[106] Wilhelm Magnus. "On the exponential solution of differential equations for a linear operator". In: *Communications on Pure and Applied Mathematics* 7.4 (1954), pp. 649–673.

[107] P. Mansfield. "Multiple-Pulse Nuclear Magnetic Resonance Transients in Solids". In: *Phys. Rev.* 137 (3A Feb. 1965), A961–A974. DOI: 10.1103/PhysRev.137.A961. URL: https://link.aps.org/doi/10.1103/PhysRev.137.A961.

[108] P. Mansfield. "Pulsed NMR in solids". In: *Progress in Nuclear Magnetic Resonance Spectroscopy* 8.1 (1971), pp. 41–101. ISSN: 0079-6565. DOI: https://doi.org/10.1016/0079-6565(71)80002-X. URL: https://www.sciencedirect.com/science/article/pii/007965657180002X.

[109] N. B. Manson, J. P. Harrison, and M. J. Sellars. "Nitrogen-vacancy center in diamond: Model of the electronic structure and associated dynamics". In: *Phys. Rev. B* 74.10 (2006), pp. 104303–+. DOI: 10.1103/PhysRevB.74.104303.

[110] M Matti Maricq. "Long-time limitations of the average Hamiltonian theory: A dressed-states viewpoint". In: *Advances in Magnetic Resonance: The Waugh Symposium*. Academic Press. 1990, pp. 151–182.

[111] M Matti Maricq. "Spin thermodynamics of periodically time-dependent systems: The quasistationary state and its decay". In: *Physical Review B* 36.1 (1987), p. 516.

[112] M. Mehring. *Principle of High Resolution NMR in Solids*. Springer-Verlag, 1983.

[113] Xiao Mi et al. "Time-Crystalline Eigenstate Order on a Quantum Processor". In: *Nature* (2021), pp. 1–1. DOI: https://doi.org/10.1038/s41586-021-04257-w.

[114] M. Mishkovsky and L. Frydman. "Progress in hyperpolarized ultrafast 2D NMR spectroscopy." In: *Chemphyschem : a European journal of chemical physics and physical chemistry* 9 16 (2008), pp. 2340–8. DOI: 10.1002/cphc.200800461.

[115] T. Mori, T. Kuwahara, and K. Saito. In: *Phys. Rev. Lett.* 116 (2016), p. 120401. URL: http://journals.aps.org/prl/abstract/10.1103/PhysRevLett.116.120401.

[116] John J. L. Morton et al. "Solid-state quantum memory using the 31P nuclear spin". In: *Nature* 455.7216 (2008), pp. 1085–1088. DOI: 10.1038/nature07295.

[117] N Niketic et al. "Polarization analysis in neutron small-angle scattering with a novel triplet dynamic nuclear polarization spin filter". In: *Journal of Applied Crystallography* 48.5 (2015), pp. 1514–1521.

[118] ED Ostroff and JS Waugh. "Multiple spin echoes and spin locking in solids". In: *Physical Review Letters* 16.24 (1966), p. 1097.

[119] Soham Pal et al. "Temporal Order in Periodically Driven Spins in Star-Shaped Clusters". In: *Phys. Rev. Lett.* 120 (18 May 2018), p. 180602. DOI: 10.1103/PhysRevLett.120.180602. URL: https://link.aps.org/doi/10.1103/PhysRevLett.120.180602.

[120] Pai Peng et al. "Floquet prethermalization in dipolar spin chains". In: *Nature Physics* (2021), pp. 1–4.

[121] Pai Peng et al. "Floquet prethermalization in dipolar spin chains". In: *Nature Physics* 17.4 (2021), pp. 444–447. URL: https://www.nature.com/articles/s41567-020-01120-z.

[122] Matthias Pfender et al. "High-resolution spectroscopy of single nuclear spins via sequential weak measurements". In: *Nature Communications* 10.1 (2019), pp. 1–8.

[123] Andrea Pizzi, Andreas Nunnenkamp, and Johannes Knolle. "Classical Prethermal Phases of Matter". In: *Phys. Rev. Lett.* 127 (14 Sept. 2021), p. 140602. DOI: 10.1103/PhysRevLett.127.140602. URL: https://link.aps.org/doi/10.1103/PhysRevLett.127.140602.

[124] I. Popa et al. "Energy levels and decoherence properties of single electron and nuclear spins in a defect center in diamond". In: *Phys. Rev. B* 70.20, 201203 (2004), p. 201203. DOI: 10.1103/PhysRevB.70.201203.

[125] J.G. Powles and P. Mansfield. "Double-pulse nuclear-resonance transients in solids". In: *Physics Letters* 2.2 (1962), pp. 58–59. ISSN: 0031-9163. DOI: https://doi.org/10.1016/0031-9163(62)90147-6. URL: https://www.sciencedirect.com/science/article/pii/0031916362901476.

[126] N V Prokof'ev and P C E Stamp. "Theory of the spin bath". In: *Reports on Progress in Physics* 63.4 (2000), pp. 669–726.

[127] Chandrasekhar Ramanathan. "Dynamic nuclear polarization and spin diffusion in nonconducting solids". In: *Applied Magnetic Resonance* 34.3 (2008), pp. 409–421.

[128] J Randall et al. "Many-body-localized discrete time crystal with a programmable spin-based quantum simulator". In: *Science* 374 (6574), pp. 1474–1478. DOI: 10.1126/science.abk0603.

[129] Andreas Reiserer et al. "Robust quantum-network memory using decoherence-protected subspaces of nuclear spins". In: *Physical Review X* 6.2 (2016), p. 021040.

[130] E.C. Reynhardt. "Spin lattice relaxation of spin-ï¿½ nuclei in solids containing diluted paramagnetic impurity centers. I. Zeeman polarization of nuclear spin system". In: *Concepts in Magnetic Resonance Part A* 19A.1 (2003), pp. 20–35. URL: http://dx.doi.org/10.1002/cmr.a.10077.

[131] EC Reynhardt and CJ Terblanche. "13C Relaxation in Natural Diamond". In: *Chemical Physics Letters* 269.5-6 (1997), pp. 464–468.

[132] W-K Rhim, DP Burum, and DD Elleman. "Calculation of spin–lattice relaxation during pulsed spin locking in solids". In: *The Journal of Chemical Physics* 68.2 (1978), pp. 692–695.

[133] W-K Rhim, DP Burum, and DD Elleman. "Multiple-pulse spin locking in dipolar solids". In: *Physical Review Letters* 37.26 (1976), p. 1764.

[134] W-K. Rhim, D. D. Elleman, and R. W. Vaughan. "Analysis of multiple pulse NMR in solids". In: *The Journal of Chemical Physics* 59.7 (1973), pp. 3740–3749.

[135] W.-K. Rhim, A. Pines, and J. S. Waugh. "Time-Reversal Experiments in Dipolar-Coupled Spin Systems". In: *Phys. Rev. B* 3 (1971), pp. 684–696.

[136] Jared Rovny, Robert L Blum, and Sean E Barrett. "Observation of discrete-time-crystal signatures in an ordered dipolar many-body system". In: *Physical Review Letters* 120.18 (2018), p. 180603.

[137] Jared Rovny, Robert L. Blum, and Sean E. Barrett. "^{31}P NMR study of discrete time-crystalline signatures in an ordered crystal of ammonium dihydrogen phosphate". In: *Phys. Rev. B* 97 (18 May 2018), p. 184301. DOI: 10.1103/PhysRevB.97.184301. URL: https://link.aps.org/doi/10.1103/PhysRevB.97.184301.

[138] Antonio Rubio-Abadal et al. "Floquet Prethermalization in a Bose-Hubbard System". In: *Phys. Rev. X* 10 (2 May 2020), p. 021044. DOI: 10.1103/PhysRevX.10.021044. URL: https://link.aps.org/doi/10.1103/PhysRevX.10.021044.

[139] Antonio Rubio-Abadal et al. "Floquet prethermalization in a Bose-Hubbard system". In: *Physical Review X* 10.2 (2020), p. 021044.

[140] Krzysztof Sacha. "Modeling spontaneous breaking of time-translation symmetry". In: *Phys. Rev. A* 91 (3 Mar. 2015), p. 033617. DOI: 10.1103/PhysRevA.91.033617. URL: https://link.aps.org/doi/10.1103/PhysRevA.91.033617.

[141] Krzysztof Sacha and Jakub Zakrzewski. "Time crystals: a review". In: *Reports on Progress in Physics* 81.1 (2017), p. 016401. URL: https://iopscience.iop.org/article/10.1088/1361-6633/aa8b38.

[142] Ozgur Sahin et al. "Continuously tracked, stable, large excursion trajectories of dipolar coupled nuclear spins". In: *arXiv preprint arXiv:2206.14945* (2022).

[143] Dimitris Sakellariou, Paul Hodgkinson, and Lyndon Emsley. "Quasi equilibria in solid-state NMR". In: *Chem. Phys. Lett.* 293.1 (1998), pp. 110–118. ISSN: 0009-2614. DOI: https://doi.org/10.1016/S0009-2614(98)00725-8. URL: https://www.sciencedirect.com/science/article/pii/S0009261498007258.

[144] Dimitris Sakellariou et al. "Experimental observation of periodic quasi-equilibria in solid-state NMR". In: *Chem. Phys. Lett.* 308.5 (1999), pp. 381–389. ISSN: 0009-2614. DOI: https://doi.org/10.1016/S0009-2614(99)00648-X. URL: https://www.sciencedirect.com/science/article/pii/S000926149900648X.

[145] Edward P Saliba et al. "Electron decoupling with dynamic nuclear polarization in rotating solids". In: *Journal of the American Chemical Society* 139.18 (2017), pp. 6310–6313.

[146] Lea F Santos. "The quick drive to pseudo-equilibrium". In: *Nature Physics* (2021), pp. 1–2.

[147] Adrisha Sarkar et al. "Rapidly enhanced spin polarization injection in an optically pumped spin ratchet". In: *arXiv preprint arXiv:2112.07223* (2021).

[148] Ting Ann Siaw et al. "Effect of electron spin dynamics on solid-state dynamic nuclear polarization performance". In: *Physical Chemistry Chemical Physics* 16.35 (2014), pp. 18694–18706.

[149] K. Singh et al. "Quantifying and Controlling Prethermal Nonergodicity in Interacting Floquet Matter". In: *Phys. Rev. X* 9 (4 Oct. 2019), p. 041021. DOI: 10.1103/PhysRevX.9.041021. URL: https://link.aps.org/doi/10.1103/PhysRevX.9.041021.

[150] K. Singh et al. "Quantifying and Controlling Prethermal Nonergodicity in Interacting Floquet Matter". In: *Phys. Rev. X* 9 (4 Oct. 2019), p. 041021. DOI: 10.1103/PhysRevX.9.041021. URL: https://link.aps.org/doi/10.1103/PhysRevX.9.041021.

[151] C. P. Slichter. *Principles of Magnetic Resonance*. 3rd. Springer-Verlag, 1996.

[152] J. Smits et al. "Observation of a Space-Time Crystal in a Superfluid Quantum Gas". In: *Phys. Rev. Lett.* 121 (18 Oct. 2018), p. 185301. DOI: 10.1103/PhysRevLett.121.185301. URL: https://link.aps.org/doi/10.1103/PhysRevLett.121.185301.

[153] Mark Srednicki. "Chaos and quantum thermalization". In: *Phys. Rev. E* 50 (2 Aug. 1994), pp. 888–901. DOI: 10.1103/PhysRevE.50.888. URL: https://link.aps.org/doi/10.1103/PhysRevE.50.888.

[154] Quentin Stern et al. "Direct observation of hyperpolarization breaking through the spin diffusion barrier". In: *Science Advances* 7.18 (2021), eabf5735.

[155] Susumu Takahashi et al. "Quenching spin decoherence in diamond through spin bath polarization". In: *Physical review letters* 101.4 (2008), p. 047601.

[156] Kenichiro Tateishi et al. "Room temperature hyperpolarization of nuclear spins in bulk". In: *Proceedings of the National Academy of Sciences* 111.21 (2014), pp. 7527–7530.

[157] D Tse and SR Hartmann. "Nuclear spin-lattice relaxation via paramagnetic centers without spin diffusion". In: *Physical Review Letters* 21.8 (1968), p. 511.

[158] Masahito Ueda. "Quantum equilibration, thermalization and prethermalization in ultracold atoms". In: *Nature Reviews Physics* (2020), pp. 1–13.

[159] Szabolcs Vajna et al. "Replica Resummation of the Baker-Campbell-Hausdorff Series". In: *Phys. Rev. Lett.* 120 (20 May 2018), p. 200607. DOI: 10.1103/PhysRevLett.120.200607. URL: https://link.aps.org/doi/10.1103/PhysRevLett.120.200607.

[160] JA Van Wyk et al. "The dependences of ESR line widths and spin-spin relaxation times of single nitrogen defects on the concentration of nitrogen defects in diamond". In: *Journal of Physics D: Applied Physics* 30.12 (1997), p. 1790.

[161] Konrad Viebahn et al. "Suppressing dissipation in a Floquet-Hubbard system". In: *Physical Review X* 11.1 (2021), p. 011057.

[162] Lorenza Viola, Emanuel Knill, and Seth Lloyd. "Dynamical Decoupling of Open Quantum Systems". In: *Phys. Rev. Lett.* 82.12 (1999), pp. 2417–2421. DOI: 10.1103/PhysRevLett.82.2417.

[163] J.S.a b Waugh. "Equilibrium and ergodicity in small spin systems". In: *Molecular Physics* 95.5 (1998), pp. 731–735.

[164] Simon A Weidinger and Michael Knap. "Floquet prethermalization and regimes of heating in a periodically driven, interacting quantum system". In: *Scientific Reports* 7.1 (2017), pp. 1–10.

[165] Phillip Weinberg and Marin Bukov. "QuSpin: a Python Package for Dynamics and Exact Diagonalisation of Quantum Many Body Systems part I: spin chains". In: *SciPost Phys.* 2 (1 2017), p. 003. DOI: 10.21468/SciPostPhys.2.1.003. URL: https://scipost.org/10.21468/SciPostPhys.2.1.003.

[166] Ralph M Wilcox. "Exponential operators and parameter differentiation in quantum physics". In: *Journal of Mathematical Physics* 8.4 (1967), pp. 962–982.

[167] W. M. Witzel and S. Das Sarma. "Concatenated dynamical decoupling in a solid-state spin bath". In: *Phys. Rev. B* 76 (24 Dec. 2007), p. 241303. DOI: 10.1103/PhysRevB.76.241303. URL: https://link.aps.org/doi/10.1103/PhysRevB.76.241303.

[168] W. M. Witzel and S. Das Sarma. "Quantum theory for electron spin decoherence induced by nuclear spin dynamics in semiconductor quantum computer architectures: Spectral diffusion of localized electron spins in the nuclear solid-state environment". In: *Phys. Rev. B* 74.3, 035322 (2006), p. 035322. DOI: 10.1103/PhysRevB.74.035322.

[169] Ralf Wunderlich et al. "Investigation of room temperature multispin-assisted bulk diamond 13C hyperpolarization at low magnetic fields". In: *Journal of Physics: Condensed Matter* 30.30 (July 2018), p. 305803. DOI: 10.1088/1361-648X/aacc32. URL: https://dx.doi.org/10.1088/1361-648X/aacc32.

[170] N. Y. Yao et al. "Discrete Time Crystals: Rigidity, Criticality, and Realizations". In: *Phys. Rev. Lett.* 118 (3 Jan. 2017), p. 030401. DOI: 10.1103/PhysRevLett.118.030401. URL: https://link.aps.org/doi/10.1103/PhysRevLett.118.030401.

[171] N. Y. Yao et al. "Many-Body Localization in Dipolar Systems". In: *Phys. Rev. Lett.* 113 (24 Dec. 2014), p. 243002. DOI: 10.1103/PhysRevLett.113.243002. URL: https://link.aps.org/doi/10.1103/PhysRevLett.113.243002.

[172] Norman Y Yao et al. "Classical discrete time crystals". In: *Nature Physics* 16.4 (2020), pp. 438–447. URL: https://www.nature.com/articles/s41567-019-0782-3.

[173] Bingtian Ye, Francisco Machado, and Norman Y. Yao. "Floquet Phases of Matter via Classical Prethermalization". In: *Phys. Rev. Lett.* 127 (14 Sept. 2021), p. 140603. DOI: 10.1103/PhysRevLett.127.140603. URL: https://link.aps.org/doi/10.1103/PhysRevLett.127.140603.

[174] Chao Yin et al. "Prethermal quasiconserved observables in floquet quantum systems". In: *Physical Review B* 103.5 (2021), p. 054305.

[175] Jiehang Zhang et al. "Observation of a discrete time crystal". In: *Nature* 543.7644 (2017), pp. 217–220. DOI: https://doi.org/10.1038/nature21413.

[176] Hongzheng Zhao et al. "Random Multipolar Driving: Tunably Slow Heating through Spectral Engineering". In: *Physical Review Letters* 126 (4 Jan. 2021), p. 040601. DOI: 10.1103/PhysRevLett.126.040601. URL: https://link.aps.org/doi/10.1103/PhysRevLett.126.040601.